Schweizerische Eidgenossenschaft
Confédération suisse
Confederazione Svizzera
Confederaziun svizra

Road – landslide interaction: Applications

Interaktion Strasse – Hangstabilität: Umsetzung

Interaction route – stabilité des versants: Applications

ETH Zürich
Institut für Geotechnik

Alexander Puzrin, Prof. Dr.
Markus Caprez, Dr.
Andreas Schmid, Dr.
Markus Schwager, Dr.
Dominik Hauswirth, MSc ETH
Pascal Minder, MSc ETH
Philipp Oberender, MSc ETH
Frank Fischli, MSc ETH

Road – landslide interaction: Applications

Interaktion Strasse – Hangstabilität: Umsetzung

Interaction route – stabilité des versants: Applications

ETH Zürich
Institut für Geotechnik

Alexander Puzrin, Prof. Dr.
Markus Caprez, Dr.
Andreas Schmid, Dr.
Markus Schwager, Dr.
Dominik Hauswirth, MSc ETH
Pascal Minder, MSc ETH
Philipp Oberender, MSc ETH
Frank Fischli, MSc ETH

Impressum

Forschungsstelle und Projektteam
Projektleitung
Alexander Puzrin, Prof. Dr.

Mitglieder
Markus Caprez, Dr.
Andreas Schmid, Dr.
Markus Schwager, Dr.
Dominik Hauswirth, MSc ETH
Pascal Minder, MSc ETH
Philipp Oberender, MSc ETH
Frank Fischli, MSc ETH

Federführende Fachkommission
Fachkommission 5: Bautechnik

Begleitkommission
Präsident
Jean-Louis Amiguet

Mitglieder
Walter Steiner, Dr.
Hansjürg Gysi
Françoise Geiser, Dr.
Christoph Gassmann

Antragsteller
Schweizerischer Verband der Strassen- und Verkehrsfachleute (VSS)

Bezugsquelle
Das Dokument kann kostenlos von http://www.mobilityplatform.ch heruntergeladen werden.

Inhaltsverzeichnis

Summary

The goal of this project was to develop new approaches for the monitoring and analysis of creeping landslides affecting the transportation infrastructure, and applying these new approaches to a number of Swiss landslides. In addition, new approaches towards landslide stabilization measures have been investigated. All three goals, monitoring, analysis and stabilisation of landslides are interconnected. Analysis requires monitoring data, stabilization requires understanding of the mechanical behaviour of the landslide through analysis, and to measure effectiveness of stabilization monitoring technologies are required.

This report covers these three major topics.

Tasks one and two describe novel monitoring techniques. **Task three** focuses on chemical and biological stabilization of landslides. Finally **tasks four to nine** demonstrate the analysis of some well known cases of creeping landslides in Switzerland and application of lessons learned from these cases towards other cases concerning danger prevention. Finally the **last section (ten)** draws conclusions and gives recommendations on application of the results and further research.

Overall during this project it became possible to develop new monitoring technologies (fibre optic distributed strain sensing and earth pressure measurements by Inclinodeformeter) to a level where they can be applied successfully in the field. Both of them allow collecting unique data for the analysis of landslides. Bio-chemical stabilization has been evaluated with respect to its application in real soils. By analysing several landslides in Switzerland it was possible to come up with simple mechanical models that are helpful for understanding the complex mechanical behaviour of several types of these landslides. For some of these landslide mechanisms closed form solutions are provided (Brattas, Combe Chopin, Ganter). The effectiveness of laboratory tests in combination with back analysis for determining parameters of a landslide is demonstrated (Braunwald). In cases with insufficient information, the application of the lessons learned from other landslides allows for formulation of investigation programs (Leimbach and God Ruinas).

In general, the project covered all main areas related to creeping landslide analysis. Its conclusions and recommendations will allow for better application of novel analysis, monitoring and stabilization techniques; for better understanding of the existing and future landslides and for mitigation of the landslide hazards in Switzerland. The findings and developments of this research have been presented in numerous scientific publications and have been well received and even awarded by the international geotechnical community.

Zusammenfassung

Die Zielsetzung dieses Projektes war es neue Ansätze für die Überwachung und Analyse von kriechenden Hangrutschungen, welche die Verkehrsinfrastruktur beeinflussen, zu finden. Die Anwendung dieser Ansätze sollte exemplarisch bei mehreren Schweizer Rutschungen demonstriert werden. Des Weiteren wurden auch neue Ansätze für die Stabilisierung von Hangrutschungen untersucht. Diese drei Zielsetzungen, Überwachung, Analyse und Stabilisierung sind natürlich vernetzt. Für die Analyse von Rutschungen benötigt man Daten aus der Überwachung, für Stabilisierungsmassnahmen muss man das mechanische Verhalten der Rutschung analysieren und um wiederum die Wirksamkeit der stabilisierenden Massnahmen zu beurteilen bedarf es neuerlicher Überwachungsmassnahmen.

Dieser Bericht behandelt die besagten drei Hauptthemen:

In den **Tasks eins und zwei** sind neuartige Überwachungstechnologien beschrieben. **Task drei** fokussiert auf chemische und biologische Stabilisierungsmassnahmen. Die übrigen **Tasks vier bis neun** zeigen exemplarisch die Analyse einiger bekannter Hangrutschungen in der Schweiz, sowie die Anwendung der dabei gemachten Erfahrungen zur Gefahrenreduktion bei weiteren Rutschungen. Zuletzt werden in **Task zehn** die Erkenntnisse zusammengefasst und Empfehlungen für die Anwendung in der Praxis respektive für weitere Forschung abgegeben.

Insgesamt konnten während des Projekts neuartige Überwachungstechnologien für Rutschungen (Faser-optische verteilte Dehnungsmessung und Erddruckmessung mittels Inclinoderformeter) soweit entwickelt werden, dass sie jetzt erfolgreich im Feld eingesetzt werden können. Beide Technologien erlauben es Daten über Parameter zu erheben die bisher nur schwer gemessen werden konnten. Die bio-chemische Stabilisierungsmassnahmen wurden betreffend ihrer Einsetzbarkeit in natürlichen Böden untersucht. Durch die Analyse mehrerer Rutschungen in der Schweiz war es möglich einfache mechanische Modelle zu entwickeln, die dabei helfen das komplexe mechanische Verhalten verschiedener Arten von Rutschungen zu verstehen. Für einige dieser Mechanismen werden geschlossene analytische Lösungen gezeigt (Brattas, Combe Chopin, Ganter). In einem anderen Fall ist ein effizientes Verfahren zur Bestimmung von Parametern einer Rutschung durch Labortests und Rückrechnung aufgezeigt (Braunwald). In Fällen mit schlechter Datenlage, erlaubten es die Erfahrungen aus den übrigen Fällen Überwachungsprogramme zu entwickeln (Leimbach und God Ruinas).

Allgemein wurden in diesem Projekt alle Hauptaspekte der Analyse von Hangrutschungen behandelt. Die hier gezogenen Schlussfolgerungen sowie die abgegebenen Empfehlungen werden es erlauben neue Techniken der Analyse, Überwachung und Stabilisierung von Hangrutschungen anzuwenden. Dies sollte zu einem besseren Verständnis der existierenden und zukünftigen Rutschungen in der Schweiz beitragen, sowie dabei helfen die Bedrohung die sich aus diesen Rutschungen ergibt zu entschärfen. Die hier vorgestellten Forschungserkenntnisse und Entwicklungen wurden in zahlreichen wissenschaftlichen Publikationen präsentiert. Sie wurden mit grossem Interesse von der internationalen geotechnischen Gemeinde aufgenommen und sogar ausgezeichnet.

Résumé

Le but de ce projet a été de développer de nouvelles approches pour le monitorage et l'analyse de glissements de terrain en reptation qui influencent les infrastructures de transport, et d'appliquer ces nouvelles approches à un certain nombre de glissements suisses. En plus, de nouvelles approches pour des mesures de stabilisation des glissements ont été étudiées. Tous les trois buts, monitorage, analyse et stabilisation sont interconnectés. L'analyse requiert des données de monitorage. La stabilisation requiert une compréhension du comportement mécanique du glissement par analyse et, pour mesurer l'efficacité d'une stabilisation, des technologies du monitorage sont nécessaires.

Ce rapport traite ces trois buts principaux.

Les Tâches 1 et 2 décrivent des techniques de monitorage innovatrices. **La Tâche 3** attire l'attention sur la stabilisation chimique et biologique des glissements. Enfin, **les Tâches 4 à 9** montrent l'analyse de quelques cas très connus de glissement en reptation en Suisse et l'application de leçons apprises de ces cas à d'autres cas concernant la prévention de danger. Enfin, **le dernier chapitre (10)** tire des conclusions et fournit des recommandations pour l'application des résultats et pour une poursuite de la recherche.

Globalement pendant ce projet, il est devenu possible de développer des nouvelles technologies de monitorage (des mesures par fibre optique de la distribution des déformations et des mesures des pressions de terres par inclinodeformeter) à un tel niveau qu'elles puissent être utilisées avec succès sur le terrain. Tous les deux permettent le rassemblement de données uniques pour l'analyse des glissements. La stabilisation biochimique a été évaluée par rapport à une application dans les sols réels. A travers l'analyse de plusieurs glissements en Suisse, il a été possible de définir des modèles mécaniques simples qui sont utiles pour la compréhension du comportement mécanique complexe de plusieurs types de glissements. Pour quelques-uns de ces mécanismes de glissements, des solutions intrinsèques sont présentées (Brattas, Combe Chopin, Ganter). L'efficacité des essais au laboratoire en combinaison avec une analyse à rebours (back analysis) pour la détermination des paramètres du glissement est démontrée (Braunwald). En cas d'informations insuffisantes, l'application des leçons apprises sur d'autres glissements permet la planification de programmes d'investigation (Leimbach and God Ruinas).

En général, le projet a traité tous les sujets principaux liés à l'analyse de glissements par fluage. Ses conclusions et ses recommandations permettront une meilleure application des techniques innovatrices d'analyse, de monitorage et de stabilisation, pour une amélioration de la compréhension des glissements en cours et futurs et pour la mitigation des risques de glissements en Suisse. Les résultats et les développements de cette recherche ont été présentés dans de nombreuses publications scientifiques et ont été bien reçus et même reconnus par la communauté géotechnique internationale.

Proposed research

This report provides a summary of the results obtained in the research project VSS 2010/502. The tasks according to the research proposal are listed below:

Task 1: Further development of the IDM

The Inclinodeformeter (IDM) is a novel device developed by IGT for back-calculation of the changes of earth pressure with support from the ASTRA/VSS grant VSS 2005/502 "Road-Landslide Interaction" (Schwager et al., 2009). In the first step, IDM measures the change in dimensions of an inclinometer pipe in the sliding layer. The change in shape is assumed to be caused by the changes in the surrounding stress field. In the second step, the measured deformations are used to back-calculate the change in pressure via inverse analysis of the corresponding boundary value problem of a plastic pile surrounded by grout and soil under a changing stress state.

Subtask 1.1: Improvement of accuracy

Subtask 1.2: New analytical and numerical approaches to back-calculation of pressures

Subtask 1.3: Time dependency of measurements

Subtask 1.4: Effects of grout

Task 2: Further development of the FO landslide monitoring techniques

Distributed fibre optic strain sensing technology (BOTDA Brillouin optical time domain analysis) opens new horizons in the field of landslide detection and infrastructure monitoring compared to traditional technologies. The technology uses special tight buffered single mode fibre optic cable for strain and temperature measurement along the fiber. It offers a high resolution of a few microstrains at a spatial resolution of 1m and large application lengths up to 30km.

Subtask 2.1: Design of cables and micro anchors

Subtask 2.2: Full scale shear zone simulation

Subtask 2.3: Further monitoring of the instrumented landslides approaches to back-calculation

Subtask 2.4: Improvement of interpretation techniques

Task 3: Development of chemical and biological stabilization techniques

Drainage of pore water pressures is an effective means to reduce the driving forces of creeping landslides. As conventional drainage systems have a high risk of failure due to differential displacement, a locally increased permeability in the soil itself provides an appropriately deformable drainage system. Infiltration of chemicals, that change the permeability of clayey soils, produces pipe-like zones around boreholes serving as flexible drainage pipes.

Using microorganisms and their specific metabolism is another possibility to improve soil properties in-situ. Soil bacteria can be placed and fed in critical zones by infiltration. Causing the formation of new minerals, these bacteria increase the cohesion between soil particles and thereby contribute to the improvement of slope stability.

Based on laboratory tests the efficiency of the above proposed methods to change soil parameters will be evaluated.

Subtask 3.1: Chemically enhanced drainage

Subtask 3.2: Bioremediation of the negative effects of the chemicals

Subtask 3.3: Strength increase via biomineralization

Task 4: Study of a naturally constrained landslide (Brattas, St. Moritz)

The Brattas landslide stops abruptly in the middle of the town of St. Moritz-Dorf. A special construction law for the effected area exists. The structures in this area have to be strong enough to resist the additional earth pressure and "swim" in the creeping landslide. But what about its long-term stability? If the earth pressure in the compression zone at the bottom of the landslide increases, it may eventually reach the passive pressure and lead to a catastrophic failure of the landslide. The task is to investigate the probability of this scenario. To this end the following subtasks will be performed.

Subtask 4.1: field measurements

Subtask 4.2: laboratory tests

Subtask 4.3: back-calculation using analytical model

Subtask 4.4: numerical verification of the analytical model

Subtask 4.5: conclusions and recommendations

Task 5: Study of an artificial constrained landslide (Combe Chopin)

For construction of the foundation of a bridge, a small landslide was stabilized by a retaining wall. During the construction, the anchors in the retaining wall were prestressed excessively, so that the landslide in its bottom part started moving uphill. At the moment the direction of the displacement has changed and it is now moving downhill. But will the retaining wall be overflown by the landslide in the future? The task is to investigate the probability of this scenario. To this end the following subtasks will be performed.

Subtask 5.1: field measurements

Subtask 5.2: laboratory tests

Subtask 5.3: back-calculation using analytical model

Subtask 5.4: numerical verification of the analytical model

Subtask 5.5: conclusions and recommendations

Task 6: Study of an unconstrained landslide (Braunwald)

The village of Braunwald is built on a creeping landslide. Special for this creeping land-slide is the free pressure boundary condition at the bottom part of the landslide because the village is located on a natural terrace. An extensive drainage system has been planned but not yet installed. For assessment of the effectiveness and optimization of the drainage system the pore water pressure development in the landslide and shear strength degradation are of the greatest interest. How does this pore pressure effect the displacements? The task is to investigate these phenomena. To this end the following subtasks will be performed.

Subtask 6.1: field measurements

Subtask 6.2: laboratory tests

Subtask 6.3: back-calculation using analytical model

Subtask 6.4: numerical verification of the analytical model

Subtask 6.5: conclusions and recommendations

Task 7: Study of the boundry conditions at the bottom of the landslide (Ganter)

The Ganter Bridge is built on an active creeping landslide. Some of its piers are founded in a creep-ing area within large caissons. The upper part of such pier can be shifted uphill to correct the dis-placements. At the bottom part of the creeping landslide there is a riverbed which provides a boundary. Is this a stiff or an elastic boundary? Will the pressure at the bottom grow and exceed the passive pressure causing a collapse? The task is to investigate the probability of this scenario. To this end the following subtasks will be performed.

Subtask 7.1: field measurements

Subtask 7.2: laboratory tests

Subtask 7.3: back-calculation using analytical model

Subtask 7.4: numerical verification of the analytical model

Subtask 7.5: conclusions and recommendations

Task 8: Study of the effect of reactivation of a landslide by construction (Via Laret, St. Moritz)

Via Laret landslide in St Moritz has been discovered in 2008. The hypothesis is that this is a dormant landslide being sporadically reactivated by the construction in the area. When reactivated it causes devastating damage to the property. The task is to collect information to verify this hy-pothesis. To this end the following subtasks will be performed.

Subtask 8.1: field measurements

Subtask 8.2: laboratory tests

Subtask 8.3: numerical model

Subtask 8.4: conclusions and recommendations

Task 9: A novel method for determining soil stiffness in a creeping body (Leimbach)

Leimbach landslide is a slowly creeping landslide in Zurich. It has been used as a testing ground for the IDM application. The task is to demonstrate that combining IDM measurements with inclinometer and geodetic measurements allows for determination of not only the pressure changes but also of the stiffness of the sliding layer.

Subtask 8.1: field measurements

Subtask 8.2: laboratory tests

Subtask 8.3: back-calculation of the soil stiffness by using IDM

Subtask 8.4: validation

Task 10: General conclusions and recommendations

Based on the results of the proposed research the conclusions and recommendations will be made.

I. Further development of the IDM (Task 1)

1 Introduction of the inclinodeformeter device for back-calculation of earth pressure changes

1.1 Abstract

The inclinodeformeter (IDM) is a novel device for measuring changes in earth pressure. The device makes use of the existing and widely used technology of inclinometer measurements. An advantage of the inclinodeformeter is that it does not require any additional infrastructure than standard inclinometer pipes, even long after they have been sheared and become unsuitable for inclinometer measurements. Changes in earth pressure lead to changes in the inclinometer pipe shape and dimensions. If these changes are carefully measured, the pressure increment can be back-calculated from the solution of a boundary value problem with properly described constitutive behaviors of the pipe, the grout and the surrounding soil. The precision of the device is within the range of 0.1 kPa to 0.7 kPa, depending on the stiffness of the soil and the grout surrounding the pipe. Full-scale laboratory tests performed in a 2 m high calibration chamber demonstrate that simple constitutive models can be used for back-calculation as a first approximation.

1.2   Introduction

Earth pressure changes in a sliding layer of a creeping landslide are critical for under-standing, analysis and stabilization of such landslides. Combining measurements of the displacements and the changes in pressure in two sections of a long thin sliding layer (Figure 1-1) allows back-calculation of the average shear strength on the sliding surface and the average lateral stiffness of the soil in the sliding layer.

$$\Delta\tau^* = \frac{H}{L}\left(\Delta p_2 - \Delta p_1\right) \qquad E = \frac{\Delta p}{\Delta\varepsilon} \approx \frac{\left(\Delta p_1 + \Delta p_2\right)/2}{\left(\Delta\delta_1 - \Delta\delta_2\right)/L}$$
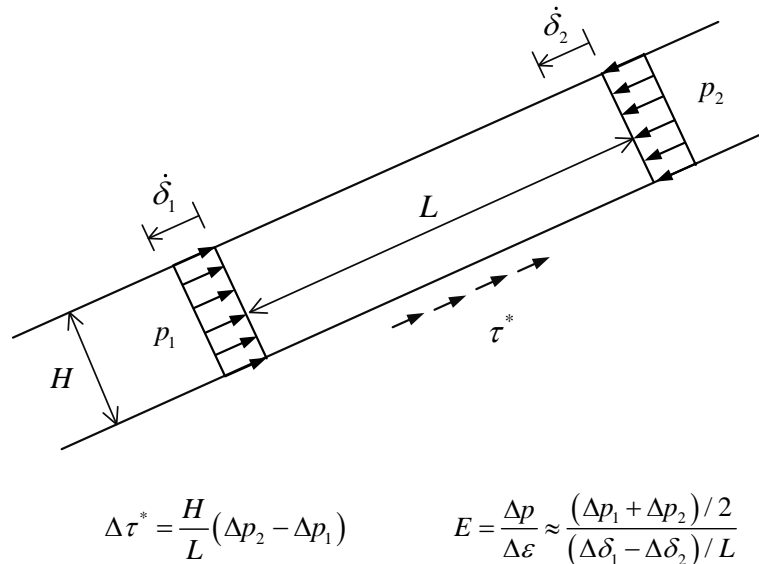
Figure 1-1: Back-calculation of the average shear strength on the sliding surface and average lateral stiffness of soil.

Of even greater importance is information about the earth pressure changes and the stiff-ness for constrained landslides, where the pressures in the compression zone could reach the passive pressure and lead to catastrophic failure (Puzrin and Sterba, 2006). The measurement of the change in earth pressure in a section close to the constrained boundary allows back-calculation of the lateral stiffness (Figure 1-2).

Unfortunately, measuring the earth pressures is also one of the most challenging prob-lems in geotechnical monitoring.

$$E = \frac{\Delta p}{\Delta\varepsilon} \approx \frac{\Delta p L}{\Delta\delta}$$
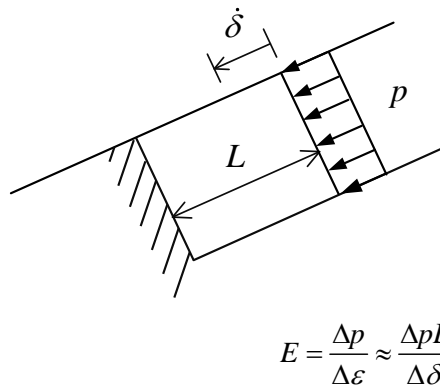
Figure 1-2: Back-calculation of the average lateral stiffness of soil in a constrained landslide.

This chapter introduces a novel device called the inclinodeformeter (IDM) which allows back-calculation of the changes of earth pressure. In the first step, the IDM measures the change in dimensions of an inclinometer pipe in the sliding layer. The change in shape is assumed to be caused by the changes in the surrounding stress field. In the second step, the measured deformations are used to back-calculate the change in pressure via inverse analysis of the boundary value problem of a plastic pipe surrounded by soil under a changing stress state.

This chapter explains the IDM design and the required correction procedure for the deformation measurements, as well as the procedure for back-calculation of the pressure changes in the surrounding soil. These procedures are then validated in full-scale calibration chamber tests.

1.3 Measuring the pipe deformations

1.3.1 IDM design

The inclinodeformeter (IDM) makes use of the existing and widely used technology of in-clinometer measurements. The IDM probe is lowered down the pipe on three wheels, guided along the channels (Figure 1-3). Continuous diameter measurements in two per-pendicular directions can be taken, as described below. The upper and the lower wheels roll in the same channel. These wheels are fixed to the probe. The middle wheel is con-nected via a lever with two springs, so that it can be pressed against the opposite chan-nel. A change in the diameter of the pipe leads to a change of the position of the middle wheel with respect to the probe. There are two tilt sensors (see section 1.3.2) which de-tect the relative inclination between the probe and the lever of the middle wheel. One sensor is located on the top of the probe, another on the middle wheel (Figure 1-3).

In addition to the two tilt sensors in the plane of the measured diameter, there is another tilt sensor which measures in the perpendicular direction out of this plane. This sensor is used for correction of the measurements due to the out-of-plane inclination of the pipe (see section 1.3.3). Above the top wheel there is a temperature sensor and a pressure cell to measure the water pressure in the inclinometer pipe.

At the top of the borehole, the cable on which the device is hanging goes around a wheel (Figure 1-3d). An incremental rotation sensor measures the wheel rotation, which deter-mines the depth position of the probe in the inclinometer pipe. As the probe is lowered down into the inclinometer pipe, all the sensor measurements are saved on the computer for the corresponding depth position in the pipe.

The IDM is built to fit inside the two most common diameters of inclinometer pipes in Switzerland: 71 and 84 mm. The device can be easily switched between the different in-clinometer pipe diameters.

a)

b)

tilt sensors

300 mm

84/71 mm

c)

d)
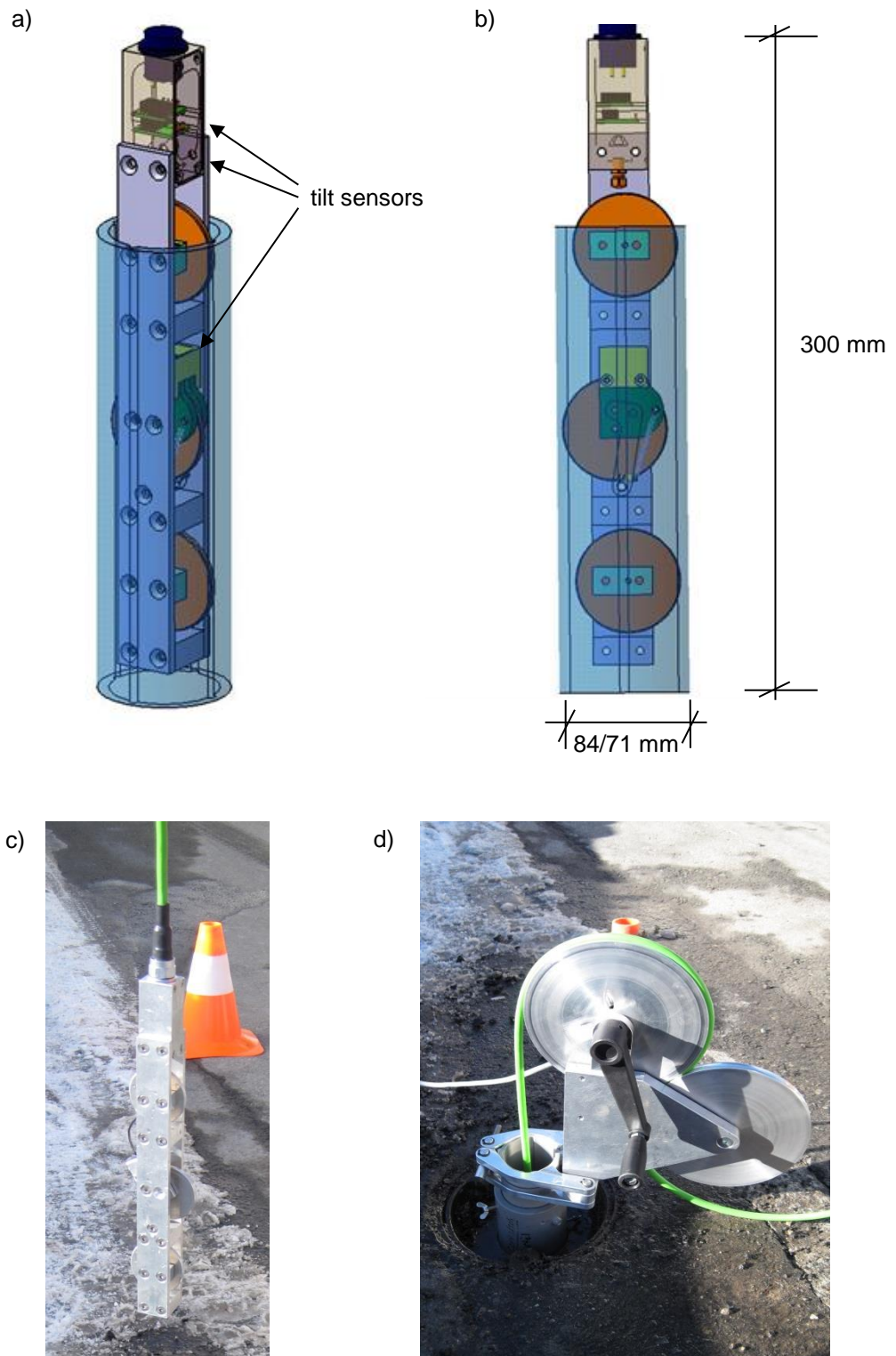
Figure 1-3: *The inclinodeformeter: a) The complete probe, b) The probe without the front panel, c) Picture of the probe, d) Installation at the top of the borehole.*

1.3.2   Performance of the tilt sensors

The tilt sensors are of the type of MEMS accelerometers described e.g. by Sellers and Taylor (2008). This kind of sensor is advantageous for geotechnical monitoring because of the high repeatability and long-term stability of the measurement (Sheahan *et al.*, 2008), as well as extremely high shock resistance. The tilt sensors built into the IDM provide a resolution in terms of the pipe diameter change of 0.1 micrometer. There are two major disadvantages of these tilt sensors. First, the measurements are not independent of the inclination out of the plane. This can be resolved by an external correction (see section 1.3.3). Second, the tilt measurement is dependent on temperature. The measured deformation of the pipe could be affected by +/– 0.5 micrometers per °C in the worst case of accumulation of the errors of both sensors. Measuring the temperature of the ground water in the pipe allows this influence to be corrected for most of the applications.

1.3.3   Correction for the pipe out-of-plane inclination

The measured diameter D inside of the pipe is a function of the two angles α_L and α_P measured at the lever of the middle wheel and at the probe:

$$D = d + X + Y \sin\left(\alpha_L - \alpha_P\right) \tag{1-1}$$

where X, Y and d are constants depending on geometry.

The measurements of α_L and α_P are not independent of the inclination β of the device out of the plane. Assuming that the sensors give the true $(\alpha_L - \alpha_P)$ value at $\beta = 0°$, there is an error occurring in the tilt measurements when β is different from 0°. Because the diameter is just a function of the difference $(\alpha_L - \alpha_P)$, it is sufficient to describe the error Δ affecting this difference. This error can be found by calibration measurements on a biaxial inclinable table (Figure 1-4a).

The error due to the device inclination out of the plane can be described as a function of α_L, α_P and β as follows:

$$\Delta = \left(A_1\alpha_L + A_2\alpha_P + A_3\right)\beta^2 + \left(C_1\alpha_L + C_2\alpha_P + C_3\right)\beta \tag{1-2}$$

where A_1, A_2, A_3, C_1, C_2 and C_3 are constants derived by a regression analysis of the calibration measurements. Correcting the difference $(\alpha_L - \alpha_P)$ by the error function leads to the corrected diameter D_{cor}:

$$D_{cor} = d + X + Y \sin\left(\alpha_L - \alpha_P - \Delta\right) \tag{1-3}$$

By using the error function from Equation (1-2), the corrected measurements of the diameter D reach a precision of +/– 0.5 micrometers within $\beta = +/- 4°$, compared with the measurement at $\beta = 0°$ (Figure 1-4b).
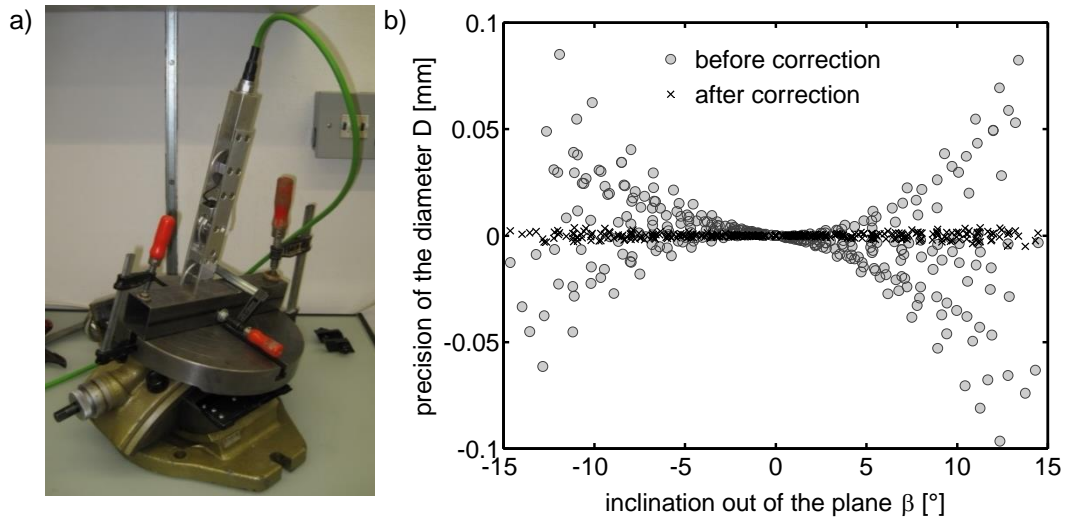
Figure 1-4: *a) The inclinodeformeter on a biaxial inclinable table for calibration measurements, b) The precision of the diameter D compared with the measurement at $\beta = 0°$.*

1.3.4 Ovalization of the inclinometer pipe

The aim of IDM is to obtain measurements of deformations of the inclinometer pipes over a period of several years. It is therefore important to avoid the influence of a possible shift of the device reference. This issue is resolved by describing the shape of the pipe in terms of the difference of two measured diameters. For field applications (as presented in chapter 5), the ovalization value Ω is introduced in the form

$$\Omega = \frac{D_B - D_A}{R} \tag{1-4}$$

where D_A and D_B are the two inner diameters of the inclinometer pipe, and R is the nominal outer radius of the pipe (Figure 1-5). The outer radius R is equal to 35.4 mm and 42 mm for the two most common inclinometer pipes in Switzerland.
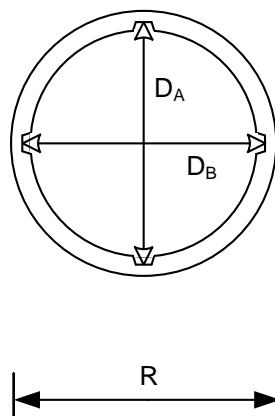
Figure 1-5: *Geometry of the inclinometer pipe.*

Hence, the change in shape of the pipe can be described by the change in ovalization value

$$\Delta\Omega = \Omega - \Omega_0 = \frac{\Delta D_B - \Delta D_A}{R} \tag{1-5}$$

where Ω_0 is the ovalization value at the zero measurement.

The definition of the ovalization value allows for effective reduction of errors affecting both diameter measurements (e.g. influence of the long-term stability of the probe; influence of the actual field conditions: temperature, humidity, water pressures inside and outside the pipe).

1.3.5   Precision of IDM measurements

The precision of a single IDM diameter measurement for a length section of 35 cm of a vertical inclinometer pipe is +/– 1.5 micrometers. Because the tilt sensors on the probe are not independent of the inclination out of the plane, additional scattering is taken into account. Calibration measurements show a remaining error of +/– 0.5 micrometers after the correction of the measurements applying a calibrated error function (section 1.3.3). Hence, the precision of a single diameter reading can be assumed to be around +/– 2 micrometers by combining the variance.

Owing to the definition of the ovalization value (see section 1.3.4), earth pressure changes in field applications are obtained as a function of the change in the difference of the two measured diameters. Taking the difference of several diameter measurements increases the scattering. Nevertheless, the repeatability in field measurements is +/– 2 micrometers as the measurements are averaged over a larger pipe section of 211 cm (section 5.3). Therefore, the precision of the IDM diameter measurements $[\Delta D_B - \Delta D_A]_{min}$ is considered to be 2 micrometers, which corresponds to a precision in terms of ovalization value $\Delta\Omega_{min}$ of $4.8 * 10^{-5}$ or $5.6 * 10^{-5}$ for the different pipes.

1.4   Back-calculating pressures

1.4.1   Boundary value problem

The pressure changes can be back-calculated from a solution of an inverse generalized plane stress boundary value problem (Figure 1-6), from the measured changes in pipe diameters, provided the stiffness of the soil, the stiffness of the grout and the stiffness of the pipe in this range of stresses are known. The boundary conditions in a general case are static: the two principal earth pressures. The major principal stress direction is assumed to coincide with the direction of displacement vector which is known from the conventional inclinometer measurements.
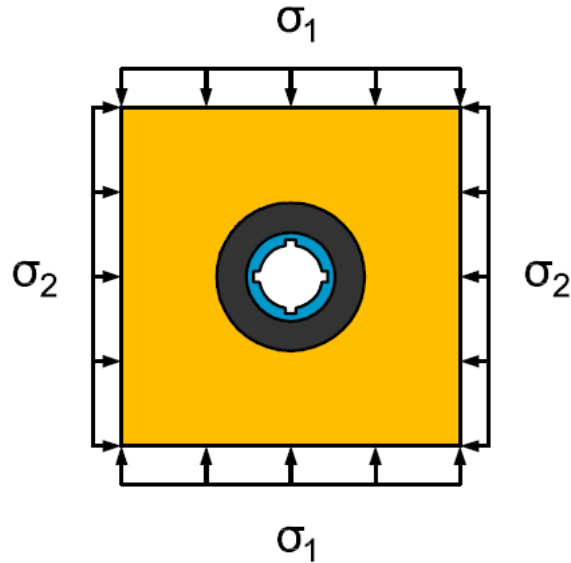
Figure 1-6: *Generalized plane stress model in the case of principal stresses parallel to the axes of the pipe.*

The measured diameters are not only affected by the earth pressure changes. The bending of the inclinometer pipe produced by the movement of the landslide also causes changes in diameter. This correction has to be carried out before modeling in the generalized plane stress problem. The issue of diameter changes due to bending is addressed in chapter 4. An approach allowing for correction of the measurements is provided.

1.4.2 Effects of stiffness

The stiffness of the pipe, the grout and the soil affect the result of the back-calculation significantly. Therefore, it is very important to describe the constitutive behavior of the pipe, the grout annulus and the surrounding soil in an appropriate way. Within this chapter, simplifying assumptions will help to introduce the back-calculation of earth pressures. The influence of the deformation characteristics of the involved materials on the back-calculation is investigated in the following chapters. Chapter 2 deals with the time-dependent behavior of the PVC pipe. The influence of stiffness of the grout is addressed in chapter 3.

Stiffness of the inclinometer pipe

The short-term Young's modulus for fast loading of the inclinometer pipe was determined by compression tests. The pipe was loaded by a linear distributed load in a purpose-built test apparatus (Figure 1-7a). The deformations were measured for several angles between the direction of the force and the direction of the channels in the pipe.
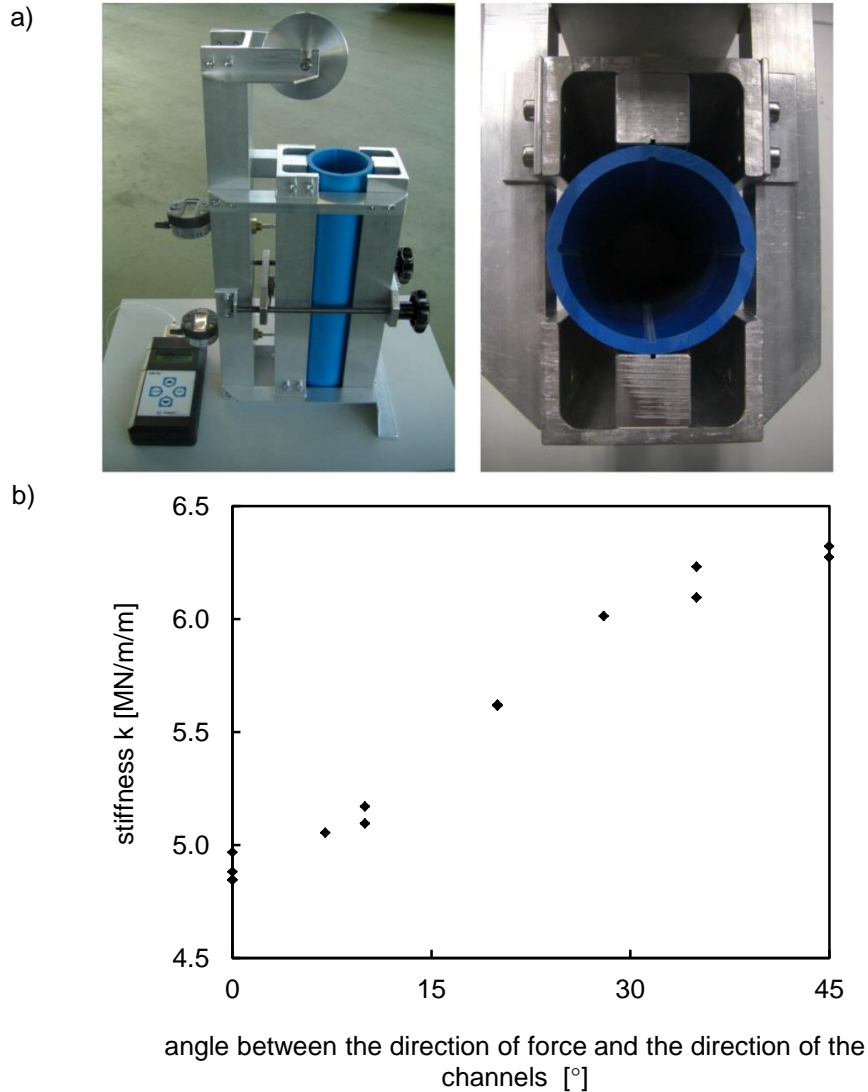
Figure 1-7: a) Compression test on the inclinometer pipe, b) Stiffness k of the pipe as a function of the direction of force.

The tangent stiffness of the pipe k is defined as the ratio between the increment of force f divided by the increment of displacement u (or, more precisely, half of the displacement, owing to the symmetry of the setup):

$$k = \frac{\Delta f}{(\Delta u)/2} \tag{1-6}$$

The stiffness is strongly dependent on the angle between the direction of force and the direction of the channels in the pipe, since they soften the pipe cross-section. The highest stiffness is achieved when there is an angle of 45° between the force direction and the channels (Figure 1-7b). In this configuration, there is hardly any bending moment acting in the area of the channels, where the bending stiffness is reduced significantly.

The Young's modulus of the pipe E_p is related to k by an analytical elastic solution for a solid pipe (without channels) loaded by two opposite forces (e.g. Bouma (1993)):

$$E_p = \frac{2R_m k}{\pi A} + \frac{2R_m^3 k}{\pi I}\left(1/9 + 1/225 + 1/1225 + \ldots\right) \tag{1-7}$$

where R_m = middle radius; A = area of the pipe section; and I = moment of inertia of the pipe section.

Using Equation (1-5) with the stiffness k from the 45° force direction measurement (Figure 1-7b) leads to the immediate Young's modulus of $E_p = 2850$ MPa for fast loading. For back-calculations of pressures in creeping landslides, however, the long-term modulus is of much greater concern than the immediate modulus for fast loading. The viscous behavior of the pipe has to be considered. Within the scope of this chapter, this aspect is not further discussed. More information on this topic is given in chapter 2. The Poisson's ratio of the inclinometer pipe is specified by the producer of the pipe as 0.34.

Stiffness of the grout surrounding the pipe

In many cases, the inclinometer pipe is fixed in the borehole by grouting the annulus using a cement-bentonite mixture. The stiffness of the grout can be estimated from results of laboratory tests (e.g. unconfined compression tests). If the stiffness of the grout differs significantly from that of the surrounding soil, the grouted annulus has to be incorporated into the boundary value problem. In practice, however, it is common to use a grout mixture with a stiffness as close as possible to the surrounding soil. More information on this topic is given in chapter 3.

Stiffness of the surrounding soil

The stiffness of the surrounding soil can be determined from dilatometer tests performed in the same borehole as was drilled for the inclinometer. If no field measurements are available, the stiffness of the soil can be roughly estimated from the results of laboratory tests (e.g. consolidation tests). The loading history and the nonlinearity due to stress dependency have major effects on the soil stiffness, so it is essential to determine the stiffness both in loading and unloading–reloading modes within the stress range expected to be measured by the inclinodeformeter.

The stiffness of the soil may be found from the combination of IDM measurements with measurements of relative displacements. Both earth pressure changes and lateral stiffness can be back-calculated provided lateral strains are known. More information on this topic is given in chapter 5.

1.4.3 Inverse analysis

In general, the soil and the grout behavior have to be modeled as visco-elasto-plastic and that of the pipe as viscoelastic with geometric non-linearity due to the channels. Therefore, the forward boundary value problem is usually solved using numerical analysis. The back-calculation of pressures is performed in two steps: first, a finite element program computes the deformations caused by the trial stresses. An inverse analysis uses the Levenberg–Marquardt algorithm to solve the optimization problem by minimizing the objective function F (the sum of squared errors between the measured and the computed pipe deformations) for the changing trial stresses. This approach based on numerical analysis is used in chapters 1, 2 and 3, regarding laboratory tests.

For certain simplifications of the boundary value problem, an analytical solution can be obtained (chapter 5). For this, the constitutive behavior of the soil is assumed to be linear elastic and the influence of the grout is neglected. Hence, the solution can be applied if the deformation characteristics of the sand can be assumed to be linear within the pressure increment and the stiffness of the grout is similar to the stiffness of the soil. No optimization problem has to be solved using the analytical solution for back-calculation. The analytical solution and its application to field measurements in creeping landslides are shown in chapter 5.

General case with static boundary conditions

In a general case the boundary conditions are given by the two trial principal stresses σ_1 and σ_2. Figure 1-8 shows the objective function F as a function of σ_1 and σ_2. Both the soil and the pipe are assumed to be elastic, with Young's moduli of the soil and the pipe being set to 50 MPa and 2850 MPa, respectively. The Poisson ratios were assumed to be 0.25 and 0.34, respectively. The minimum of the objective function is located at $\sigma_1 = 100 \text{ kPa}$ and $\sigma_2 = 60 \text{ kPa}$.
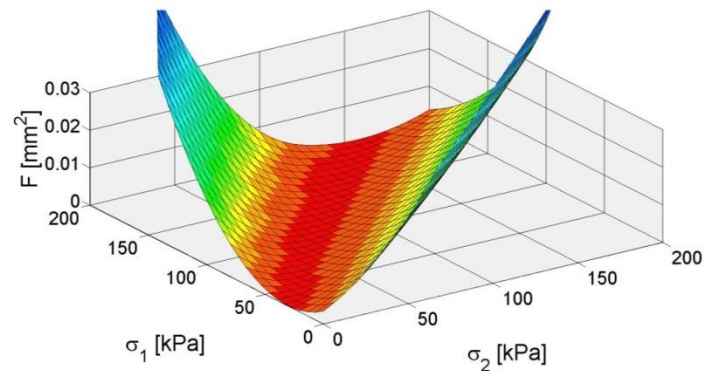
Figure 1-8: *Objective function for inverse analysis with static boundary conditions.*

The low gradient along the objective function "valley" as seen in Figure 1-8 implies that a variety of stress states may lead to similar pipe deformations. This can be explained in that the bending moments cause much bigger deformations of the pipe than normal forces, and different combinations of the stress ratio σ_2/σ_1 and the average stress $(\sigma_1 + \sigma_2)/2$ can produce the same bending moments at different levels of compression of the pipe. From Figure 1-8 it follows that variation in σ_2/σ_1 at a fixed $(\sigma_1 + \sigma_2)/2$ produces larger pipe deformation than the other way round. This makes back-calculation of stress increments more challenging.

Particular case with constrained boundaries

For large creeping landslides with a wide moving front, plane strain conditions can be assumed in the vertical plane parallel to the slope gradient. This implies that there are no displacements perpendicular to that plane. In this particular case, we can solve a problem with kinematically constrained boundary conditions in the direction of the minor principal stress (Figure 1-9). This assumption makes the back-calculation problem well-posed, and the solution can be much more easily reached.
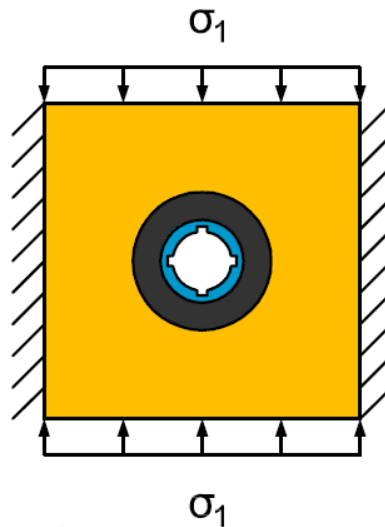
Figure 1-9: *Generalized plane stress model in the case of constrained boundaries in direction of the minor principal stress.*

Figure 1-10 shows the objective function F as a function of σ_1 in this particular case for the same constitutive behavior as in Figure 1-8. Because the behavior of both the pipe and the soil is assumed to be elastic, the plot in Figure 1-10 is in principle a cross-section of the general surface in Figure 1-8 by the plane $\sigma_2/\sigma_1 = \nu_s$ (the Poisson ratio of the soil).
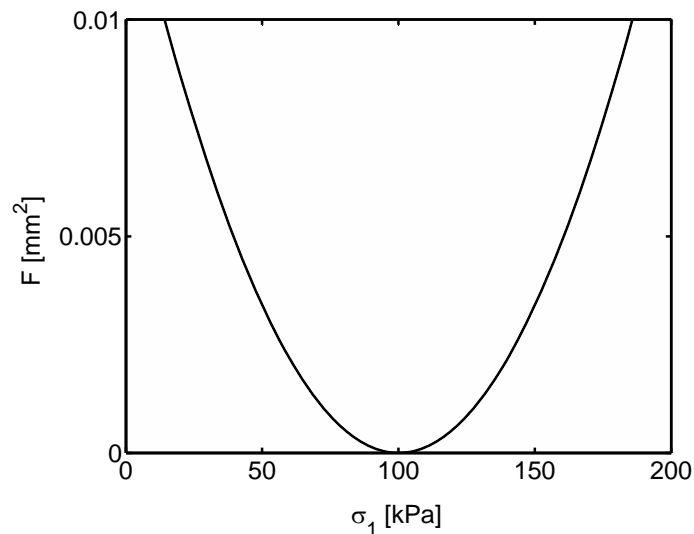
Figure 1-10: *Objective function for inverse analysis with constrained boundary conditions to the sides.*

Using the results of inverse analysis, it is possible to back-calculate the precision of the IDM stress measurements by taking the change in diameters of the pipe equal to the precision of the diameter measurements $[\Delta D_B - \Delta D_A]_{min}$ of 2 micrometers (section 1.3.5). The precision of the IDM for common stiffness of soil and grout is within the range of 0.1 kPa to 0.7 kPa (Figure 1-11). Softer soil leads to a higher precision. It seems that the right choice of grout and its stiffness improves the device capacity: the softer the grout, the higher becomes the precision. This rule is limited to grout stiffness higher than 20 MPa and to stiffness of the ground lower than about 500 MPa. More information on the influence of the grout is given in chapter 3.

a)

b)
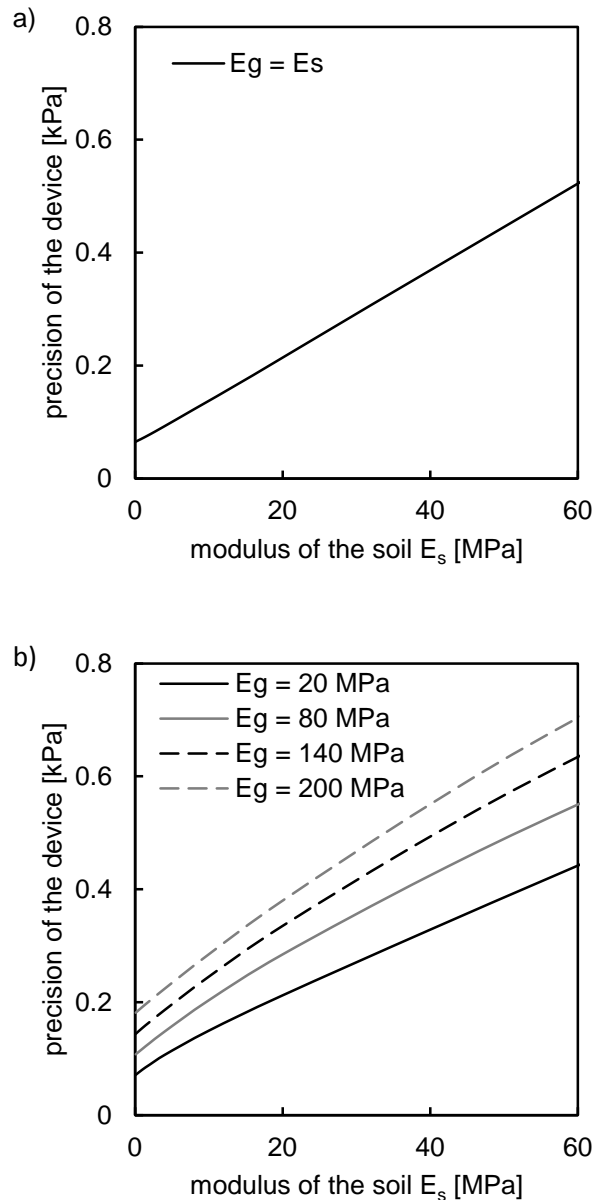
Figure 1-11: *Precision of the IDM stress measurements assuming constrained boundaries, $E_p = 2000\ MPa$, $v_p = 0.34$, $v_s = 0.25$ and $v_g = 0.2$: a) For the grout having the same stiffness as the soil ($E_g = E_s$), b) For different moduli of the grout E_g.*

This precision strongly depends on the model applied for the back-calculation, especially on its boundary conditions. All the three materials involved were assumed to be elastic. Based on chapter 2, the long-term modulus of the pipe is estimated at 2000 MPa in order to account approximately for viscous behavior. The Poisson's ratios of the pipe, the soil and the grout were assumed to be 0.34, 0.25 and 0.2. The outer diameter of the grout annulus is set to a common drilling diameter of 131 mm. A friction coefficient of 0.5 is assumed within the interface surrounding the pipe.

1.5   Validation: IDM box

1.5.1   IDM box: Test setup

For validation of the back-calculation procedure, full-scale laboratory tests were performed in a 2 m high calibration chamber (IDM box) with a cross-section of 40 by 40 cm (Figure 1-12). Each of the four vertical walls of the chamber is equipped with a pressure membrane. The setup allows the application of two independent principal horizontal stresses. The chamber is filled with sand in absence of grout, and the inclinometer pipe is fixed in the middle of the chamber. An increase in principal stresses results in deformations in the pipe which are measured using the inclinodeformeter. More information on the IDM box tests is provided in chapter 3.
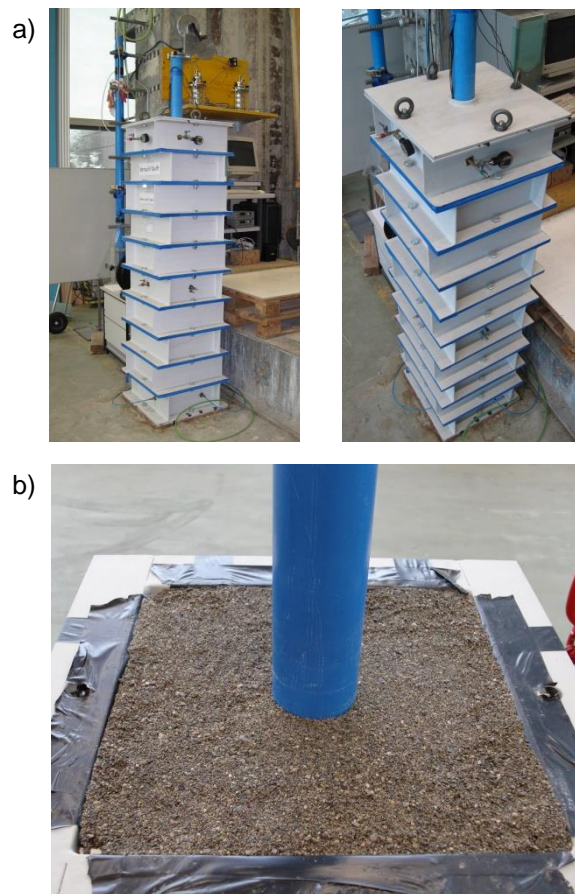
Figure 1-12: a) The IDM box, b) Sand surrounding the pipe in the opened IDM box.

1.5.2   Comparison of applied and back-calculated pressures

The boundary conditions applied during the test are shown in Figure 1-9. The top boundary in the IDM box is constrained, and therefore we consider a boundary value problem with plane strain conditions in vertical direction. The major principal stress σ_1 was applied via a couple of two opposite pressure membranes. The other two pressure membranes were empty and opened to atmospheric pressure in such a way that the boundaries had zero displacements. The loading path was: loading, unloading, reloading and final unloading. The numerical model and its parameters for the back-calculation of pressures are presented in chapter 3. The comparison between applied pressures and pressures back-calculated for both pipe diameters is given in Figure 1-13. It can be seen that an elastic model can be used for back-calculation as a reasonable first approximation. Precision of the pressure measurement corresponding to the precision of the diameter meas-

urement (section 1.3.5) in initial loading is 0.2 kPa, while in unloading–reloading it is 0.6 kPa. As expected, softer soils provide higher precision for pressure measurements.
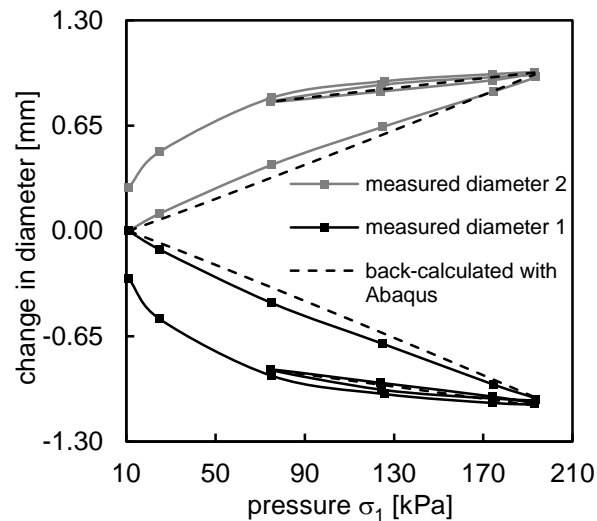
Figure 1-13: *The comparison between the back-calculated and applied pressures in the IDM box experiment with boundary conditions as shown in Figure 1-9.*

Validation using finite elements (Abaqus) showed that for the inclinometer pipe with diameter 84 mm, dimensions of 40 by 40 cm are sufficient to avoid the effect of the boundaries, when comparing with a free field solution. The error in back-calculated pressure for the example considered is within a range of 7%. The error in averaged pressures at the constrained boundaries is within a range of 10%.

1.6 Conclusions

The novel inclinodeformeter device looks promising, owing to its simplicity and accuracy of measurements. In addition, it does not require any additional infrastructure other than standard inclinometer pipes, which are regularly installed anyway for landslide monitoring. Furthermore, these pipes can be used for pressure change measurements in the sliding layer long after they were sheared along the slip surface and became unsuitable for inclinometer measurements. Back-calculation of pressures is a challenging task, which requires the study of such effects as viscosity of the pipe material, stiffness of grout and non-linearity of soil behavior. Nevertheless, full-scale laboratory tests performed in a 2 m high calibration chamber demonstrate that simple constitutive models can be used for back-calculation as a first approximation.

References

Bouma, A. L. (1993). *Mechanik Schlanker Tragwerke: Ausgewählte Beispiele in der Praxis.* Berlin: Springer Verlag.

Puzrin, A. M. & Sterba, I. (2006). Inverse long-term stability analysis of a constrained landslide. *Geotechnique* **56**, No. 7, 483-489.

Sellers, J. B. & Taylor, R. (2008). MEMS basics. *Geotechnical Instrumentation News* **26**, No. 1, 32-33.

Sheahan, T. C., Mazzei, D. & Mcrae, J. (2008). Performance testing of MEMS-based tilt sensors. *Geotechnical Instrumentation News* **26**, No. 1, 33-35.

Notation

A	area of the cross-section of the pipe
A_1	coefficient of the error function
A_2	coefficient of the error function
A_3	coefficient of the error function
C_1	coefficient of the error function
C_2	coefficient of the error function
C_3	coefficient of the error function
D	inner diameter of the inclinometer pipe
D_A	inner diameter of the pipe within the channels in direction A
D_B	inner diameter of the pipe within the channels in direction B
D_{cor}	corrected inner diameter of the inclinometer pipe
d	diameter of the wheels of the probe
E	average lateral modulus of the soil
E_g	Young's modulus of the grout
E_p	Young's modulus of the pipe
E_s	Young's modulus of the soil
F	objective function
H	thickness of the sliding layer
I	moment of inertia of the cross-section of the pipe
k	tangent stiffness of the pipe
L	distance between measurement sections
p	lateral earth pressure
R_m	mean radius of the pipe
X	distance describing the location of the center of rotation of the lever
Y	base length of the lever
α_L	inclination of the lever
α_P	inclination of the probe
β	inclination of the probe out of the plane
Δ	error function due to the inclination out of the plane
ΔD_A	change in diameter in direction A
ΔD_B	change in diameter in direction B
Δf	increment of force
Δp	lateral pressure increment
Δu	increment of radial displacement

$\Delta\delta$	displacement increment
$\Delta\varepsilon$	lateral strain increment
$\Delta\Omega$	change in ovalization value
$\dot{\delta}$	displacement rate
v_g	Poisson's ratio of the grout
v_p	Poisson's ratio of the pipe
v_s	Poisson's ratio of the soil
σ_1	principal lateral earth pressure
σ_2	principal lateral earth pressure
τ^*	average shear strength on the sliding surface
Ω	ovalization value
Ω_0	zero measurement of the ovalization value

$\Delta\delta$ displacement increment

$\Delta\varepsilon$ lateral strain increment

2 Effects of time-dependency on earth pressure measurements taken by inclinodeformeter

2.1 Abstract

The inclinodeformeter (IDM) is a novel device for measuring changes in earth pressures in a sliding layer of a creeping landslide. The change of earth pressures in the sliding layer leads to changes in the shape and dimensions of the inclinometer pipe. If these changes are carefully measured, the pressure increment can be back-calculated from the solution of a boundary value problem with properly described constitutive behaviour of all the materials involved: i.e. the pipe, the grout and the soil.

This chapter focuses on time-dependent mechanical properties of the inclinometer pipe and their effect on the measured changes in pipe diameter. Viscoelastic parameters of the pipe material have been obtained from creep tests and loading tests at a constant stress rate. For validation, full-scale laboratory creep tests were performed in a 2 m high calibration chamber. A numerical model allows for a reasonably accurate back-calculation of the applied pressures at any time during the creep test.

2.2 Introduction

2.2.1 Inclinodeformeter

The inclinodeformeter (IDM) is a novel device for measuring changes in earth pressure in a sliding layer of a creeping landslide (chapter 1). The device makes use of the existing and widely used technology of inclinometer measurements. The change of lateral earth pressures in the sliding layer leads to changes in the shape and dimensions of the inclinometer pipe. If these changes are measured, the pressure increment can be back-calculated from the solution of a boundary value problem with properly described constitutive behaviours of all the materials involved: i.e. the pipe, the grout and the soil.

The deformation characteristics of the pipe are a crucial component of the boundary value problem. Thanks to its industrial production, the behaviour of the pipe is less variable than the behaviour of the grout and the soil. This chapter focuses on time-dependent mechanical properties of a plastic pipe, which is the most commonly used type of inclinometer pipe in Switzerland.

The pipe is made of unplasticized PVC, which is an amorphous thermoplastic polymer. For an ideal thermoplastic material, deformations at constant stress will continuously increase with time (e.g. Brinson & Brinson (2008)). Therefore, in order to be able to back-calculate changes in earth pressures at the time scale of creeping landslides, it is important to describe the long-term stiffness of the pipe in an appropriate way. Unplasticized PVC follows a linear viscoelastic behaviour below the yield point and below the glass transition temperature T_g (Povolo *et al.*, 1996), which was determined to lie within the range of 347 K to 353 K by Becker (1955), Povolo *et al.* (1996) and Domininghaus *et al.* (2008), i.e. considerably higher than the temperature in soil.

The viscous properties of the plastic pipes are normally derived from axial tests, because these are elementary tests with easy interpretation. In this study, viscoelastic parameters of the pipe material have been obtained in the longitudinal and transversal direction by calibrating the linear four-parameter model (Burgers model) against the results of creep tests and element tests at constant rate. The influence of stiffness anisotropy of the pipe material was found to be significant. The viscoelastic model was then incorporated into the finite element analysis of the boundary value problem for the back-calculation of earth pressures and successfully validated against full-scale laboratory tests.

2.3 Pipe behavior in the longitudinal direction

2.3.1 Element test setup

To obtain the time-dependent mechanical properties of the pipe, compression tests were performed on samples in the axial direction. Three different type of compression tests were conducted: displacement controlled loading tests at high stress level to obtain strength (see section 2.3.2), creep tests at low stress level (see section 2.3.4), and loading tests at constant stress rate at low stress level (see section 2.3.5). The different tests were performed with different loading machines: fast loading tests at high stresses were conducted with a hydraulic press (Figure 2-1a). Short-term creep tests and loading tests at constant stress rate were controlled by a step motor (Figure 2-1b). The samples for long-term creep tests were loaded by weight (Figure 2-1c).

a)   b)   c)
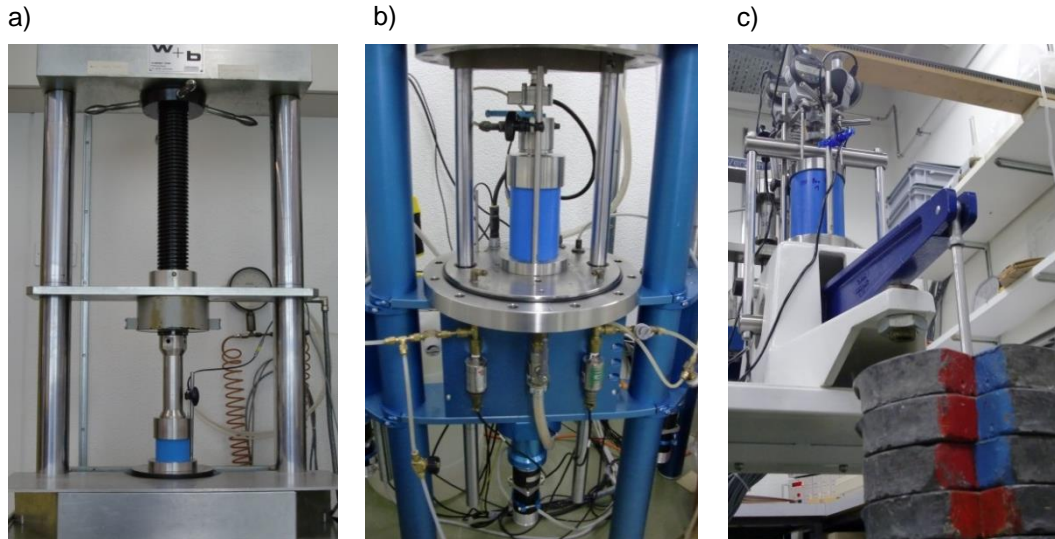
Figure 2-1: Element compression test: a) In a hydraulic press, b) Controlled by a step motor, c) By weight.

The samples have a diameter of 84 mm and a wall thickness of 6.2 mm. The height of the samples in the displacement controlled loading test at high stress level was 55 mm (section 2.3.2). All the experiments performed at low stress level were conducted on samples with a height of 120 mm (sections 2.3.4 and 2.3.5). Numerical calculations with finite elements showed that these experiments can be considered as element tests.

Different pipes were used in the two full-scale experiments which are shown in section 2.5.1. Although they are of the same type of pipe, these two pipes do not have exactly the same properties. Therefore the element tests were performed on samples of both pipes, which are denoted as pipe samples A and B respectively. The difference in properties may be due to different ageing or due to different conditions in production.

2.3.2 Stress-strain behavior

In order to obtain an indication of the stress level below which viscoelastic behavior can be assumed, the pipe was brought to failure. Figure 2-2 shows the stress–strain behavior of samples which were loaded in axial compression at constant strain rates. Uniaxial compressive strength is dependent on the strain rate. The compressive strength for fast loading is about 56 MPa, which is very close to the strength obtained by Pink (1976) and Povolo *et al.* (1996).
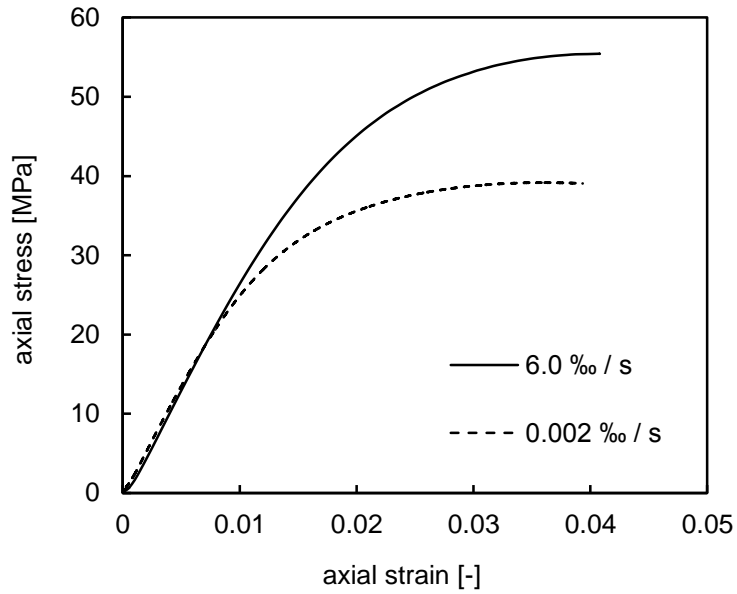
Figure 2-2: *Element compression tests at constant strain rates and 296 K.*

For the slow test the uniaxial compression strength is around 39 MPa. In both tests, the stress–strain behavior could be observed to be completely reversible up to at least 15 MPa. Further considerations within this chapter are focusing on long-term pipe deformations caused at stresses below 15 MPa, because this stress level seems to be sufficient for most of the applications of IDM. Within this range, in accordance with the results of Povolo *et al.* (1996), viscoelastic behavior was assumed.

2.3.3 The four-parameter model

The mechanical analog of the viscoelastic four-parameter model introduced by Burgers (1935) consists of a Maxwell and a Kelvin element connected in series (Figure 2-3).
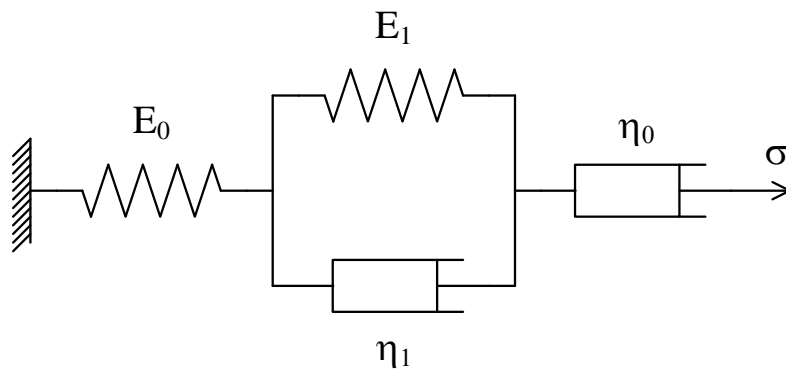
Figure 2-3: *The four-parameter model.*

Its differential stress–strain relation is shown in Equation (2-1).

$$\sigma + \left(\frac{\eta_0}{E_0} + \frac{\eta_1}{E_1} + \frac{\eta_0}{E_1} \right)\dot{\sigma} + \left(\frac{\eta_0 \eta_1}{E_0 E_1} \right)\ddot{\sigma} = \eta_0 \dot{\varepsilon} + \left(\frac{\eta_0 \eta_1}{E_1} \right)\ddot{\varepsilon} \tag{2-1}$$

The strain response for the case of creep with constant stress σ_0 results in (e.g. Brinson & Brinson (2008)):

$$\varepsilon(t) = \sigma_0 \left(\frac{1}{E_0} + \frac{1}{E_1}\left(1 - e^{-\frac{E_1}{\eta_1}t}\right) + \frac{t}{\eta_0} \right)$$ (2-2)

The strain due to loading at constant stress rate $\dot{\sigma}_0$ can be derived in a similar way:

$$\varepsilon(t) = \dot{\sigma}_0 \left(-\frac{\eta_1}{E_1^2}\left(1 - e^{-\frac{E_1}{\eta_1}t}\right) + \frac{1}{2\eta_0}t^2 + \left(\frac{1}{E_0} + \frac{1}{E_1}\right)t \right)$$ (2-3)

For the IDM device both cases of constant stress and of constant stress rate are of special interest: e.g., in Switzerland in some constrained creeping landslides the lateral earth pressure stays constant over the fall and winter and increases linearly with time over the spring and summer (chapter 9). Even if there is expected to be no change in the stress field, pipe deformations at constant stress should be predictable in order to check the hypothesis of no change in earth pressure.

2.3.4   Element creep test

The four-parameter model is assumed to describe the stiffness in uniaxial loading with time. In order to calibrate the four-parameter model, uniaxial element creep tests were performed on samples of both pipes at several stress levels between 4.7 MPa and 8.7 MPa. Figure 2-4 shows the measured strains with time normalized by the constant creep stress σ_0. Initial deformations when applying σ_0 are included. The parameters (Table 2-1) of the four-parameter model were obtained by adjusting the analytical solution in Equation (2-2) to the measured data in Figure 2-4.
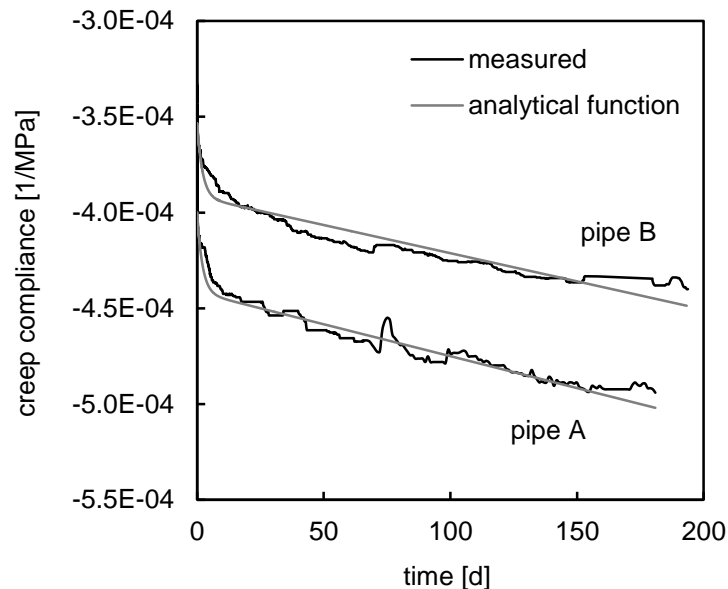
Figure 2-4: *Element creep tests on pipe A and B and analytical creep functions of the four-parameter model. Creep tests at 293.2 K, $\sigma_{0,pipe\,A} = 4.7\,MPa$, $\sigma_{0,pipe\,B} = 8.7\,MPa$.*

The sample of pipe A shows considerably softer behavior. The main difference occurs in the very first day after loading. Therefore initial modulus E_0 is the most affected parameter of the model. To obtain viscoelastic properties for another pipe of the same type it

would be sufficient to perform an element creep test of one day, with loss of minor precision.

Table 2-1: *Parameters of the four-parameter model determined by longitudinal loading of the pipe.*

parameters		pipe A	pipe B
$E_{0\,axial}$	[MPa]	2500	2830
$\eta_{0\,axial}$	[MPa×day]	3.0×10^{6}	3.4×10^{6}
$E_{1\,axial}$	[MPa]	24000	26000
$\eta_{1\,axial}$	[MPa×day]	5.0×10^{4}	5.5×10^{4}

2.3.5   Element test at constant stress rate

Element tests at constant stress rate were also performed, because of its relevance for the application of IDM in creeping landslides. Samples of both pipes were loaded in axial direction with 0.57 MPa/min up to 14 MPa. Figure 2-5 shows the comparison between the measured strain and the strain derived from the analytical function provided by Equation (2-3) and parameters derived from the creep tests and listed in Table 2-1.
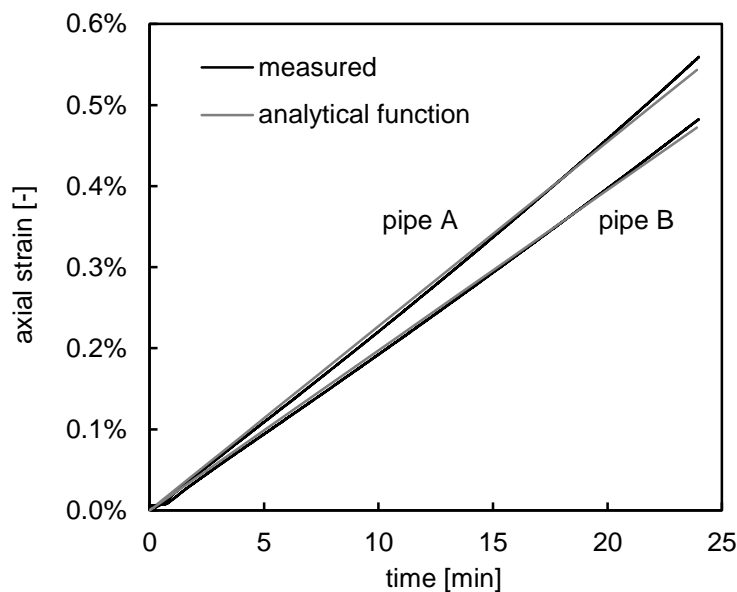
Figure 2-5: *Element tests at constant stress rate on pipes A and B, and analytical creep functions of the four-parameter model. Element tests at 293.2 K, $\dot{\sigma}_0 = 0.57\ MPa/min$.*

The relatively high stress rate and the short duration of the element tests are not representative for creeping landslides. Nevertheless these results may be meaningful with respect to long-term behavior, because the strain is expected to develop almost linearly with time according to the viscoelastic model. The term in Equation (2-3) that depends linearly on time is dominant for the derived parameters (Table 2-1). According to the model, strains should grow for about one year almost uniformly with time for any stress rate.

2.3.6   Influence of water

Inclinometer pipes often go down below the ground water table. Therefore it is essential to check the influence of the water on the stiffness of the material. Preliminary stress relaxation element tests showed that the viscoelastic properties of the pipe material are not affected by the presence of water. Even under water pressure of 500 kPa, the stress relaxation of the sample was identical to that in the test with air at atmospheric pressure surrounding the sample.

2.4   Pipe behavior in transversal direction

2.4.1   Stiffness anisotropy

The anisotropy of the pipe stiffness is a result of its production process. During the extrusion the polymer melt is strained in the flow direction, orientating the polymer molecules and producing stiffer behavior in the axial direction. After the extrusion the melt is cooled from outside. Internal stresses form because parts of the cross-section of the pipe become solid while other parts are still molten. These so-called thermal stresses can also produce anisotropy.

In order to detect this anisotropy, samples of the pipe material (Figure 2-6a) were heated within glycerin above the glass transition temperature T_g. In the rubber elastic state between $T_g = 353$ K and the melting temperature $T_m = 453$ K (Dominghaus *et al.*, 2008) internal stresses are released, producing deformations (Figure 2-6b).

The samples expand in the transversal direction but shrink in the axial direction of the pipe (Figure 2-6c). The observed deformations are indications of the thermal stresses resulting in the stiffness anisotropy.
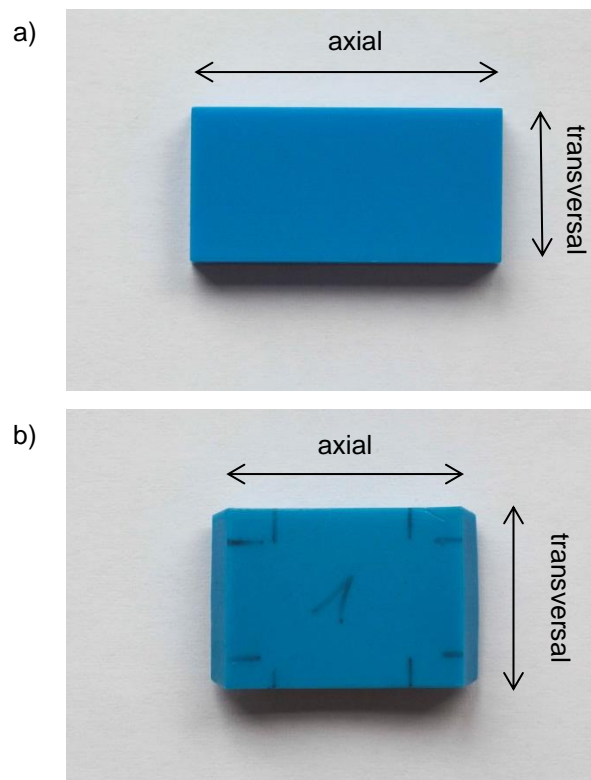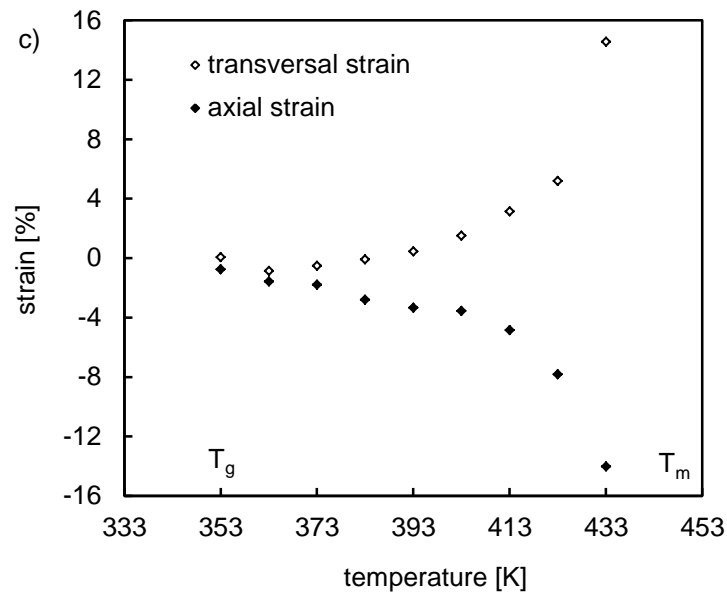
Figure 2-6: *Heating experiment on pipe samples: a) Sample before heating, b) Deformed sample after heating to 433 K, c) Measured strains due to released internal stresses.*

2.4.2   **Transversal loading test setup**

In order to quantify the influence of the observed anisotropy, loading tests were performed on the pipe in the transversal direction. A piece of pipe with a length of 55 mm was subjected to a load applied along a line (Figure 2-7a). For the creep tests, the load was kept constant with time at 200 N. For the constant rate tests, the load was continually increased with time up to 200 N. The load was controlled by a step motor; radial deformations were measured by an LVDT (linear variable differential transformer). On the inside of the pipe there are two pairs of channels, which are used to guide the IDM probe. Loading tests were conducted with the channels rotated by 0° and by 45° with respect to the direction of the force.
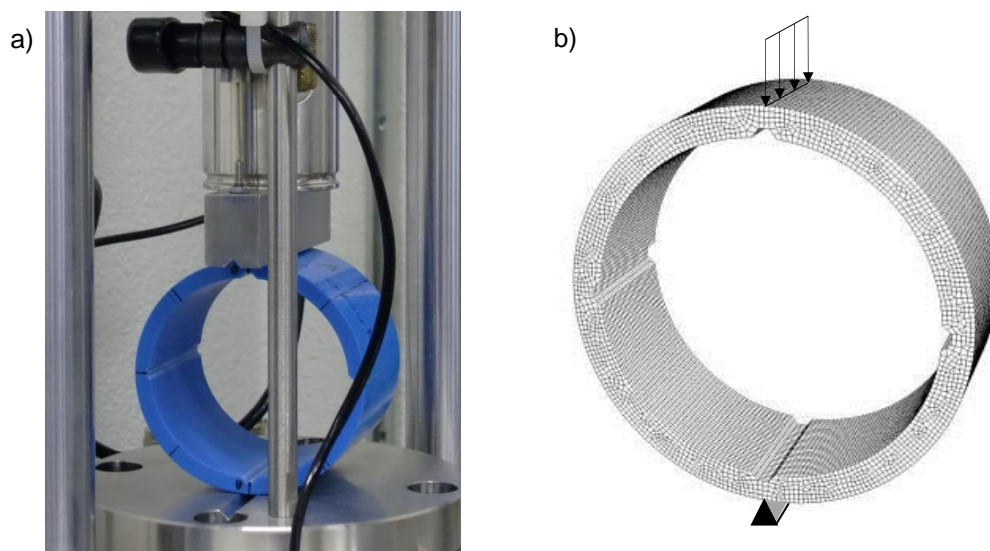
Figure 2-7: *Loading test in transversal direction with the channels parallel to the force: a) Test setup, b) Finite element model.*

2.4.3   Numerical model of transversal loading tests

The boundary value problem of the transversal loading test is solved numerically using finite elements (Abaqus) to be able to compare the observed transversal and axial stiffness on the material level. Because of symmetry, only half of the real length of the pipe has to be taken into account for the finite element model. The piece of pipe loaded on one side by a linear distributed load and supported on the other side along a line is considered as a three-dimensional boundary value problem. The finite element mesh with boundary conditions is shown in Figure 2-7b. Three-dimensional elements (C3D8) with linear shape function and full integration scheme were chosen. Implementation of the viscoelastic constitutive model is described in section 2.5.3.

2.4.4   Transversal creep test

Transversal creep tests indicate considerably softer material behavior in the transversal direction than in the longitudinal direction. Anisotropy is introduced via the elastic components of the four-parameter model (Figure 2-3):

$$f_A = \frac{E_{0transversal}}{E_{0axial}} = \frac{E_{1transversal}}{E_{1axial}} \tag{2-4}$$

The viscous components of the four-parameter model are assumed not to be affected by the anisotropy:

$$\eta_{0axial} = \eta_{0transversal} , \quad \eta_{1axial} = \eta_{1transversal} \tag{2-5}$$

Good agreement between the measured and the calculated creep deformations (Figure 2-8) could be achieved with the parameters (Table 2-2) of the four-parameter model based on a rather reasonable value of $f_A = 0.88$.
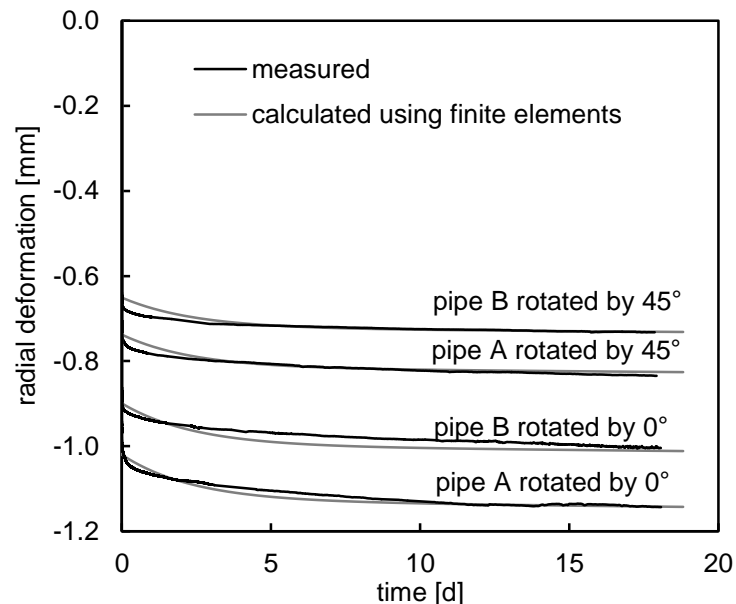
Figure 2-8: *Creep loading tests in transversal direction on pipe A and B and calculated creep deformations using the four-parameter model considering anisotropy with $f_A = 0.88$. Creep tests at 293.2 K.*

The Poisson's ratio of the pipe is assumed to be time independent. It is specified by the producer as 0.34.

Table 2-2: Parameters of the four-parameter model determined by transversal loading of the pipe.

parameters		pipe A	pipe B
$E_{0\ transversal}$	[MPa]	2200	2490
$\eta_{0\ transversal}$	[MPa×day]	3.0×10^6	3.4×10^6
$E_{1\ transversal}$	[MPa]	21120	22880
$\eta_{1\ transversal}$	[MPa×day]	5.0×10^4	5.5×10^4

2.4.5 Transversal test at constant rate

Transversal loading tests at constant rate were also performed, because of their relevance for the application of IDM in creeping landslides. In all the tests, the samples were loaded from 0 to 200 N. Figure 2-9 shows the comparison of the measured and calculated deformations for loading at constant rate over a period of 4 days. The factor of anisotropy $f_A = 0.88$ and the model parameters according to Table 2-2 can be confirmed.
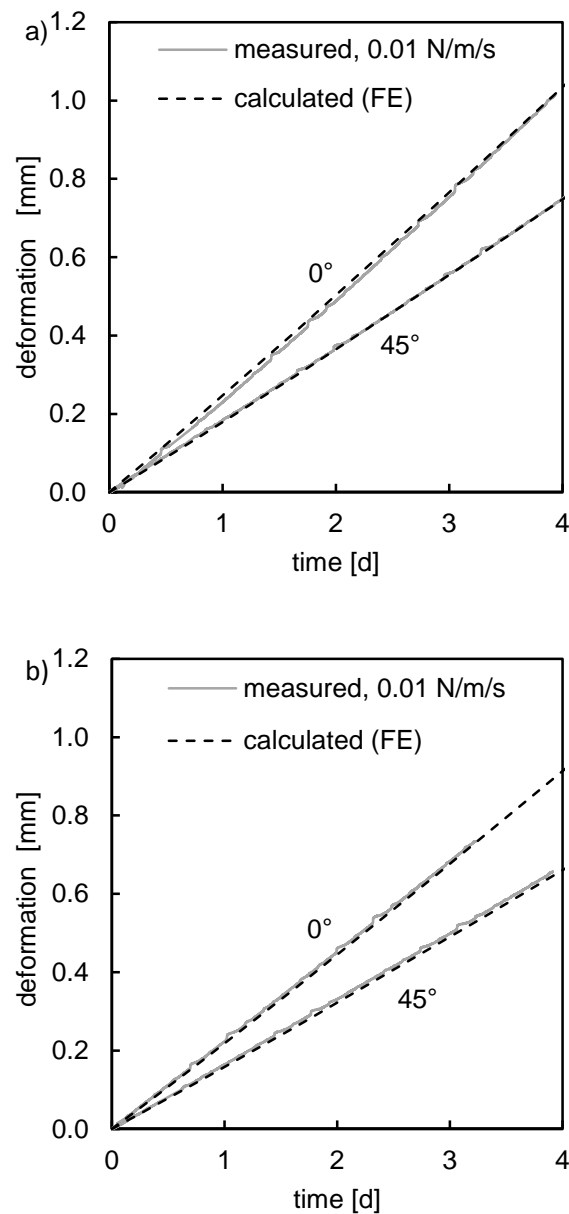
Figure 2-9: Comparison of measured and calculated deformations in loading tests in transversal direction at constant rate of 0.01 N/m/s: a) On pipe A, b) On pipe B. Constant rate tests at 293.2 K.

The loading rate in these tests is too high to be representative for creeping landslides. Nevertheless, the results may be meaningful with respect to long-term behavior. According to the viscoelastic model and the obtained parameters, the deformations should develop proportionally to the loading rate and almost linearly with time. Verification in short-term laboratory tests both of proportionality to the loading rate and linearity with time may allow the proposed model to be assumed in creeping landslides. Therefore, the loading rate was changed in different tests across four orders of magnitude. Measured deformations are normalized by the loading rate (Figure 2-10).
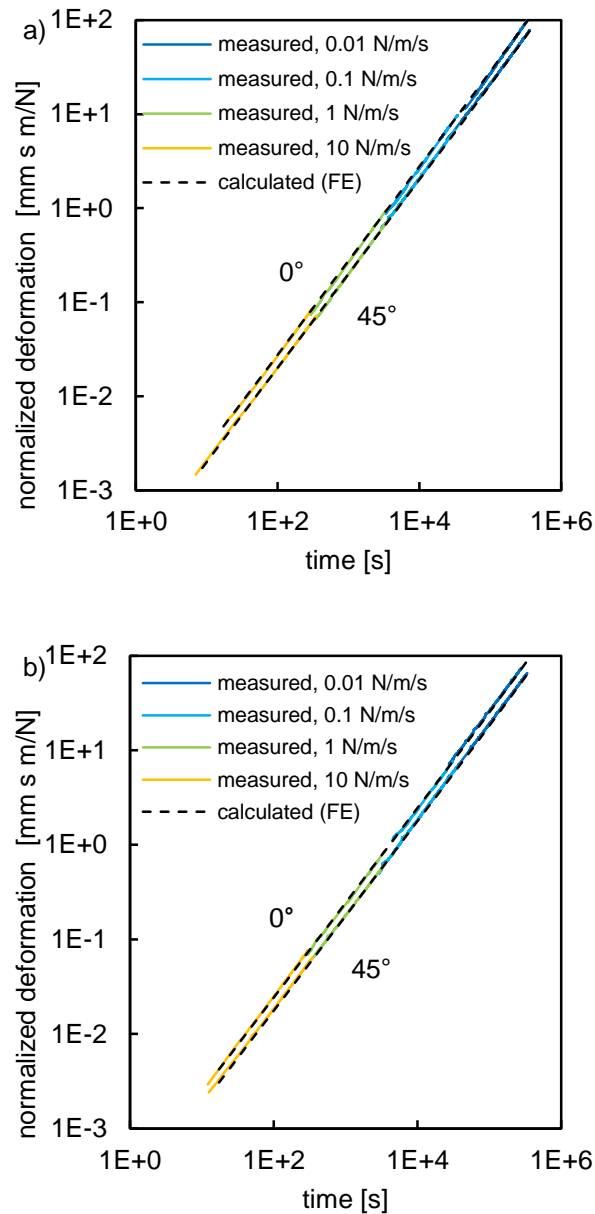
Figure 2-10: *Comparison of measured and calculated deformations in loading tests in transversal direction at constant rate of 10 N/m/s, 1 N/m/s, 0.1 N/m/s, 0.01 N/m/s: a) On pipe A, b) On pipe B. Constant rate tests at 293.2 K.*

The good agreement with the numerical calculations confirms the proportional dependency of the deformations on the loading rate across four orders of magnitude. Also, the linearity with time can be observed between 10 seconds and about 4 days. These results may allow the proposed model to be assumed for long-term behavior.

2.5 Validation of the model

2.5.1 Full-scale laboratory creep test

For validation of the viscoelastic model, full-scale laboratory creep tests were performed in a 2 m high chamber (IDM box). The pipe embedded into a test chamber was subjected to an immediate change in earth pressure. Once the earth pressure reached 125 kPa it was kept constant for more than 300 days.

The calibration chamber has a cross-section of 40 cm by 40 cm. The pipe stands in the middle of the IDM box. In the first test setup, pipe A is surrounded by sand representing the soil; in the second test setup, pipe B is surrounded by a grouted annulus embedded in sand (Figure 2-11).
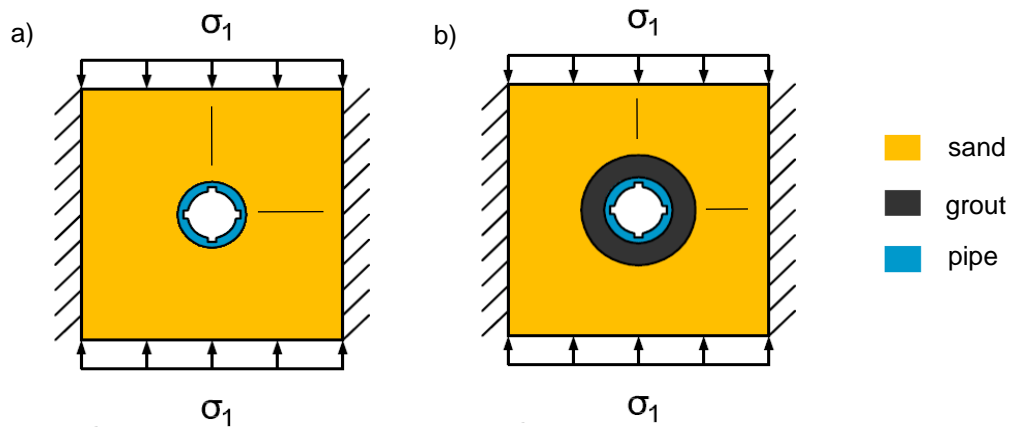
Figure 2-11: *Boundary conditions in IDM box creep tests: a) Test setup without grout, b) Test setup with grout surrounding the pipe, $\sigma_1 = 125\ kPa$, test setup according to chapter 3.*

The earth pressure σ_1 in the principal direction is applied with pressure membranes. The boundary conditions in the minor principal direction are constrained. Deformation measurements of inner diameters are taken by the inclinodeformer.

2.5.2   Numerical model

A horizontal, two dimensional cross-section of the IDM box can be considered as the boundary value problem to be solved using finite elements. The complex visco-elasto-plastic behavior of the grout and the sand is simplified in the numerical analysis in order to focus on effects due to viscoelasticity of the pipe. The stiffness of the sand was measured in element tests (chapter 3). The equivalent stiffness which is applied to the intact grout was determined in order to take the influence of the cracks into account (chapter 3). The derived elastic parameters are adjusted to the actual stress level of the performed creep test and listed in Table 2-3.

Table 2-3: *Elastic parameters of the sand and of the grout.*

parameters		sand	grout
E	[MPa]	6.7	4.5
ν	[-]	0.24	0.2

2.5.3   Implementation of the viscoelastic model

The four-parameter model of Figure 2-3 is equivalent to a generalized Maxwell model consisting of two Maxwell elements connected in parallel (e.g. Bland and Lee (1956)), subject to the proper mapping between the corresponding sets of model parameters.
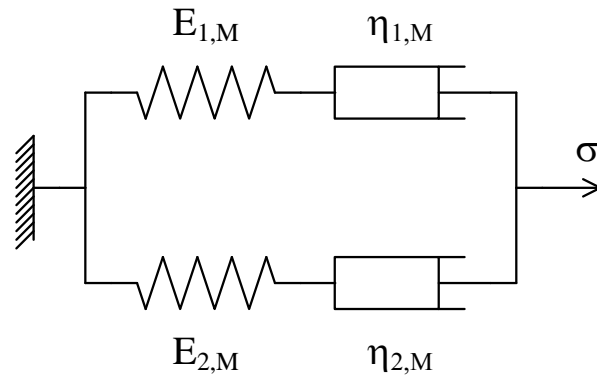
Figure 2-12: *Generalized Maxwell model with two elements.*

The four parameters of the generalized Maxwell model (Figure 2-12) are related to the original four parameters of the model in Figure 2-3 by a set of algebraic expressions. A generalized Maxwell model can be easily incorporated into common finite element codes using a Prony series. Parameters in Table 2-1 and Table 2-2 were therefore transferred into parameters of a generalized Maxwell model (Table 2-4) for implementation.

Table 2-4: *Parameters of the generalized Maxwell model in axial and transversal directions of the pipe.*

parameters		pipe A	pipe B
$E_{1,M\ axial}$	[MPa]	2263	2551
$\eta_{1,M\ axial}$	[MPa×day]	3.0×10^6	3.4×10^6
$E_{2,M\ axial}$	[MPa]	237	279
$\eta_{2,M\ axial}$	[MPa×day]	446	531
$E_{1,M\ transversal}$	[MPa]	1992	2245
$\eta_{1,M\ transversal}$	[MPa×day]	3.0×10^6	3.4×10^6
$E_{2,M\ transversal}$	[MPa]	208	245
$\eta_{2,M\ transversal}$	[MPa×day]	446	531

2.5.4   Comparison

Comparisons of the measured and the calculated changes in pipe diameters during the creep tests in the IDM box are shown in Figure 2-13. The linear (viscous) term in the model (see Equation 2-2) seems to reproduce the observed behavior very well after 10 days. Rather good agreement has also been achieved in the period between 1 and 10 days, which is mainly controlled by the exponential (delayed elastic) term. The defor-mations occurring in the very first day of the creep tests are underestimated by about 11% by the numerical model based on the parameters derived from element tests in the pipe's longitudinal direction.

Significantly better agreement can be achieved by using the parameters of the four-parameter model obtained in the transversal direction of the pipe to take account of the stiffness anisotropy (Figure 2-13).
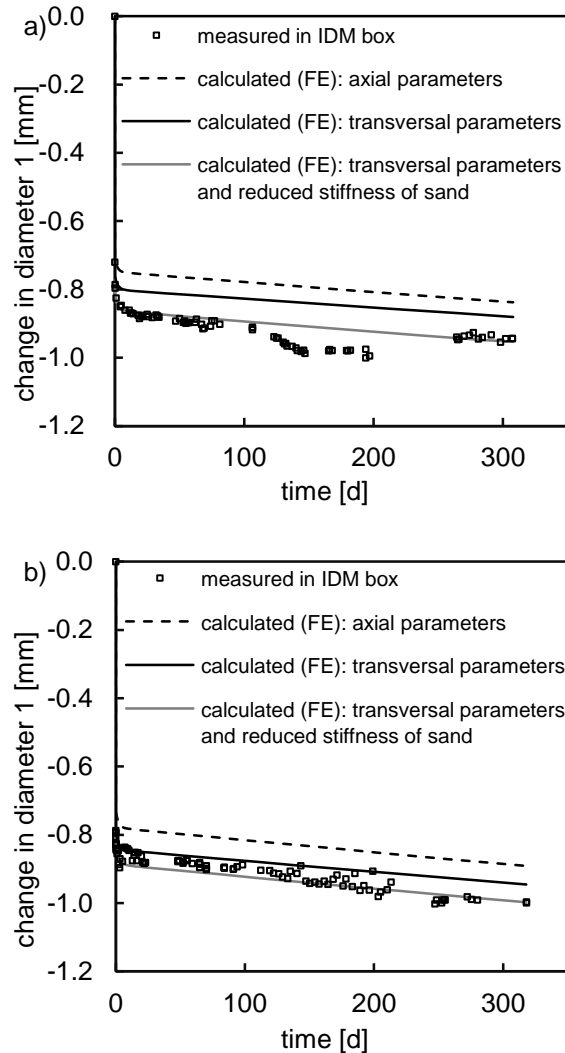
Figure 2-13: *Comparison between the measured and the calculated changes in diameter: a) Experiment with only sand surrounding the pipe A, b) Experiment with grout surrounding the pipe B.*

2.5.5 Discussion

Even after taking anisotropy into account, the calculated initial deformations are still about 6% smaller than the measured deformations. One possible explanation is that the stiffness of the sand in the box is likely to be lower at low pressures than that obtained from the element tests owing to the better controlled preparation of the sample in the element tests.

In order to quantify this effect, the stiffness of the sand was adjusted to provide the best fit to the data in Figure 2-13. The resulting value of Young's modulus taken for the sand, 5.8 MPa, appeared to be consistent with the stiffness values back-calculated from the previous box experiments with fast loading. This confirms that the lower stiffness of the sand is the likely reason for the remaining deviation (Figure 2-13).

2.6   Back-calculating pressures

The pressure changes can be back-calculated from the measured diameter changes using the solution of the inverse boundary value problem, provided the stiffness of the materials involved is known (see chapter 1).

For a time-dependent inverse analysis the pressure history has to be known or assumed. The applied pressure in the IDM box test could be back-calculated because both the time when the pressure was applied and the fact that it stayed constant are known. Based solely on the parameters derived from element tests, the back-calculated pressures for both tests are about 11% higher than the applied pressure. While for the majority of field applications this accuracy is reasonable, efforts to account for the pipe's anisotropy can improve the accuracy of back-calculation of pressures. The error in the back-calculated pressures could be demonstrated to be as low as 6% when pipe anisotropy is taken into account.

2.7   Conclusions

Time-dependent deformations of an inclinometer pipe can be described by the viscoelastic four-parameter model. Normally, viscous properties of the plastic pipes are derived from axial tests, because these are elementary tests with easy interpretation. In this study, stiffness anisotropy between axial and transversal pipe directions was found to have a significant influence and could be effectively introduced into the model in a rather simple way. The model and its independently determined parameters could be successfully validated in full-scale laboratory experiments.

The viscoelastic model with parameters defined from the transversal direction tests is essential for field applications of IDM. It can provide reliable back-calculation of pressures both for instantaneous and continuously applied loads.

References

Becker, G. W. (1955). Mechanische Relaxationserscheinungen in nicht weichgemachten hochpolymeren Kunststoffen. *Colloid and Polymer Science* **140**, No. 1, 1-32.

Bland, D. R. & Lee, E. H. (1956). On the determination of a visco-elastic model for stress analysis of plastics. *Journal of Applied Mechanics* **23**, 416–420.

Brinson, H. F. & Brinson, L. C. (2008). *Polymer Engineering Science and Viscoelasticity, An Introduction.* New York: Springer.

Burgers, J. M. (1935). Mechanical considerations, model systems, phenomenological theories of relaxation and of viscosity. *First Report on Viscosity and Plasticity.* New York: Nordemann Publishing Company.

Domininghaus, H., Elsner, P., Eyerer, P. & Hirth, T. (2008). *Kunststoffe, Eigenschaften und Anwendungen.* Berlin: Springer.

Pink, E. (1976). Thermally-activated yield behavior of glassy polyvinyl-chloride in tension and compression – conventional analysis. *Materials Science and Engineering* **24**, No. 2, 275-282.

Povolo, F., Schwartz, G. & Hermida, E. B. (1996). Stress relaxation of PVC below the yield point. *Journal of Polymer Science Part B – Polymer Physics* **34**, No. 7, 1257-1267.

Notation

E	Young's modulus
E_0	elastic parameter of the Burgers model (four-parameter model)
E_1	elastic parameter of the Burgers model (four-parameter model)
$E_{1,M}$	elastic parameter of the generalized Maxwell model
$E_{2,M}$	elastic parameter of the generalized Maxwell model
f_A	factor of anisotropy for the elastic stiffness components
T_g	glass transition temperature
T_m	melting temperature
t	time
ε	strain
η_0	viscous parameter of the Burgers model (four-parameter model)
η_1	viscous parameter of the Burgers model (four-parameter model)
$\eta_{1,M}$	viscous parameter of the generalized Maxwell model
$\eta_{2,M}$	viscous parameter of the generalized Maxwell model
ν	Poisson's ratio of the pipe
σ	stress
σ_0	constant creep stress
$\dot{\sigma}_0$	constant stress rate

3 Influence of the grout on earth pressure measurements taken by inclinodeformeter

3.1 Abstract

The grout is used as a backfill of the free space in the borehole around the pipe. It transfers the earth pressure from the ground to the pipe, effecting its deformation. Therefore, understanding the influence of the mechanical behavior of the grout is important for earth pressure measurements taken by IDM. The mechanical properties of the grout can be chosen via its composition. Based on laboratory tests on different grout compounds, a procedure is developed to design the optimal grout composition according to the requirements of IDM measurements.

In this chapter, the effects of the grout on the back-calculation of lateral earth pressures are investigated using physical and numerical modeling. In the analysis, the linear elastic model is used for the grout and the soil; the linear viscoelastic four-parameter model is used for the pipe. The required material parameters are derived from independent element tests. The back-calculation is successfully validated against full-scale laboratory tests. The parameters obtained from the element material tests allowed a precise back-calculation of the applied pressures. The back-calculation of pressure increments is shown to be reliable and almost independent of initial conditions. The smallest detectable pressure increment is as small as 0.2 kPa.

Cracks in the cement-bentonite grout ring can reduce its stiffness significantly. Fortunately, the back-calculation of pressures is not sensitive to the stiffness of the grout ring. Less than a twofold increase in the back-calculated stress increments is caused by a tenfold increase in the stiffness of the grout. Below the ground water table, the grout is likely to be intact. In dry soils, where the cement-bentonite grout is prone to shrink and crack, sand may be used as an alternative to refill the borehole.

3.2 Introduction

The inclinodeformeter (IDM) is a novel device for back-calculation of changes in lateral earth pressure. A change in lateral earth pressure leads to changes in shape and dimensions of the inclinometer pipe. Provided that these changes are measured, the pressure increment can be back-calculated from the solution of the corresponding boundary value problem.

The grout is used as a backfill of the free space in the borehole around the pipe. It transfers the earth pressure from the ground to the pipe, causing its deformation. Therefore, understanding the influence of the mechanical behavior of the grout is important for earth pressure measurements taken by IDM.

Cement-bentonite grout is used most commonly to refill boreholes. Guidelines for the composition of the mixture and for the mixing process are provided by Mikkelsen (2002) regarding application to borehole instruments. If the grout is used for inclinometers, it should satisfy the criteria of maximum and minimum strength according to Dunnicliff (1988, 1993).

Choosing the composition of the grout mixture provides the opportunity to control the mechanical properties of the grout. The general rule is to mimic the strength and deformation characteristics of the surrounding soil (Mikkelsen, 2002). The stiffness of the grout is of major concern for IDM. The stiffness of the grout affects the measured deformations of the pipe. Therefore, the potential for back-calculation of earth pressures is influenced by the stiffness of the grout. Based on laboratory tests on different grout compounds, a procedure is developed to design the optimal grout composition according to the requirements of IDM measurements.

In this chapter, the effects of the grout on the back-calculation of lateral earth pressures are investigated using physical and numerical modeling. In the analysis, the linear elastic model is used for the grout and the soil; the linear viscoelastic four-parameter model is used for the pipe. The required material parameters are derived from independent element tests. The back-calculation is successfully validated against full-scale laboratory tests.

3.3 Full-scale laboratory tests

3.3.1 Test setup

Full-scale laboratory tests were carried out in a 2 m high calibration chamber (IDM box, Figure 3-1) to study the influence of the mechanical behavior of the grout. Within the chamber, the pipe surrounded by a grouted annulus surrounded by soil is subjected to earth pressure changes. For comparison, the experiment is also performed in the absence of grout with only soil surrounding the pipe. A well-graded sand is used for the soil.
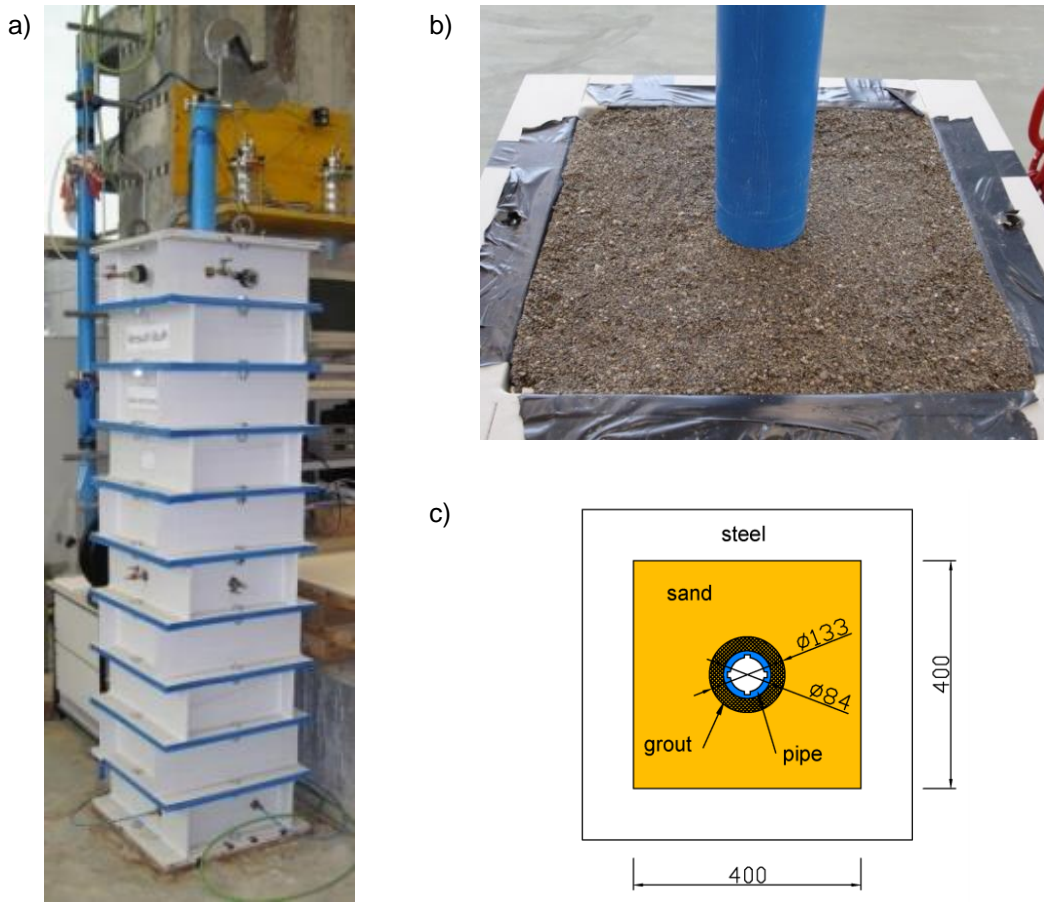
Figure 3-1: *The IDM box: a) View from outside, b) Sand surrounding the pipe in the opened IDM box, c) Dimensions of the cross-section of the IDM box.*

The calibration chamber has a cross-section of 40 by 40 cm^2 and is equipped with pressure membranes on each of the four inner walls (Figure 3-1c). Two independent principal horizontal stresses can be applied. The inclinometer pipe is fixed in the middle of the box. It is surrounded by either sand alone or a grout annulus surrounded by sand (Figure 3-2).
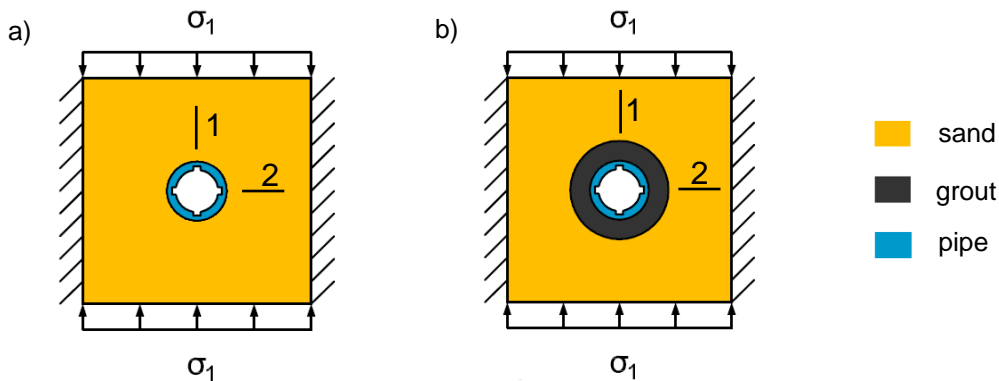
Figure 3-2: *Boundary conditions in IDM box loading tests: a) Experiment without grout, b) Experiment with grout surrounding the pipe.*

The pressure membranes are generally inflated by compressed air. The membranes in the major principal direction (direction 1) are inflated, applying pressure on the soil. The membranes in the minor principal direction (direction 2) are opened to atmospheric pressure, providing constrained boundary conditions. The pressure membranes can also be operated with water. Closing the water-filled membranes in the minor principal direction

provides the opportunity to measure the minor principal stress at the constrained boundary. The kinematically constrained boundary conditions to the sides in the direction of the minor principal stress are representative for many problems in geotechnical engineering. In particular, for large landslides with a wide moving front, plane strain conditions can be assumed in the vertical plane parallel to the slope. The IDM box is closed at its top with a steel plate. Therefore, no deformation can occur in the vertical and third principal direction. The deformations of the pipe are measured. The IDM device is used to take readings of the inner diameters in direction 1 and direction 2.

Numerical calculations showed that the differences in pressures and deformations due to the dimensions of the IDM box are small compared with a model with larger dimensions representing a free field solution.

3.3.2 Composition of the grout

A cement-bentonite grout is used for the experiments, because this type of grout is widely used in geotechnical practice. The grout mixture is made of water, type 1 Portland cement and sodium bentonite. The grout compound was chosen to fulfill requirements of workability (feasibility to pump), sedimentation (no bleeding), strength and stiffness (see section 3.8). The chosen grout compound has a weight ratio of water : cement : bentonite equal to 2.6 : 1: 0.4.

The water and the cement are mixed first, as described by Mikkelsen (2002). The bentonite is added later. This mixing procedure allows control of the water–cement ratio of the grout, which has a strong influence on its properties. Hence, the strength and the stiffness of the grout are better controlled. The water–cement paste and the cement–bentonite grout were both mixed for five minutes in a planetary paddle mixer as described by Contreras *et al.* (2008).

3.3.3 Experimental results

The soil in the calibration chamber was subjected to loading, unloading, reloading and eventually full unloading (Figure 3-3). Therefore, the pressure σ_1 at the static boundary condition in direction 1 was increased to 200 kPa, then reduced to 75 kPa, increased to 200 kPa and eventually released to zero pressure. Diameter 1 in direction of the applied stress becomes smaller with increasing pressure σ_1, whereas diameter 2 in the perpendicular direction becomes larger. The measurements at low pressures were ignored before the membranes opened overcoming the earth pressure at rest. Owing to leaking of the membranes, the experiment in absence of grout could only be conducted up to 194 kPa.

Non-reversible deformations are observed in both experiments. In both experiments, deformations due to unloading or reloading seem to be reversible provided the pressure does not drop too much in the unloading phase. Pipe deformations are observed to depend almost linearly on the pressures in the loading phase and in the reversible part of the unloading phase. The behavior is even more linear in the experiment with grout than in the experiment without grout.
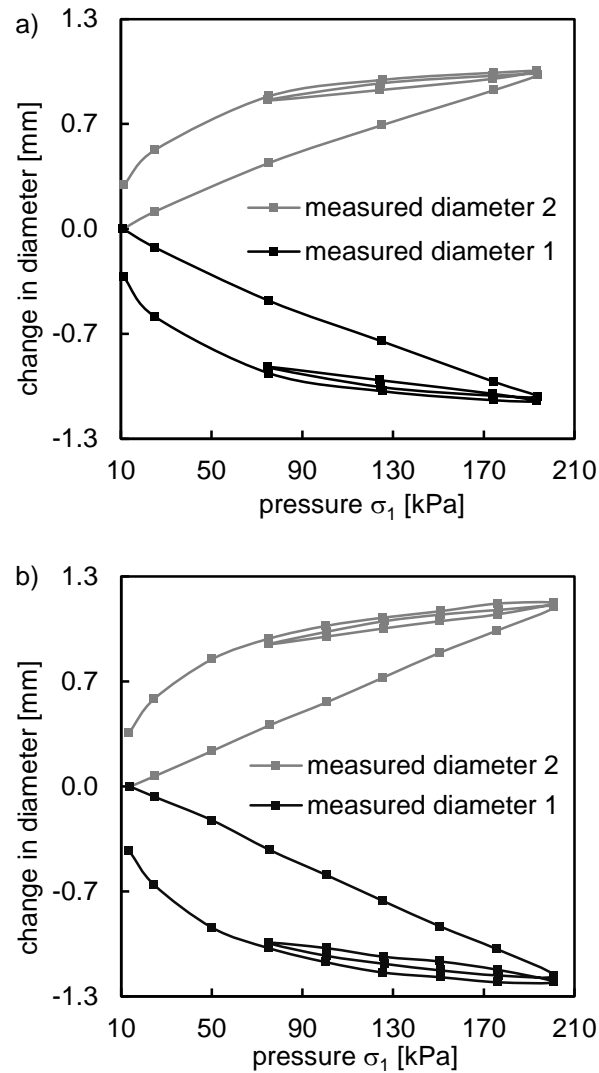
Figure 3-3: *Measured changes in diameter for applied pressure in the IDM box: a) Experiment without grout, b) Experiment with grout surrounding the pipe.*

The pressure σ_2 at the boundary in the minor principal direction was measured when applying the pressure σ_1 at the boundary in the major principal direction (Figure 3-4). The ratio σ_2/σ_1 is denoted as K_0 which is practically constant for both configurations. The ratio K_0 is found to be the same in both experiments.
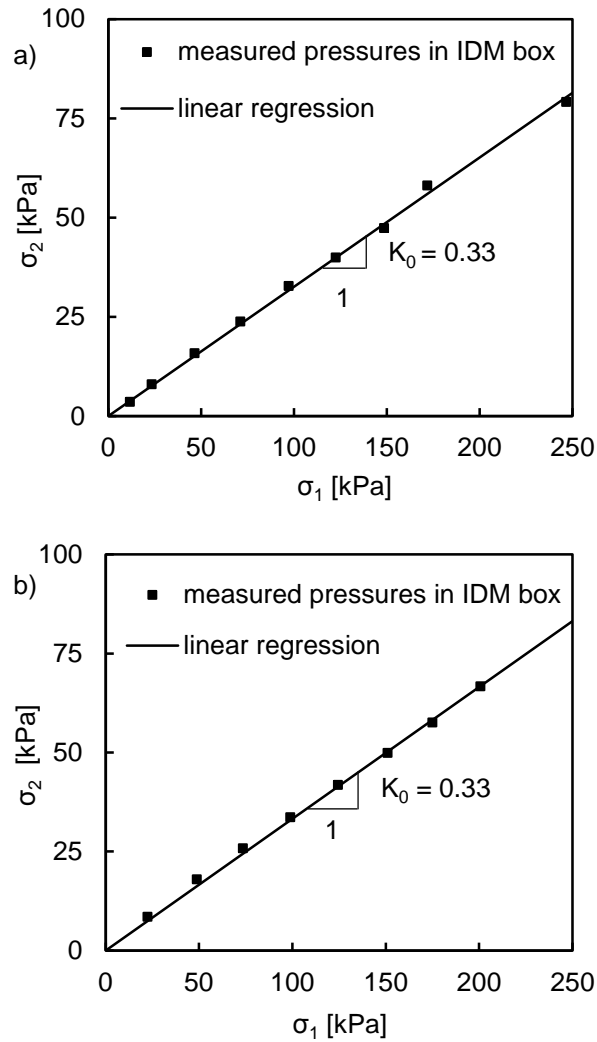
Figure 3-4: *Measured contact pressure σ_2 at the constrained boundary condition in the minor principal direction for applied pressure σ_1 in the major principal direction: a) Experiment without grout, b) Experiment with grout surrounding the pipe.*

3.3.4   Discussion of experimental results

Large pressure increments are applied in the full-scale laboratory experiments in order to study the behavior of the grout across a large range of pressures. However, the pressure increments in field applications may be considerably smaller. Therefore, the precision of IDM diameter measurements of +/– 2 micrometers (see section 1.3.5) is considered in order to assess the smallest pressure increment that can still be detected by IDM. The precision in terms of pressure is obtained by comparing the measured deformations with the precision of the IDM diameter measurement. For the loading phase, the precision in terms of pressure is 0.2 kPa. For the reloading phase, the precision is 0.6 kPa in the experiment without grout and 0.5 kPa in the experiment with grout.

The relation between earth pressure changes and pipe deformation becomes more linear due to the grout (Figure 3-3). Therefore, the back-calculation procedure will become more reliable and less dependent on the initial stress state.

3.4 Tests on the materials used in the full-scale laboratory experiment

The applied pressure increments can be back-calculated provided that the stiffness of all the materials is known and described in an appropriate way. Therefore, laboratory tests are performed on the material of the pipe, the grout and the soil in order to measure their deformation characteristics. The linear elastic model is assumed for the constitutive behavior of the soil and the grout for simplification, although the real material behavior is visco-elasto-plastic. The pipe is considered to be viscoelastic. Parameters are derived for all three materials at the range of stress of the full-scale experiment. The parameters are used for the validation of the numerical model.

3.4.1 Stiffness of the pipe

Two different pipes are used in the two full-scale experiments presented in this chapter. Although they are of the same type, the two pipes do not have exactly the same properties. Therefore, the loading tests were performed on samples of both pipes, denoted as pipe samples A and B respectively. The difference in properties may be due to different aging or due to different conditions in production. Pipe A was used in the experiment with only sand; pipe B was used in the experiment with grout (Figure 3-2).

The viscoelastic four-parameter model (Figure 3-5) is found to be appropriate to describe the time-dependent behavior of the pipe material (chapter 2). The parameters of the model (Table 3-1) were determined from creep tests performed in the transversal direction of the pipe and successfully validated against full-scale creep experiments conducted in the IDM box (chapter 2).
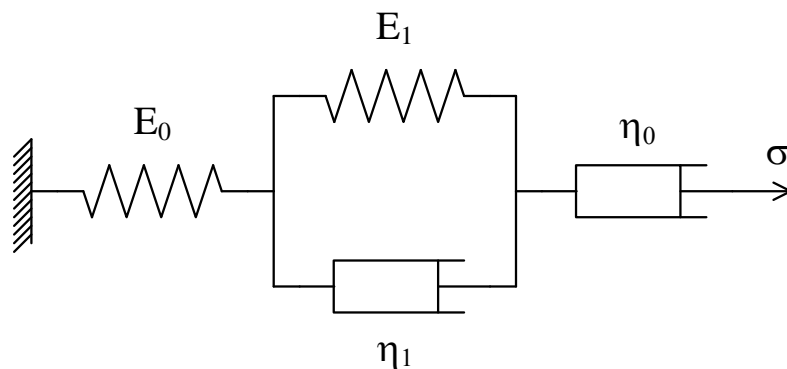
Figure 3-5: *Mechanical analog of the viscoelastic four-parameter model (Burgers model).*

Table 3-1: *Parameters of the four-parameter model determined by transversal loading of the pipe.*

parameters		pipe A	pipe B
E_0	[MPa]	2200	2490
η_0	[MPa d]	3.0×10^6	3.4×10^6
E_1	[MPa]	21120	22880
η_1	[MPa d]	5.0×10^4	5.5×10^4

In addition, loading tests at constant rate were performed in the transversal direction in order to check whether the model and its parameters still hold for the different loading conditions applied in the IDM box experiments. The test at the loading rate of 1 N/m/s is similar to the experiments performed in the IDM box in terms of loading condition and deformation. The test setup and the numerical model for interpretation are described in section 2.4. In

Figure **3-6**, the measured deformations are compared with the results of numerical calculations using finite elements. Because of the good agreement, the four-parameter model and its parameters are assumed to be appropriate for the analysis of the experiments performed in the IDM box. The Poisson's ratio of the inclinometer pipe is specified as 0.34 by the manufacturer of the pipe.
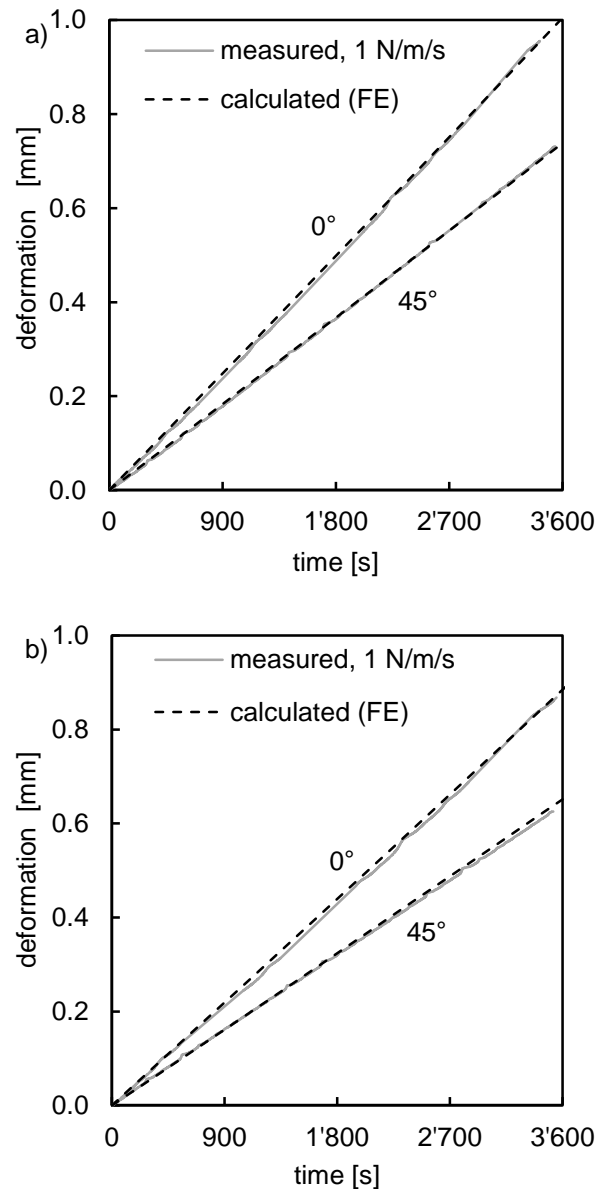
Figure 3-6: *Comparison of measured and calculated deformations in loading tests in transversal direction at constant rate of 1 N/m/s: a) On pipe A, b) On pipe B.*

3.4.2   Stiffness of the sand

Element tests were performed on the sand in order to determine its stiffness. The sample tested in triaxial compression was at a similar density to the sand in the IDM box (Table 3-2). The tested sample was slightly overconsolidated owing to its preparation.

Table 3-2: *Relative density of the sand given by the density index* I_D.

test	I_D
IDM box test without grout	69 %
IDM box test with grout surrounding the pipe	63 %
triaxial compression test: built in sample before saturation	63 %
triaxial compression test: slightly overconsolidated sample after saturation	88 %

The change in volume was measured via the excess of pore water while changing the mean effective stress p' (Figure 3-7). The bulk stiffness is found to be dependent on pressure and stress path.
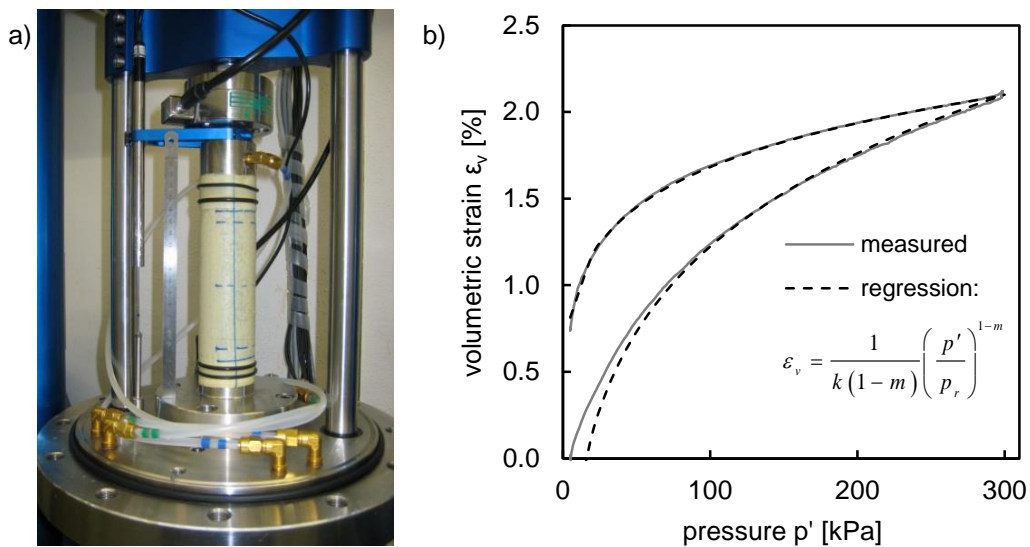
Figure 3-7: *a) Sample of sand built in a triaxial apparatus, b) Triaxial compression test on the sand in a triaxial shear apparatus.*

The tangent bulk modulus K_t is assumed to depend on the mean effective pressure p' according to the analytical function

$$K_t = k \cdot p_r \left(\frac{p'}{p_r} \right)^m \tag{3-1}$$

where $p_r = 1\,\text{kPa}$ is the reference pressure. The parameters $k = 245$ for loading, $k = 520$ for unloading and $m = 0.87$ are derived by a regression analysis, fitting the integrated function

$$\varepsilon_v = \frac{1}{k\left(1-m\right)}\left(\frac{p'}{p_r}\right)^{1-m}$$ (3-2)

to the measured volumetric strains (Figure 3-7b). On the initial loading path, k was fitted to higher pressures to make sure that the regression is not affected by the overconsolidation caused by the preparation of the sample.

The secant bulk modulus K is derived for the range of pressure in the sand in the IDM box experiment ($K = 5.6\,\text{MPa}$ in initial loading; $K = 25\,\text{MPa}$ in reloading). Measurements of the shear modulus G in triaxial shear tests provide a range for the Poisson's ratio of the sand. The Poisson's ratio of the sand was determined within this range as 0.23 in order to reproduce the measured K_0 in the IDM box experiments (see section 3.5.2). Assuming elasticity, K can be translated into $E_s = 9$ MPa for the loading phase and 40 MPa for the unloading–reloading phase.

Triaxial shear tests were performed in order to investigate the frictional behavior of the sand. The samples were sheared in triaxial compression in drained conditions. The failure stress state at constant volume is shown in Figure 3-8. Assuming the Mohr–Coulomb failure envelope, its inclination in triaxial stress space M is equal to 1.54, which corresponds to the angle of internal friction at constant volume φ'_{CV} of 37.8°.
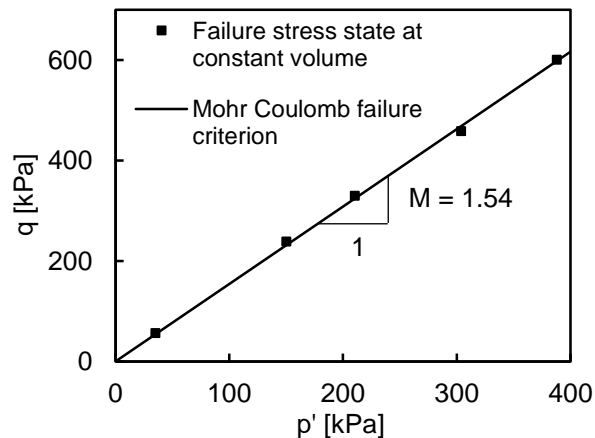
Figure 3-8: Drained triaxial shear tests on sand: failure stress at constant volume and Mohr–Coulomb failure envelope.

3.4.3   Stiffness of the grout

Unconfined compression tests were performed in order to assess the stiffness of the grout. The grout was mixed as in section 3.3.2 but using a smaller mixing device (Figure 3-9a). Two half pipes prescribing the diameter of the sample were filled with the liquid paste. After the first hardening phase (7 days), the sample was pre-consolidated within the half pipes by applying 20 kPa of vertical pressure by weight. Subsequently, the half pipes were removed after 28 days and the samples were tested in uniaxial compression at the strain rate of 0.08% / min (Figure 3-9b and Figure 3-9c). The force was measured corresponding to the applied displacement.
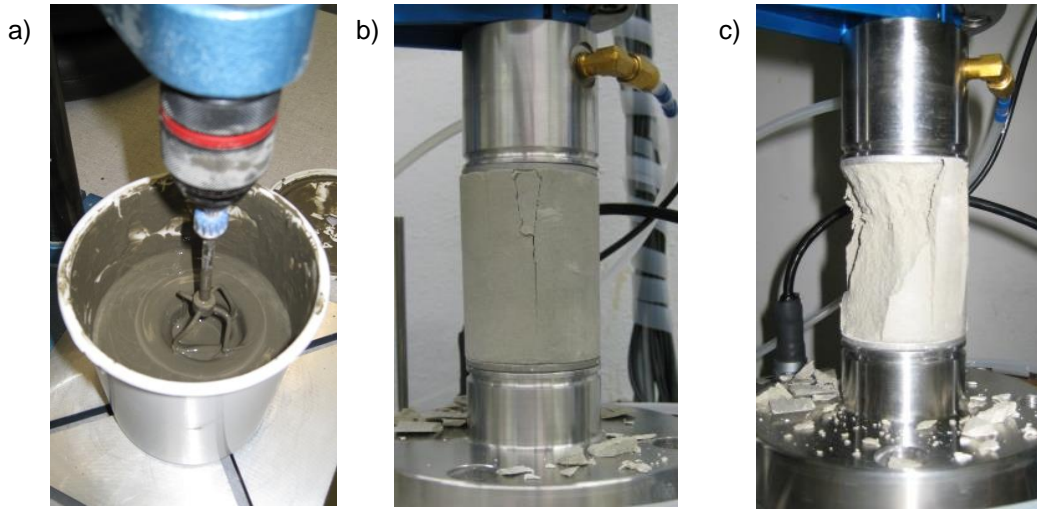
Figure 3-9: *Unconfined compression test: a) Grout suspension during mixing, b) Failed sample (diameter = 56 mm, height = 75 mm, loading rate = 0.01 mm/s), c) Sample after large displacements.*

For the grout mixture used in the IDM box experiment, the Young's modulus was measured to be 71 MPa (Figure 3-10). The softer behavior at small strains is expected to be due to the limited contact between the press and the grout sample. The unconfined compressive strength was found to be 755 kPa. The Poisson's ratio of the grout is assumed to be 0.2.

Several different grout mixtures were tested in uniaxial compression. The results obtained are reported in section 3.8.1.
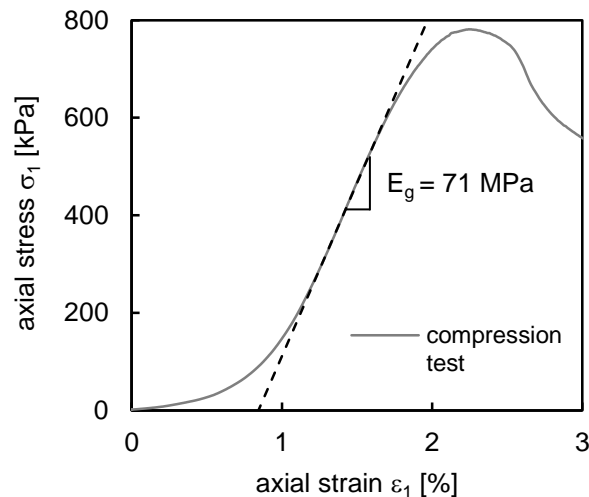
Figure 3-10: *Uniaxial unconfined compression test on grout.*

3.5   Numerical analysis of full-scale tests

3.5.1   Boundary value problem

The pressure change can be back-calculated from the measured change in pipe diameters, provided the stiffness of the involved materials in this range of stress is known. A horizontal, two-dimensional cross-section of the IDM box is considered as the boundary value problem to be solved in inverse analysis using finite elements (Figure 3-2). The dimensions of the cross-section are 400 mm by 400 mm, corresponding to the inner dimensions of the IDM box (Figure 3-1c). The element behavior perpendicular to the cross-section is assumed to be plain strain for the sand and the grout, and plain stress for the pipe. Pressure boundary conditions are applied in the major principal direction (direction 1). The boundary conditions in the minor principal direction (direction 2) are constrained. The boundary value problem is solved for the two different setups: the inclinometer pipe is surrounded by either (a) only sand or (b) a grout annulus surrounded by sand. The outer diameter of the grout annulus was measured to be 133 mm (see Figure 3-1c) after the experiment was completed.

3.5.2   Numerical model

IDM box tests were modeled with finite elements using the Abaqus code to back-calculate the applied pressures. The finite element meshes considered are shown in Figure 3-11. For the sand and the grout, quadratic plain strain elements (CPE4) with linear shape function and full integration scheme were chosen. Triangular plain stress elements (CPS6) with quadratic shape function are used for the pipe. Coulomb friction is assumed for the tangential behavior in the interface surrounding the pipe. The friction angle δ_p between the pipe and the sand is chosen according to the common assumption of $\delta_p = 2/3\,\varphi'_{CV}$, which corresponds to a friction coefficient of 0.47. The friction coefficient in the interface between the pipe and the grout is also considered to be 0.47. The sand and the grout are connected with a tie constraint; there is no interface taken into account.
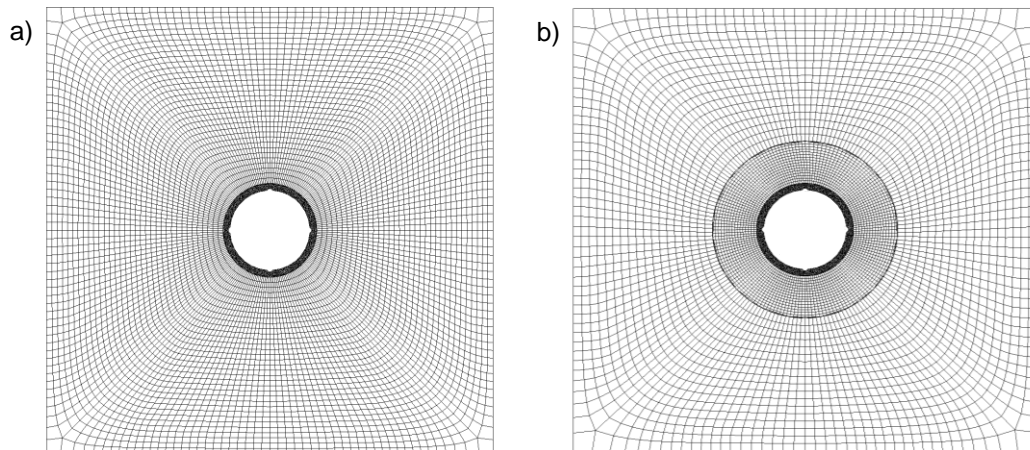
Figure 3-11: *Finite element meshes: a) Model without grout, b) Model with grout.*

For the pipe, the viscoelastic four-parameter model is implemented according to chapter 2. The complex deformation behavior of the grout and the soil is simplified for back-calculation to a linear constitutive model defined by elastic parameters. The Young's moduli of the sand and the grout are obtained in element tests; the Poisson's ratio of the grout is assumed (section 3.4.2 and 3.4.3). The Poisson's ratio of the sand is the main parameter controlling the contact pressure at the constrained boundaries. Therefore, the Poisson's ratio v_s is back-calculated using the finite element model in order to fit the

measured K_0 ratio (section 3.3.3). The parameters of the pipe, the grout and the sand are listed in Table 3-3, which is a summary of sections 3.4.1, 3.4.2 and 3.4.3.

Table 3-3: Material parameters: summary of sections 3.4.1–3.4.3.

parameter description	parameter value	derivation
E_o parameter of the pipe A / B	2200 / 2490 MPa	transversal loading tests
η_o parameter of the pipe A / B	3.0×10^6 / 3.4×10^6 MPa d	transversal loading tests
E_1 parameter of the pipe A / B	21120 / 22880 MPA	transversal loading tests
η_1 parameter of the pipe A / B	5.0×10^4 / 5.5×10^4 MPa d	transversal loading tests
ν_p Poisson's ratio of the pipe	0.34	specified by the producer
$E_{s,l}$ modulus of the soil in loading	9 MPa	triaxial comp. test
$E_{s,ul}$ modulus of the soil in unloading	40 MPa	triaxial comp. test
ν_s Poisson's ratio of the soil	0.23	K_o measured in IDM box
E_g modulus of the grout	71 MPa	unconf. comp. test
ν_g Poisson's ratio of the grout	0.2	assumed

3.6 Validation

The results of the full-scale laboratory experiments are compared with numerical calculations based on the parameters listed in Table 3-3.

The back-calculated pressures are very close to the applied pressures for the experiment with only sand surrounding the pipe (Figure 3-12a). The linear constitutive model and the derived material parameters are found to be appropriate. The difference between the initial loading path and the unloading–reloading path is explained by the difference in the bulk stiffness of the sand. Knowledge of the volumetric behavior of the sand allowed a precise and reliable back-calculation of pressures. Taking the nonlinearity of the volumetric behavior into account could even allow for more precise back-calculation. Nevertheless, for practical application the linear constitutive model is shown to be appropriate; it also makes the back-calculation independent of initial stress conditions.
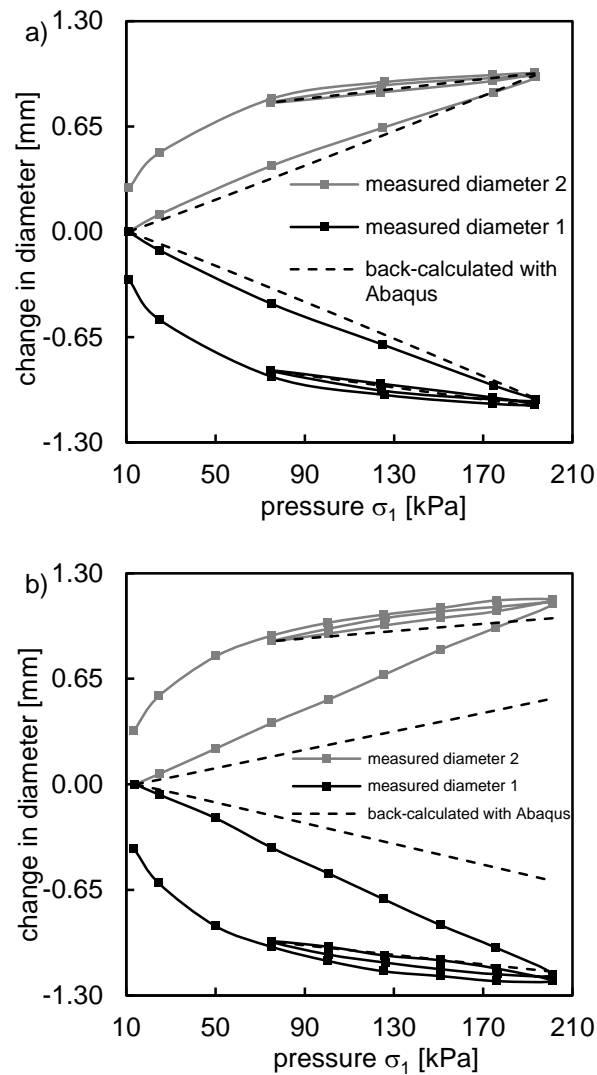
Figure 3-12: *The comparison between back-calculated and applied pressures: a) Experiment without grout, b) Experiment with grout surrounding the pipe.*

The pressures back-calculated from the experiment with grout surrounding the pipe are considerably larger than the applied pressures (Figure 3-12b). The pressure increments are over-estimated by around a factor of 2. The discrepancy is likely to be due to over-estimation of the stiffness of the grout ring. In order to check the condition of the grout, the IDM box was opened after the experiment was completed. The grout was found to be well-shaped but cracked. Two major cracks are forming on both sides in the direction of diameter 2 throughout the height of the grout (Figure 3-14a). Two minor cracks through the cylinder are observed in direction 1. The crack opening of the major cracks was less than 1 mm (Figure 3-13a); the minor cracks were very thin and could hardly be recognized. A regular pattern of cracks could be observed (Figure 3-13b).
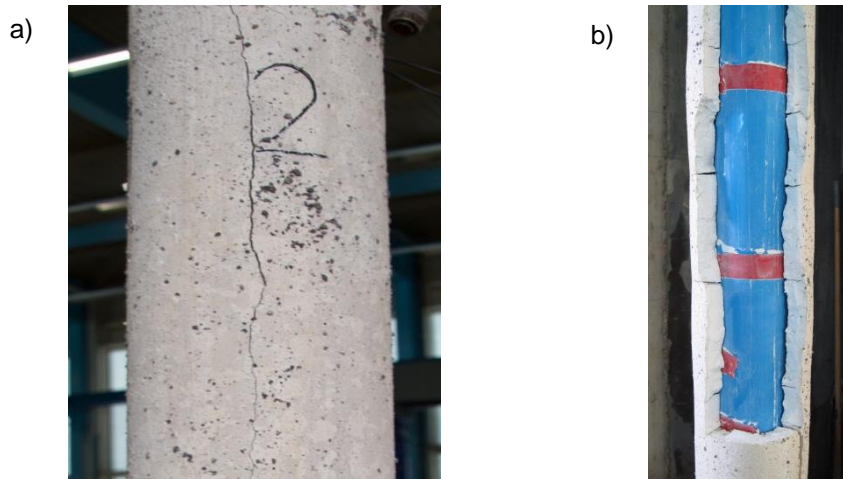
Figure 3-13: *Cracks in the grout annulus: a) Major crack in direction 2, b) Pattern of cracks after one quarter of the hollow cylinder has fallen down.*

A preliminary numerical analysis was performed to check whether the cracks could cause the softer behavior of the grout ring. Cracks were introduced into the finite element model where the large major cracks are observed in the experiment. For simplification, no normal and no shear forces were assumed to act within the cracks. The calculated deformations were found to be remarkably close to the measured pipe deformations (Figure 3-14b). Therefore, the softer behavior of the grout ring is probably due to the observed cracks.
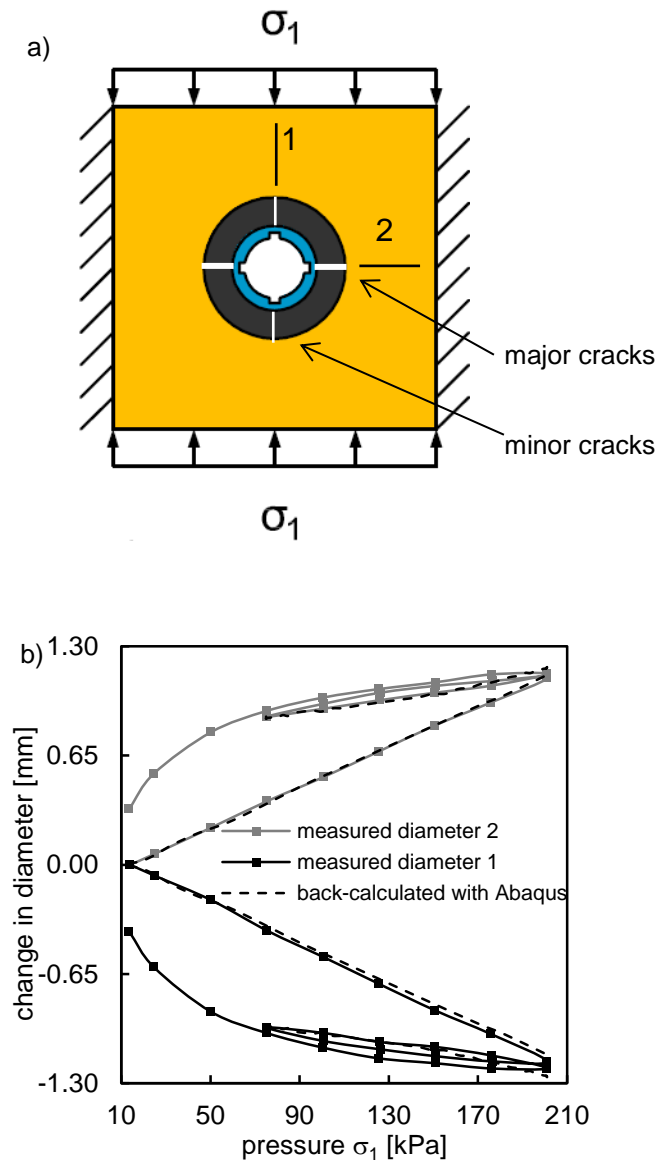
Figure 3-14: Cracks in the grout annulus: a) Location of the cracks, b) Numerical simulations taking the major cracks into account.

3.7 Discussion

Reliable and precise back-calculation of pressures can be provided if the materials can be considered as a continuum. Unfortunately, cracks within the grout annulus can reduce the stiffness of the grout ring considerably. The equivalent stiffness of the continuum would be more than 20 times smaller owing to the cracks. Nevertheless, the IDM pressure measurements still provide a relatively good result because the back-calculated pressures are only affected by a factor of 2, owing to the low sensitivity to the grout stiffness.

The measured pipe deformations are similar in the experiment with only sand to the experiment with the cracked grout annulus surrounding the pipe. Therefore, the equivalent stiffness of the cracked grout body may be assumed to be similar to the stiffness of the soil. For the cracked grout, the analytical solution (presented in chapter 6) may be applied, which assumes the same stiffness for the grout and for the soil.

There are applications where this approach may not be appropriate. In the case of an intact grout ring surrounded by soft soil, the stiffness of the grout may be considerably larger than the stiffness of the soil. In this case, the grout stiffness may be taken into account by performing numerical simulations in order to back-calculate the pressures.

The question remains as to whether the grout ring can be considered to be intact or cracked in field applications. The cracks in the laboratory tests may have occurred because of shrinkage of the grout. The dry sand surrounding the grout and the indoor climate may have supported the grout shrinking. Therefore, the grout ring is less likely to be damaged in ground water. Below the ground water table, the hypothesis of an intact grout ring may be made. If the grout is cracked above the ground water table, it may be recognized by a change in pipe deformations of around a factor of 2 at the level of the water table. For applications in very dry soils, where the grout is expected to shrink, the cement-bentonite grout may be replaced by sand to refill the borehole.

However, further research is required to understand the conditions under which the grout becomes cracked. In addition, the deformation behavior of the cracked ring needs to be further investigated.

3.8   Design of the grout composition

3.8.1   Influence of the grout composition on its properties

IDM pressure measurements are influenced by the properties of the grout which is used to refill the borehole. Therefore, the properties of the cement-bentonite grout are investigated for different compositions. This section focuses on the workability, the bleeding, the strength and the stiffness of the grout. All the grout mixtures were produced as described in section 3.3.2 and tested after 28 days.

The influence of the composition on the workability and stability towards sedimentation was reported by Jones (1963). Grout mixtures in the consistency regions a, b, c and d are pumpable (Figure 3-15). Grout compositions in the consistency region d are additionally indicated to be stable towards sedimentation. To refine the area of stable grouts, sedimentation tests were carried out on 40 different mixtures. The ratio between the volume of the segregated water at the top and the total volume was measured after 28 days of hardening. Several lines were obtained describing mixtures with the same amount of bleeding (Figure 3-15).

a   unstable suspension: settles

b   temporarily stable suspen-
    sions settle before setting

c   clay cement gels of low
    compressive strength

d   free flowing, stable and
    pumpable suspensions

e   stable, putty-like suspensions

f   solid, unworkable mixes,
    normally powders
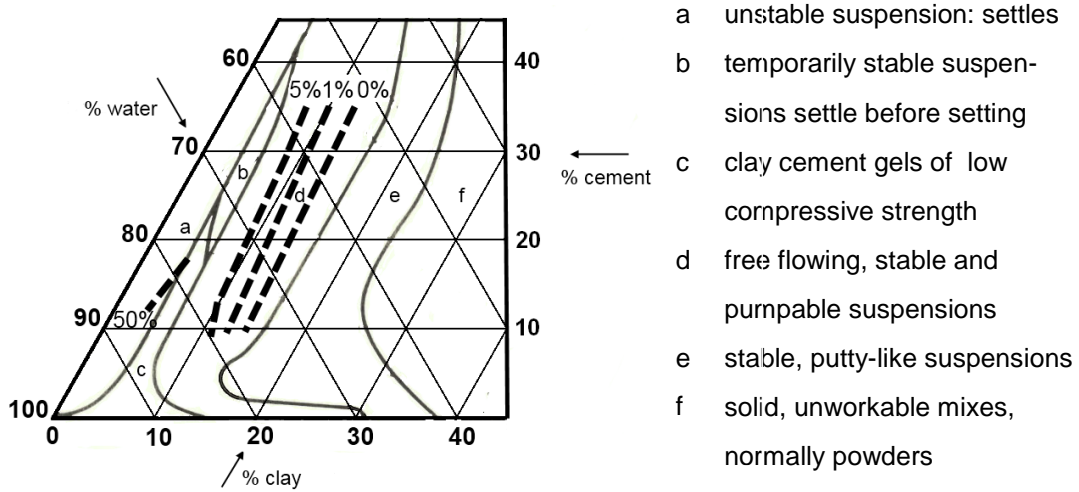
Figure 3-15: *Workability and bleeding depending on grout composition (portion of the compounds by weight): diagram and consistency regions a, b, c, d, e, f after Jones (1963).*

The strength of different grout mixtures was determined in unconfined compression tests as described in section 3.4.3 (Figure 3-16). The mixture marked with the black dot was used in the full-scale experiment in the IDM box (Figure 3-16). The strength of the grout is mainly controlled by the water–cement ratio (Marsland, 1973). The lower the water–cement ratio the higher is the unconfined compressive strength. The relation obtained between the strength and the water–cement ratio is similar to that of Contreras *et al.* (2008). Nevertheless, at high water–cement ratio, the results of Contreras *et al.* (2008) show higher strength than presented here.
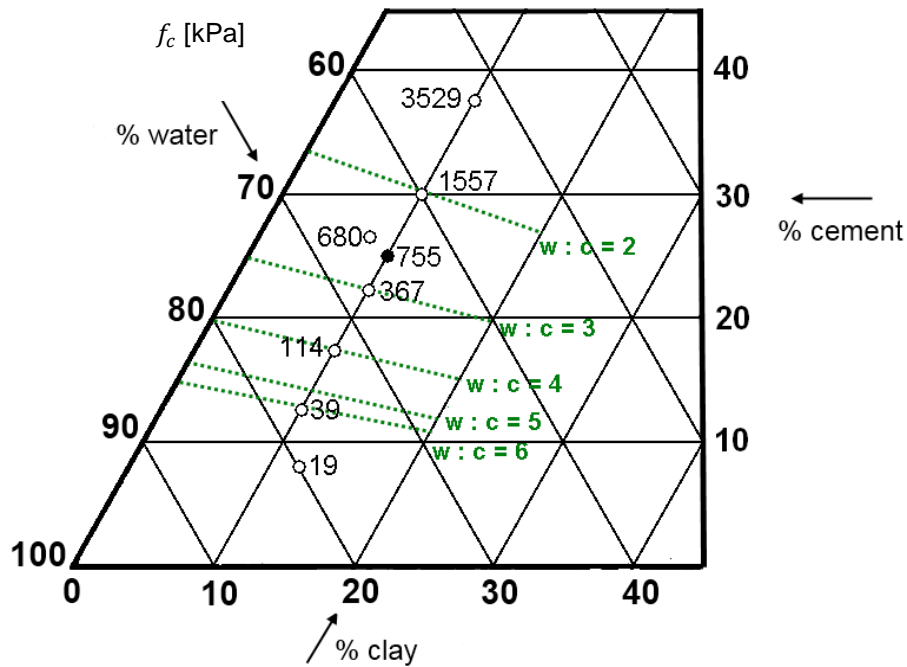
Figure 3-16: *Unconfined compressive strength f_c depending on the grout composition (portion of the compounds by weight).*

The stiffness of different grout mixtures was obtained in uniaxial compression tests as in section 3.4.3. The measured Young's modulus is shown in Figure 3-17 for different compositions.

The stiffness is found to be correlated to the unconfined compressive strength. Therefore it is not possible to match strength and stiffness with the same mix (Mikkelsen, 2002), especially if other requirements such as workability or stability towards sedimentation are considered as well.
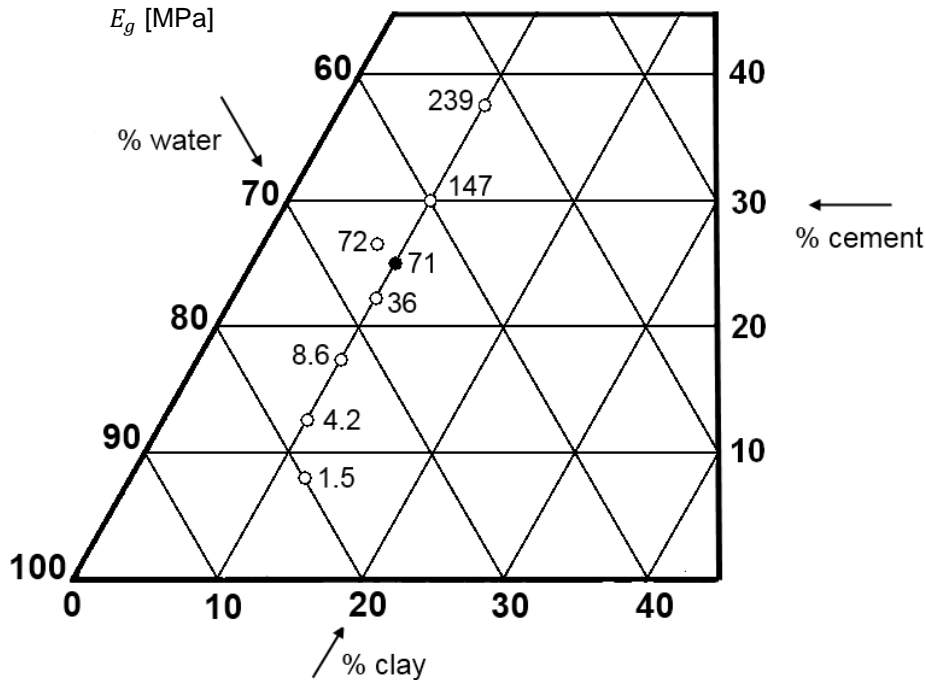
Figure 3-17: *Young's modulus E_g in uniaxial loading depending on the grout composition (portion of the compounds by weight).*

3.8.2   Adjusting the grout mixture to the requirements of IDM

In order to be appropriate for IDM pressure measurements, the grout mixture is recommended to follow certain requirements:

1)   The grout suspension should be pumpable.

2)   To avoid the suspension settling in the borehole and hence risking a borehole with the topmost part filled with segregated water only, the grout mix should not show any bleeding.

3)   The back-calculation of earth pressure changes becomes more difficult and less reliable if the grout has cracks or has entirely failed. Therefore, the grout should not fail.

4)   The precision and sensitivity of the IDM pressure measurements are depending on the stiffness of the grout (Figure 3-18). The choice of the grout should allow for a high precision and sensitivity.

For a cement-bentonite grout, the following approach is expected to follow the requirements. The proposed approach is based on Figure 3-15, Figure 3-16 and Figure 3-17:

1) Workability: The grout suspension is pumpable as long as it belongs to consistency region d in Figure 3-15.

2) Stability towards sedimentation: The suspension is considered to be stable if the grout composition stays around the line of 1% of bleeding in Figure 3-15. This condition reduces the choice of the grout into a one-dimensional problem (Figure 3-15).

3) Strength: To avoid failure, a minimum strength is required. Therefore, grout compositions may not be admissible with water–cement ratio higher than the corresponding water–cement ratio (Figure 3-16).

4) Stiffness: Figure 3-17 and Figure 3-18 may be used to determine the composition of the grout in order to enhance precision and sensitivity. Figure 3-18 shows the precision as a function of the stiffness of the grout for an assumed set of parameters. The choice of grout composition may be based on the information provided by this figure. For many applications, the softest grout composition still admissible may be favorable in terms of precision and sensitivity. Therefore, the stable mixture providing the required minimum strength may be chosen.
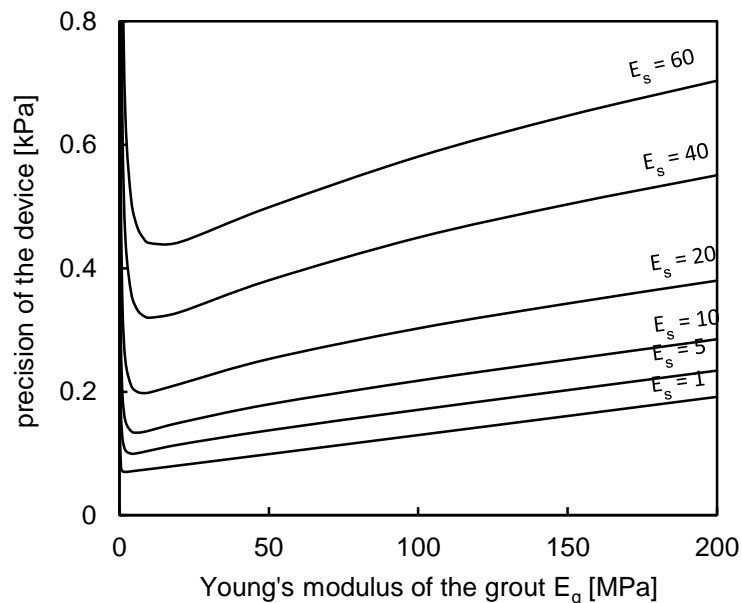
Figure 3-18: *Precision of the IDM pressure measurement as a function of the Young's modulus of the grout for the following assumptions: constrained boundary conditions to the sides, plane stress boundary condition in vertical direction due to constant overburden, $E_p = 2000\ MPa$, $\nu_p = 0.34$, $\nu_g = 0.2$, $\nu_s = 0.2$.*

The optimum stiffness of the grout, where the highest precision can be achieved, is found to be quite low. The grout is recommended to be on the stiff side of the optimum stiffness, because the precision strongly deteriorates at stiffness smaller than the optimum (Figure 3-18). Therefore, Young's modulus of the grout is recommended to be larger than 10 MPa.

3.9   Conclusions

Adjusting the mechanical properties of the grout to the soil is essential for earth pressure measurements taken by IDM. Based on laboratory tests on different grout compounds, a procedure is developed to design the optimal grout composition for the requirements of IDM measurements. The sensitivity of the IDM pressure measurements can be enhanced by using softer grout provided the Young's modulus of the grout is no smaller than 10 MPa. In addition, there are other constraints for the design of the optimal grout compound: i.e. the workability, the stability towards sedimentation and the strength.

Full-scale laboratory tests were performed in a 2 m high calibration chamber incorporating the grout. The full-scale tests demonstrated that simple linear constitutive models can successfully be used as a first approximation for back-calculation. The back-calculation of pressure increments becomes reliable and independent of initial conditions. The smallest detectable pressure increment is shown to be as small as 0.2 kPa.

In general, the grout is expected to be designed to have similar deformation characteristics to the surrounding soil. Thus, the influence of the stiffness of the grout can be neglected for back-calculation of pressures, and an analytical solution may be applied, which assumes the same stiffness for the grout as for the soil. If the grout is stiffer than the soil but cracked, the influence of the stiffness of the grout remains small and may be neglected, so the analytical solution may again be applied. For an intact grout ring, which is considerably stiffer than the surrounding soil, the grout stiffness can be taken into account by performing numerical simulations in order to back-calculate the pressures. Fortunately, the back-calculation of stresses is not sensitive to the stiffness of the grout. Less than a twofold increase in the back-calculated stress increments is caused by a tenfold increase in the stiffness of the grout. Below the ground water table, the grout is likely to be intact. In dry soils, where the cement-bentonite grout is prone to shrink and crack, sand may be used as an alternative to refill the borehole.

Further research is required to understand the conditions under which the grout becomes cracked. The deformation behavior of the cracked ring also needs to be further investigated.

References

Contreras, I. A., Grosser, A. T. & Ver Strate, R. H. (2008). The use of the fully-grouted method for piezometer installation. *Geotechnical News* **26**, No. 2, 30-37.

Dunnicliff, J. (1988, 1993). *Geotechnical Instrumentation for Monitoring Field Performance.* New York: J. Wiley.

Jones, G. K. (1963). Chemistry and flow properties of bentonite grouts. *Proceedings of the Symposium on Grouts and Drilling Muds in Engineering Practice*, *London*, 22-28.

Marsland, A. (1973). Discussion, principles of measurement. *In:* Society, B. G. (ed.) *Field Instrumentation in Geotechnical Engineering.* Halsted Press, a Division of John Wiley.

Mikkelsen, P. E. (2002). Cement-bentonite grout backfill for borehole instruments. *Geotechnical News* **20**, No. 4, 38-42.

Notation

E_0	elastic parameter of the Burgers model (four-parameter model)
E_1	elastic parameter of the Burgers model (four-parameter model)
E_g	Young's modulus of the grout
$E_{s,l}$	Young's modulus of the soil in loading
$E_{s,ul}$	Young's modulus of the soil in unloading and reloading
f_c	unconfined compressive strength
I_D	density index of the sand
K	secant bulk modulus of the sand
K_0	ratio between the principal lateral stresses: $\sigma_2 \, / \, \sigma_1$
K_t	tangent bulk modulus of the sand
k	empirical parameter
M	inclination of the Mohr–Coulomb failure envelope in triaxial stress space
m	empirical parameter
p	mean effective stress
q	deviatoric stress
δ_p	angle of friction in the interface between the pip and the soil / grout
ε_v	volumetric strain
η_0	viscous parameter of the Burgers model (four-parameter model)
η_1	viscous parameter of the Burgers model (four-parameter model)
ν_g	Poisson's ratio of the grout
ν_p	Poisson's ratio of the pipe
ν_s	Poisson's ratio of the soil
σ_1	major principal lateral stress; applied at boundary condition
σ_2	minor principal lateral stress; measured at boundary condition
φ'_{CV}	angle of internal friction at constant volume of the sand

4 Effects of longitudinal bending on earth pressure measurements taken by inclinodeformeter

4.1 Abstract

A change in ovalization of an inclinometer pipe does not only occur because of changes in earth pressure. As a pipe is bent longitudinally its cross-section flattens into an oval shape. The inclinometer pipe is subjected to bending due to displacements of the surrounding soil, which may not be related to changes in pressure. Therefore, the IDM measurements have to be corrected. The amount of change in ovalization value due to longitudinal bending $\Delta\Omega^{\chi}$ is subtracted from the measured change in ovalization value $\Delta\Omega$.

An analytical solution calibrated using numerical simulations describes the change in ovalization due to bending as a function of the curvature of the pipe. The curvature is obtained by numerical differentiation of the inclination of the pipe, which is measured by IDM in a profile with depth. The calculated change in ovalization value due to bending $\Delta\Omega^{\chi}$ may not fully develop. If the length of the section of intense curvature is shorter than the required length of the transition zone, smaller pipe deformations will be observed.

However, the calibrated solution shows that the effects of longitudinal bending can be neglected for many applications. The cross-sectional deformations due to bending are usually smaller than the precision of the IDM device. The effects of bending can be ignored in particular within the sliding layer of a creeping landslide.

4.2   Introduction

As a thin tube is bent longitudinally, its cross-section flattens into an oval shape. The inclinometer tube is subjected to bending due to displacements of the surrounding soil, which may not be related to earth pressure changes. Therefore, the measured pipe deformations have to be corrected for the amount of ovalization due to bending.

One may think of examples in which ovalization changes due to bending with hardly any change in pressure. Figure 4-1 shows an inclinometer pipe in a creeping landslide. A thick shear zone at residual strength is assumed between the sliding layer and the stable ground. Within the shear zone, pressures do not change during shearing. The inclinometer pipe, which is embedded in the stable ground, is bent within the shear zone. The cross-section of the pipe is deformed by bending. A change in ovalization of the inclinometer pipe is observed by IDM measurements, although the lateral earth pressures do not change.
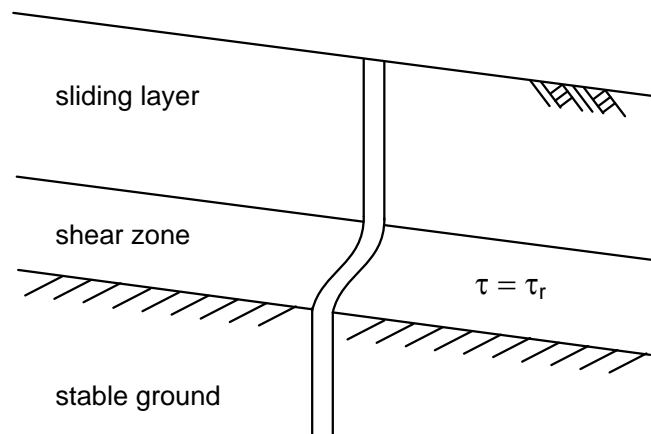
Figure 4-1: *Example of change in ovalization which is not related to pressure change: shear zone of a creeping landslide at residual strength.*

Another example is given by an inclinometer pipe embedded in soil in active failure behind a retaining wall (Figure 4-2). Although the wall continues rotating, the earth pressures behind the wall hardly change because of the failure. Nevertheless, the pipe is bent because of the displacements of the surrounding soil, causing ovalization of the pipe. Without correction of the effects due to bending, IDM measurements can be misleading. Therefore, the pipe deformations caused by bending should be calculated and subtracted from the measured deformations in order to correct the IDM pressure measurements.
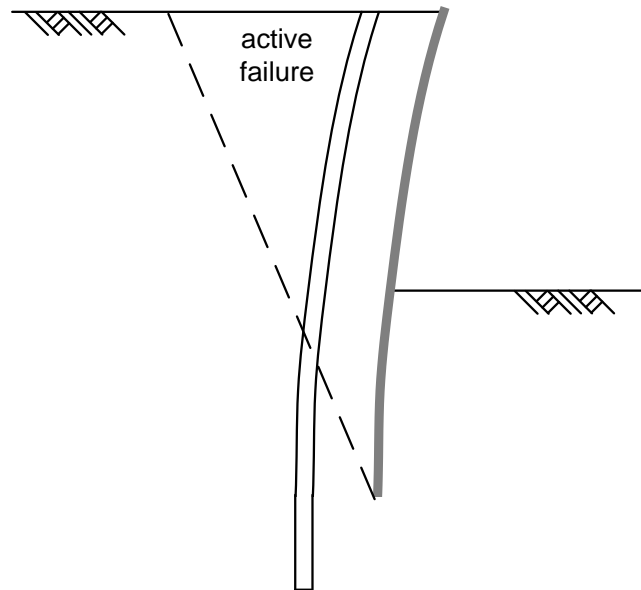
Figure 4-2: *Example of change in ovalization which is not related to pressure change: active failure behind a retaining wall.*

4.3   Correction of the change in ovalization due to bending

The nonlinear bending response of initially straight tubes was studied by Brazier (1927). Assuming an oval shape, isotropic elastic material and no pressures, the ovalization is obtained by minimizing the total strain energy:

$$\Delta D^{\chi} = -\frac{2\chi^2 \left(R - h/2\right)^5}{h^2}\left(1 - \nu_p^2\right)\cos(2\theta^{\chi}) \tag{4-1}$$

ΔD^{χ} change in diameter due to bending
χ curvature
θ^{χ} circumferential coordinate with respect to direction of the curvature
R outer radius of the tube
h thickness of the tube
ν_p Poisson's ratio of the pipe

For this solution, higher order terms of the longitudinal stretching strain energy were neglected on the assumption of small ovalization. The curvature χ_{max} of an inclinometer pipe was observed to be always smaller than 0.0001 mm^{-1} even in the case of a pipe which was almost sheared. Within this range the ovalization can be considered as small, and higher order terms can be neglected. Numerical analysis confirms that Brazier's solution provides an extremely close approximation for curvature smaller than χ_{max}.

Although the analytical solution was developed for thin tubes, numerical analysis indicates that the solution can also be applied for thicker tubes such as inclinometer pipes subjected to curvatures smaller than χ_{max}. In accordance with the work of Karamanos (2002) the cross-sectional radius (R-h / 2) was used as the reference line in Equation (4-1).

a)

b)

c)
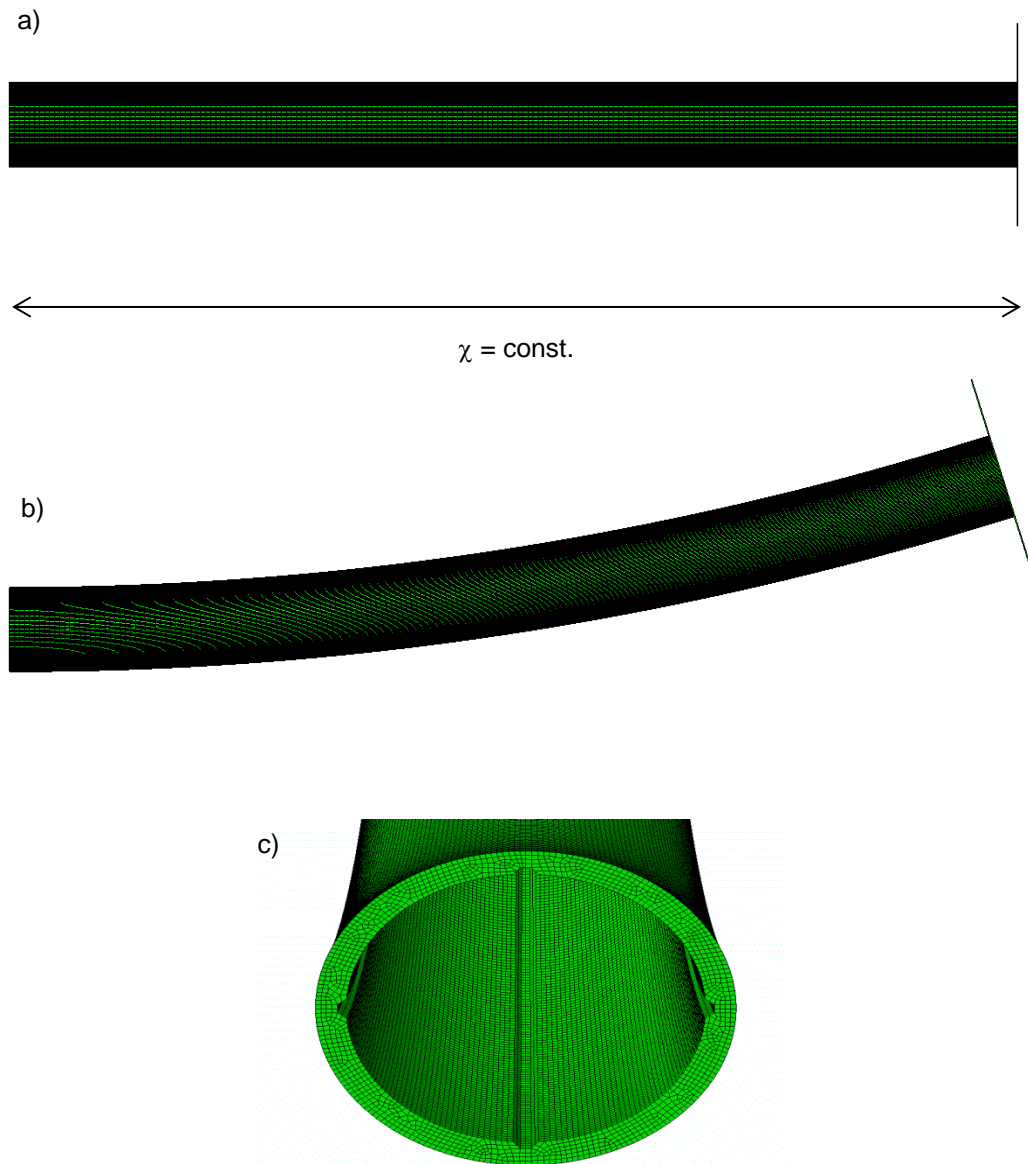
Figure 4-3: Finite element model of the inclinometer pipe subjected to constant curvature assuming linear elasticity: a) Undeformed pipe, b) Deformed pipe, c) Deformed cross-section due to curvature.

Equation (4-1) cannot be applied to an inclinometer pipe because of its channels, which affect the deformed shape induced by bending. Nevertheless the analytical formula can be used as an approximation for the change of the diameters in the channels if the thickness h of the tube is reduced. The reduced thickness $h_{red} = 5.35\text{mm}$ was calibrated using finite element simulations (Figure 4-3). The change in ovalization value due to bending is derived. The change in ovalization value is defined in the framework of IDM as the change in the difference of the two measured diameters normalized by the outer radius of the pipe. The amount of change in ovalization value due to bending must be subtracted:

$$\Delta\Omega^{\chi} = \frac{\Delta D_B^{\chi} - \Delta D_A^{\chi}}{R} = \frac{4\chi^2\left(R - {h_{red}}\big/{2}\right)^5}{R\, h_{red}^2}\left(1 - v_p^2\right)\cos(2\theta_A^{\chi}) \tag{4-2}$$

The angle between the channel in direction A and the direction of the curvature is denoted as δ_A^χ. Figure 4-4 shows the comparison of the analytical approximation of Equation (4-2) to finite element calculations for different angles δ_A^χ.
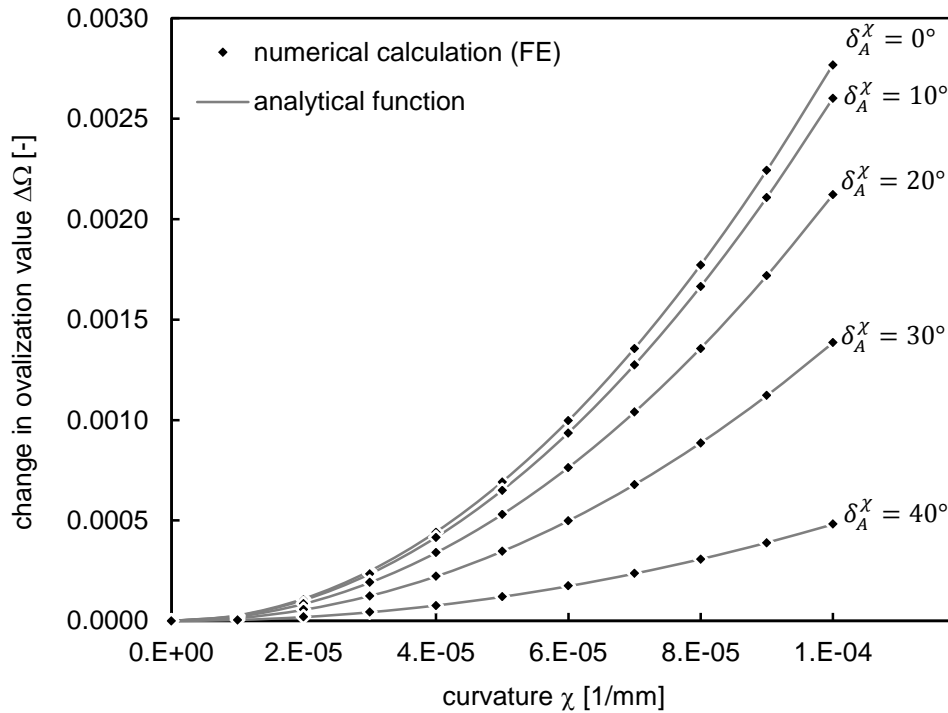
Figure 4-4: *Change in ovalization value due to bending of pipes at different rotation: comparison of the analytical function of Equation (4-2) with finite element calculations. The angle δ_A^χ denotes the rotation of the pipe with respect to the direction of the curvature.*

IDM measurements are always taken with respect to an initial zero reading. If the pipe is considered to be initially curved, the initial curvature χ_0 should be taken into account:

$$\Delta\Omega^\chi = \frac{\Delta D_B^\chi - \Delta D_A^\chi}{R} = \frac{4\left(\chi^2 - \chi_0^2\right)\left(R - {h_{red}}\big/{2}\right)^5}{R\,h_{red}^2}\left(1 - v_p^2\right)\cos(2\theta_A^\chi) \qquad (4\text{-}3)$$

No correction is needed if the change in ovalization due to bending is smaller than the precision of the IDM measurement. The precision of the IDM measurement of $[\Delta D_B - \Delta D_A]_{min}$ of 2 micrometers yields the precision in terms of ovalization value $\Delta\Omega_{min}$ (see section 1.3.5). Thus, the effects of bending can be neglected if

$$\left|\Delta\Omega^\chi\right| \le \Delta\Omega_{min} = 4.8 * 10^{-5} \qquad (4\text{-}4)$$

Hence, the condition for the curvature to be neglected is obtained from Equation (4-3) for the conservative assumption of $\delta_A^\chi = 0°$ and $v_p = 0.34$:

$$\left|\chi^2 - \chi_0^2\right|_{max} \le 1.7 * 10^{-10}\ \mathrm{mm}^{-2} \qquad (4\text{-}5)$$

For many applications, no correction of the measured ovalization is needed because the curvature is within the bounds provided by Equation (4-5).

4.4   Influence of pressure

The pressures acting on the installed inclinometer pipe have an influence on the deformations due to bending which has not been considered so far. An inclinometer pipe is usually filled with water during installation to prevent the pipe lifting up in the borehole. The water table remains inside the pipe. Lateral earth pressure and most often also ground water pressure act on the outside of the pipe. The total pressure from outside is expected to be larger than the pressure inside the pipe.

Numerical calculations show that pipe deformations due to bending are considerably different in the two principal axes, when pressures are taken into account. Therefore Equation (4-1) is not appropriate when pressures are considered. Equations (4-2) and (4-3) still provide a remarkably good agreement to the numerical calculations, although they slightly overestimate the change in the difference of the diameter. Closed form solutions for thin pipes that do take pressures into account, e.g. Reissner (1959), are not applicable owing to the relative thickness of the inclinometer pipe and owing to its channels.

Therefore, the error incurred by applying Equations (4-2) and (4-3) is assessed by numerical calculations under simplified conditions. Because the water table inside the pipe is often observed at a similar level to the ground water table, both are assumed to be at the level of the ground surface. A density γ of 20 kN/m^3 and lateral earth pressure coefficient K of 0.5 are assumed to derive horizontal earth pressures. The influence of pressures increasing with depth on the change in ovalization value is shown in Figure 4-5. The ovalization value influenced by pressures can be normalized for different curvature by the ovalization value in absence of pressures, which is obtained from the analytical function. The largest error occurs for very soft pipe material (e.g. $E_p = 1500$ MPa; $\nu_p = 0.34$) at a large depth. For this worst case scenario, the deformations due to bending are overestimated by Equations (4-2) and (4-3) by about 19% at a depth of 50 m (Figure 4-5).
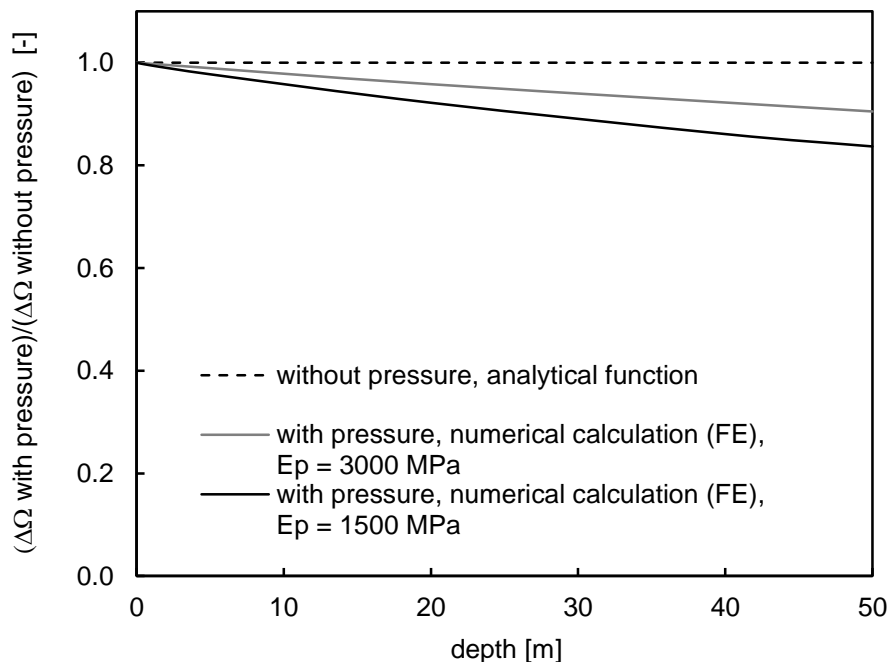
Figure 4-5: Effects of pressure change with depth on the change in ovalization value due to curvature, for simplified conditions.

4.5   Transition between sections of different curvature

If the curvature is changing along the tube, the deformations due to bending form a kind of transition zone up to the point where the constant deformation described by the analytical solution is reached. According to Millard and Roche (1984), the length of this transition zone depends on geometrical parameters and on Poisson's ratio. Therefore the propagation length can be considered to be constant, because the same type of inclinometer pipe is used. Finite element calculations (Figure 4-6) confirm that the length of the transition zone does not depend on the amount of change in curvature (Figure 4-7) nor on the length of sections with constant curvatures (Figure 4-8). The length of the transition zone was determined to be about 433 mm. If the section of constant curvature is long enough, the deformation will reach the analytical solution (Figure 4-7). The wave-like shape of the propagating ovalization is according to the analytical solution provided by Millard and Roche (1984).
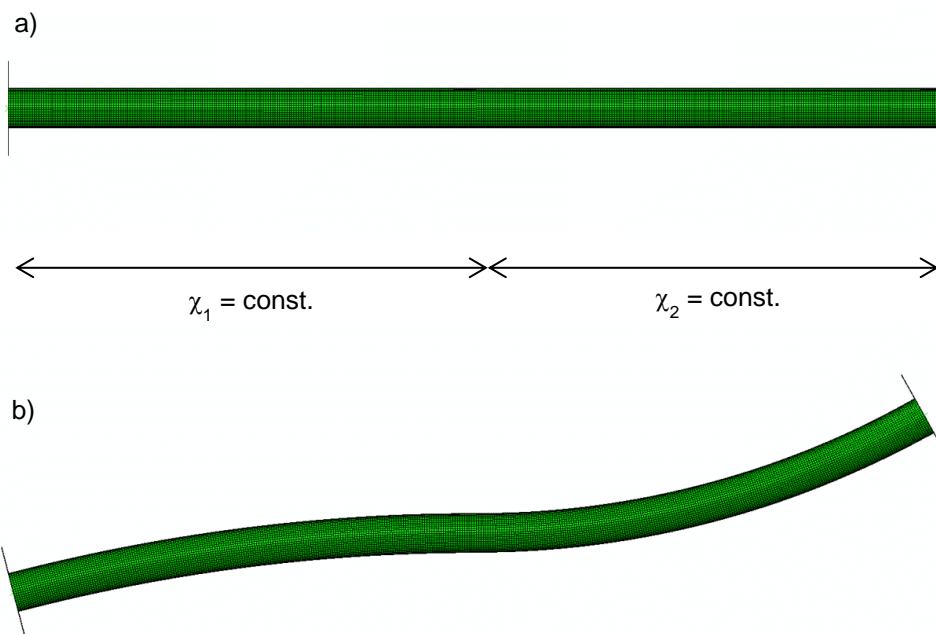
Figure 4-6: *Finite element model of the inclinometer pipe with two sections subjected to constant different curvature (χ_1 and χ_2) assuming linear elasticity: a) Undeformed pipe, b) Deformed pipe.*
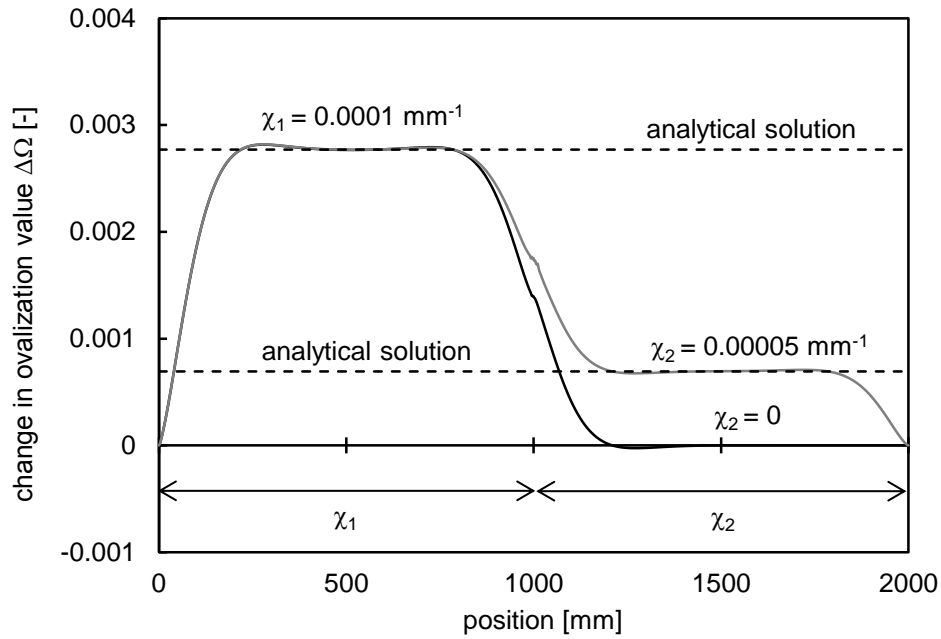
Figure 4-7: *Propagation of the change in ovalization value for two sections of different constant curvature (χ_1 and χ_2).*
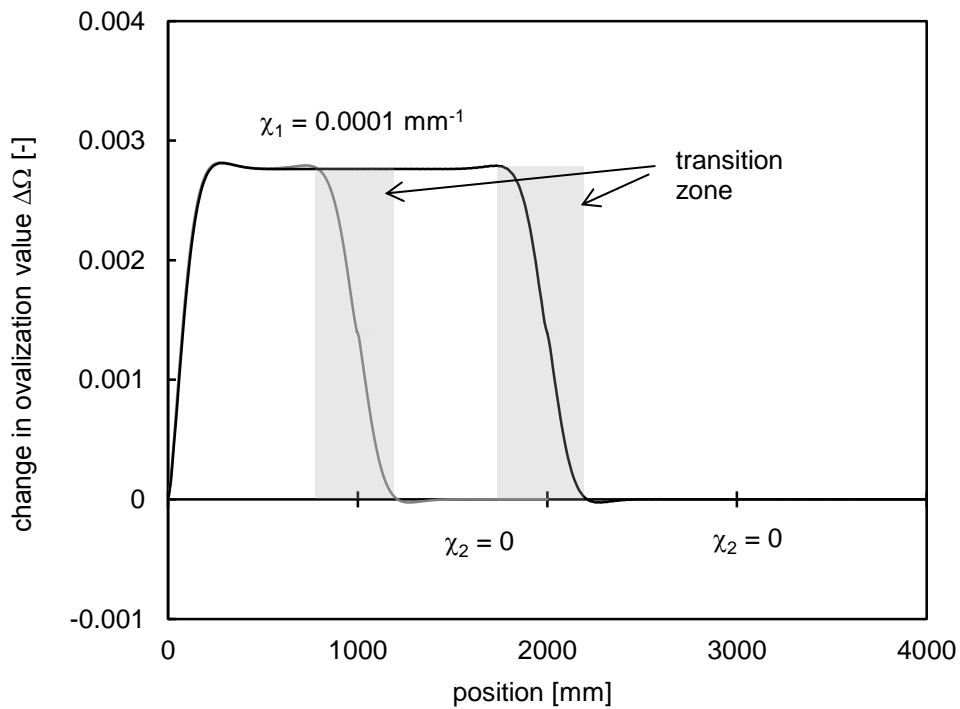
Figure 4-8: *Propagation of the change in ovalization value for two sections of constant curvature ($\chi_1 = 0.0001$ mm^{-1}; $\chi_2 = 0$ mm^{-1}) and different length.*

4.6   Application

To quantify the influence of the deformations due to bending, the calibrated solution is applied to a specific IDM reading which can typically be observed in creeping landslides. Figure 4-9 shows the initial curvature χ_0 and the curvature χ of an inclinometer pipe located in the Brattas landslide in St Moritz (see chapter 5). The curvature is obtained by numerical differentiation of the inclination of the pipe, which is measured by IDM as a

depth profile. The slip surface is located at a depth of 23 m, where large curvature is observed. However, the curvature is found to be small in the sliding layer above the slip surface.
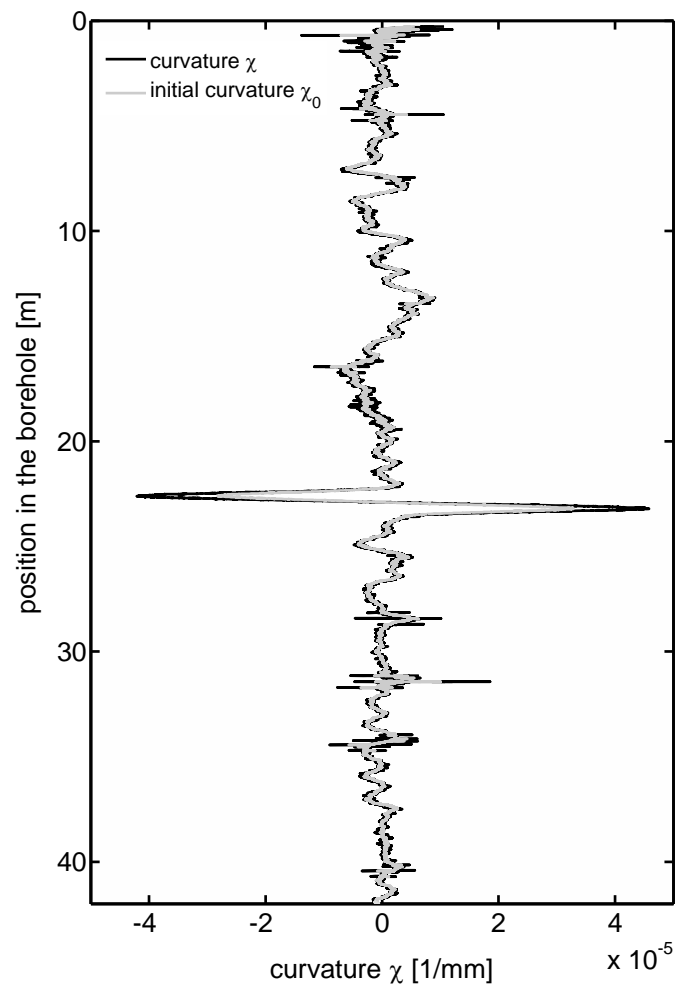
Figure 4-9: *Curvature of an inclinometer pipe in a creeping landslide measured by IDM.*

The change in ovalization value due to bending $\Delta\Omega^\chi$ can be calculated using Equation (4-3). Equation (4-5) provides a band within which no correction for bending is needed for the conservative assumption of the curvature occurring in the direction of the channels ($\delta_A^\chi = 0°$).

The pipe deformations due to bending can be ignored within the sliding layer (see Figure 4-10), because they are smaller than the precision of the IDM diameter measurements. In the shear zone, the effects of longitudinal bending are considerably larger. Because pressures are not expected to change within the shear zone (see section 4.2), the ovalization of this pipe section is not of interest. Therefore, no correction for the influence of bending is needed for IDM measurements in creeping landslides.
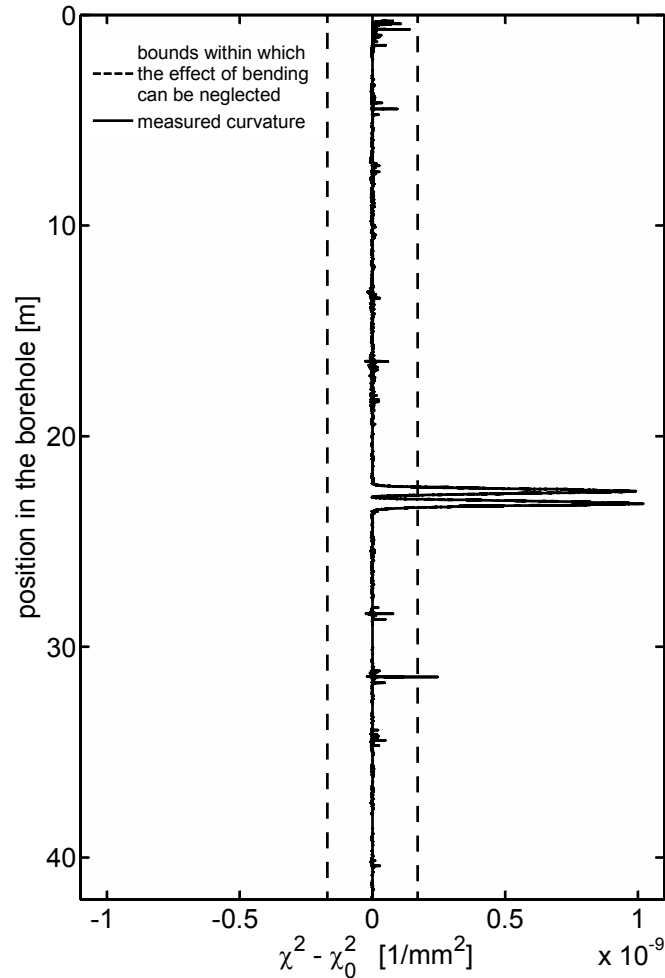
Figure 4-10: *Criterion for correction of ovalization due to bending: within the band shown in the figure no correction for bending is needed.*

In other applications where the curvature is larger, the effects of bending may no longer be negligible. The change in ovalization value can be corrected using Equation (4-3), although the pipe deformations caused by bending are overestimated for several reasons. The cross-sectional deformations are reduced by the effects of pressure (section 4.4). In addition, the ovalization caused by bending is reduced if the length of the section of intense curvature is limited compared with the length required to build up the full deformation (section 4.5).

4.7   Conclusions

An analytical solution calibrated using numerical simulations can describe the change in ovalization of an inclinometer pipe due to bending. The solution is able to capture the effects of the channels and the rotation of the pipe by considering a pipe section of constant curvature. The solution allows identification of many applications for IDM with relatively small curvature where the effects of longitudinal bending can be neglected. In particular, in the sliding layer of creeping landslides, the effects of longitudinal bending can be ignored. In the case of an application with intense curvature, longitudinal bending has to be considered. The solution can provide a preliminary estimate for correction of the measured deformation, although the correction is overestimated. The calculated deformations due to bending are overestimated owing to the surrounding pressures and to the limited length of the curved section. Additional studies are required in order to introduce these effects into an approach for the correction of the measured deformation.

References

Brazier, L. G. (1927). On the flexure of thin cylindrical shells and other "thin" sections. *Proceedings of the Royal Society of London Series A – Containing Papers of a Mathematical and Physical Character* **116**, No. 773, 104-114.

Karamanos, S. A. (2002). Bending instabilities of elastic tubes. *International Journal of Solids and Structures* **39**, No. 8, 2059-2085.

Millard, A. & Roche, R. (1984). Elementary solutions for the propagation of ovalization along straight pipes and elbows. *International Journal of Pressure Vessels and Piping* **16**, No. 2, 101-129.

Reissner, E. (1959). On finite bending of pressurized tubes. *Journal of Applied Mechanics, ASME* **26**, 386–392.

Notation

E_p	Young's modulus of the pipe
h	thickness of the pipe
h_{red}	reduced thickness of the inclinometer pipe
K	lateral earth pressure coefficient
R	outer radius of the pipe
γ	density of soil
ΔD^χ	change in pipe diameter due to bending
ΔD_A^χ	change in diameter in direction A due to bending
ΔD_B^χ	change in diameter in direction B due to bending
$\Delta \Omega_{min}$	precision of the IDM device in terms of ovalization value
$\Delta \Omega^\chi$	change in ovalization value due to bending
δ_A^χ	angle between the channel in direction A and the direction of the curvature
θ^χ	circumferential coordinate with respect to direction of the curvature
ν_p	Poisson's ratio of the pipe
χ	curvature
χ_0	initial curvature
χ_{max}	maximum curvature

5 Inclinodeformeter pressure measurements in creeping landslides: analytical solutions and field applications

5.1 Abstract

The chapter derives analytical solutions for the deformation of a viscoelastic pipe in elastic soil under far-field principal stress increments. These solutions are validated in laboratory tests and numerical analysis and provide the basis for the back-calculation of earth pressure increments from measured changes in shape of an inclinometer pipe cross-section using inclinodeformeter (IDM) technology. The procedure has been applied to back-calculating earth pressure changes and soil stiffness in three creeping landslides in Switzerland, which are similar in size but have a range of different boundary conditions and displacement rate fields. In these applications, pressure increments of less than 1 kPa could be reliably back-calculated allowing for identification of compression and extension zones, as well as yielding and failure of soil in the landslides under study, confirming the previously developed models of the landslide mechanisms and suggesting that IDM pressure measurements could serve as a reliable tool for analysis and monitoring of creeping landslides.

5.2   Introduction

Understanding the earth pressure changes in a sliding layer of a creeping landslide is essential for analysis and stabilization of such landslides. In particular, the rate of change of the lateral earth pressure has been found to be a critical parameter for the validation of models for constrained creeping landslides (chapter 9 and chapter 10; Puzrin *et al.*, 2012).

The inclinodeformeter (IDM) is a device for back-calculation of the changes of earth pressure in the sliding layer of creeping landslides. IDM measures the change in dimensions of an inclinometer pipe and uses the measured deformations to back-calculate the change in pressure by solving the corresponding boundary value problem.

IDM makes use of the widespread inclinometer technology. In addition to the regular displacement profile, the IDM probe also provides a continuous profile of lateral earth pressures, using the same inclinometer pipe and requiring no further installation on the site.

In this chapter a simplified procedure is introduced for back-calculating the earth pressure changes. This procedure required derivation of analytical solutions for the deformation of viscoelastic pipes in elastic space under corresponding boundary conditions and calibration of these solutions against results of laboratory tests and numerical analysis. The procedure has then been applied to measuring earth pressure changes in three creeping landslides in Switzerland. These landslides are similar in size but have different boundary conditions and displacement rate fields, as listed below.

a)   The St Moritz-Brattas landslide is slowing downhill towards a rock outcrop at the bottom.

b)   The Braunwald landslide is accelerating downhill towards a vertical rock wall falling into a valley.

c)   The Ganter landslide is moving uniformly downhill towards a river bed.

Pressure measurements taken by IDM allow the identification of compression and extension zones in the sliding body and provide unique quantitative data for understanding and mechanical analysis of these creeping landslides.

5.3   Measuring deformations of the inclinometer pipe

In order to measure inclinometer pipe deformations, the IDM probe is lowered down the pipe guided by three wheels along a pair of its channels. There are two tilt sensors on the probe to measure the inner diameter of the pipe: one sensor is located on the top of the probe; another tilt sensor is located on the lever of the middle wheel (see section 1.3.1). The inner diameter D is a function of the relative inclination.

Diameter D_A (Figure 5-1) between the channels in direction A, where the larger displacements are expected, is measured first; direction B is perpendicular to A (Figure 5-1). In addition, continuous measurements are taken of the inclination of the probe in both directions A and B, of the temperature and of the water pressure in the pipe, at a frequency of 40 readings per 1 cm of depth.

After completing measurements of diameter D_A, the probe is rotated by 90° and lowered down again, guided along the second pair of channels, so that the diameter D_B can be measured along the pipe length. Because the tilt sensors are not independent of the inclination of the pipe out of the plane, both diameter readings are corrected for the influence of this inclination (see section 1.3.3). A correction function calibrated in laboratory tests is applied.
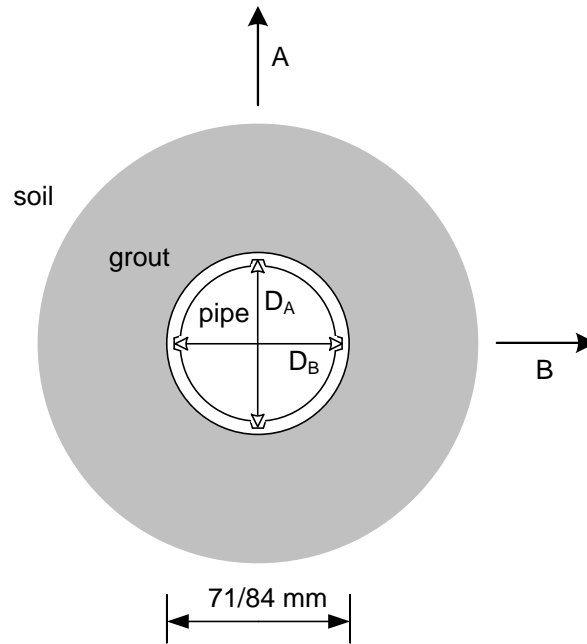
Figure 5-1: *Measured diameters in a horizontal cross-section of the installed inclinometer pipe.*

Next, the pipe ovalization value Ω is calculated, defined as the difference of the perpendicular diameters normalized by the nominal outer radius of the inclinometer pipe R.

$$\Omega = \frac{D_B - D_A}{R} \tag{5-1}$$

Unlike individual diameter measurements, the difference between the measured diameters does not appear to be sensitive to the temperature of the probe, long-term instability of the probe sensors, wear of the wheels, or to the influence of actual measurement conditions causing a uniform radial expansion or contraction of the pipe (such as temperature of the pipe, water pressures inside and outside of the pipe). Deformation changes of the pipe are always measured (and the corresponding pressure changes are back-calculated) relative to the first measurement in time, the so called zero-measurement. Further measurements at later points in time are taken after an expected change in lateral earth pressure has taken place. The deformation is described by the change in ovalization value $\Delta\Omega$ with respect to the zero measurement

$$\Delta\Omega_n = \Omega_n - \Omega_0 = \frac{\left(D_{B,n} - D_{A,n}\right) - \left(D_{B,0} - D_{A,0}\right)}{R} \tag{5-2}$$

Deformations of the pipe cross-section occur not only due to changes in earth pressures, but also as a result of the inclinometer pipe bending, causing its cross-section to flatten into an oval. The inclinometer pipe is subjected to bending due to displacements of the surrounding soil, which may not be related to earth pressure changes. The measured change in ovalization value can be corrected for bending, as described by an analytical formula calibrated against numerical simulations (chapter 4). However, if the pipe curvature is reasonably small, as is the case for many applications for IDM, no correction is necessary. The field measurements presented in this chapter have been obtained sufficiently far from the shear surface, so that the bending curvature did not exceed the threshold value defined in section 4.3. Therefore the cross-section deformation due to bending could be neglected for this study.

While the ovalization measurements are taken continuously over the thickness of the sliding layer, for back-calculation of the pressure changes a certain level of averaging and

discretization is required to eliminate measurement noise. The inclinometer pipe is made out of 3 m long casing elements. Each casing element is treated as one sensor, with the measurements averaged within the element over the length of 12 times the circumference of the wheels of the probe in order to reduce the influence of their imperfection. This leaves about 44 cm at the edges of the casing element which are neglected to eliminate the effects of the joints between the elements.

5.4 Analytical solutions for back-calculation of pressures

5.4.1 Boundary value problem: assumptions

The pressure increments causing deformations of a pipe cross-section in soil can be back-calculated from a solution of the corresponding boundary value problem, provided that the stiffness of the pipe, grout and soil are known in this range of pressures. Owing to the overburden, the vertical direction is assumed to be a principal stress direction with constant normal stress. The remaining non-zero components of the incremental stress tensor (i.e. the two principal stress increments $\Delta\sigma_1$ and $\Delta\sigma_2$ in the horizontal plane) are back-calculated by considering the boundary value problem given by a horizontal cross-section under generalized plane stress conditions (Figure 5-2). Within the plane, one principal stress direction of the increment is assumed to coincide with the direction of displacement, which is known from the conventional inclinometer measurements. The creeping landslides under consideration have wide moving fronts. Therefore, far away from the inclinometer pipe no horizontal displacements are assumed to occur in the direction perpendicular to the inclinometer measured displacement. Full slippage is assumed at the interface between the pipe and the soil. Radial deformations through the thickness of the pipe are assumed to be small.

Inclinometer pipes are fixed in the boreholes by grouting the annulus (Figure 5-1), with the grout around inclinometer pipes often chosen to mimic the deformation characteristics of the surrounding soil. The influence of the grout stiffness on the back-calculation of stresses is addressed in chapter 3. It appears that the back-calculation of stresses is not sensitive to the grout stiffness (Figure 3-18), with a ten-fold increase in the grout stiffness causing less than 30% maximum error in the back-calculated stress increments. Therefore, in the solution below it is assumed that the grout has the same stiffness as the sliding mass.
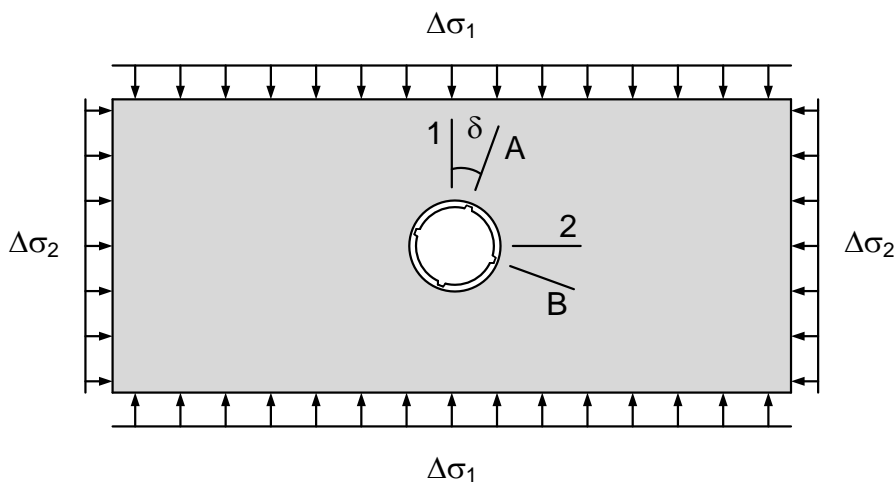
Figure 5-2: *Schematic layout of the boundary value problem.*

5.4.2 Boundary value problem: solution strategy

The solution for deformations of the viscoelastic pipe embedded in elastic soil under the far-field principal stress increments is derived through the following auxiliary steps.

a) First, deformations of the unsupported cylindrical cavity in elastic soil under far-field principal stress increments are calculated.

b) Second, a solution of the same problem, but with loaded cavity and zero far-field principal stress increments is derived.

c) Third, the general solution is derived for the deformations of the viscoelastic pipe subjected to variable radial pressures.

Finally, the pipe deformations caused by far-field changes in lateral earth pressure are obtained by combination of the three solutions derived above (i.e. deformation of the cylindrical cavity due to lateral earth pressure increments $u^{\Delta\sigma_1}$, deformation of the cavity due to pressure at the inclusion u^q and deformation of the pipe due to external pressure u^p).

Indeed, compatibility of the soil and the pipe displacements in the radial direction requires

$$u^{\Delta\sigma_1}\left(r = R, \theta, t\right) + u^q\left(r = R, \theta, t\right) = u^p\left(r = R, \theta, t\right) \tag{5-3}$$

which, combined with the equilibrium of pressures at the boundary between the pipe and the cavity, allows for calculation of the deformation of the cross-section of a viscoelastic pipe embedded in elastic soil under the far-field principal stress increments.

5.4.3 Unsupported cylindrical cavity under far-field principal stress increments

In the first auxiliary step, deformations of the unsupported cylindrical cavity under far-field principal stresses are going to be derived (Figure 5-3a). The principal pressures at infinite distance from the cavity are assumed to be $\Delta\sigma_1$ and $\Delta\sigma_2 = K_0\Delta\sigma_1$ owing to the far-field plane strain condition perpendicular to the landslide front, where $K_0 = v_s$. The static boundary conditions are decomposed into a hydrostatic component $\Delta\sigma_1(1 + K_0)/2$ and a deviatoric component $\pm\Delta\sigma_1(1 - K_0)/2$. The uniform contraction of the cavity caused by the hydrostatic component can be neglected because it has to be identical to the uniform contraction of the pipe, which is negligible compared to its ovalization. For the remaining deviatoric component, solution of the boundary value problem is the well-known Michell solution (e.g., Barber, 2002)

$$u^{\Delta\sigma_1}\left(r = R, \theta\right) = -\frac{2R\Delta\sigma_1\left(1 - K_0\right)\cos\left(2\theta\right)}{E_s} \tag{5-4}$$

where E_s is the Young's modulus and v_s is the Poisson's ratio of the soil; R is the radius of the cavity (identical to the outer radius of the pipe) and K_0 is the ratio between the two principal stresses in the plane.
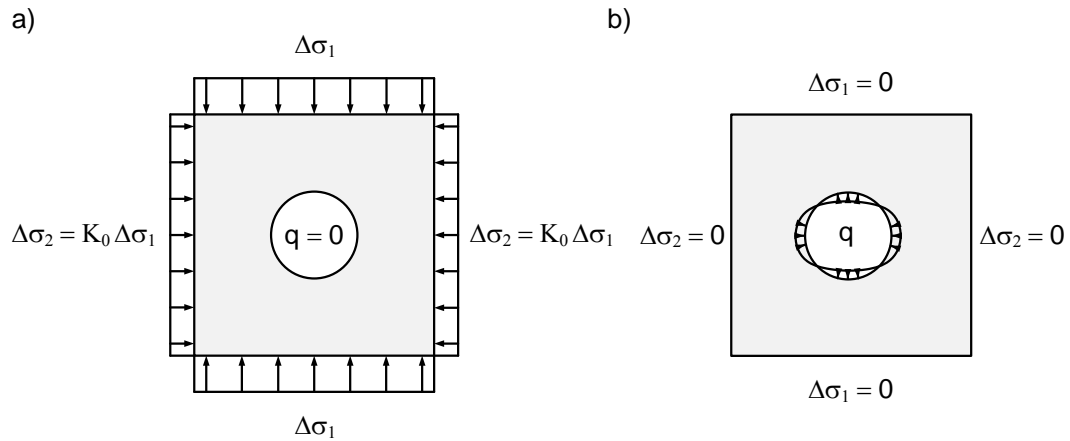
Figure 5-3: *Schematic layout of the two auxiliary boundary value problems: a) Unsupported cylindrical cavity under far-field principal stress increments, b) Loaded cylindrical cavity with zero far-field principal stress increments.*

5.4.4   Unsupported cylindrical cavity loaded by a variable radial pressure

The second auxiliary step requires solving the boundary value problem for the cylindrical cavity loaded by the pressure $-q(t)\cos(n\theta)$ at $r = R$, $n = 2, ...$ and zero far-field principal stresses (Figure 5-3b). Solution of this boundary value problem is another well-known Michell solution (e.g. Penzien and Wu, 1998; Barber, 2002):

$$u^{q}\left(r = R, \theta\right) = \frac{R q\left(t\right) \cos\left(n\theta\right)\left(5 - v_{s}\right)}{3 E_{s}} \tag{5-5}$$

5.4.5   Viscoelastic solution for the pipe under plane stress conditions

In the third auxiliary step, viscoelastic deformations are derived for the pipe subjected to a variable radial pressure. Inclinometer pipes used in this study are made out of PVC. They show a time-dependent mechanical behavior, which can be described by the viscoelastic Burgers model (chapter 2). An analytical solution for the radial deformation of a pipe without channels is derived below for the case of constant pressure (creep) and constantly increasing pressure (constant rate), relevant for the long-term loading conditions in creeping landslides.

The external pressure $p(\theta, t)$ acting on the pipe is assumed to be the following function of the circumferential coordinate and time

$$p\left(\theta, t\right) = -p_{n}\left(t\right)\cos\left(n\theta\right) \qquad n \geq 2 \tag{5-6}$$

where n is an integer number. The hydrostatic case of $n = 0$ is neglected, because no ovalization is formed. The case of $n = 1$ is ignored owing to the lack of equilibrium. Static equilibrium of the thin-walled pipe in plane stress conditions is given by (Figure 5-4a)

$$V d\theta + dN = 0 \tag{5-7}$$

$$dV - N d\theta + p\left(\theta, t\right) R_{m} d\theta = 0 \tag{5-8}$$

$$dM - V R_{m} d\theta = 0 \tag{5-9}$$

where R_m is the mean radius of the pipe, N is the internal normal force, V is the shear force and M is the moment.
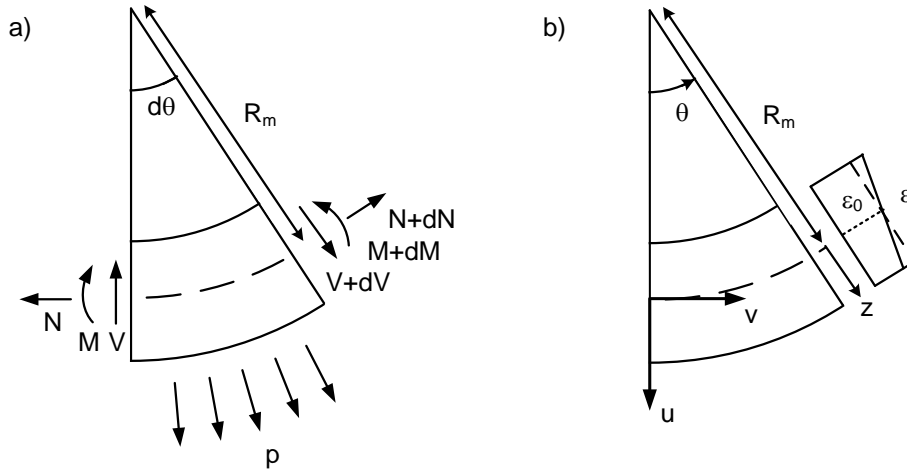
Figure 5-4: *a) Notation of internal and external forces, b) Notation of displacements and strains.*

Combining equilibrium Equations (5-7)-(5-9), the following differential equations are obtained for the normal force and the moment

$$\frac{d^2 N}{d\theta^2} + N = -p_n(t)R_m\cos(n\theta) \tag{5-10}$$

$$\frac{d^2 M}{d\theta^2} + M = p_n(t)R_m^2\cos(n\theta) \tag{5-11}$$

Because the symmetry is required to be the same as for the applied pressure, the solutions of the Equations (5-10) and (5-11) are given by

$$N(\theta,t) = \frac{1}{n^2 - 1}p_n(t)R_m\cos(n\theta) \tag{5-12}$$

$$M(\theta,t) = \frac{-1}{n^2 - 1}p_n(t)R_m^2\cos(n\theta) \tag{5-13}$$

According to Bouma (1993), from the compatibility considerations, the strain profile through the thickness of the pipe (Figure 5-4b) can be described as

$$\varepsilon(z) = \frac{R_m}{R_m + z}(\varepsilon_0 + \chi z) \tag{5-14}$$

where $\varepsilon_0 = \varepsilon(0)$ and $\chi = \varepsilon'(0) + \varepsilon(0)/R_m$, which are related to the radial displacement u and the tangential displacement v by the kinematic equations

$$\varepsilon_0(\theta,t) = \frac{1}{R_m}\left(\frac{\partial v}{\partial\theta} + u\right) \tag{5-15}$$

$$\chi(\theta,t) = \frac{1}{R_m^2}\left(\frac{\partial v}{\partial \theta} - \frac{\partial^2 u}{\partial \theta^2}\right)$$

(5-16)

The constitutive equation of the pipe material in terms of circumferential stress and strain is given by the Burgers model (Figure 5-5)

$$\sigma + p_1\dot{\sigma} + p_2\ddot{\sigma} = q_1\dot{\varepsilon} + q_2\ddot{\varepsilon}$$

(5-17)

where q_1, q_2, p_1 and p_2 are parameters of the Burgers model

$$p_1 = \frac{\eta_0}{E_0} + \frac{\eta_1}{E_1} + \frac{\eta_0}{E_1}; \quad p_2 = \frac{\eta_0\eta_1}{E_0 E_1}; \quad q_1 = \eta_0; \quad q_2 = \frac{\eta_0\eta_1}{E_1}$$

(5-18)
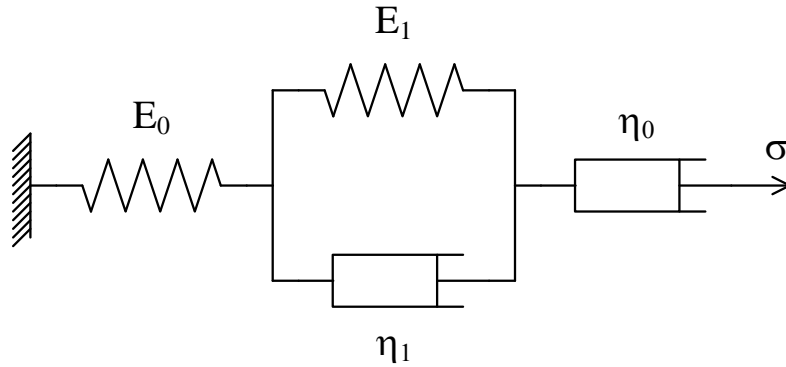
Figure 5-5: *The linear viscoelastic Burgers model.*

The wall of the ring is considered to be thin. Therefore, neglecting higher order terms (Bouma, 1993) gives the following viscoelastic constitutive equations in terms of forces and moments (Appendix I)

$$N + p_1\dot{N} + p_2\ddot{N} = q_1\left(A\dot{\varepsilon}_0 - \frac{I}{R_m}\dot{\chi}\right) + q_2\left(A\ddot{\varepsilon}_0 - \frac{I}{R_m}\ddot{\chi}\right)$$

(5-19)

$$M + p_1\dot{M} + p_2\ddot{M} = q_1\left(-\frac{I}{R_m}\dot{\varepsilon}_0 + I\dot{\chi}\right) + q_2\left(-\frac{I}{R_m}\ddot{\varepsilon}_0 - I\ddot{\chi}\right)$$

(5-20)

where $A = 1 \times h$ is the area and $I = 1 \times h^3/12$ is the moment of inertia of the cross-section.

Equations (5-12) and (5-13), Equations (5-15) and (5-16), and Equations (5-19) and (5-20) are static, kinematic and constitutive equations, respectively, constituting together with the loading condition (Equation 5-6) the viscoelastic boundary value problem for a thin pipe under plane stress-conditions. This problem will be solved using the elastic–viscoelastic correspondence principle (e.g. Findley *et al.*, 1976).

As the first step, a simpler elastic problem will be solved. Assuming for the pipe material purely elastic constitutive behavior in terms of circumferential stress and strain $\sigma = E\varepsilon$, Equations (5-19) and (5-20) reduce to the following elastic constitutive equations in terms of forces and moments

$$N = E\left(A\varepsilon_0 - \frac{I}{R_m}\chi\right)$$

(5-21)

$$M = E\left(-\frac{I}{R_m}\varepsilon_0 + I\chi\right) \tag{5-22}$$

Combining Equations (5-12) and (5-13), Equations (5-15) and (5-16), and Equations (5-21) and (5-22) results in the following differential equation of the elastic boundary value problem

$$u + \frac{\partial^2 u}{\partial\theta^2} = \frac{1}{n^2 - 1}\frac{R_m^4}{EI}p_n\cos(n\theta) \tag{5-23}$$

which has the solution

$$u(\theta) = -\frac{1}{(n^2 - 1)^2}\frac{R_m^4}{EI}p_n\cos(n\theta) \tag{5-24}$$

In the second step, Equations (5-12) and (5-13), Equations (5-15) and (5-16), and Equations (5-19) and (5-20) of the viscoelastic boundary value problem are transformed into Laplace space

$$\hat{N}(\theta, s) = \frac{1}{n^2 - 1}\hat{p}_n(s)R_m\cos(n\theta) \tag{5-25}$$

$$\hat{M}(\theta, s) = \frac{-1}{n^2 - 1}\hat{p}_n(s)R_m^2\cos(n\theta) \tag{5-26}$$

$$\hat{\varepsilon}_0(\theta, s) = \frac{1}{R_m}\left(\frac{\partial\hat{v}}{\partial\theta} + \hat{u}\right) \tag{5-27}$$

$$\hat{\chi}(\theta, s) = \frac{1}{R_m^2}\left(\frac{\partial\hat{v}}{\partial\theta} - \frac{\partial^2\hat{u}}{\partial\theta^2}\right) \tag{5-28}$$

$$\hat{N} = \frac{q_1 s + q_2 s^2}{1 + p_1 s + p_2 s^2}\left(A\hat{\varepsilon}_0 - \frac{I}{R_m}\hat{\chi}\right) \tag{5-29}$$

$$\hat{M} = \frac{q_1 s + q_2 s^2}{1 + p_1 s + p_2 s^2}\left(-\frac{I}{R_m}\hat{\varepsilon}_0 + I\hat{\chi}\right) \tag{5-30}$$

Equations (5-25)-(5-30) are equivalent to Equations (5-12) and (5-13), Equations (5-15) and (5-16), and Equations (5-21) and (5-22) of the elastic boundary value problem where the elastic modulus E is replaced by the transformed modulus

$$\hat{E}(s) = \frac{q_1 s + q_2 s^2}{1 + p_1 s + p_2 s^2} \tag{5-31}$$

Finally, according to the elastic–viscoelastic correspondence principle, the solution is equivalent to the elastic one in Equation (5-24) where true variables are replaced by the corresponding transformed ones

$$\hat{u}(\theta, s) = -\frac{1}{(n^2 - 1)^2} \frac{R_m^4}{I \dfrac{q_1 s + q_2 s^2}{1 + p_1 s + p_2 s^2}} \hat{p}_n \cos(n\theta) \tag{5-32}$$

The inverse Laplace transformation is applied to Equation (5-32) first for the case of a load function of $p_n = const$ corresponding to the transformed value of

$$\hat{p}_n(s) = \frac{p_n}{s} \tag{5-33}$$

and then for the case of a load function of $\dot{p}_n = const$ corresponding to

$$\hat{p}_n(s) = \frac{\dot{p}_n}{s^2} \tag{5-34}$$

The resulting transformation to the time domain yields the viscoelastic solution

$$u(\theta, t) = -\frac{1}{(n^2 - 1)^2} \frac{R_m^4}{I} p_n \cos(n\theta) \left(\frac{1}{E_0} + \frac{1}{E_1}\left(1 - e^{-\frac{E_1}{\eta_1}t}\right) + \frac{1}{\eta_0}t \right) \tag{5-35}$$

for creep conditions with constant pressure p_n, and

$$u(\theta, t) = -\frac{1}{(n^2 - 1)^2} \frac{R_m^4}{I} \dot{p}_n \cos(n\theta) \left(\frac{\eta_1}{E_1^2}\left(e^{-\frac{E_1}{\eta_1}t} - 1 \right) + \frac{1}{2\eta_0}t^2 + \left(\frac{1}{E_0} + \frac{1}{E_1} \right)t \right) \tag{5-36}$$

for constant stress rate conditions with constant pressure rate $\dot{p}_n$.

5.4.6 Combined solution for the pipe – soil interaction

As is seen from Equation (5-4), the increment of the far-field principal stresses causes radial displacements of the cylindrical cavity proportional to $\cos(n\theta)$, where $n = 2$. These displacements will have to be compatible with the corresponding pipe displacements from Equations (5-35) and (5-36), that is, the deformation mode of the pipe will also be defined by $\cos(n\theta)$, with $n = 2$. According to Equation (5-6), this is only possible if the pressures acting on the pipe are proportional to $\cos(2\theta)$. According to the Third Law of Newton, the same pressures with the opposite sign will act on the boundary of the cavity. Therefore, in the second auxiliary step the cylindrical cavity will be loaded by the pressure $-q(t)\cos(2\theta)$ at $r = R$ and zero far-field principal stresses, which, following Equation (5-5), also produce the cavity deformation mode proportional to $\cos(2\theta)$, compatible with the corresponding pipe deformation mode.

Thus, the pipe deformations caused by changes in lateral earth pressure are obtained by combination of the derived solutions (i.e. deformation of the cylindrical cavity due to lateral earth pressure increments $u^{\Delta\sigma_1}$, deformation of the cavity due to pressure at the inclusion u^q and deformation of the pipe due to external pressure u^p, both for the deformation mode of $n = 2$), provided the equilibrium of pressures at the boundary between the pipe and the cavity and the compatibility of the soil and the pipe displacements in the radial direction are satisfied

$$u^{\Delta\sigma_1}(r = R, \theta, t) + u^q(r = R, \theta, t) = u^p(r = R, \theta, t) \approx u^p(r = R_m, \theta, t) \tag{5-37}$$

For formulating the equilibrium condition for the pressures at the boundary between the pipe and cylindrical cavity, the true pressure q on the outside radius R of the pipe has to

be related to the pressure boundary condition for the thin-walled pipe solution: the pressure p acting at the radius R_m. For this, the thin-walled solution and the thick-walled solution are required to produce the same displacements at R_m (Appendix II). After neglecting higher terms, this gives the equilibrium equation for the pressures needed for solving Equation (5-37)

$$p\left(r = R_m, t\right) = \frac{R}{R_m} q\left(r = R, t\right) \tag{5-38}$$

Equations (5-4), (5-5), (5-6), (5-38) and (5-35) for $n = 2$ are then substituted into Equation (5-37) and resolved with respect to the constant pressure p_n, which, after being substituted back into pipe deformation Equation (5-35) for $n = 2$, produces for creep conditions $(\sigma_1 = const)$

$$u^p\left(\theta, t\right) = -\frac{2R\left(1 - K_0\right)\cos\left(2\theta\right)\sigma_1}{E_s + \alpha E_p} \tag{5-39}$$

where

$$\alpha = \frac{3\left(5 - \nu_s\right)I}{R_m^3}; \quad E_p = \frac{1}{\dfrac{1}{E_0} + \dfrac{1}{E_1}\left(1 - e^{-\frac{E_1}{\eta_1}t}\right) + \dfrac{1}{\eta_0}t} \tag{5-40}$$

Next, Equations (5-4), (5-5), (5-6), (5-38) and (5-36) for $n = 2$ are substituted into Equation (5-37) and resolved with respect to the constant pressure change $\dot{p}_n$, which, after being substituted back into pipe deformation Equation (5-36) for $n = 2$, produces for constant rate conditions $(\dot{\sigma}_1 = const)$

$$u^p\left(\theta, t\right) = -\frac{2R\left(1 - K_0\right)\cos\left(2\theta\right)\dot{\sigma}_1 t}{E_s + \alpha E_p} \tag{5-41}$$

where

$$\alpha = \frac{3\left(5 - \nu_s\right)I}{R_m^3}; \quad E_p = \frac{t}{\dfrac{\eta_1}{E_1^2}\left(e^{-\frac{E_1}{\eta_1}t} - 1\right) + \dfrac{1}{2\eta_0}t^2 + \left(\dfrac{1}{E_0} + \dfrac{1}{E_1}\right)t} \tag{5-42}$$

Equations (5-39) and (5-41) can be used for interpretation of the IDM measurements by adopting the definition of the ovalization increment from Equation (5-2). Indeed, if the zero measurement is taken before the onset of loading, the major principal lateral pressure increment depends on the measured change in ovalization value by way of

$$\Delta\sigma_1\left(t_n\right) = \frac{E_s + \alpha E_p\left(t_n\right)}{8\left(1 - K_0\right)\cos\left(2\delta\right)} \Delta\Omega\left(t_n\right) \tag{5-43}$$

where t_n is the time of the current measurement, with the time origin taken at the onset of loading; E_p and α are given by Equations (5-40) and (5-42), for creep and constant rate conditions, respectively; δ is the angle between the direction of the inclinometer pipe channels and the direction of principal stresses (Figure 5-2).

In case the onset of loading takes place before the zero measurement, Equation (5-43) evolves into the following two equations. For creep conditions, the pressure increment is obtained from the change in ovalization value measured over the time period (t_0, t_n):

$$\Delta\sigma_1(t_0,t_n) = \frac{\Delta\Omega(t_0,t_n)}{8(1-K_0)\cos(2\delta)} \frac{1}{\dfrac{1}{E_s+\alpha E_p(t_n)} - \dfrac{1}{E_s+\alpha E_p(t_0)}}$$ (5-44)

where E_p and α are given by Equation (5-40) with the time of the zero measurement t_0 and the time of the current measurement t_n measured from the onset of loading.

For constant rate conditions, the pressure increment is given by

$$\Delta\sigma_1(t_0,t_n) = \frac{\Delta\Omega(t_0,t_n)}{8(1-K_0)\cos(2\delta)} \frac{t_n-t_0}{\dfrac{t_n}{E_s+\alpha E_p(t_n)} - \dfrac{t_0}{E_s+\alpha E_p(t_0)}}$$ (5-45)

where E_p and α are defined from Equation (5-42).

The second principal lateral pressure increment is then given by

$$\Delta\sigma_2 = K_0\Delta\sigma_1$$ (5-46)

Equations (5-43)-(5-46) represent analytical formulas allowing for back-calculation of the principal stress increments from the measured ovalization values of the inclinometer pipe cross-section.

5.5 Validation of the analytical solutions

5.5.1 Validation of the solution for the pipe

The analytical solution derived above for the pipe can be validated against laboratory tests on pipe samples performed in a simple test setup (Figure 5-6) by applying two equivalent opposing forces to the pipe in the transversal direction (see section 2.4).
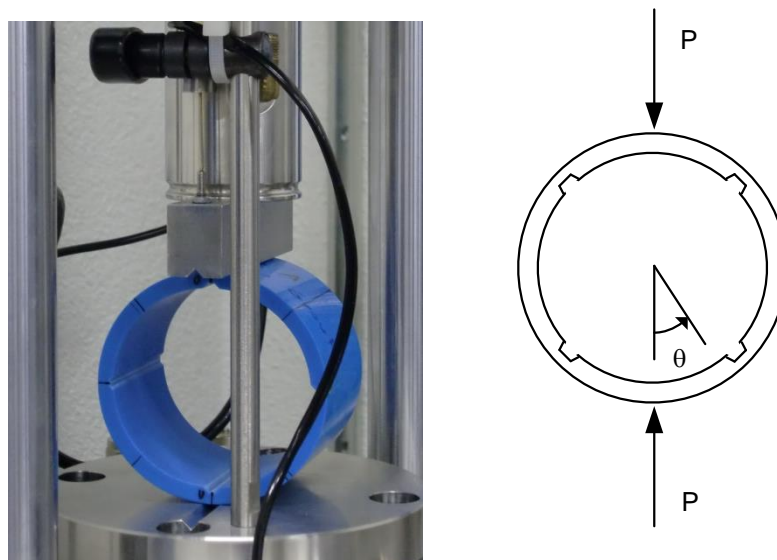
Figure 5-6: *Laboratory tests performed on pipe samples: a) Test setup, b) Schematic layout of the test setup.*

Loading by two opposite forces $P(t)$ acting at $\theta = 0$ and $\theta = \pi$ can be presented by way of Fourier series

$$p(\theta,t) = -\frac{P(t)}{\pi R_m} - \frac{2P(t)}{\pi R_m} \sum_{n=1}^{n=\infty} \cos(2n\theta) \qquad (5\text{-}47)$$

where the first term (hydrostatic pressure) is neglected due to its minor influence on the deformations. After substitution of Equation (5-47) into Equations (5-35) and (5-36), the solution is given by

$$u(\theta,t) = -\frac{2PR_m^3}{\pi I}\left(\frac{1}{E_0} + \frac{1}{E_1}\left(1 - e^{-\frac{E_1}{\eta_1}t}\right) + \frac{1}{\eta_0}t\right) \sum_{n=1}^{n=\infty} \frac{\cos(2n\theta)}{\left((2n)^2 - 1\right)^2} \qquad (5\text{-}48)$$

for creep conditions with constant force P, and

$$u(\theta,t) = -\frac{2\dot{P}R_m^3}{\pi I}\left(\frac{\eta_1}{E_1^2}\left(e^{-\frac{E_1}{\eta_1}t} - 1\right) + \frac{1}{2\eta_0}t^2 + \left(\frac{1}{E_0} + \frac{1}{E_1}\right)t\right) \sum_{n=1}^{n=\infty} \frac{\cos(2n\theta)}{\left((2n)^2 - 1\right)^2} \qquad (5\text{-}49)$$

for constant rate conditions with constant change in force $\dot{P}$.

The inclinometer pipes installed in the landslide areas are assumed to have the same properties as the material of pipe A tested and described in chapter 2. Parameters of the Burgers model were obtained in independent laboratory tests with the pipe compressed in the longitudinal direction. In order to model the transversal behavior, the stiffness anisotropy in transversal direction has to be taken into account. This was achieved by reducing the elastic components of the Burgers model by a factor determined from back-analysis of transversal creep tests. This factor was found to be constant for different pipes. Resulting parameters for transversal modeling are presented in Table 5-1.

Table 5-1: *Parameters of the four-parameter Burgers model for transversal loading of the pipe.*

parameter	value
E_0	2200 MPa
η_0	3.0×10^6 MPa×day
E_1	21120 MPa
η_1	5.0×10^4 MPa×day

The analytical solutions, Equations (5-48) and (5-49), were validated against results of lab tests, where a sample of the pipe was loaded in the transversal direction by two opposite forces, in both the creep and constant rate modes (Figure 5-6b). In order to assess the effect of the inclinometer wheel channels, tests were performed on pipe samples at different axes rotation angles and finite element analysis was used for test interpretation (see section 2.4). These tests allowed for successful validation of the viscoelastic model for the true geometry of the channels. Because at the rotation of 45° the stiffness reduction caused by the channels is very small, the behavior of the pipe is well described by the analytical solution, allowing for back-calculation of the parameters of the viscoelastic model.

The measured pipe deformations are compared with the analytical solutions provided by Equations (5-48) and (5-49) using parameters in Table 5-1 (Figure 5-7). Figure 5-7a shows the comparison between measured and calculated deformations for a creep test lasting 10 days. Figure 5-7b shows deformations (normalized by the load rate) for four different tests at four different loading rates within four orders of magnitude. The longest test duration is 4 days. As can be seen, both analytical solutions provide remarkably good visual fit to the experimental data and their finite element simulations.
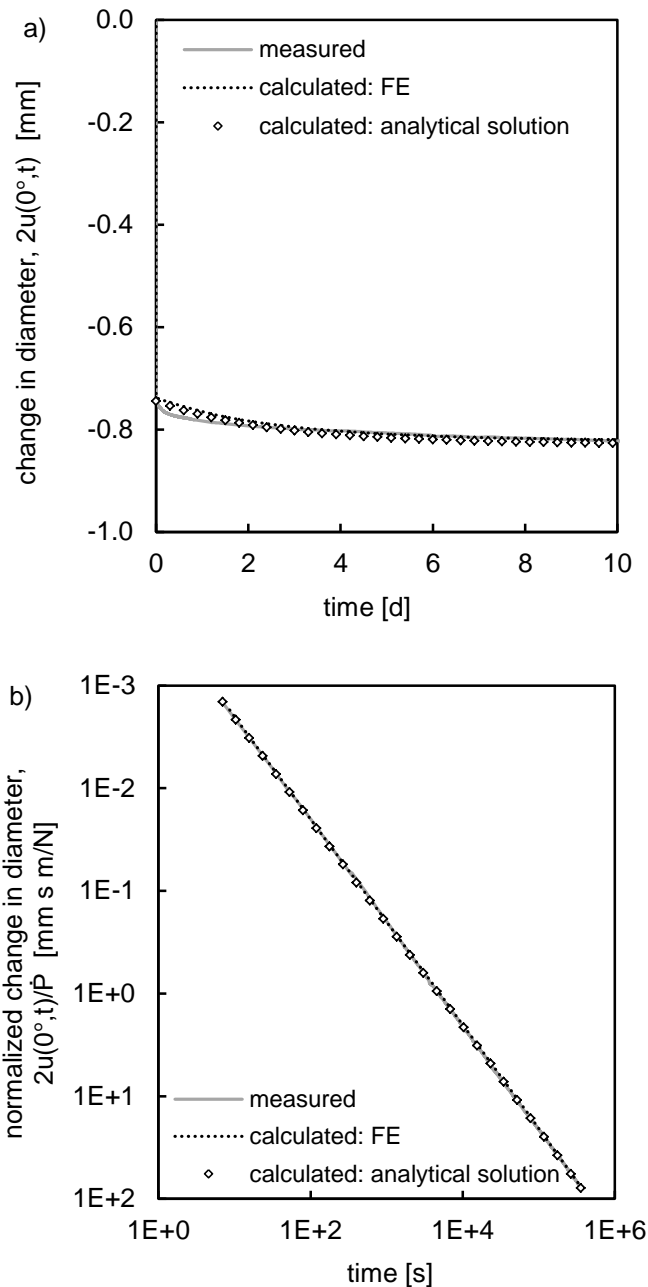
Figure 5-7: *Comparison of measured and calculated deformations: a) Pipe sample loaded with constant opposite forces of $P = 3636\ N/m$, b) Pipe sample loaded in four different tests with constantly increasing opposite forces at the rates of $\dot{P} = 0.01\ N/m/s$, $\dot{P} = 0.1\ N/m/s$, $\dot{P} = 1\ N/m/s$ and $\dot{P} = 10\ N/m/s$.*

For other types of the inclinometer casing, parameters of the Burgers model can be found from the longitudinal and transversal compression, creep and constant rate lab tests similar to those presented in Figure 5-6 and Figure 5-7.

5.5.2   Validation of the combined solution

Validation of the combined solution was carried out against the results of numerical simulations, which in turn were validated against results of the full-scale laboratory tests performed in a 200 cm tall calibration chamber (IDM box) with a horizontal cross-section of 40 cm by 40 cm (see section 3.3). This two-step procedure allowed for eliminating of the effect of the boundaries present in the experimental setup.

In the first step, a numerical finite-element solution for a 40 cm by 40 cm model (see section 3.5) was calibrated against short-term (see section 3.6) and long-term (see section 2.5) laboratory tests, where the lateral pressure σ_1 was applied using pressure membranes with constrained kinematic boundary conditions in perpendicular direction (see Figure 3-2a). At each loading step the soil was assumed linear elastic with its parameters obtained in laboratory tests. The viscoelastic four-parameter Burgers model with parameters from Table 5-1 was used for the material of the pipe, which was modeled using true geometry with channels. As can be seen from Figure 3-12a and Figure 2-13a, both for the short term and long-term loading, the finite-element model managed to reproduce the experimental behavior reasonably well.

In the second step, the same numerical model, as validated in the first step, was applied to a different set of boundary conditions, which were closer to those of the analytical solution and more appropriate for the landslide applications. In particular, in order to eliminate effects of the boundaries, dimensions of the horizontal cross-section were increased to 2 m by 2 m. Plane stress conditions were introduced in the vertical direction. The major principal stress, increasing at a constant rate, was applied to one set of the boundaries. On the second perpendicular set of the boundaries, displacements were kinematically constrained. Comparison between numerical and analytical solutions is shown in Figure 5-8, where the obtained change in ovalization value is normalized by the stress rate in kilopascals per year. Although the channels lower the moment of inertia locally, the analytical solution, Equations (5-43)-(5-46), can provide a good approximation to the numerical one for a broad range of different Young's moduli of soil E_s and different angles δ between the principal stresses and pipe channels (Figure 5-8), provided the real thickness of the pipe is reduced to an equivalent value h_{red} (see Table 5-2).
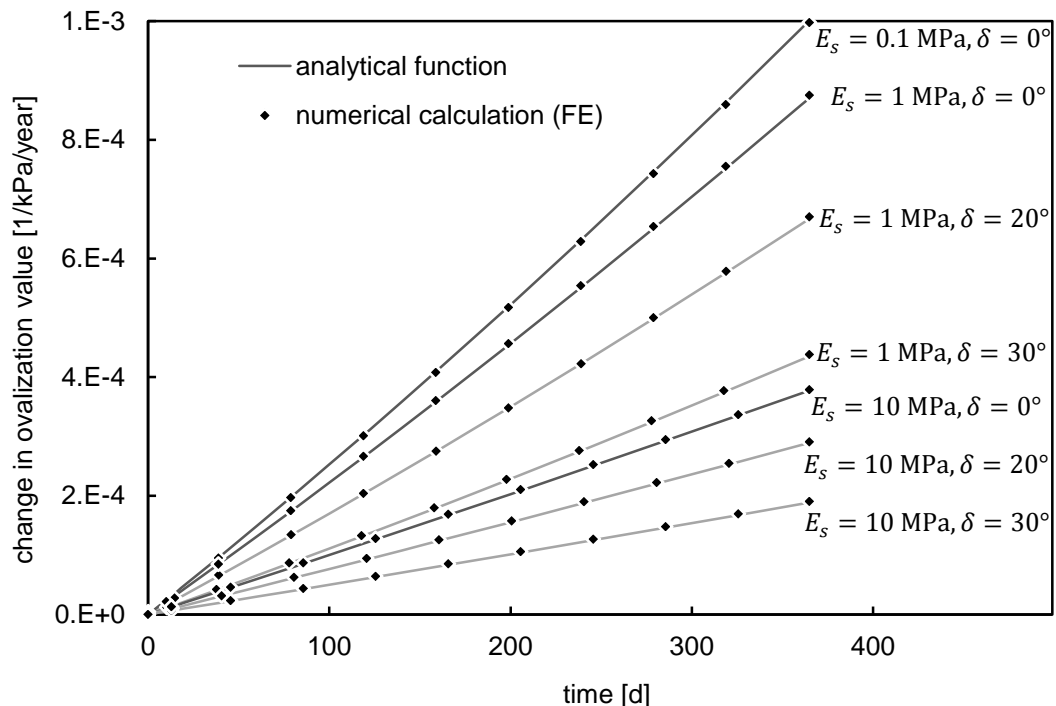
Figure 5-8: *Change in ovalization value at constant stress rate: comparison of the analytical solution with finite-element calculations (pipe 84) for a 2 × 2 m model.*

Table 5-2: Geometric parameters of the two most common inclinometer pipes used in Switzerland.

symbol	parameter description	pipe 84	pipe 71
R	outer radius of the pipe	42 mm	35.35 mm
R_m	mean radius of the pipe	38.925 mm	32.275 mm
h_{red}	reduced thickness	5.5 mm	5.25 mm

5.6 Application of the analytical solutions to back-calculation of earth pressures in the creeping landslides

Application of the analytical solutions, Equations (5-43)-(5-46), to back-calculation of increments of earth pressures in creeping landslides requires the knowledge of the soil stiffness and of the principal stresses at the time of the inclinometer pipe installation. These values introduce significant uncertainty into the proposed method, and the present section describes procedures allowing for these uncertainties to be significantly reduced in the back-calculation of the earth pressure increments.

5.6.1 Incorporating in-situ strain measurements

The incremental soil stiffness can be defined from laboratory or field tests, but considering its stress dependency, in particular when the soil exhibits yielding, this requires the knowledge of the in-situ stress state, which is another source of uncertainty. A practical way to reduce these uncertainties is by measuring soil displacements in the vicinity of the inclinometer pipe and calculating the average lateral strain increments $\Delta\varepsilon$. The major principal stress increment $\Delta\sigma_1$ is then expected to occur in the direction of the observed major strain increment (assumed to coincide with the direction of the incremental displacement vector)

$$\Delta\sigma_1\left(t_0,t_n\right) = \frac{E_s}{1-v_s^2}\Delta\varepsilon\left(t_0,t_n\right) \tag{5-50}$$

Each of the Equations (5-43)-(5-45) has two unknowns: the pressure increment and the soil stiffness. Equation (5-50) has the same two unknowns and, being solved together with one of the Equations (5-43)-(5-45), appropriate for a particular case under study, would allow for back-calculation of both the principal stress increments and the tangent stiffness of the soil by way of measured ovalization and average lateral strain.

5.6.2 Assumption of the isotropic initial stress state

Initial stress state after installation of the inclinometer pipe causes creep of the pipe and effects its deformations as described by Equations (5-39) and (5-40), even if no further changes in the earth pressures take place. When the major principal stress does experience changes (at the constant rate), pipe deformations are described by superposition of the solutions (5-39) and (5-41). Either way, the solution requires the knowledge of both principal stresses at the time of installation, which is a source of uncertainty.

This uncertainty can be significantly reduced by using the fact that the drilling of the borehole, installation and grouting of the pipe change the initial stress state around the pipe from anisotropic towards the isotropic state. The isotropic stress state does not contribute

to the pipe ovalization, therefore the creep component of the pipe ovalization can be neglected, and the only solution to be used for calculating pipe deformations is given by Equations (5-41) and (5-42), resulting in Equation (5-45), which allows for back-calculation of the major principal stress increment at any point in time, with the time origin taken at the moment of the completion of the pipe installation. The stiffness of PVC in short-term loading is found to be less than 2% higher at 8° compared to 20° (Domininghaus *et al.*, 2008). Therefore, the influence of the temperature difference between the lab and the field on the viscoelastic model seems to be relatively small compared to other uncertainties of the presented approach.

The system of Equations (5-45) and (5-50) produces a quadratic equation for the soil stiffness, which has only one positive root. This solution is used in analysis of the three case studies presented in the following sections.

5.7 Case study: St Moritz-Brattas landslide

5.7.1 Description

The St Moritz slide is 1500 m long, 600–800 m wide and with average inclination of about 20° (Schlüchter, 1988). This landslide is constrained by the rock outcrop at the bottom of the sliding layer along the Via Maistra (Figure 5-9), which can be clearly identified from the contours of yearly horizontal displacements. The displacement rates increase uphill from the rock outcrop, while the field pressures in the sliding layer are expected to increase towards the toe of the slope.

A one-dimensional mechanical model considering the propagation of a zone of intense shearing along the slip surface is proposed for the St Moritz landslide in chapter 9. For validation of the model IDM measurements (inclinometer pipe 601) were taken close to the bottom boundary of the landslide (Figure 5-9). Additional IDM measurements (inclinometer pipe 702) were performed further away from the bottom boundary, but closer to the side boundary of the landslide.

Long-term stability of the landslide is of the greatest concern for the St Moritz community. Information about the earth pressure changes is essential, because the high pressures in the compression zone are suspected to be the cause of the landslide accelerations.
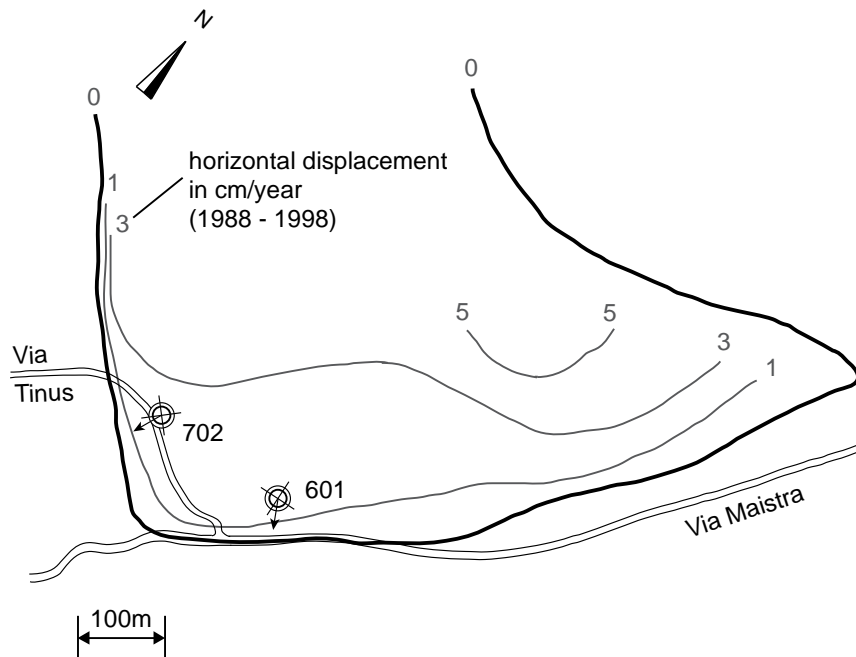
Figure 5-9: *The St Moritz-Brattas slide with displacement rates and location of the boreholes (after Schlüchter, 1988).*

5.7.2 IDM pressure measurements

IDM measurements were taken in the borehole 601 from 2008 to 2012 (Figure 5-9). Inclinometer measurements could be performed in the same borehole from 2008 to 2011, after which the inclinometer probe could not pass through the shear zone any longer. The shear zone is observed at the depth of 16.5 m being less than 0.5 m thick. The average annual displacement at the ground surface is 22 mm. The average annual strain increment $\Delta\varepsilon$ is obtained between the borehole and the landslide boundary of zero displacement (Table 5-3).

The major principal stress increments are expected to occur in the direction of the observed compressive strain increments, that is, downslope. The change in ovalization of the pipe measured by IDM confirms the increase in pressures over almost the whole depth and measuring period (Figure 5-10). The inner diameter of the pipe in the direction of the slope became smaller with respect to the perpendicular diameter. Hence the ovalization value is increasing with time. The averaged change of the ovalization value $\Delta\Omega$ in time is calculated as 0.014 %/yr for the inclinometer pipe elements between 7.0 m and 12.1 m (the elements close to the ground surface or influenced by the shear zone were not considered).

The corresponding pressure increments and the tangent stiffness of soil can be back-calculated from Equations (5-45) and (5-50), after substituting Equation (5-42), and accounting for the angle δ between the pipe axes and the principal stress directions (Table 5-3).

The pressure increment $\Delta\sigma_1$ of 0.2 kPa/yr compares well with the range of 0.11–1.1 kPa/yr for the years 2008–2010 predicted by the analytical model (chapter 9), which concluded that the earth pressure at the bottom reached the passive pressure around 1993. Comparing the very small back-calculated deformation modulus of the soil E_s of 0.3 MPa with the elastic modulus of 17.9 MPa based on Marchetti dilatometer tests (chapter 9; Puzrin *et al.*, 2008) confirms that the soil exhibits secondary compression and post-failure hardening.
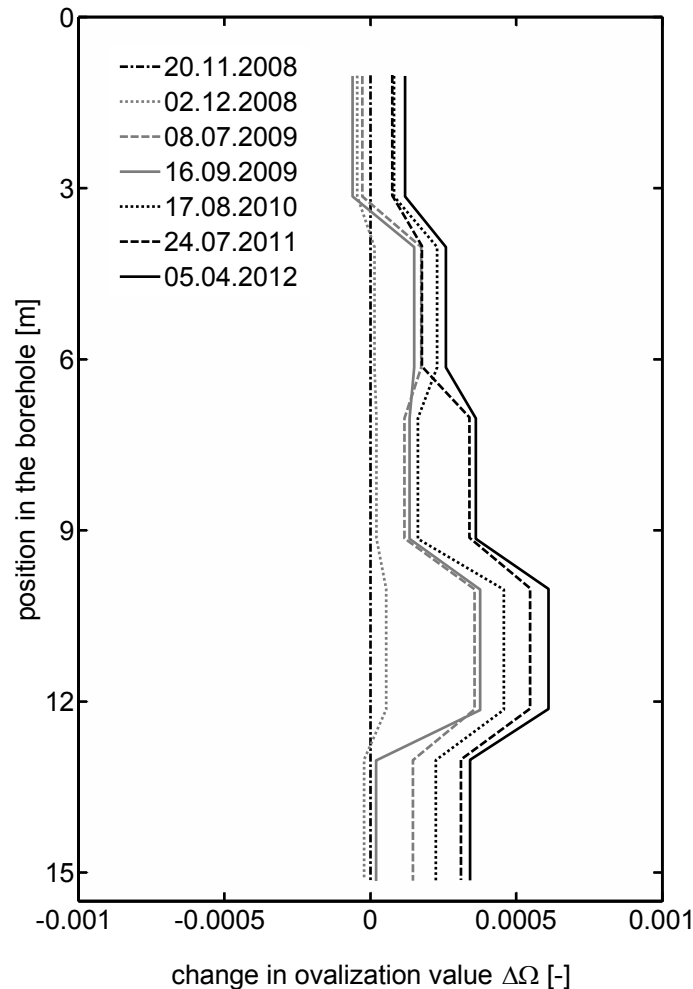
Figure 5-10: *Pipe deformation of inclinometer 601 measured by IDM, St Moritz.*

IDM measurements were also taken in borehole 702 (Figure 5-11) in the inclinometer pipe, which was sheared in 1997. The location of the slip surface at a depth of 21 m and the direction of the displacement vector are known from inclinometer measurements performed from 1995 to 1997. The current displacement rate of 33 mm/yr is obtained from nearby geodetic measurements. Although the strain rate is similar to that of inclinometer 601, the change in ovalization value ΔΩ is considerably higher in the upper part of the borehole (Figure 5-11 and Table 5-3). Pipe elements from 1.8 m to 6.8 m were taken for averaging. In spite of the larger change in ovalization, the back-calculated deformation modulus E_s of 0.6 MPa and the pressure increment of 0.4 kPa/yr are comparable to those in the borehole 601. This again confirms the soil failure, strain hardening and secondary compression in the compression zone, while the larger change in ovalization in the pipe of the borehole 702 can be explained by the fact that it was installed 16 years earlier than the pipe in the borehole 601, resulting in the lower viscoelastic stiffness of the pipe.
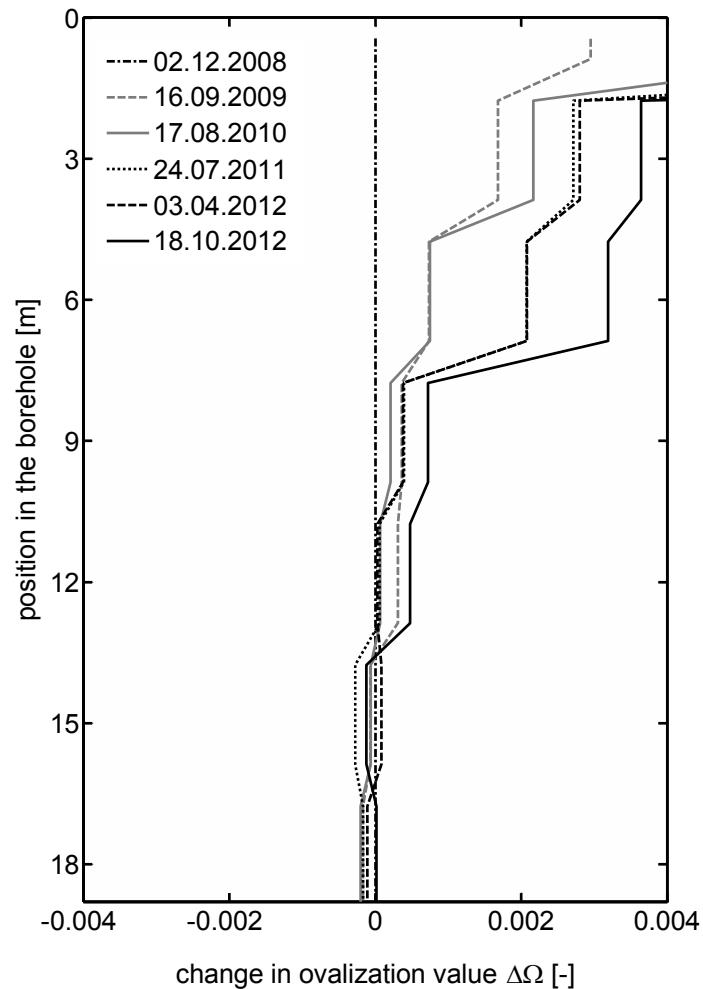
Figure 5-11: *Pipe deformation of inclinometer 702 measured by IDM, St Moritz.*

Table 5-3: *Back-calculation of pressures in the St Moritz slide: parameters of each inclinometer pipe.*

parameter description	601	702	derivation
year of completion	2006	1990	
displacement rate	22 mm/yr	33 mm/yr	measured
distance to the boundary	40 m	56 m	measured
strain increment: $\Delta\varepsilon$	0.056 %/yr	0.059 %/yr	measured
change in ovalization value: $\Delta\Omega$	0.014 %/yr	0.088 %/yr	measured
angle of the pipe: δ	22.2°	19.3°	measured
deformation modulus of the soil: E_s	0.3 MPa	0.6 MPa	back-calculated
pressure increment: $\Delta\sigma_1$	0.2 kPa/yr	0.4 kPa/yr	back-calculated

5.8   Case study: Braunwald slide

5.8.1   Description

The village of Braunwald (Figure 5-12) is built on a natural terrace with an area of 4 km^2, creeping towards the cliff facing the valley (Schindler, 1982; Schindler and Rageth, 1990), resulting at the bottom in an active pressure boundary condition. The slip surface is inclined by only 10–12° and mostly formed within a several-meters-thick clay layer of weathered schist above the moraine (Figure 5-13).

The upper part of the terrace is moving as one block, while the sliding mass in the lower part of the landslide is moving faster towards the cliffs (Figure 5-14). Locally, high spontaneous acceleration can be observed in the area close to the cliffs. Smaller local slides of several 10,000 m^3 are often triggered by heavy rainfall and fall over the cliffs (Bollinger *et al.*, 2004). The authorities expect such larger events to happen every 15–20 years. Some parts of the village are located close to the cliffs.

The observed gradient in the displacement rate suggests that earth pressures in the sliding layer are expected to decrease towards the boundary. IDM measurements were performed in two boreholes (inclinometers KB2 and KB6) in the lower part of the landslide, where most of the buildings and infrastructure are located.
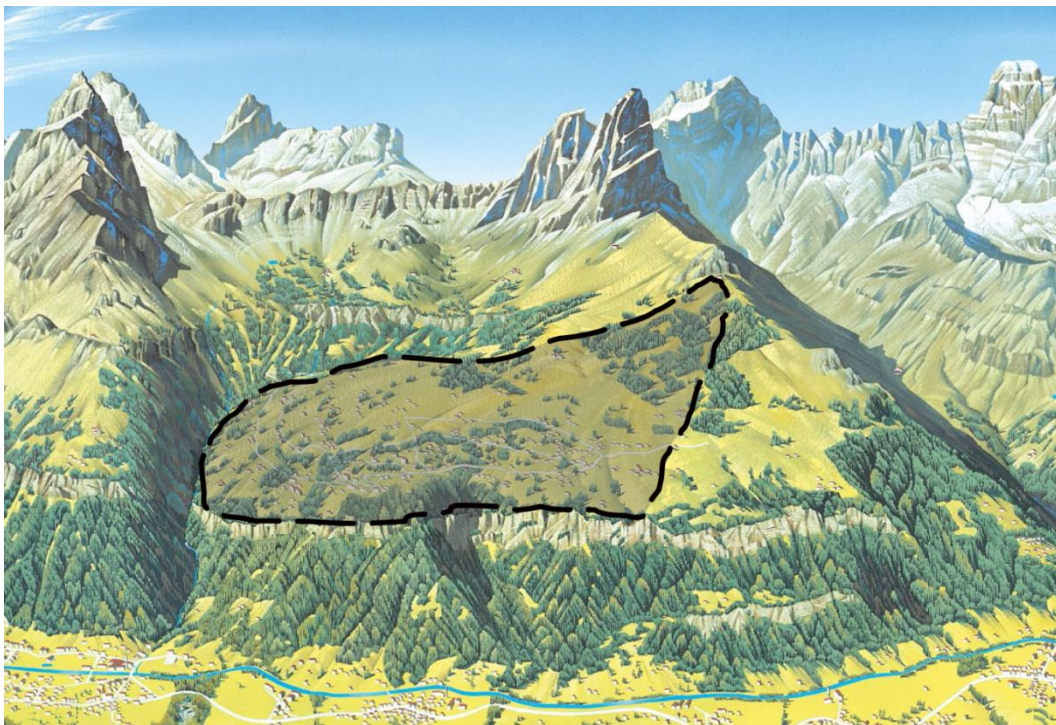
Figure 5-12: *The sliding terrace of Braunwald (after Braunwald-Klausenpass Tourismus).*
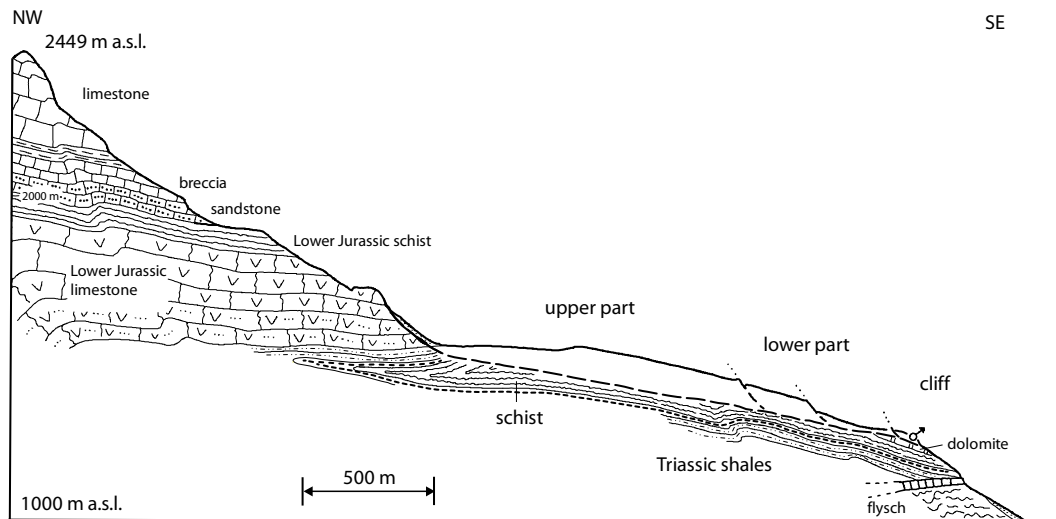
Figure 5-13: *The geology of the Braunwald slide (after Schindler, 1982).*
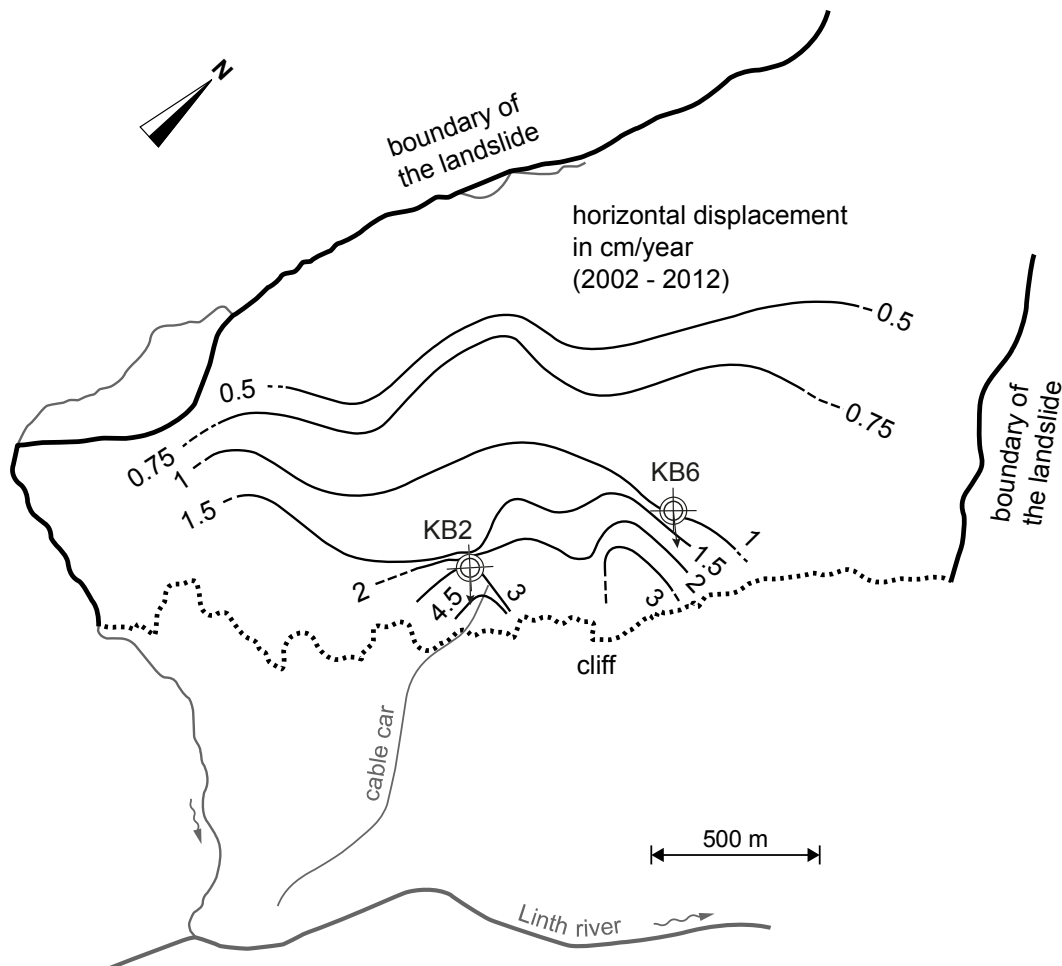
Figure 5-14: *The Braunwald slide with displacement rates and location of the boreholes.*

5.8.2   IDM pressure measurements

Borehole KB2 is located next to the cable car station in an area of larger movements close to the cliff (Figure 5-14). The inclinometer pipe in the borehole has been sheared at the slip surface 10.5 m below the ground surface before 2009. The current ground movement of 34 mm/yr is known from a permanent GPS station installed at the station of the cable car. The strain rate of –0.034 %/yr has been derived between KB2 and a near-by inclinometer located in the same slope profile for the period of 2002–2006.

Borehole KB6 is located in a different area further up the slope, where the observed displacements are smaller (Figure 5-14). The inclinometer pipe has not yet been sheared. Nevertheless, IDM measurements have only been possible in the top 27 m. Inclinometer measurements show a surface displacement of 8 mm/yr. The strain rate of –0.011 %/yr for the period of 2009–2012 is obtained by considering another inclinometer further downhill in the same profile. Constant gradient in the displacement rate is assumed over the distance between the inclinometers.
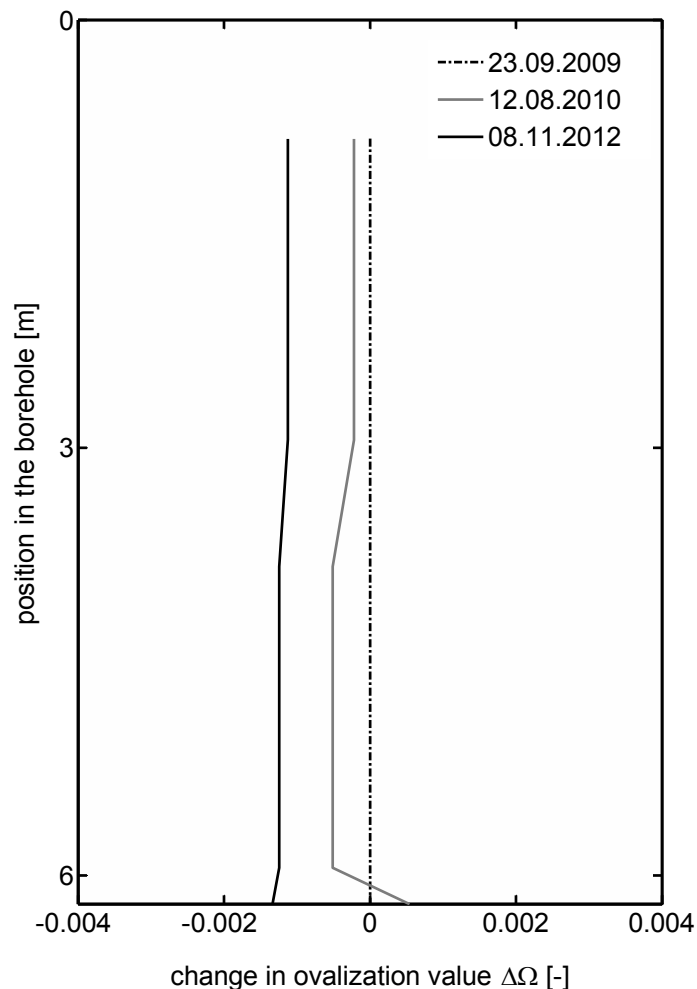
Figure 5-15: *Pipe deformation of inclinometer KB2 measured by IDM, Braunwald.*

IDM measurements were performed in both inclinometer pipes in the period between 2009 and 2012 (Figure 5-15 and Figure 5-16). The pipe elements in KB6 above the depth of 13.4 m were ignored, owing to possible local shallow slides in the area. Negative change in ovalization value $\Delta\Omega$ clearly indicates extension in the slope direction. The pipe diameter in the direction of the slope becomes larger with time with respect to the perpendicular diameter. The observed changes in ovalization value $\Delta\Omega$ are similar in both boreholes (Table 5-4), whereas the strain rates are different. The pressure increments and the deformation moduli of the soil are back-calculated solving the set of Equations (5-

45) and (5-50), showing, as expected, a lower tangent stiffness and pressure drop at KB2, closer to the cliff where the soil has failed in the active mode (Table 5-4). Away from the cliff, at KB6, the soil experiences less yielding, but a very low back-calculated soil stiffness indicates its possible rate dependency.
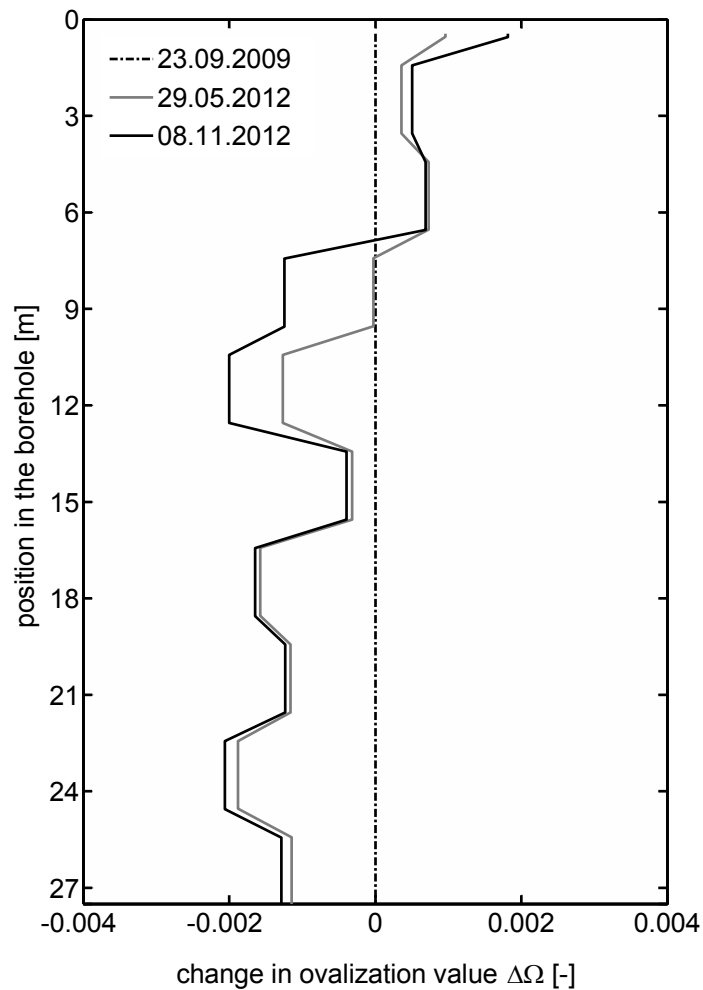
Figure 5-16: *Pipe deformation of inclinometer KB6 measured by IDM, Braunwald.*

Table 5-4: *Back-calculation of pressures in the Braunwald slide: parameters of each inclinometer pipe.*

parameter description	KB2	KB6	derivation
year of completion	2002	2002	
displacement rate	34 mm/yr	8 mm/yr	measured
distance to the cliff	180 m	360 m	measured
strain increment: $\Delta\varepsilon$	-0.034 %/yr	-0.011 %/yr	measured
change in ovalization value: $\Delta\Omega$	-0.038 %/yr	-0.042 %/yr	measured
angle of the pipe: δ	2.4°	5.6°	measured
deformation modulus of the soil: E_s 0.6 MPa		4.3 MPa	back-calculated
pressure increment: $\Delta\sigma_1$	-0.2 kPa/yr	-0.5 kPa/yr	back-calculated

5.9 Case study: Ganter landslide

5.9.1 Description

The Simplon Pass connects Switzerland to Italy via the Alps. In 1980 a bridge was built crossing the valley 140 m over the Ganter river (Menn and Rigendinger, 1979). On the left bank of the river, the bridge is founded on a creeping landslide. The slope is inclined by 24° and covers an area of about 0.4 km^2. The ground surface next to the new bridge is moving at a rather uniform velocity of 4.2 mm/yr, as measured in the period from 1994 to 2004 (chapter 10). Inclinometer measurements show displacements decreasing almost linearly with depth within the sliding body (Ritz, 1992). The soil consists of slope debris, moraine and stones of schist (Schaerer, 1975).
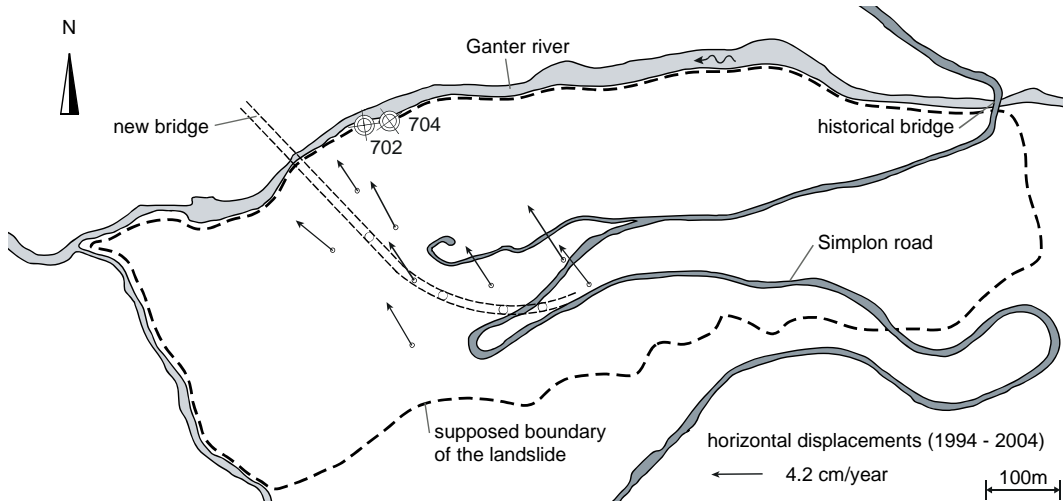
Figure 5-17: *The Ganter slide with displacement rates and location of the boreholes.*

The landslide is creeping towards the Ganter river and is constrained by the rock outcrop at the opposite riverbank. In chapter 10 it is concluded that the soil close to the riverbed has reached passive failure. IDM measurements were performed in two boreholes (inclinometer 702 and 704) next to the river in the zone where the soil has possibly failed (Figure 5-17).

5.9.2 IDM pressure measurements

Boreholes 702 and 704 are located at a distance of 17 m and 28 m from the opposite river bank, respectively. IDM and inclinometer readings were taken in the period from 2010 to 2012. The displacement rate at the surface is observed to be 1.1 mm/yr in the borehole 702. The displacements are decreasing with depth; no clear shear surface could be identified.
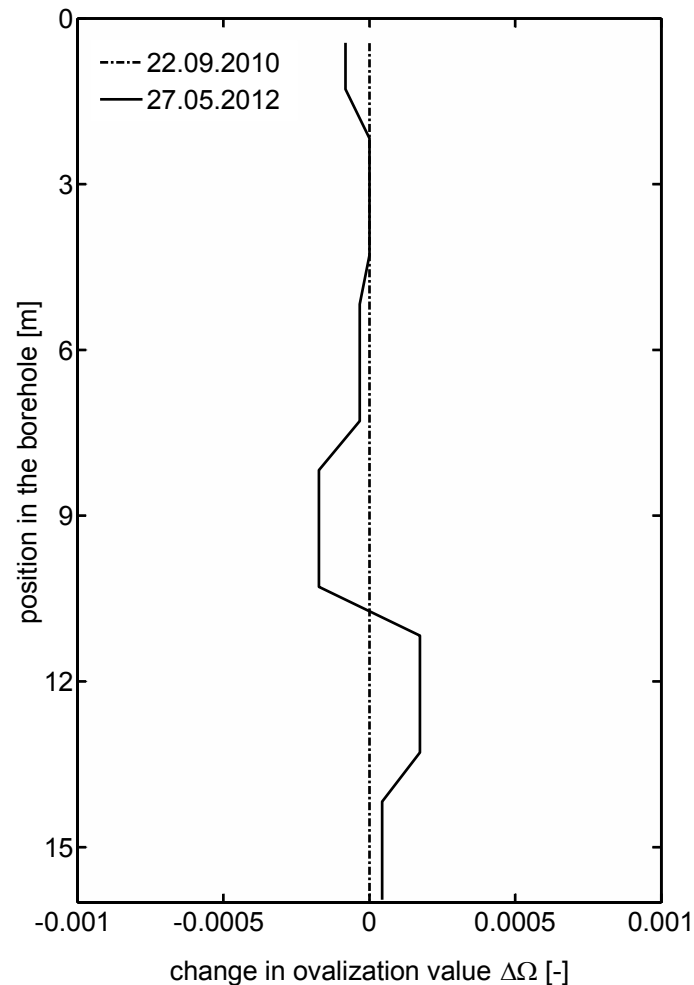
Figure 5-18: *Pipe deformation of inclinometer 702 measured by IDM, Ganter.*

An averaged strain rate of 0.006 %/yr is obtained both between borehole 702 and the boundary and between 702 and the closest uphill geodetical measurement point (Table 5-5). For the borehole 704, the strain rate is assumed to be the same. In both boreholes, the change in ovalization value ΔΩ is observed to be very small averaged over the depth of the boreholes (Figure 5-18 and Figure 5-19). The measured absolute deformations of the pipe of 0.5 micrometers for the period are within the precision of the IDM device of +/– 2 micrometers. Therefore in practice the change in ovalization value can be considered to be very close to zero, resulting from Equations (5-45) and (5-50) in zero values of both the pressure increment $\Delta\sigma_1$ and the deformation modulus of the soil E_s, confirming the passive failure of the soil close to the bottom boundary of the landslide (for details see chapter 10).
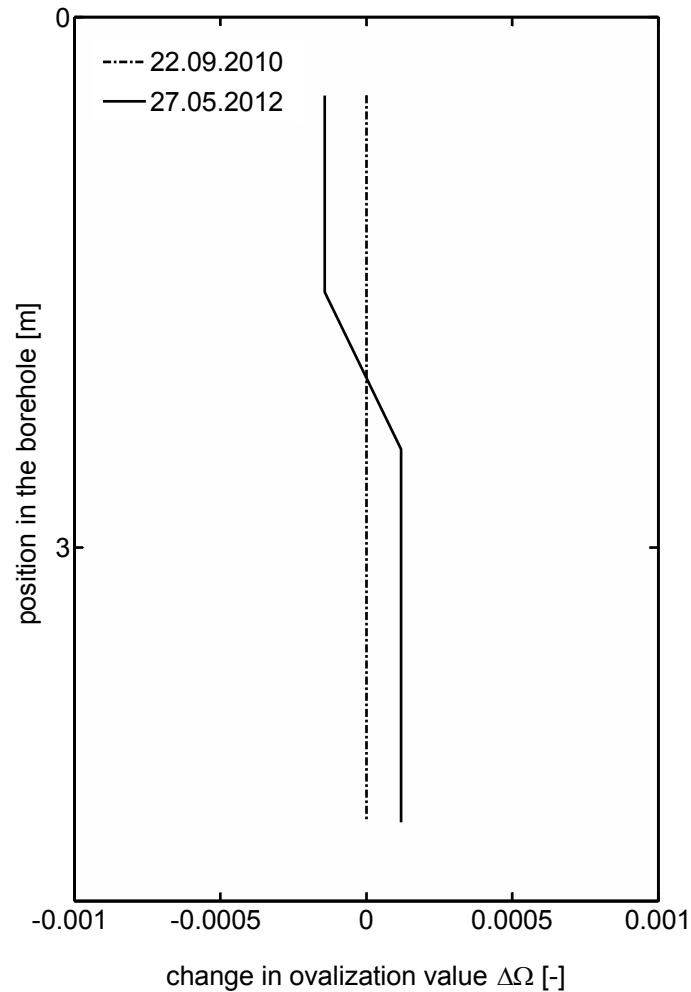
Figure 5-19: *Pipe deformation of inclinometer 704 measured by IDM, Ganter.*

Table 5-5: *Back-calculation of pressures in the Ganter slide: parameters of each inclinometer pipe.*

parameter description	702	704	derivation
year of completion	2007	2007	
displacement rate	1.1 mm/yr	-	measured
distance to the boundary	17 m	28 m	measured
strain increment: $\Delta\varepsilon$	0.006 %/yr	0.006 %/yr	measured
change in ovalization value: $\Delta\Omega$	-0.0007 %/yr	-0.0007 %/yr	measured
angle of the pipe: δ	13.8°	-	measured
deformation modulus of the soil: E_s small		small	back-calculated
pressure increment: $\Delta\sigma_1$	small	small	back-calculated

5.10 Conclusions

The chapter derives analytical solutions for the deformation of a viscoelastic pipe in elastic soil under far-field principal stress increments. These solutions are validated in laboratory tests and numerical analysis and provide the basis for the back-calculation of earth pressure increments from measured changes in shape of an inclinometer pipe cross-section using IDM technology. The procedure has then been applied to back-calculating earth pressure changes in three creeping landslides in Switzerland, which are similar in size but have a range of different boundary conditions and displacement rate fields

a)   the St Moritz-Brattas landslide, which is slowing downhill towards a rock outcrop at the bottom;

b)   the Braunwald landslide, which is accelerating downhill towards a vertical rock wall falling into a valley;

c)   the Ganter landslide, which is moving uniformly downhill towards a river bed.

In these applications, reasonably small pressure increments could be reliably back-calculated by applying the obtained analytical solution which takes the time-dependency of the pipe material properties into account. These pressure increments allowed for identification of compression and extension zones in the landslides under study, confirming the previously developed models of the landslide mechanisms.

Combining the IDM measurements with measurements of relative displacements, the tangent stiffness of the soil could also be clearly identified. The obtained in-situ deformation modulus for the incremental behavior indicates yielding, failure and possibly secondary compression of soil, confirming the previous landslide analysis and suggesting that IDM pressure measurements could serve as a reliable tool for analysis and monitoring of creeping landslides.

Acknowledgements

References

Barber, J. R. (2002). *Elasticity*. Dordrecht; Boston: Kluwer Academic Publishers.

Bollinger, D., Keusen, H. R., Rovina, H., Wildberger, A. & Wyss, R. (2004). Gefahreneinstufung Rutschungen i.w.S., Permanente Rutschungen, spontane Rutschungen und Hangmuren. *Berichtsentwurf der Arbeitsgruppe Geologie und Naturgefahren der Schweizerische Fachgruppe für Ingenieurgeologie.*

Bouma, A. L. (1993). *Mechanik Schlanker Tragwerke: Ausgewählte Beispiele in der Praxis.* Berlin: Springer Verlag.

Domininghaus, H., Elsner, P., Eyerer, P. & Hirth, T. (2008). *Kunststoffe, Eigenschaften und Anwendungen*. Berlin: Springer Verlag.

Findley, W. N., Lai, J. S. & Onaran, K. (1976). *Creep and Relaxation of Nonlinear Viscoelastic Materials – With an Introduction to Linear Viscoelasticity*. Amsterdam: North-Holland Publishing Company.

Menn, C. & Rigendinger, H. (1979). Ganterbrücke. *Schweizer Ingenieur und Architekt* **97**, No. 38, 733-739.

Penzien, J. & Wu, C. L. (1998). Stresses in linings of bored tunnels. *Earthquake Engineering and Structural Dynamics* **27**, No. 3, 283-300.

Puzrin, A. M., Messerklinger, S. & Schmid, A. (2008). The in-situ stiffness of the sliding layer in a creeping landslide. *Proceedings of the 4th International Symposium on Deformation Characteristics of Geomaterials*, *Atlanta* 1, 407-412.

Puzrin, A. M., Schmid, A. & Schwager, M. V. (2012). Case studies of constrained creeping landslides in Switzerland. *Proceedings of the 11th International Symposium on Landslides and Engineered Slopes ISL, Banff, Canada* 2, 1795-1800.

Ritz, P. (1992). Überwachung der Ganterbrücke. *Strasse und Verkehr* **78**, No. 5, 345-349.

Schaerer, C. (1975). Ueberquerung des Ganterbaches. *Mitteilungen der Schweizerischen Gesellschaft für Boden und Felsmechanik* **91**, Spring, 1-4.

Schindler, C. (1982). Problemreiche Hinterlassenschaft: Geologie und Wasserverhältnisse in Braunwald. *Neujahrsbote für das Glarner Hinterland (Grosstal und Sernftal)*, 1982 **16**, 131-140.

Schindler, C. & Rageth, R. (1990). Braunwald (Swiss alps) – investigation, analysis and partial stabilization of a big landslide. *Proceedings of 6th International Congress: International Association of Engineering Geology, Amsterdam* 3, 1705-1711.

Schlüchter, C. (1988). Instabilities in the area of St. Moritz, Switzerland – Geology, chronology, geotechnology. *Proceedings of the 5th International Symposium on Landslides, Lausanne* 2, 1375-1380.

Appendix I: viscoelastic constitutive equations in terms of pipe forces

Derivation of the constitutive relationships for a thin pipe in terms of its forces and moments uses compatibility considerations (Bouma,1993) to obtain the strain distribution across the thickness of the pipe (Figure 5-4b)

$$\varepsilon(z) = \frac{R_m}{R_m + z}(\varepsilon_0 + \chi z) \tag{5-51}$$

The normal force and the moment are defined as

$$N = \int_{-h/2}^{h/2} \sigma(z)\,dz \tag{5-52}$$

$$M = \int_{-h/2}^{h/2} \sigma(z)\,z\,dz \tag{5-53}$$

where h is the thickness of the pipe.

The constitutive equation in terms of circumferential stresses and strains follows from the Burgers model

$$\sigma + p_1\dot{\sigma} + p_2\ddot{\sigma} = q_1\dot{\varepsilon} + q_2\ddot{\varepsilon} \tag{5-54}$$

Integrating both sides of Equation (5-54) and substituting Equations (5-52) and (5-53) into it gives

$$N + p_1\dot{N} + p_2\ddot{N} = q_1\int_{-h/2}^{h/2}\dot{\varepsilon}(z)\,dz + q_2\int_{-h/2}^{h/2}\ddot{\varepsilon}(z)\,dz \tag{5-55}$$

$$M + p_1\dot{M} + p_2\ddot{M} = q_1\int_{-h/2}^{h/2}\dot{\varepsilon}(z)\,z\,dz + q_2\int_{-h/2}^{h/2}\ddot{\varepsilon}(z)\,z\,dz \tag{5-56}$$

Next, expressing Equation (5-51) as Taylor series (Bouma, 1993), substituting it into Equations (5-55) and (5-56), integrating and neglecting terms of higher order than h^4 (thin pipe), results in the following constitutive relationships for a thin pipe in terms of the forces and moments

$$N + p_1\dot{N} + p_2\ddot{N} = q_1\left(A\dot{\varepsilon}_0 - \frac{I}{R_m}\dot{\chi}\right) + q_2\left(A\ddot{\varepsilon}_0 - \frac{I}{R_m}\ddot{\chi}\right) \tag{5-57}$$

$$M + p_1\dot{M} + p_2\ddot{M} = q_1\left(-\frac{I}{R_m}\dot{\varepsilon}_0 + I\dot{\chi}\right) + q_2\left(-\frac{I}{R_m}\ddot{\varepsilon}_0 - I\ddot{\chi}\right) \tag{5-58}$$

where $A = 1 \times h$ is the area and $I = 1 \times h^3 / 12$ is the moment of inertia of the pipe cross-section.

Appendix II: equivalent pressure acting on a thin-walled pipe

A thin-walled pipe approximation requires a correspondence principle transforming the pressure q acting at the outer surface of the pipe at $r = R = R_m + h/2$ into the pressure p acting on the thin ring of the median radius $r = R_m$ (Figure 5-20). This principle is based on the condition that pressures q and p should produce the same radial displacements at the same $r = R_m$ for a thick-walled and a thin-walled pipe, respectively.
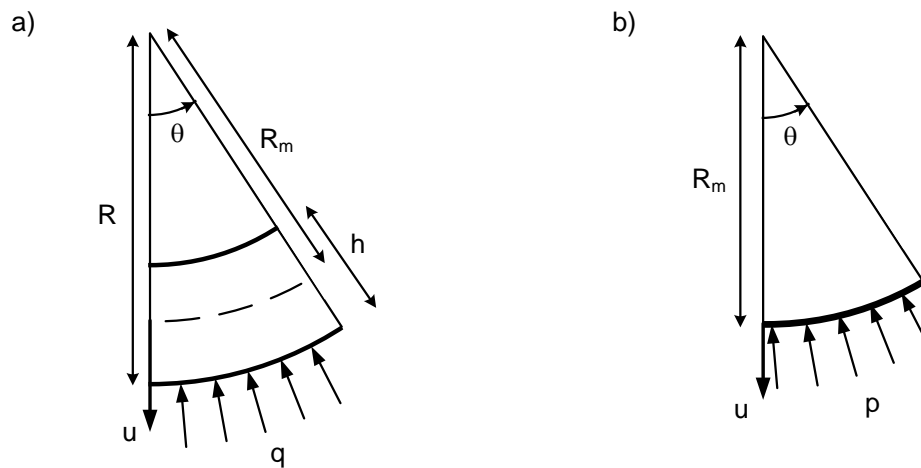
Figure 5-20: *a) Pressure q acting on the thick-walled pipe, b) Pressure p acting on the equivalent thin-walled pipe.*

First, the thick-walled pipe with thickness h is considered to be under pressure $-q\cos(2\theta)$ at the outer radius $r = R = R_m + h/2$.

The solution for the radial displacement at the center of the cross-section is given by the Michell solution (Barber, 2002) as

$$u_{thick}\left(r = R_m, \theta\right) = -\frac{4R_m^{\,4} q\cos\left(2\theta\right)}{3Eh^3}(1 + \frac{h}{2R_m} + \frac{3h^2}{4R_m^{\,2}} + \frac{3h^2 v}{8R_m^{\,2}} + \frac{h^3}{4R_m^{\,3}} + \frac{5h^3 v}{16R_m^{\,3}} -$$

$$\frac{29h^4}{128R_m^{\,4}} + \frac{5h^4 v}{128R_m^{\,4}} - \frac{9h^5}{256R_m^{\,5}} - \frac{3h^5 v}{256R_m^{\,5}} + \frac{13h^6}{512R_m^{\,6}} + \frac{h^6 v}{512R_m^{\,6}} + \frac{5h^7}{512R_m^{\,7}} + \tag{5-59}$$

$$\frac{h^7 v}{256R_m^{\,7}} + \frac{9h^8}{2048R_m^{\,8}} + \frac{3h^8 v}{2048R_m^{\,8}} - \frac{h^9}{4096R_m^{\,9}} - \frac{h^9 v}{4096R_m^{\,9}} - \frac{h^{10}}{8192R_m^{\,10}} - \frac{h^{10} v}{8192R_m^{\,10}})$$

According to the correspondence principle, pressure $-q\cos(2\theta)$, acting at the outer radius $r = R = R_m + h/2$ of the thick-walled pipe, should produce in this pipe at $r = R_m$ the same radial displacements as the pressure $-p\cos(2\theta)$, acting on the equivalent thin pipe of the radius R_m, would produce in the thin pipe

$$u_{thin}\left(r = R_m, \theta, p\right) = u_{thick}\left(r = R_m, \theta, q\right) \tag{5-60}$$

The radial displacement of the thin pipe is given by Equation (5-24) for $n = 2$ and $I = h^3/12$ as

$$u_{thin}\left(r = R_m, \theta\right) = -\frac{4R_m^4}{3Eh^3}\, p\cos\left(2\theta\right) \tag{5-61}$$

Substituting Equations (5-59) and (5-61) into Equation (5-60) and neglecting the higher order terms gives the ratio p/q

$$p\left(r = R_m\right)/q\left(r = R\right) \approx 1 + \frac{h}{2R_m} = R \,/\, R_m \tag{5-62}$$

which provides the necessary equivalent pressure acting on a thin pipe

$$p\left(r = R_m\right) = \frac{R}{R_m}\, q\left(r = R\right) \tag{5-63}$$

$$u_{thin}\left(r = R_m, \theta\right) = -\frac{4R_m^4}{3Eh^3}\, p\cos\left(2\theta\right)$$

Notation

A	area of the cross-section of the pipe
D	inner diameter of the inclinometer pipe
D_A	inner diameter of the pipe within the channels in direction A
$D_{A,0}$	zero measurement of the inner diameter of the pipe in direction A
$D_{A,n}$	further measurement of the inner diameter of the pipe in direction A
D_B	inner diameter of the pipe within the channels in direction B
$D_{B,0}$	zero measurement of the inner diameter of the pipe in direction B
$D_{B,n}$	further measurement of the inner diameter of the pipe in direction B
E	Young's modulus of the pipe
$\hat{E}$	transformed modulus of the pipe
E_p	time-dependent pipe stiffness parameter
E_s	Young's modulus of the soil
E_0	elastic parameter of the Burgers model
E_1	elastic parameter of the Burgers model
h	thickness of the pipe
h_{red}	reduced thickness of the inclinometer pipe
I	moment of inertia of the cross-section of the pipe
K_0	(incremental) earth pressure coefficient within the horizontal plane
M	bending moment in the pipe
$\hat{M}$	transformed moment
N	normal force in the pipe
$\hat{N}$	transformed normal force
P	force acting on the pipe
p	pressure acting on the pipe
$\hat{p}$	transformed pressure
p_1	parameter of the viscoelastic Burgers model
p_2	parameter of the viscoelastic Burgers model
q	pressure acting on the cavity
q_1	parameter of the viscoelastic Burgers model
q_2	parameter of the viscoelastic Burgers model
R	nominal outer radius of the inclinometer pipe, radius of the cavity
R_m	mean radius of the pipe
r	radial coordinate
s	Laplace variable
t	time
t_0	time of the zero measurement
t_n	time of the current measurement

u	radial displacement
$\hat{u}$	transformed radial displacement
u_{thick}	radial displacement of the thick-walled pipe
u_{thin}	radial displacement of the equivalent thin-walled pipe
u^p	radial deformation of the pipe due to external pressure
u^q	radial deformation of the soil due to pressure at the inclusion
u^{σ_1}	radial deformation of the soil due to lateral earth pressure
V	shear force in the pipe
v	tangential displacement
$\hat{v}$	transformed tangential displacement
z	coordinate within the cross-section of the pipe
α	dimensionless coefficient
$\gamma_{r\theta}$	shear strain
$\Delta\varepsilon$	lateral principal strain increment
$\Delta\sigma_1$	major principal stress increment in the horizontal plane
$\Delta\sigma_2$	minor principal stress increment in the horizontal plane
$\Delta\Omega$	change in ovalization value
δ	angle between the pipe channels and the direction of principal stresses
ε	strain
ε_1	lateral principal strain
ε_0	axial strain in the pipe
$\hat{\varepsilon}_0$	transformed axial strain
ε_r	radial strain
ε_θ	tangential strain
η_0	viscous parameter of the Burgers model
η_1	viscous parameter of the Burgers model
θ	circumferential coordinate
ν_s	Poisson's ratio of the soil
σ	stress
σ_1	principal stress within the horizontal plane
σ_2	principal stress within the horizontal plane
σ_r	normal stress in radial direction
σ_θ	normal stress in tangential direction
$\tau_{r\theta}$	shear stress
χ	curvature in the pipe wall
$\hat{\chi}$	transformed curvature in the pipe wall
Ω	ovalization value
Ω_0	zero measurement of the ovalization value
Ω_n	further measurement of the ovalization value

II.   Further development of the FO landslide monitoring techniques (Task 2)

6   Experimental study of a soil-embedded fibre optic strain sensor crossing a shear zone

6.1   Abstract

Distributed fibre optic strain sensors can be applied for the monitoring of soil displacements in geotechnical engineering. In order to study the effect of different fibre optic cable layouts and integration concepts, a full scale test setup was applied, where the fibre optic cable was embedded in soil and subjected to controlled soil displacements from various directions. Due to the different mechanical behaviour of the fibre optic cable and the surrounding soil as well as the slippage on their interface, the strain measured in the fibre optic cable may differ from the strain present in the soil. In this chapter, in particular the influence of decreasing longitudinal stiffness due to yielding of the outer cable sheath on the strain response of the sensor is discussed. Based on experimental results it is shown, how initially stiff cables are able to localize soil displacement with increasing level of strain. Furthermore, tests with existing cable topology concepts, involving more than one cable, were made with this test setup.

6.2   Introduction

Geotechnical engineering has a large demand for monitoring solutions. Construction sites in urban areas being located close to existing buildings or important infrastructures crossing areas endangered by natural hazards need to be monitored during construction and operating time. Fibre optic sensing technologies offer new monitoring possibilities in this field which could replace and outreach existing monitoring technologies in terms of the amount and accuracy of available data.

6.3   Soil-embedded fibre optic strain sensor

In order to monitor geotechnical structures and facilities, fiber optic strain sensors can be attached to the endangered structure itself. However, soil displacements should be monitored also in cases where no structure is available for attachment of the sensor, and thus, the fiber optic cable has to be embedded directly in the soil (e.g. for landslide monitoring, Iten *et al*., 2009). In the recent past, several authors have presented studies where distributed fiber optic sensors were attached to pipes (e.g. Dewynter *et al.* 2009) or connected to geotextiles (e.g. Villard & Briancon, 2008; Belli *et al.* 2009; Artières *et al.* 2010) in order to monitor soil displacements in large scale tests or test applications in the field. A different approach, in which the fiber optic cable is directly embedded in soil, without using a hosting structure such as geotextiles or pipes, is presented in this study.

Table 6-1: *Cable properties, 1$\mu\varepsilon$ (microstrain) = 10^{-6}.*

Cable type	V1a	V2	V3	V4
Metallic protection	No	Yes	Yes	Yes
Diameter *d*	2.8mm	2.9 / 5.7mm	6.9mm	3.2mm
Surface	Smooth	Smooth	Corrugated	Smooth
Elastic stiffness *EA*	2.5-3kN	140kN	500kN	56kN
Yield limit ε_y	-	-	2000 $\mu\varepsilon$	6000 $\mu\varepsilon$

6.3.1   Distributed fibre optic measurement technology

Different types of fibre optic sensing technologies have been developed and this development is still ongoing. Each technology has its specific advantages and limitations in terms of sensor length, spatial resolution, strain range and economics. In order to monitor large perimeters, distributed sensors based on stimulated Brillouin scattering, such as Brillouin optical time domain analysis (BOTDA) (Niklès *et al.* 1996; Niklès 2007) or Brillouin echo distributed sensing (BEDS) (Foaleng Mafang *et al*. 2009) may be an adequate solution due to its possibility of having large sensor lengths. Conventional BOTDA allows for sensing lengths in the range of tens of kilometers with spatial resolution of 1m, whereas BEDS is applicable up to few kilometers with the advantage of enhanced spatial resolution down to a few centimeters.
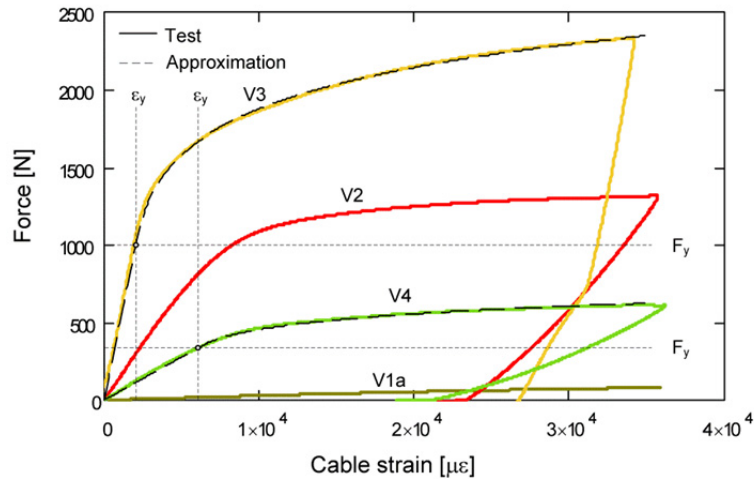
Figure 6-1: Tension test results, $\dot{\varepsilon}$ *=2300$\mu\varepsilon$/min.*
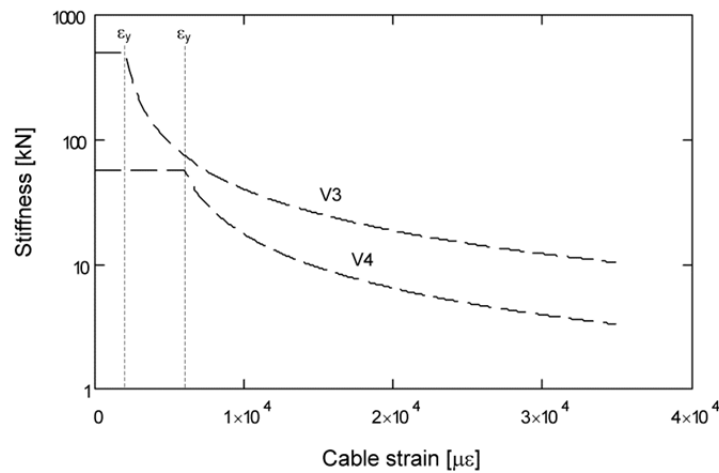
Figure 6-2: Tangent stiffness for V3 and V4.

6.3.2 Fibre optic cables designed for soil environment

Bringing vulnerable fibre optics into the harsh soil environment requires for special cable designs. First of all, the fibre has to be protected against the rough environment on construction sites during the cable integration process (crushing and folding) and secondly, the cable needs a protection against detrimental effects from soil environment during its operating time (e.g. rodents). In co-operation with a cable manufacturer (Brugg Kabel AG), who produced a series of cables, which is in particular designed for the application in soil. In this study, four cable versions out of this group are being presented. In order to quantify their mechanical parameters, tension tests of 2.1m long cable specimens were carried out (Figure 6-1, Table 6-1).The cables V2-V4 include a thin metallic tube which is hosting the silica fibre and V3 is additionally armoured with metal wires. These metal wires provide on one hand an improved protection, on the other hand they increase longitudinal stiffness in the elastic range, with a clearly decrease of stiffness once the yield limit is reached. The behaviour of the cables V3 and V4 was approximated with an analytical expression consisting of a linear elastic section and a nonlinear logarithmic section for the purpose of measurement evaluation in section 4 of this chapter (Figure 6-1, 6-2).

6.4 Full scale test

6.4.1 Motivation

Soil-embedded fibre optic cables may measure strains different from the strain present in surrounding soil due to two reasons. Firstly, a cable consisting from several layers may not transfer the strain applied on the jacket perfectly down to the sensing fibre and, secondly, the sensor can suffer from differential displacements in longitudinal or lateral direction between cable and soil due to limited bond or limited lateral bearing capacity of the cable. In particular thin and stiff cables are prone to lose connection to soil in longitudinal direction and therefore to distribute strains of a local soil displacement over a large length. In order to quantify the performance of several cable designs and integration concepts, a test setup was built, which allows for subjecting the soil-embedded fibre optic strain sensors to controlled soil displacements.

6.4.2 Test setup

The test setup consists of two sand-filled rigid boxes and a mechanism in between, which allows for a relative translation of one box to the other, without any rotation on a chosen displacement path (Figure 6-3). In principal any displacement direction α is possible. Of special interest is the sensor response to α being equal to 0° and 90°. The test setup is around 9.1m long, with an adaptable width of 0.8m in maximum. The aim of this test setup is to simulate the sensor behaviour in a shear or extension zone, when a cable is for example crossing a boundary from stable to slowly moving ground in a creeping landslide. The applied box displacements were controlled in the points A – F. At both sides of the test setup a possible move-in of the cable was measured. The cables were embedded in compacted moist sand with maximum grain size of 5.6mm at different level of depth. The fibre optic strain measurements were taken on a commercially available BOTDA measurement unit for subsequent displacement steps, with spatial resolution of 1m and a sampling interval of 0.1m.
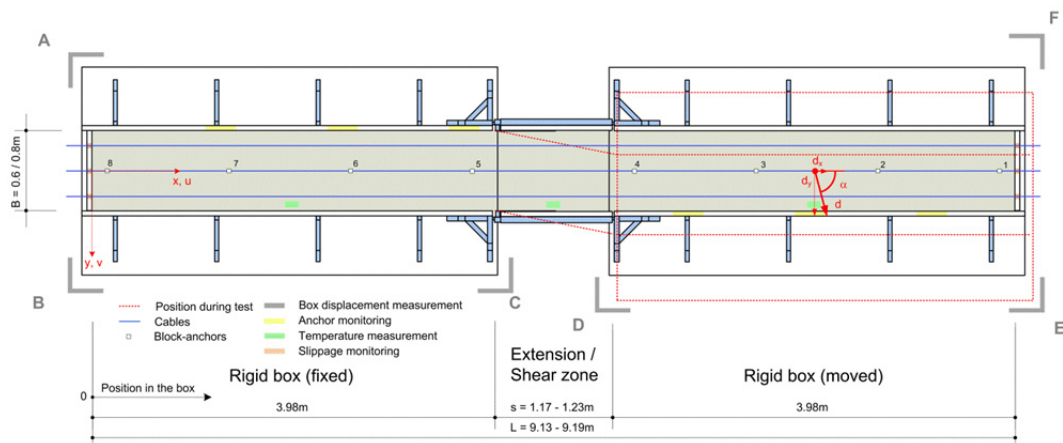
Figure 6-3: Test setup.

This test setup was applied for a set of experiments with different types of cables and integration concepts (cable corrugation, anchors). The sensors were subjected to displacements from different directions and additionally the effect of the compaction level of the sand was investigated. Based on a part of these tests results, the problem of differential displacements between the cable and soil in longitudinal direction is discussed in this chapter, with a particular emphasis on the ability of initially stiff cables to localize soil displacements due to yielding of their metallic protection.

6.4.3   Measurement results

Differential displacements between the sensor and surrounding soil

The problem of limited connection between the fibre optic strain sensor and soil becomes apparent from Figure 6-4. In this figure, strain measurements of three subsequent displacement steps are shown for the soft V1a and the stiff V2 cable. Both cables were embedded in a shallow depth of 0.1m in slightly compacted sand. In the case of the soft V1a cable, the strain penetrates from the shear zone (s_1, s_2), where the displacement is applied, with each step deeper into the box. If small block anchors (edge length 40mm) are attached on the same cable type, the strain is fully accumulated between the central pair of anchors, as shown in Figure 6-4. Up to failure load, the anchors provide a local connection of the cable to surrounding soil. The results of this improved sensor connection to soil show that there exist almost no soil displacements except those applied in the shear zone. The strains in the cable without anchors indicate the length necessary to transfer the longitudinal force of the cable in the shear zone into surrounding soil, but not the strains present in soil. In case of the stiff V2 cable without anchors, this length exceeded the size of this test setup already at very small displacements steps, resulting in slippage of the cable at both box ends with strains in the shear zone being almost equal to zero and no further increase in strain for the later displacement steps.
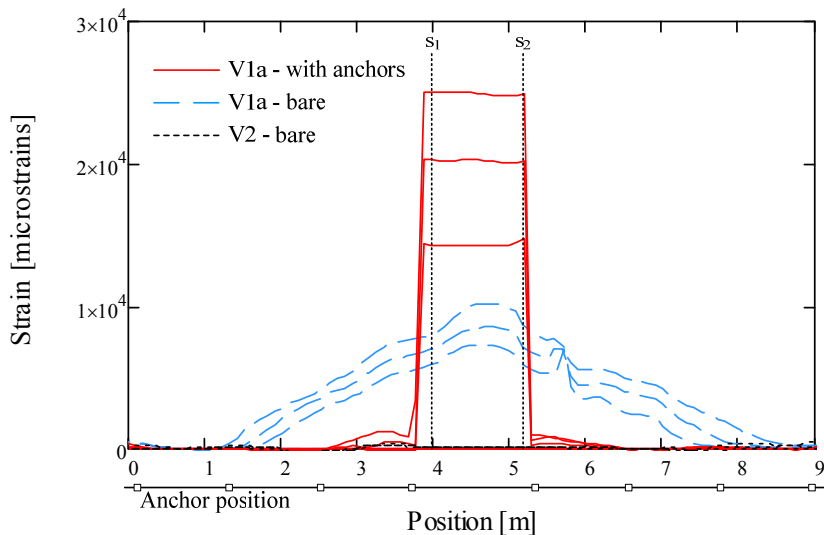
Figure 6-4: *Comparison of V1a / V2 in 0.1m depth.*

Localization of strains due to yielding in the cable sheath

The connection of the sensor cable to soil can be improved by increasing the shear stress acting on the surface of the cable sheath by means of increasing embedment depth and sand density. Figure 6-5 – 6-8 show the strain measurement results of a test, where the box was shifted in longitudinal direction (α = 0°) in 11 steps from 1mm to 39mm and the sand was highly compacted with a vibrating plate. Note that in these measurements some obvious outliers (occurring due to processing difficulties of the device owing to the high spatial variability of strains towards large displacement steps) in the strain distribution were manually corrected by replacing them by the average of the adjacent measurement points. The measured Brillouin frequency shift was converted to strain using results from a strain test bed. In this highly compacted condition, the stiff and well protected cable versions V3 and V4 were tested in the depth of 0.5m and 0.7m. In a depth of 0.5m the strain is still propagating in a trapezoidal shape through the whole box, leading to slippage at both box ends in the last step with no further increase in strain. However, the

reduction in stiffness of V4 compared to V2 and the increase of shear stress on the cable surface allow at least for certain limitation of the strain propagation. By means of additional 40mm anchors attached on the V4 cable in the same conditions, it is possible to concentrate the strain around the extension zone, as Figure 6-6 shows. In contradiction to Figure 6-4, not only the first pair of anchors, but also the second pair was activated, indicating the onset of anchor bearing capacity failure due to the higher stiffness of V4 compared to V1a cable. This behaviour can be prevented with the application of larger anchors. If the V4 cable is even deeper embedded (0.7m, Figure 6-7), the slope of the trapezoidal distributed strains can be increased, due to higher shear stress acting on the cable surface. Once the yield limit in strain ε_y is exceeded, the stiffness is not distributed uniformly along the cable anymore and the strain starts to accumulate in the section with reduced stiffness. This behaviour becomes apparent from the strains measured in the last step. A measurement after the last step, when the cable was carefully excavated, shows that indeed irreversible strains occurred in the extension zone and that the strain penetration is temporary and not caused by cable internal slippage (e.g. Figure 6-5).
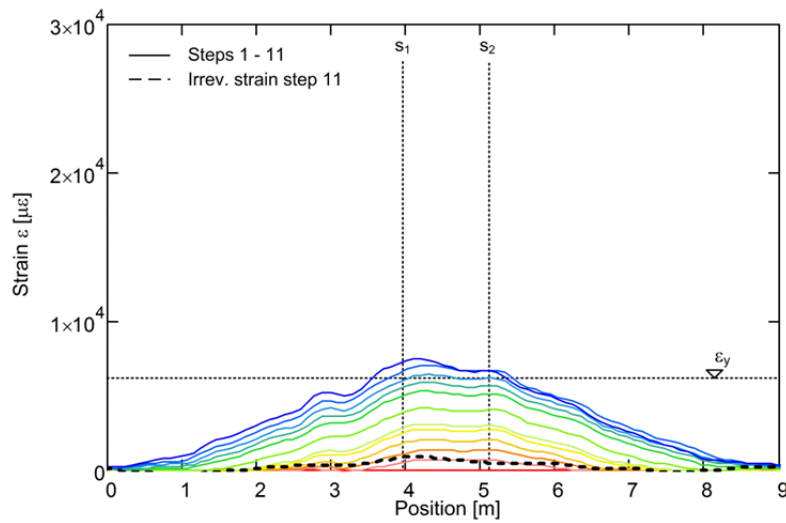
Figure 6-5: *V4 in 0.5m depth.*
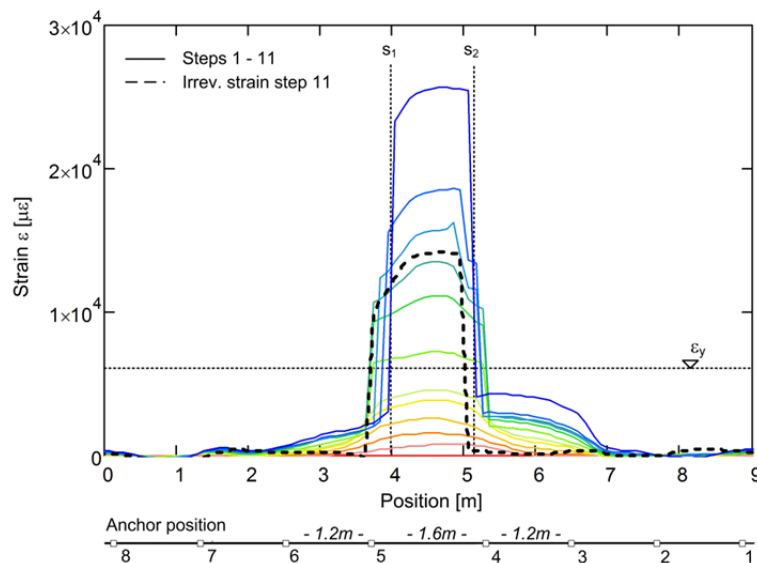
Figure 6-6: *V4 cable with anchors in 0.5m depth.*
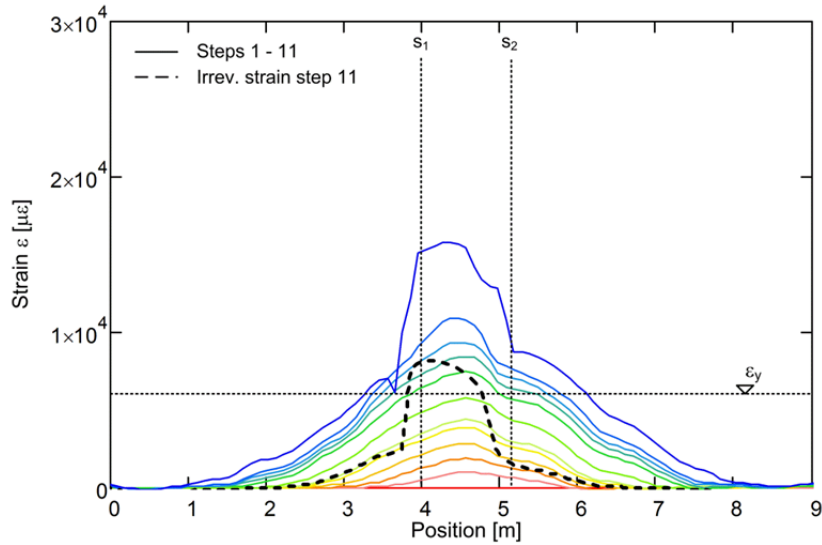
Figure 6-7: V4 cable in 0.7m depth.
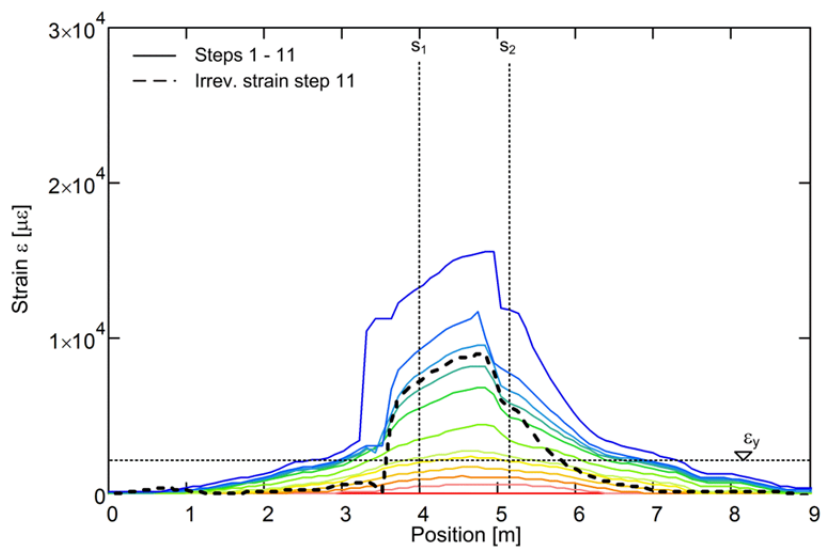
Figure 6-8: V3 cable in 0.5m depth.

Due to its additional metallic armouring, cable version V3 is in the linear elastic range approximately an order of magnitude stiffer than the version V4 (Figure 6-2). Its larger diameter and surface corrugation are only partially able to compensate for this, as a comparison of Figures 6-8 and 6-5 in the elastic range shows. The metallic protection in the V3 cable experiences at very early stage plastic strains. Therefore the propagation of strain is efficiently reduced after the first few steps in the elastic range. This results in an even stronger localization of strains as observed with the V4 cable in the same depth. However, for many applications an elasto-plastic behaviour of the sensor may be a drawback. In other applications, where the strain level is expected to increase monotonically (e.g. landslides, excavations), it is not. Additionally it should be noted, that these irreversible cable deformations introduce the option of having a sensor with some sort of memory.

6.5   Evaluation of measurements

6.5.1   Integration of strains along the cable

Even though some cables distribute the strain applied in the extension zone over a certain length, an integration of the strains along the cable should equal the applied displacement as long as no slippage occurred at the box end. Figure 6-9 and 6-10 show the "measured cable elongation" (which is the integrated strain over the whole length of the box) for all displacement steps applied and all types of sensors discussed in the previous section compared to the applied box displacement in *x*-direction. With exception of the last displacement step (39mm), all sensors match the applied displacement adequately. The band of +-1mm represents approximately the measurement uncertainty of the applied box displacement. Note that this comparison depends slightly on the used factor to convert measured Brillouin frequency shift to strain and is furthermore influenced by the high spatial variability of strains present in the test. During the last displacement step, as already mentioned, slippage was detected in case of the V4 cable in 0.5m depth; therefore this sensor was not able to indicate the correct displacement.
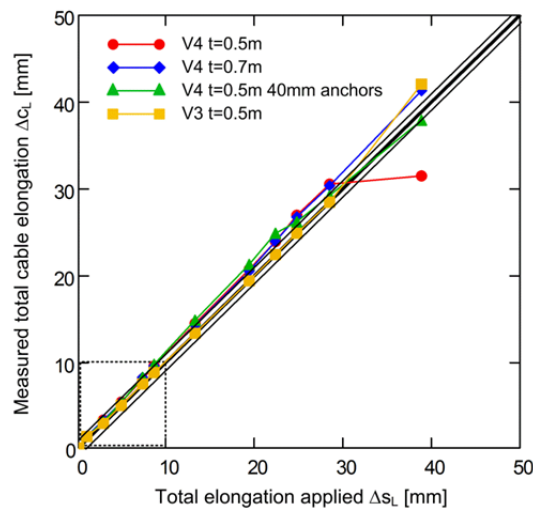
Figure 6-9: Cable elongation.
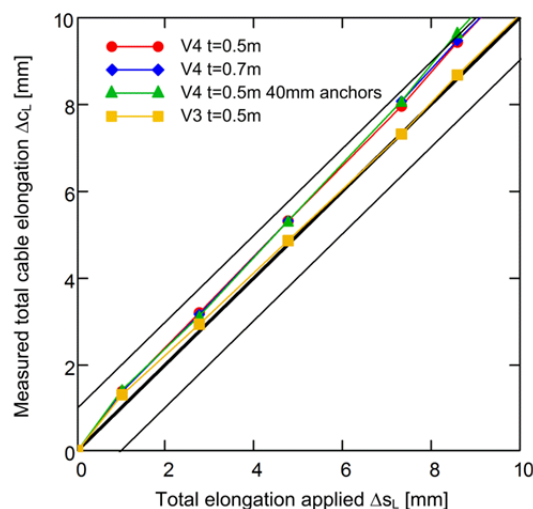
Figure 6-10: Scale-up of Figure 6-9.

6.5.2   Estimation of the cable response in the extension zone

For the design of soil-embedded fibre optic sensors, it would be advantageous to be able to estimate the sensor response to a certain event in advance in order to assess whether the sensor connection to soil is sufficient. For this purpose, a simple model was applied, which describes the strain distribution along the sensor in an extension zone as a function of the cable stiffness, the shear force per unit length q_x acting on the outer cable sheath and the length of the extension zone s where a certain soil displacement Δs is expected. Within this model, the cable is assumed to behave linear elastic up to the yield strain ε_y, followed by an elasto-plastic part, approximated with a logarithmic function for the case of monotonic loading (Figure 6-1). The interaction between cable and soil is reduced to a shear force per unit length acting on the cable, which is for simplification assumed to be constant and independent from the relative displacement between cable and soil, once a differential displacement occurred. In reality, the shear force may not be constant, as detailed laboratory test results obtained e.g. by Puzrin *et al.* (2011) suggest. However, for the purpose of this chapter, they are assumed to be constant. Furthermore, no deformation of surrounding soil is taken into account. In the extension zone the shear stress is considered to be zero (Figure 6-11). The application of such simplified model on to the strain measurements for the case of the V3 cable in 0.5m depth is shown in Figure 6-12. All model parameters except q_x are defined from the test setup or the cable tension test. The shear force per unit length q_x was adjusted to the strain measurement results in Figure 6-12, and kept constant for all displacement steps. The strain expected by the model in the extension zone ε_m is compared to the average strain measured in the extension zone (s_1, s_2) in Figure 6-13 for the two cables V3 and V4 in 0.5m depth. By comparing the purely linear elastic to the elasto-plastic solution in Figure 6-13 it becomes apparent, that the reduction of stiffness due to strain hardening leads to more than two times higher strains in the extension zone for the case of the V3 cable in 0.5m depth.
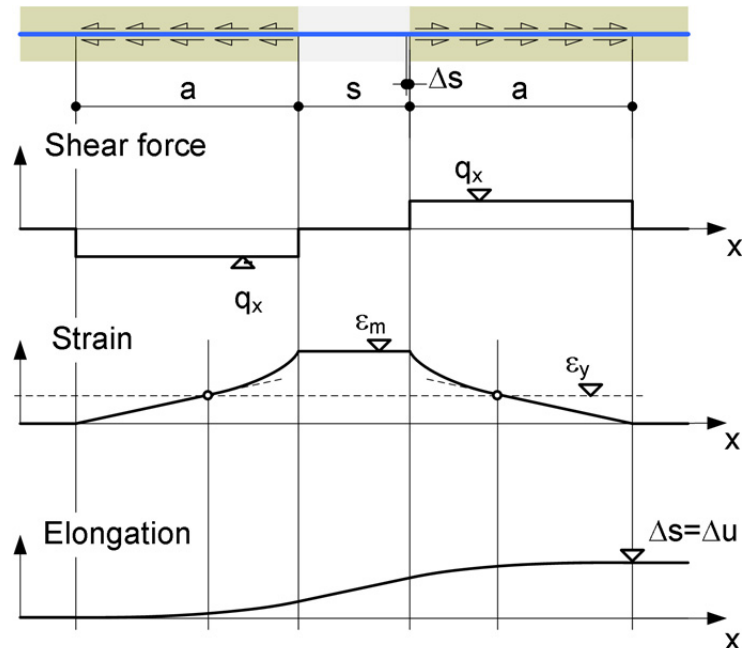
Figure 6-11: *Model assumptions.*
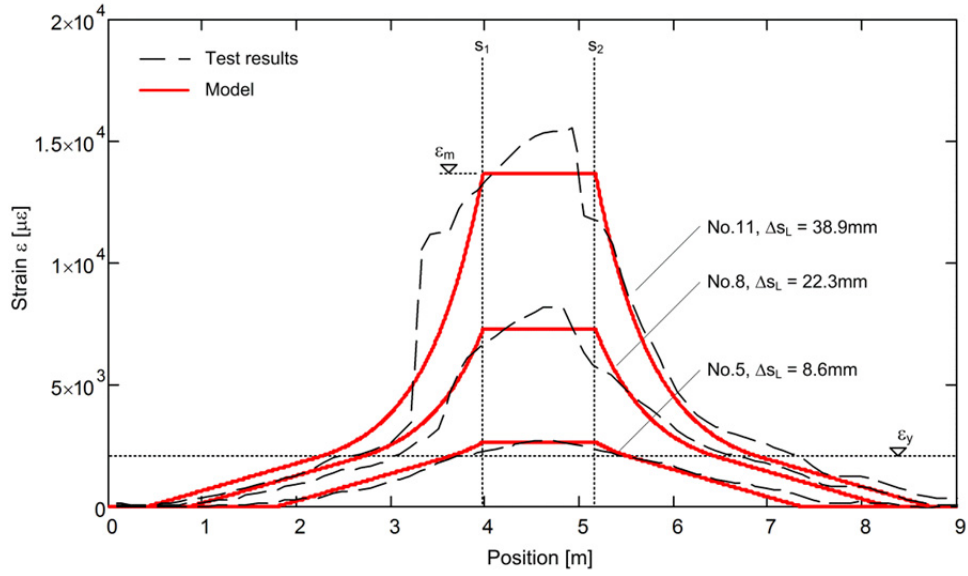
Figure 6-12: *Comparison Model – Test for V3 0.5m.*
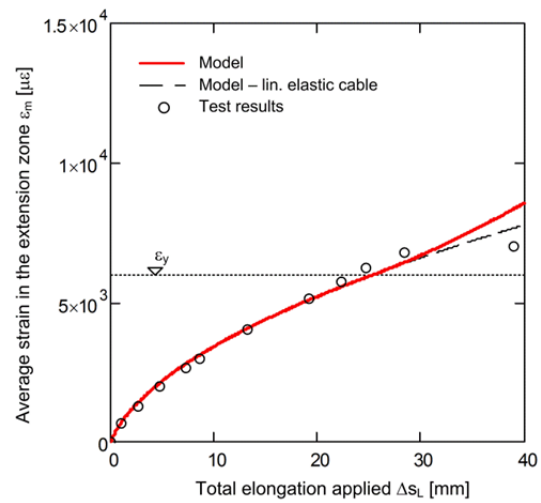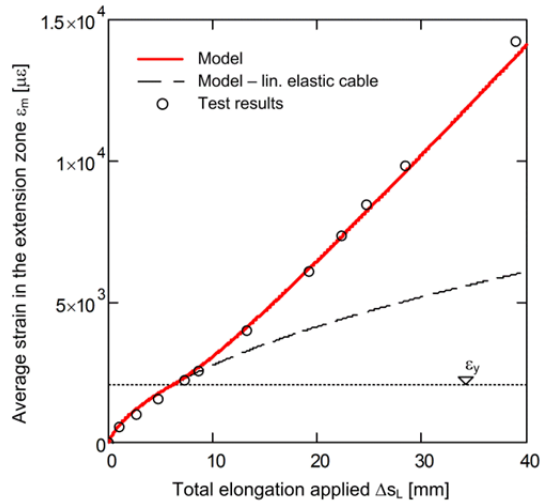
Figure 6-13: *Comparison Model – Test, cable V3 (top), cable V4 (bottom).*

6.6   Conclusions

Soil-embedded fibre optic cables need a certain protection of the fibre. However, a strong metallic protection can increase their longitudinal stiffness significantly. Due to limited bond between the cable and the surrounding soil, strain induced by a local event can distribute over several meters or even tens of meters, if the cables are too stiff or not embedded adequately in soil. This behaviour complicates the interpretation of the measurement results in field applications, as the increase of strain in the cable for a given displacement is very small and also not clearly localized. By means of cable surface corrugation or even more effectively, by attaching small block anchors on the cable, the propagation of strains into zones without displacement in soil, can be strongly reduced. It should be noted, that this improved connection to soil on the other hand may reduce the sensor lifetime due to reaching earlier the upper limit of the sensor strain range, if large local displacements are expected.

A concentration of strains can also be achieved for stiff and well protected cables, due to their elasto-plastic cable properties, if irreversible strains can be accepted (cases of monotonic loading). Once the yield limit of the metallic cable protection has been overcome, strain accumulates in the zone where yielding occurred due to the reduction in stiffness. The propagation of strains into adjacent zones is limited to a certain amount, dependent on the hardening properties of the cable.

6.7   Further monitoring concepts

So far the fiber optic system was basically only used as a continuous extensometer. By introducing a second cable, which is non-parallel to the first cable, it is possible to not only detect a movement, but also to calculate the magnitude and direction of the displacement, given the displacement occurred in the plane which also contains both cables and the anchor points experienced the same displacement. Such a system was proposed e.g. by Naruse *et al.* (2009) for the monitoring of discrete movements (cracks) in mines and tested in a laboratory test setup. Glisic & Inaudi (2007) used a crossed topology in order to monitor shear strains in structures and proposed also more sophisticated topologies in order to obtain strains and displacements in structures. In addition to that, the fiber optic cables can also be attached to a hosting structure as proposed by several authors (e.g. Glisic & Inaudi (2007)). By applying simple beam theory, the displacements along this structure can be found by means of the strains measured along this structure. Dewynter *et al.* (2009) proposed such a system consisting of 3 cables attached to a cable with sufficient bending stiffness or a tube in order to monitor soil displacements. Both existing approaches were tested additionally in the test setup shown before and are briefly discussed in the following sections.

6.7.1   Non-parallel cables

In test No. 4 two cable versions V1a with 40mm anchors attached were prestrained and embedded into medium dense sand in a depth of 0.1m (Figure 6-14). Afterwards the box on the right-hand side was shifted in steps first in longitudinal direction, afterwards simultaneously in both (longitudinal and transversal) and finally in transversal direction. Whereas cable 2 experienced in all steps increasing elongation, cable 1 started to contract after an initial phase of elongation. Negative strains resulted during the last step compared to the reference measurement (Figure 6-15, Figure 6-16). However, due to prestraining the cable while it was embedded, it was still slightly under tension compared to the initial state (short term). Only a few outliers in the measured strain distribution were manually corrected here by linear interpolation. The calculated displacements from the measured strain distribution are compared to the applied displacements in Figure 6-17 (same scale for d_x and d_y) and Figure 6-18 (d_x scaled by a factor of 5). Several procedures can be applied in order to obtain displacements from the measured strain distribution. In the figures mentioned above, two approaches are shown. In the calculation for the results denoted with (B), an averaged strain between the central pair of anchors (average length around 1.4m) was taken to calculate the displacements by assuming the cable is

"cutting" fully through the surrounding soil. On the other hand, in the case of method (A), the total cable elongation $\varDelta c_L$ in the box was lumped to an average strain between the central pair of anchors, since it can be assumed that all strains measured outside of the central pair of anchors are induced because the anchors experienced some small movements due to the normal force acting in the cable and not due to the presence of soil displacements. Furthermore, it was assumed that the cable followed perfectly the applied transversal displacements without "cutting" of the cable through soil. The latter assumption has little effect on the outcome for small transversal displacements and the particular geometry present in this test. As the results show, both processing methods (A) and (B) match roughly the applied displacement path. However, Method (A) involves also further knowledge about the length of the shear / extension zone, which may be not available in a general situation in field.
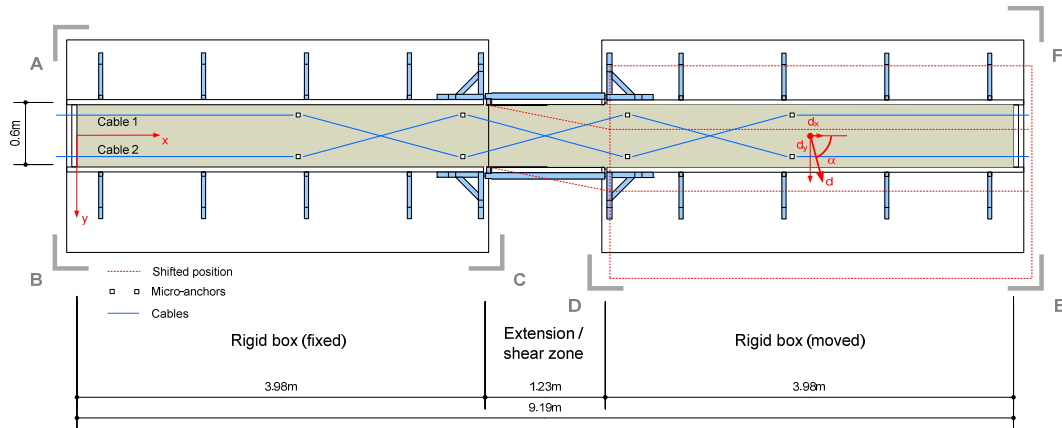
Figure 6-14: *Plan view of the test setup in case of test No. 4.*
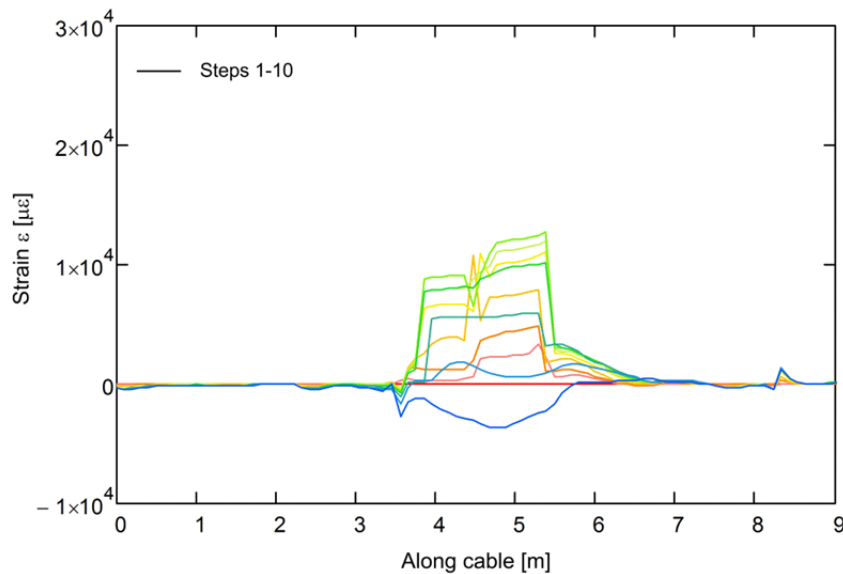
Figure 6-15: *Measured strains along cable 1 (V1a, t = 0.1m, 40mm anchors).*
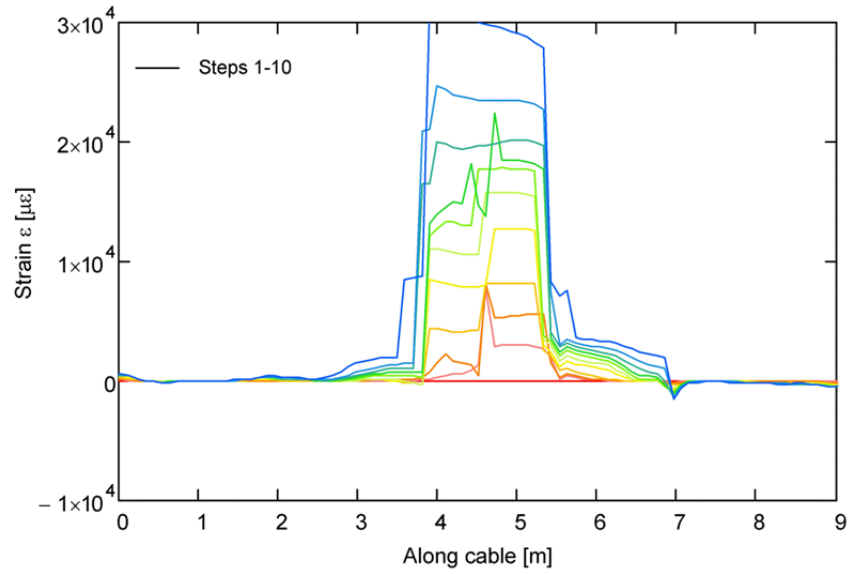
Figure 6-16: *Measured strains along cable 2 (V1a, t = 0.1m, 40mm anchors).*
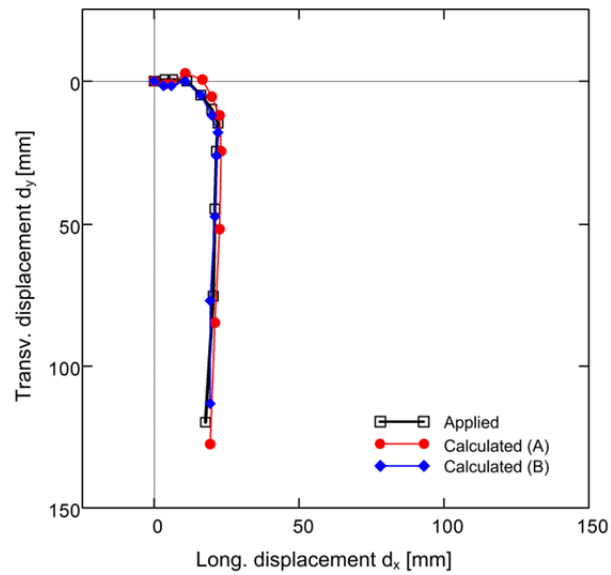
Figure 6-17: *Comparison of applied and calculated displacements (not scaled).*
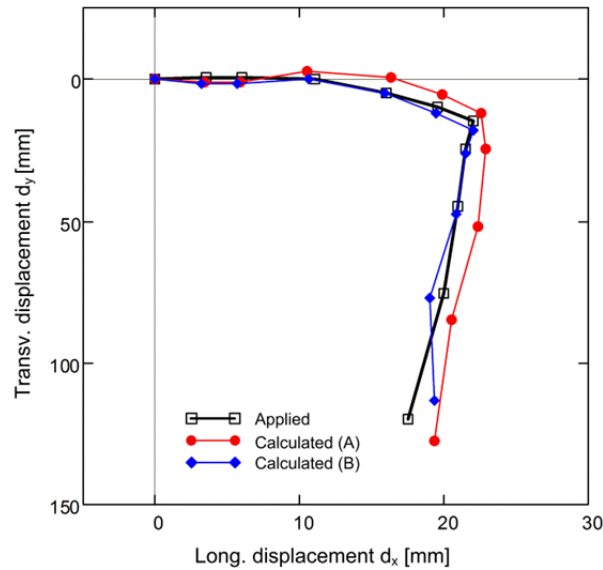
Figure 6-18: *Comparison of applied and calculated displacements (d_x scaled by a factor of 5).*

6.7.2 Cables connected to a hosting structure

An 8.75m long PE100 tube with an outer diameter of 90mm and wall thickness of 5.4mm was embedded in a depth of 0.3m in dense sand (Figure 6-19 to Figure 6-21). On the roughened outer surface of the tube, 4 V1a cables were glued and connected to the tube over a length of 8.59m (Figure 6-20). Beside of that, 4 further cables were embedded directly into soil (cables A to D). The influence of the tube on the measurement results of the cables A to D is not discussed in the present report. After the reference measurement was carried out, transversal displacements d_y were applied in 12 further steps from around 2 to 240mm to the initially straight tube. The bending stiffness of the tube added an additional resistance against the application of transversal displacements. Therefore, it was not always possible to translate the box on the right-hand side ideally without any rotations. d_y therefore denotes the transversal displacement of the center of the box. Owing to the transversal displacements and the imperfect setup, some small longitudinal displacements occurred. In order to measure strains, DITEST STA 202 device (spatial resolution 1m sampling interval 0.1m) from Omnisens SA and OBR 4600 (Gauge length 4mm, sensor spacing 6mm) device from LUNA technologies Inc. were applied. In the present report only the results measured with OBR 4600 are discussed because of the limited spatial resolution of the DITEST STA 202. Unfortunately the OBR 4600 device was not available at IGT before for earlier measurement campaigns.
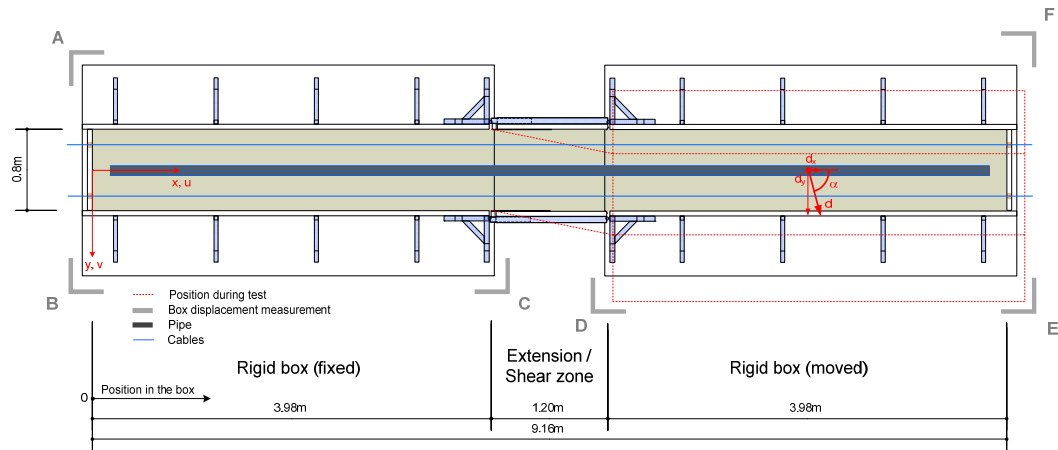
Figure 6-19: Plan view of the test setup in case of test No. 12.
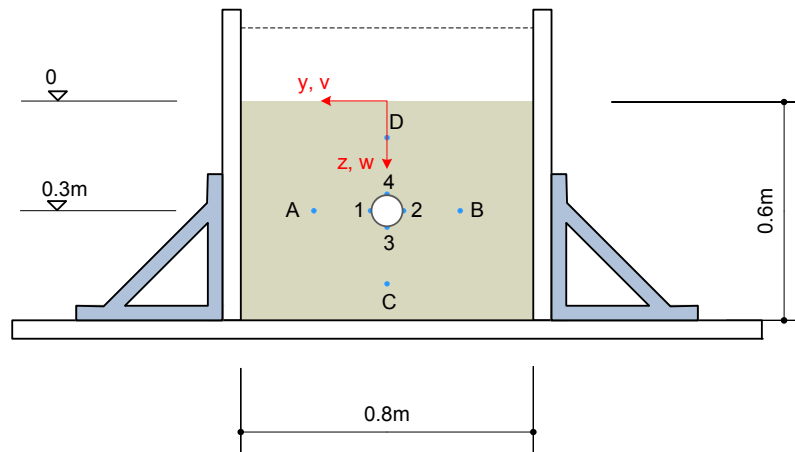
Figure 6-20: Cross section of the test setup in case of test No. 12.

Figure 6-21: Embedment of the instrumented tube into the test setup.
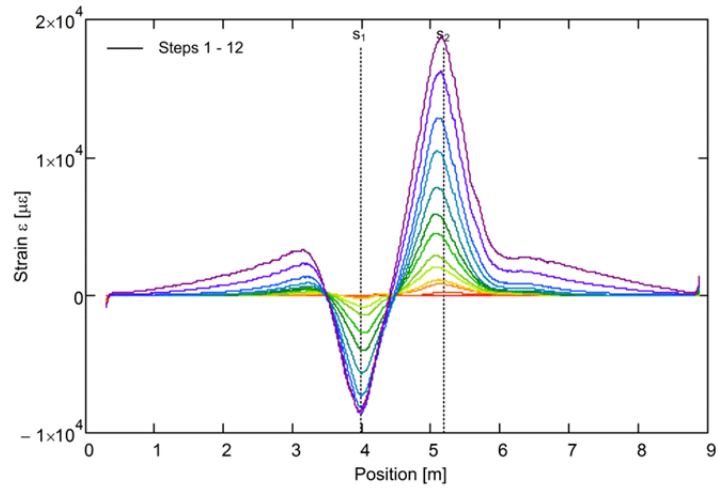
Figure 6-22: *Strains measured along cable 1.*
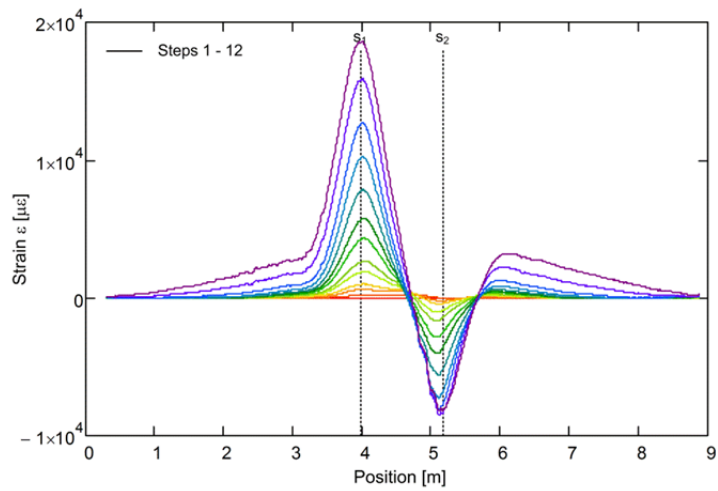
Figure 6-23: *Strains measured along cable 2.*
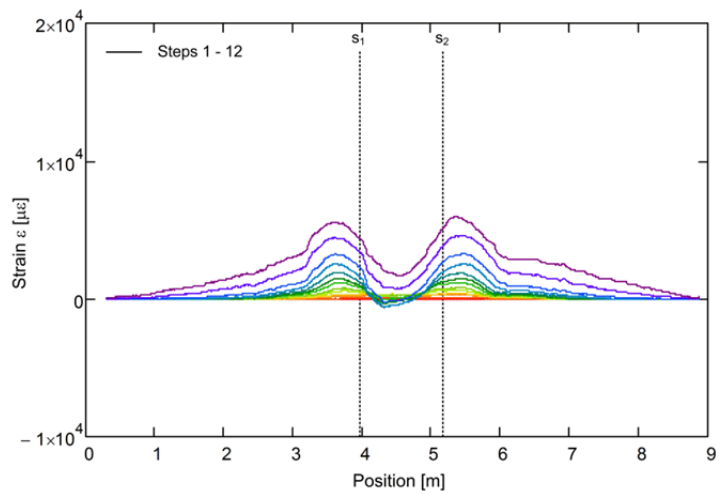
Figure 6-24: Strains measured along cable 3.
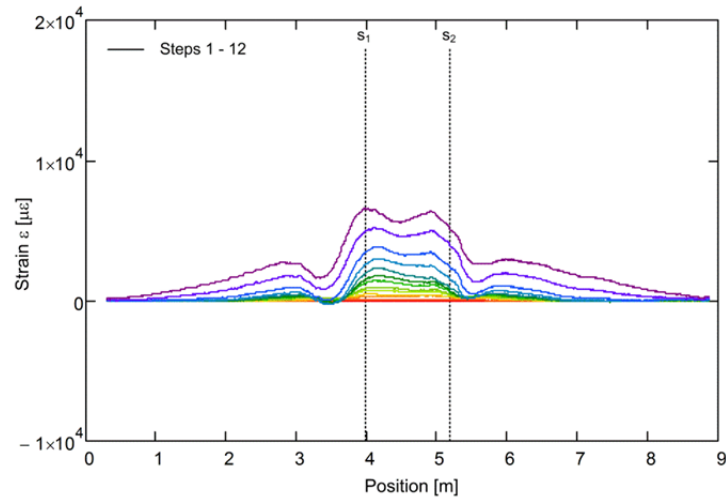
Figure 6-25: *Strains measured along cable 4.*

Figure 6-22 to Figure 6-25 show the strains measured along the 4 cables glued on the tube. The strains are caused mainly by the elongation and the biaxial bending of the tube when displacements were applied. Once again, no significant displacements of soil are expected outside of the shear / extension zone. Hence, the strains measured on the first and the last three meters are caused by differential longitudinal displacements between the tube u_t and soil u_s, since no significant bending of the tube is expected in these regions (which is also confirmed by the fact that all 4 cables are indicating almost the same strain in these zones). In the central region around the shear / extension zone from 3 to 6m, the cables indicated in case of cable 1 and 2 (in plane with applied transversal displacements) large compressive and tensile strain due to bending, whereas in case of cable 3 and 4 smaller change in strain was measured. Obviously cable 1 and 2 experienced within this zone strains from the curvature of the tube. Whereas the deformed shape of the tube in *y*-direction is symmetric with respect of the central point of the test setup, the deformed shape of the tube in *z*-direction is symmetric to the central axis of the test setup, since the tube experienced a small heave in the shear / extensions zone due to dilation of the dense sand. By assuming that the cross sections of the tube stayed planar and orthogonal to the axis of the deflected tube (often referred as Bernoulli beam, Navier hypothesis), the strains measured along the tube can be separated into parts caused by biaxial bending (curvature) and elongation of the central tube axis. For this purpose, the information of 3 parallel cables is sufficient, also other topologies might be used (e.g. Glisic & Inaudi, 2007). However, in the present case, 4 parallel cables were applied, enabling for an additional proof of the made assumptions. Hence, in intervals of 6mm, a plane can be fitted by applying the method of least squares into the strains measured and the position of the cables (Note that the particular positioning of the cables allows also for a simplified procedure, leading to equivalent results). The thereby obtained curvatures and strains on the central axis along the tube can be integrated to give the displacements of the tube. Figure 6-26 shows the obtained *y*-displacements (v_t) along the tube for all 12 displacement steps applied. The *x*-displacements (u_t) and the displacements in *z*-direction (w_t) of the tube, caused by the small heave in the shear / extension zone, are not discussed in this study.
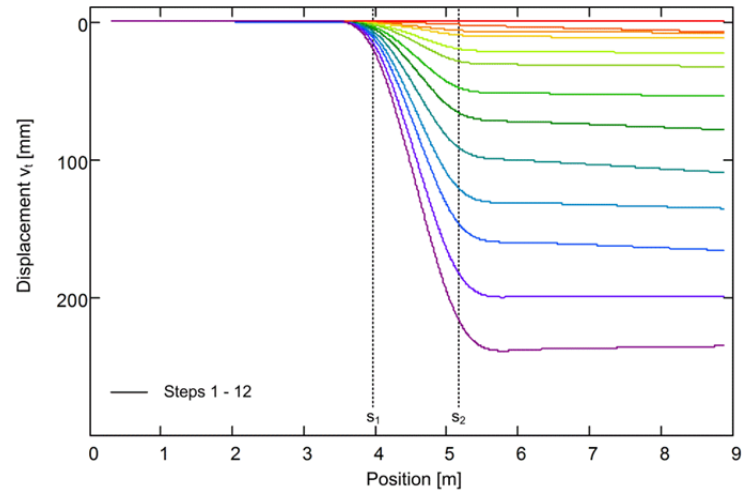
Figure 6-26: *Transversal displacements of the tube.*

Acknowledgements

References

Artières, O., Galiana, M., Royet, P., Beck, Y.-L., Cunat, P., Courivaud, J.-R., Fry, J.-J., Faure, Y.H. and Guidoux, C. (2010) Fiber Optics Monitiring Solution for Canal Dykes. *PI-ANC MMX Congress*, Liverpool, UK, 2010.

Belli, R., Glisic, B., Inaudi, D., Gebreselassie, B. 2009. Smart textiles for SHM of Geo-structures and Buildings. *Proc. of the 4th Int. Conference on Structural Health Monitoring of Intelligent Infrastructure,* Zurich.

Dewynter V., Rougeault S., Magne S., Ferdinand P., F. Vallon F., Avallone L., Vacher E., de Broissia M. Ch. Canepa Ch. and Poulain A. (2009). Brillouin optical fiber distributed sensor for settlement monitoring while tunnelling the metro line 3 in Cairo, Egypt. *Proc. of 20th International Conference on Optical Fibre Sensors (Proc. of SPIE Vol. 7503).*

Foaleng Mafang, S., Beugnot, J.-C. & Thévenaz, L. 2009. "Optimized configuration for high resolution distributed sensing using Brillouin echoes", 20th International Conference on Optical Fibre Sensors, Proc. of SPIE vol. 7503, Edinburgh, UK, pp. C1-C4.

Glisic, B. & Inaudi, D. (2007). Fibre optic methods for structural health monitoring. John Wiley & Sons Ltd., Chichester, England.

Iten, M., Schmid, A., Hauswirth, D. and Puzrin, A.M. (2009). Defining and monitoring landslide boundaries using fiber optic systems. *Proc. of Prediction and Simulation Methods for Geohazard Mitigation*. pp. 451-456.

Naruse, H., Yoshikawa, Y., Arevalo, G., Gonzalez, J.P., Alvarez, A. & Mujica, L. (2009) Displacement measurement by sensor unit with a pair of crossed optical fibers. 20th Int. Conf. on Optical Fibre Sensors (OFS-20), Proc. of SPIE Vol. 7503, pp. 3U-1-3U-4.

Niklès, M., Thévenaz, L., Robert, Ph. A. 1996. Simple distributed fiber sensor based on Brillouin gain spectrum analysis. *Optics Letters, Vol. 21*. pp. 758-760.

Niklès, M. 2007. Fibre optic distributed scattering sensing system: perspectives and challenges for high performance applications. *3rd European Workshop on Optical Fibre Sensors, Proc. of SPIE Vol. 6619*. 66190D.

Puzrin, A. M., Iten, M., Hauswirth, D. 2011. Progressive failure in soil-cable interaction. *Proc. of XV European Conference on Soil Mechanics & Geotechnical Engineering (in press).*

Villard, P. and Briancon, L. (2008). Design of geosynthetic reinforcements for platforms subjected to localized sinkholes. *Can. Geotech. J. 45*, pp. 196-209.

7 Field application in St. Moritz

7.1 Abstract

This chapter shows an application of soil-embedded fiber optic strain sensors in a landslide susceptible area for the purpose of geotechnical monitoring and site investigation by applying Brillouin optical time domain analysis (BOTDA). In a field test, two different sensor integration concepts were used and the strain measurements are compared to inclinometer readings in a neighboring borehole.

7.2   Aim

The aim of the field application in St. Moritz was primarily to gain experience in the application of a soil-embedded fiber optic sensor in a real field application. For this reason, a fiber optic strain sensor was embedded underneath a hiking path in a potentially unstable slope in St. Moritz (Iten, 2011; Hauswirth *et al.*, 2012).

7.3   Overview

The north-eastern part and also the leaning tower of St. Moritz are located on the well-known creeping "Brattas" landslide. This region is recognized as a sliding area since decades and is well-documented in literature. The building authority of St. Moritz has enacted restrictive regulations for this zone which ensure a safer construction of buildings.

The south-western part of St. Moritz (Via Laret) is located on a steep slope called "God Ruinas". Until the last decade no major problems were known in this zone. However, owing to a construction activity in the past years, large local ground deformations occurred which gave rise to concerns about the slope stability. A comparison (IGT, 2008; GEO Grischa, 2008; IGT, 2009) between existing geodetical measurements from the twenties and the nineties of the last century (Figure 7-1), as well as current data, indicated that parts of this slope may be unstable.

The cause of these surface soil displacements was unknown by that time. They might have been triggered by some single events in the past (e.g. building activities, extreme rainfall events) or developed at a low, constant rate over decades, as in the case of the creeping soil mass of the "Brattas" slide. In order to investigate the potential hazard in this area, the municipality of St. Moritz decided to monitor this slope by means of inclinometers and geodetic measurements (See also chapter 12). Independently from this, in July 2008 an 80m long trial fiber optic sensor was embedded by IGT and Brugg Kabel AG in the potentially moving soil mass in order to assess the applicability of this new measurement technology for detecting possible ground movements and to gather additional data to support the results from the traditioinal measurement campaign conducted in parallel.
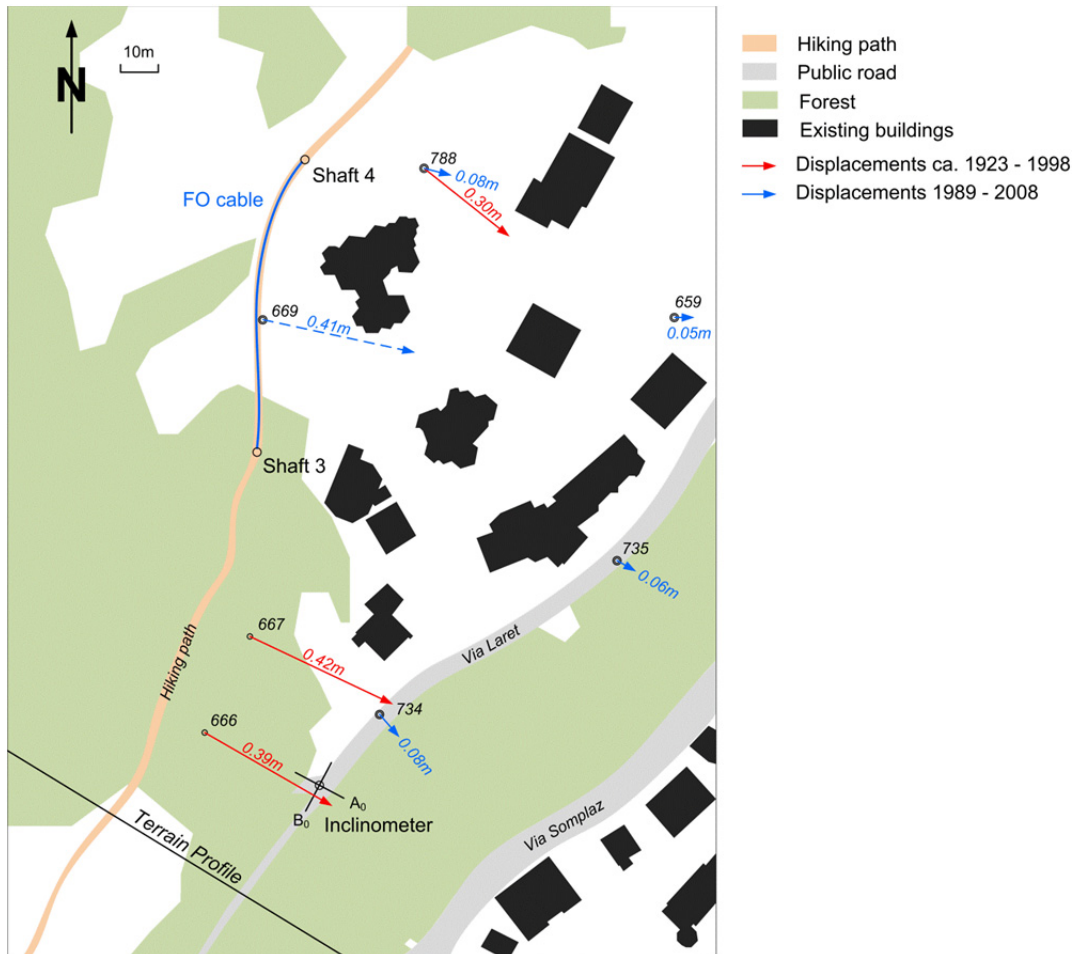
Figure 7-1: *Detail map section, part of the "God Ruinas" zone, St. Moritz, adapted from IGT (2008), GEO Grischa (2008), IGT (2009).*

7.4 Field test setup

7.4.1 Field test site

The amount of information available about the "God Ruinas" slope in 2008, at the beginning of this field study, was very limited and furthermore, the data were uncertain, as some measurement were very old. Serious concerns about the local slope stability were raised mainly because of the large displacement measured in point No. 669. This displacement may represent the local soil displacement in this area; on the other hand, it may be also simply the result of repair works on the hiking path. In order to catch differential soil displacements, either caused by a large ongoing displacement discontinuity between point No. 788 and 669 or due to smaller differential displacements in the moving soil mass in general, the fiber optic sensor was embedded in the area between points No. 788 and 669.

7.4.2 Site conditions

In the vicinity of the sensor (Terrain profile, Figure 7-1), the God Ruinas slope falls in south-east direction with an inclination of 30 to 33° (GEO Grischa, 2007). The site is not farmed, mainly covered by grass and single trees and located approximately 1900m a.s.l. The near surface region of the slope consists mainly of moraine material left from the Engadine valley glacier and some scattered hillside waste material (Swisstopo, 2005; IGT, 2008). Samples from the core drilling of the borehole for the inclinometer KB0801 consisted of gravelly and sandy silts (hillside waste) up to a depth of 16m. Beyond that depth,

a heavily weathered rock was found (IGT, 2009). During the winter season, the precipitation is mainly accumulated as snow, and the soil around the cable is expected to be frozen. The site is only accessible by foot and, in particular in winter the access is limited because of the snow. The onset of snowmelt in spring causes additional high amounts of water in this slope.

7.4.3   Strain sensor cables

The only tight buffered strain sensor cable versions (out of the variety discussed in chapter 6) available in July 2008 from Brugg Kabel AG were the vulnerable V1a and V1b prototype cables. More appropriate cable versions for the particular application in soil were developed by Brugg Kabel AG at a later point in time. Regarding the field application, this can be a certain drawback, because these cables have no metallic protection sheath against rodents. Furthermore the V1a cable jacket swells in water and is highly sensitive to temperature changes, which can cause undesired frequency shifts and may lead to data misinterpretation at the end. However, owing to the bond with surrounding soil, swelling and thermal expansion is at least partially restricted.

7.4.4   Sensor integration into ground

An approximately 0.4m deep and 0.3m wide trench was excavated along a hiking path traversing the slope. In order to prevent fiber breakage caused by the larger grains in the moraine material, the cables were embedded in a manually compacted 20cm thick sand cushion. (Figure 7-2, Figure 7-4). The V1a cable, accessorized with additional 40mm anchors (block anchors, 2m spacing), was placed in the center of the trench. Next to this, the V1b cable without block anchors and a cable in loose tube design for compensation of temperature effects were built-in. Both strain sensor cables V1a and V1b were slightly pre-strained before they were covered with sand. On top of the sand cushion, the trench was filled with compacted material that was left from the excavation.

7.4.5   Sensor layout

The fiber optic sensor has a length of around 80m and runs between shaft No. 3 and 4 (Figure 7-3). The connection of the three cables allows the response of the installation to be obtained from a single measurement (the cable in loose tube design contains more than one fiber). The shafts grant access to the fiber ends and the connections between them. The cable entrance in the shaft was formed from thin, flexible plastic tubes (Figure 7-5), in order to balance the expected differential settlements between shaft and surrounding soil, which might harm the vulnerable fiber optic cable. The loose tube cable for temperature compensation was too short to place splice box No. 2 in shaft No. 3. For this reason, it was buried directly in soil close to shaft No. 3. The total length of the fiber optic installation is around 350m.
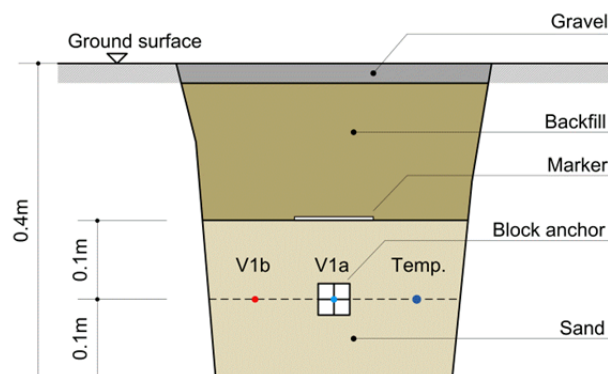
Figure 7-2: *Cross section of the trench.*
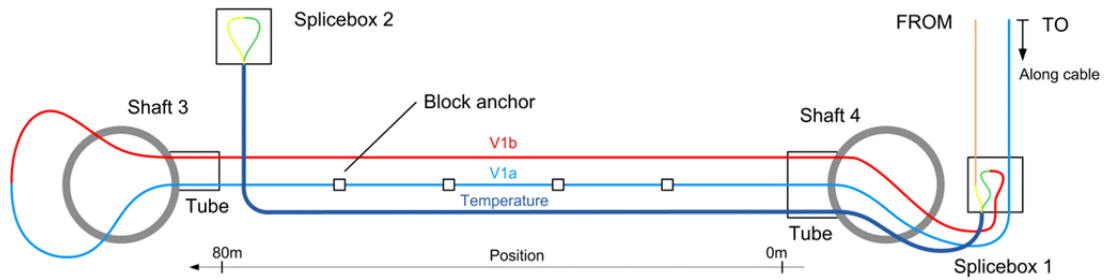
Figure 7-3: Schematic sensor layout.

Figure 7-4: Trench with fiber optic sensor.

Figure 7-5: Shaft No. 3.

7.5   Fiber optic measurement results 2008-2011

7.5.1   Measurement parameters

All fiber optic measurements were carried out using BOTDA technology with a DITEST STA 202 measurement device. Measurements were taken typically with frequency steps of 1MHz (some with 4MHz), spatial resolution of 1m and a sampling interval of 0.41m. At least two measurements were typically taken during each site visit.

7.5.2   Measurements between 2008-2011

Table 7-1 shows the date and the denotation of the measurements which were carried out on the site. A closer time interval between the measurements was not possible owing to the limited and time consuming access to the site. In February 2011, a fiber fault was detected in the V1a cable. In April and September 2011, further measurements were carried out with the remaining cables only. By means of OTDR measurements it was possible to localize the damage just before the entrance to shaft No. 3. Most likely, ice at the bottom of the shaft caused a heave larger than the flexible tube was able to compensate for. This hypothesis is supported firstly by geodetical measurements between summer 2010 and 2011 (GEO Grischa, 2011) which showed an uplift of shaft No. 3 of more than 5cm and secondly, by field observations in April 2011 (Figure 7-6). In October 2011, the broken cable was repaired, making further measurements along the whole sensor possible again. Measurements were taken until March 2013 with this sensor. However, the construction of a building in 2012 close to the inclinometer was strongly influencing the local behavior of the slope. Therefore, strain measurements in the tight buffered loop are only discussed up to November 2011 within this study, whereas for the discussion of the seasonal temperature development measurements in the loose tube loop up to March 2013 are used. The strains from the measurement carried out in January 2010, when the soil around the cable was frozen, represents a special case and is omitted in the further analysis and discussed separately in this study.

Table 7-1: Measurement dates and conditions.

Date	Name	Soil condition
02.07.2008	July 08	dry
21.10.2008	Oct 08	dry
21.07.2009	July 09	dry
15.09.2009	Sept 09	dry
03.12.2009	Dec 09	snow, wet
22.01.2010	Jan 10	snow, frozen
07.05.2010	May 10	wet
22.06.2010	June 10	moist
06.10.2010	Oct 10	dry
03.02.2011	Feb 11	snow, frozen
07.04.2011	Apr 11	wet
13.09.2011	Sept 11	dry
05.10.2011	Oct 11	moist
02.11.2011	Nov 11	moist

Figure 7-6: Shaft No. 3 on April 7th, 2011. Possible uplift.

7.5.3   Temperature distribution along the sensor

Figure 7-7 shows the Brillouin frequency shift relative to the reference measurement (July 2008) along the loose tube cable. At a slightly less than 190m along the cable the first fiber out of four in the loose tube cable leaves shaft No. 4. At around 265m the first fiber is connected within the splice box No. 2 to the second fiber in the loose tube cable, which arrives within the same cable at slightly more than 340m again in shaft No. 4. This cable setup should result in a symmetric frequency shift around the splice box No. 2, which can also be observed up to a satisfactory level. The relative frequency shift is rather uniformly distributed and, as expected in advance, strongly dependent on the season. Note that herein the whole frequency shift measured is related to temperature, since the fiber is isolated from the cable jacket by a loose tube. In other applications, a small influence of the longitudinal deformation on the fiber within the tube (strain) was anyhow observed. However, for the purpose of the present application, such possible imprecisions are negligible. Figure 7-8 shows the same measurements, each measurement being shifted by its average Brillouin frequency shift measured along the fiber. This procedure results in a deviation of a few MHz from the reference measurement in July 2008 along the whole sensor. It may be therefore concluded that, in the present case, the assumption of a uniformly distributed temperature profile along the sensor is sufficient for the purpose of temperature compensation. As the strain measurements in the later section will show, even this compensation is of minor importance, because the frequency shift induced by soil displacements is more than an order of magnitude higher.
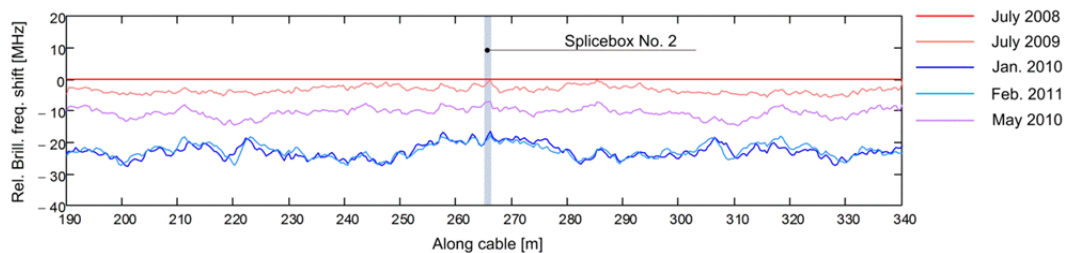
Figure 7-7: *Relative Brillouin frequency shift in the temperature loop.*
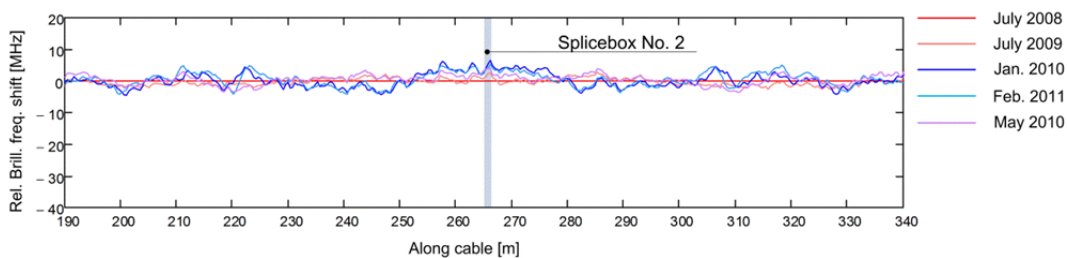
Figure 7-8: *Relative Brillouin frequency shift in the temperature loop after compensation (uniformly distributed temperature assumed).*

Freezing and thawing of the pore water in winter may affect the surrounding soil in terms of displacements. Hence, it is important to know whether temperatures below 0°C occur during the winter at the embedment depth of the cables. Since the Brillouin frequency shift of this particular cable is not exactly known at a certain temperature, no precise conclusion about the development of temperature with time could be drawn on the basis of that. Therefore, a Pt100 resistance thermometer, acting as a point sensor, was embedded in August 2012 beneath shaft No. 4 at the same depth as the cables. The absolute temperature measured in August 2012 was chosen as reference value. In two further measurements, the average relative Brillouin frequency shift along the cables was set into relation to the simultaneously measured temperature change from the resistance thermometer. Good agreement was observed by applying a thermal dependence of Brillouin frequency shift of 1.15MHz/°C, which represents also a reasonable value. Hence, this correspondence of 1.15MHz/°C was used to calculate the average absolute temperature along the cables in the measurements prior to the installation of the resistance thermometer. Figure 7-9 shows the average temperature obtained along the cables. Temper-

atures as low as -5°C were observed in soil while the measurements were carried out, with a standard deviation along the cable in the range of 2°C. Hence, the pore water in soil surrounding the cable is expected to be frozen in winter.
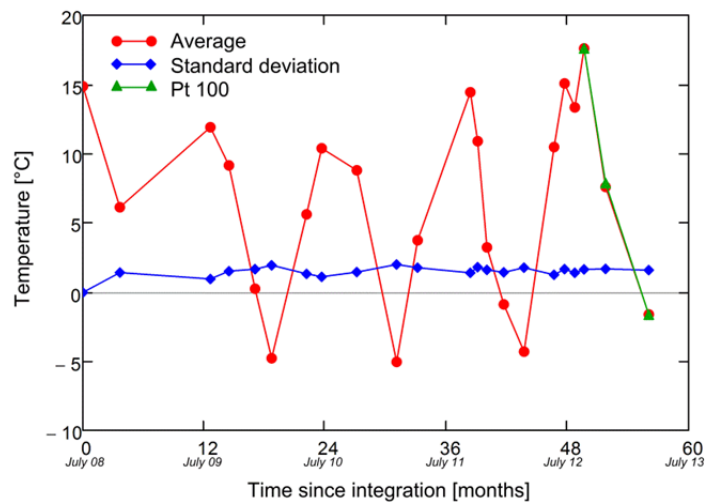
Figure 7-9: *Average temperature along the cable with time.*

7.5.4 Strain measurement results

Figure 7-10 shows the strain variation along both tight buffered cable sections obtained during the first 18 months, compared with the reference measurement in July 2008. Effects of temperature were compensated using the average frequency shift observed in the loose tube cable and assuming that soil fully restricted the thermal expansion of the tight buffered cable. In order to achieve a better comparability, the results of both sensors are plotted against the position variable from Figure 7-3, starting from shaft No. 4 and running to shaft No. 3. Note that some obvious outliers in the measurement data, owing to data processing difficulties, were manually corrected by replacing them by the average value of the adjacent measurement points (see also section 7.7.2). As can be seen from Figure 7-10, between the reference measurement in July 2008 and the next measurement in October 2008, almost no variations were obtained in both sections. In a further measurement in July 2009, large variations along the whole sensor were observed and again almost no changes were measured in the two following measurements in autumn. The same observation can be made for 2010 (Figure 7-11); simply the variation in strain is smaller than in the year before. Over the whole measurement period of two years, the same pattern can be observed for the measurements of both cable sections. Every strain peak in the V1a section has its counterpart in the V1b section, which underlines the reliability of the measured data. The V1a section equipped with additional anchors seems to be simply more sensitive, as anchors allow for a better localization of strains.

The further development of strains along the cables is shown in Figure 7-12 by means of measurements with a time interval of approximately one year. From the measurement taken in October 2011, it can be seen that the section without anchors started to level the strain distribution in some areas and its strain slightly deviates for the first time from the pattern of the other cable, which may be explained e.g. by local slippage between cable and surrounding soil (possible long term effects within the cable are not addressed within this study).
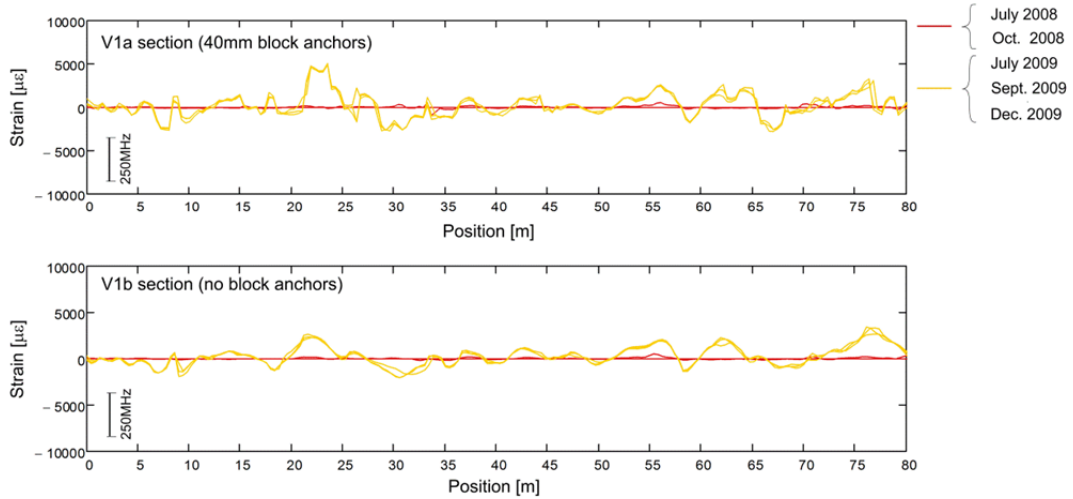
Figure 7-10: *Measurement results in the tight buffered loop for 2008-2009.*
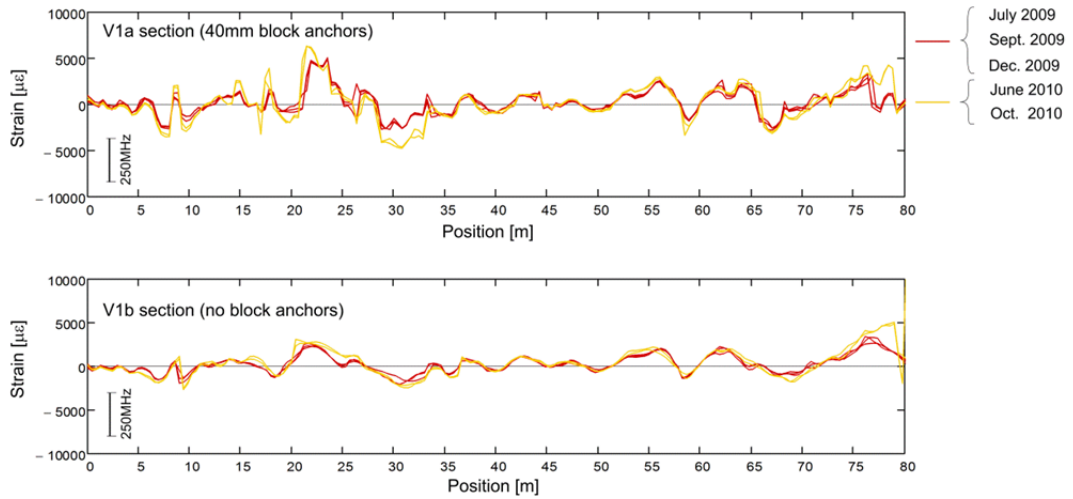
Figure 7-11: *Measurement results in the tight buffered loop for 2009-2010.*
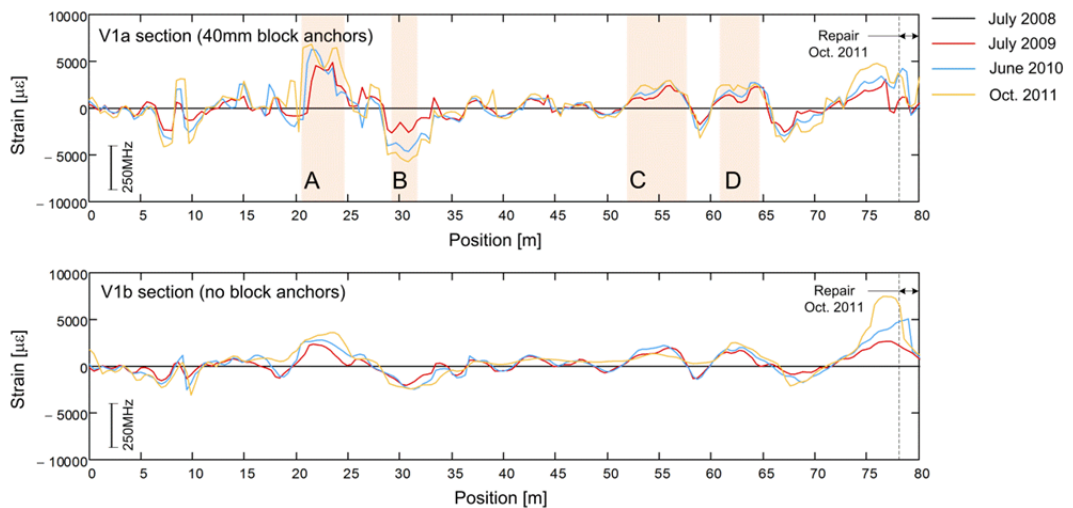
Figure 7-12: *Measurement results for the tight buffered loop 2008-2011.*

Possible sources of the measured Brillouin frequency shift

Before discussing the geotechnical relevance of the frequency shift measured along the fiber optic cable, it is necessary to exclude possible sources other than soil displacement as the reason for the measurement results. Besides soil displacements, possible sources for this relative frequency shift measured could be, in general non-uniformly distributed temperature, water content or other substances which are interacting with the cable jacket. As shown in the previous section, variations in the temperature distribution cannot cause frequency shifts as high as observed in Figure 7-10 and Figure 7-12, although V1a and V1b show a higher sensitivity to temperature changes (approximately 4-5MHz/°C). However, this temperature dependence was obtained in conditions were the cable jacket can extend freely, whereas in the present case the cable is embedded in soil, which restricts at least partially the thermal cable sheath expansion in longitudinal direction. Furthermore, also swelling of the cable jacket due to water causes not frequency shifts in this order of magnitude and, most notably, no negative frequency shifts after a wet period would be observed. For this reason, it can be assumed that soil displacements caused the measured frequency shift.

Geotechnical interpretation

At first, the strain change to the measurement taken in July 2008 seems to be randomly distributed. A comparison between the two strain sensors V1a and V1b shows that the pattern of the strain measured along both cables is identical, the only difference being in the section with block anchors which is more sensitive and shows higher absolute values. Variations in strains were measured along the whole cable compared to the status in July 2008; there is no location, where the strains stayed constant. On the other hand, there are time intervals (summer & autumn), during which the distribution did not change. From this it may be concluded, that no large single displacement discontinuity between point. No. 788 and 669 is present in this slope. The measurements indicate rather small differential soil displacements along the whole sensor with displacement velocity dependent on the season. Also the magnitude of measured strain is supporting this: Until October 2011, the cable was elongated between positions 20m and 25m (Figure 7-12), followed by a contraction of roughly the same amount between positions 28m and 33m. The overall cable elongation remains for all measurements below a few centimeters. As the fiber optic sensor is located within a potentially unstable soil mass, the measurement results imply that the differential soil displacements are caused by the slowly moving soil mass with locally non-uniformly directed displacement vectors. In addition, there is also the possibility, that freezing and thawing of surrounding soil might cause or influence the measured strains. A deeper assessment of the effects of freezing and thawing is given in section 7.7.1.

7.6 Comparison to additional measurement data

7.6.1 Inclinometer measurements

Almost at the same points in time as fiber optic measurements, inclinometer measurements were taken in the inclinometer KB0801 (Figure 7-1). This inclinometer has a depth of 61.5m, but only the first 20m at the top are of interest for the present study. Starting with the reference measurement in July 2008, the inclinometer shows an increase displacement at the head by approximately 3-6mm/year (Figure 7-13). A sliding surface can be clearly detected in a depth of 14m, just above the weathered rock, which indicates the presence of a slowly moving landslide. From this figure it becomes apparent that the topmost soil layers are moving with the same pattern, but faster than the layers just above the sliding surface and, furthermore, that the displacement velocity is clearly dependent on the season. Larger values can be observed during the snowmelt season and smaller or even zero values during summer and autumn.
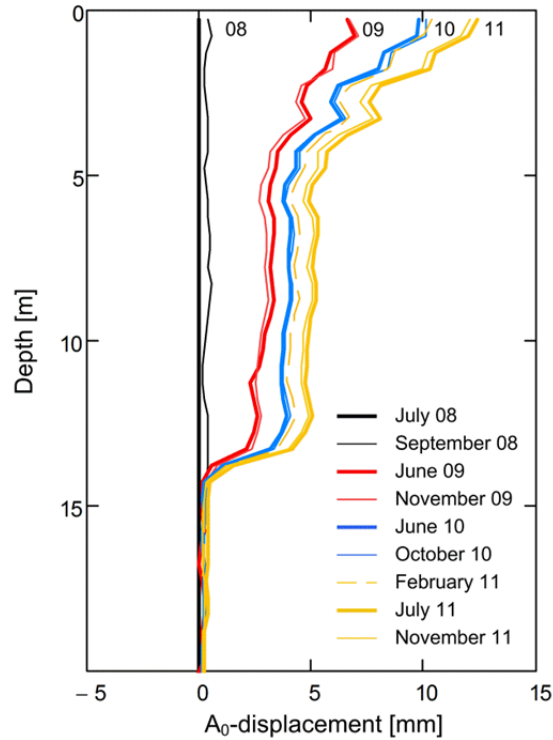
Figure 7-13: Inclinometer displacements in A$_0$-direction.

The dependence of displacement velocity on the season becomes even more apparent, if the head displacement and the sliding surface displacement are plotted versus the time (Figure 7-14). The largest displacement steps are observed during the snowmelt season (March – May, marked in blue). A similar pattern can be observed in the measurement results of the fiber optic strain sensor if, for certain zones along the sensor, the local cable elongation calculated from the measured strain is plotted against time. These zones (zone A-D, Figure 7-12) are chosen in the areas where the fiber optic sensor shows the highest sensitivity and manifested the highest local absolute strain values (the winter measurement taken in January 2010 is excluded from this plot; the possible effects of frozen ground are discussed separately in section 7.7.1). It is evident that the magnitude of cable elongation cannot be directly related to the inclinometer displacement, since different quantities are measured. However, all of the four zones show in general the same trend as the inclinometer. This type of evaluation presumes of course that the displacement field along the sensor stays stationary in the observed time interval and does not randomly change within months. It should be noted that owing to a construction activity in 2012 close to the inclinometer, larger displacements than in the years before were measured in KB0801. These displacements kept also growing during summer 2012 (not discussed in the present study).
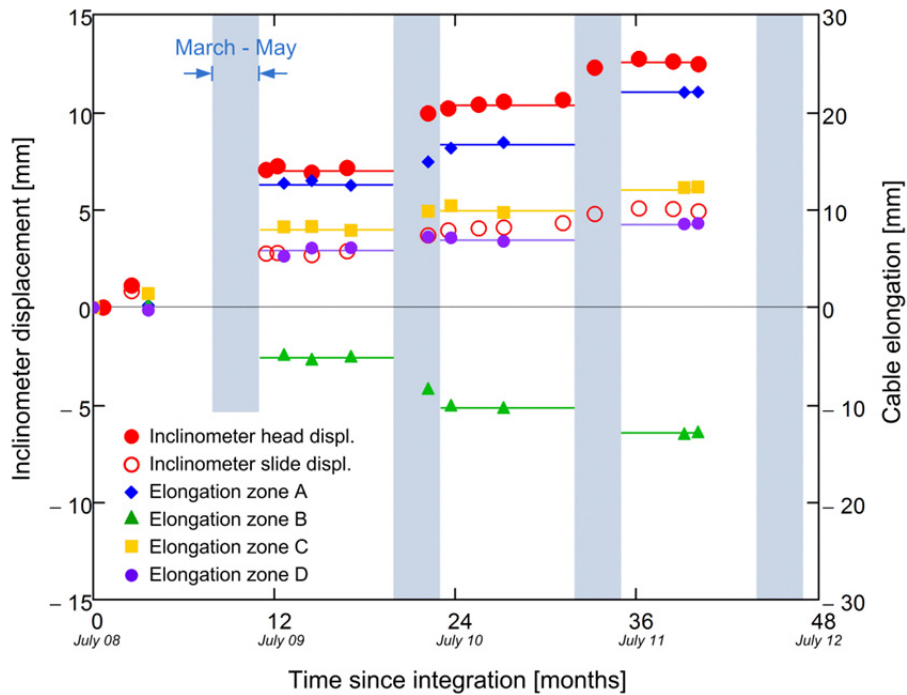
Figure 7-14: *Inclinometer head displacements and cable elongation for selected zones A to D on the V1a section with time.*

7.6.2   Geodetical measurements

Besides of the inclinometer measurements, a new geodetic survey between 2008 and 2009 was conducted using GPS (GEO Grischa, 2009). Because of the vegetation, the measurement accuracy achieved within a reasonable time effort was not satisfactory. In order to improve that, tachymetric measurements were carried out in the endangered region in September 2010. This measurement campaign was repeated in July 2011 (GEO Grischa, 2011) and the resulting displacement vectors are shown in Figure 7-15. As the fiber optic sensor and the inclinometer already indicated, also these measurements show the presence of an active slide. Furthermore, it shows that the whole region is moving and there is indeed no landslide boundary within the section which is covered by the fiber optic sensor. The displacements measured within this geodetical campaign are displacements at the ground surface. Even though the whole picture seems to be reasonable, there are still doubts about the size of the displacements, as the inclinometer head displacement and the displacements from the geodetic monitoring campaign do not coincide in their size. Although a certain discrepancy can be expected, as the geodetic measurements indicate displacements at the ground surface, which cannot be fully captured by inclinometer tube owing to its stiffness.
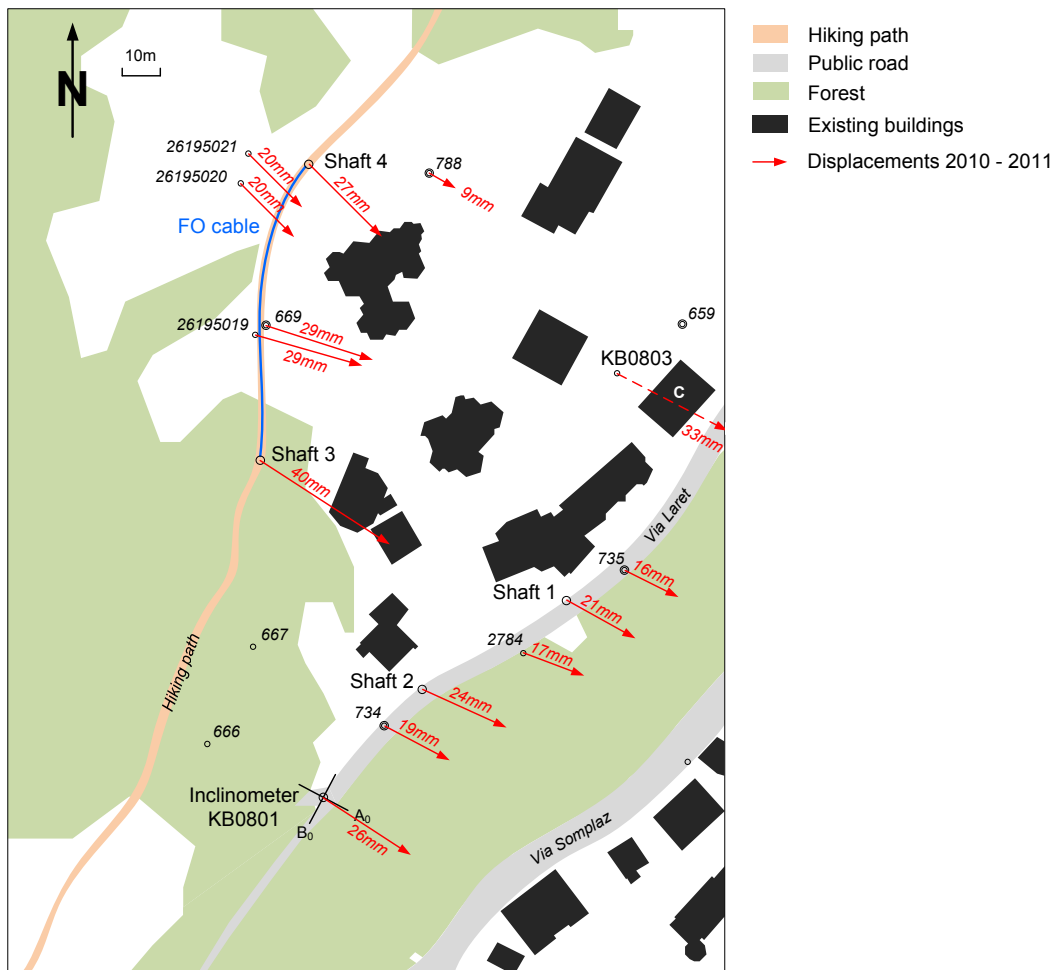
Figure 7-15: *Detail map section Via Laret, part of the God Ruinas landslide St. Moritz, 1:2000, displacement vectors 1:2 (After GEO Grischa, 2011).*

7.7　Discussion of the fiber optic measurement results

The additional measurement data obtained from the inclinometer KB0801 and the geodetical measurement campaign coincide with the interpretation of the fiber optic sensor data in section 7.5.4:

- Geodetical measurements: there is no large single displacement discontinuity between point 788 and 669. Instead, the whole area under study (and covered by the fiber optic sensor) is moving.
- Inclinometer measurements: the movements show a seasonal dependence, no movements in summer or autumn; movements during the snowmelt season.

Even though all the measurements seem to be coherent, it is important to discuss additionally the effect of freezing and thawing in soil as well as the aspect of spatial resolution.

7.7.1　Freezing and thawing effects of surrounding soil

Winter measurements

The fiber optic sensor is embedded at a depth of approximately 0.3m. In winter, the pore water in soil in this depth is frozen. This was confirmed by ground surface observation in January 2010 and also indicated by Brillouin frequency shifts measured in the loose tube

cables (Figure 7-7, Figure 7-9). The question of whether inhomogeneous freezing and thawing processes (pore water) in the soil influence the measurements, or may be even responsible for the differential displacements which were measured by the fiber optic sensor, is difficult to answer. As the inclinometer measurements show; soil displacements occur during the snowmelt season, which is also the time when possible effects of freezing and thawing would influence the fiber optic measurements. In order to explore possible effects of pore water freezing, measurements in winter were carried out, when the soil was frozen and, according to the inclinometer, no landslide displacements are expected. A first series of winter measurements was carried out between September 2009 and May 2010 (Table 7-1). As Figure 7-10 shows, no changes in strain distribution between September 2009 and December 2009 were detected, when the ground was covered by snow but not frozen. In January 2010, a measurement was conducted when the ground surface was frozen. In May 2010 another measurement was carried out, when the ground was thawed again. Figure 7-16 shows, at the top, the measured strains in the V1a section for the three measurements in December 2009, January 2010 and May 2010. At the bottom the relative strain change (differences) between these three measurements are shown. The same illustration was made for the V1b section in Figure 7-17.
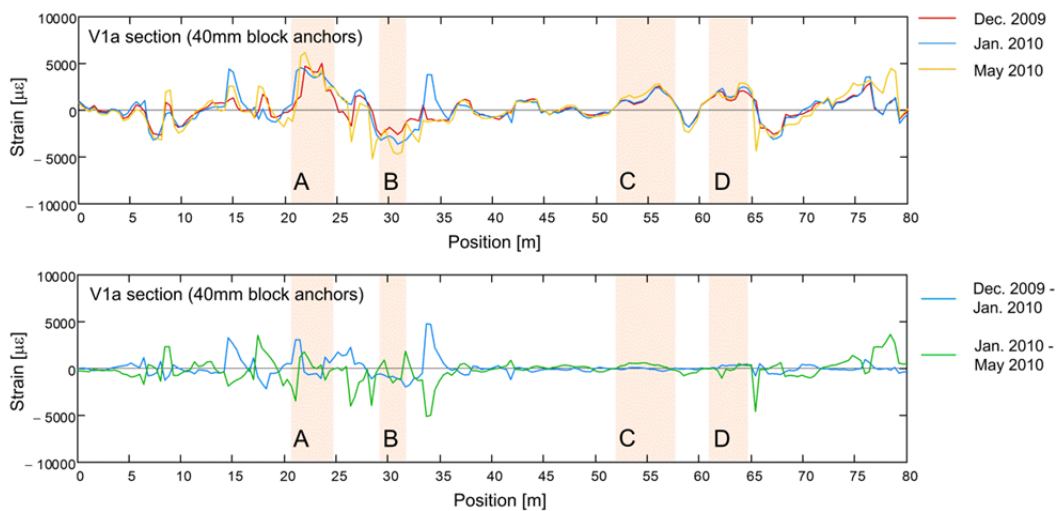
Figure 7-16: *Measurement results for winter 2009 / 2010 in the V1a section.*
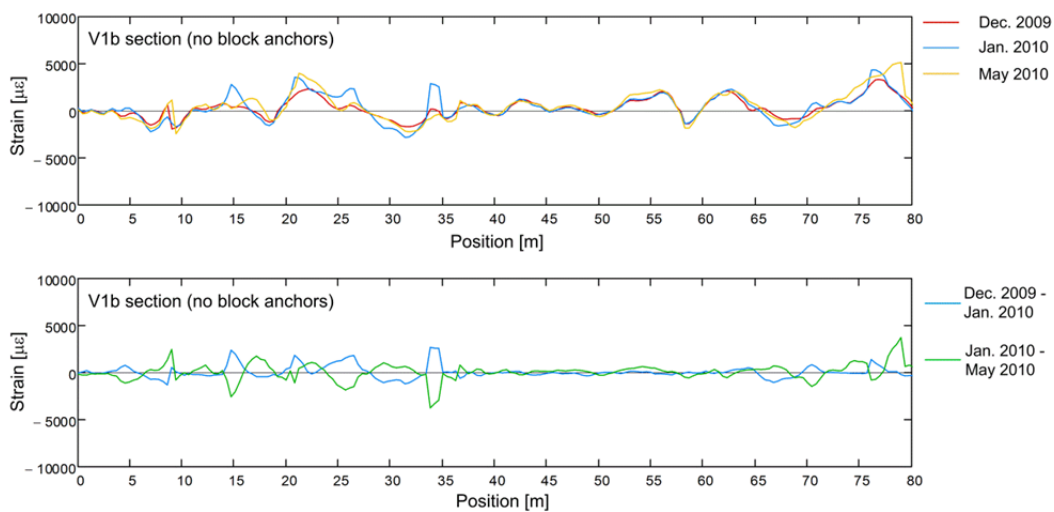
Figure 7-17: *Measurement results for winter 2009 / 2010 in the V1b section.*

Interpretation

Both tight buffered cable sections show in the range between 5m and 35m distance from shaft No. 4 and just before shaft No. 3 changes in strain, even though no displacements caused by the creeping landslide are expected (Unfortunately no inclinometer measurement for January 2010 is available, but for February 2011). On the other hand, there is a range between 35m and 65m distance from shaft No. 4, where the cables remain almost not influenced from the freezing process. The measurements in May 2010 include the effect of thawing and possible creeping landslide displacements. From the two strain differences showed in the lower graphs of Figure 7-16 and Figure 7-17, it becomes apparent that local strain peaks in the measurement from December 2009 to January 2010 (freezing) seem to be partially reversible, as the strain difference from January 2010 to May 2010 (thawing and landslide displacements) approximates a line mirrored on the abscissa. A further winter measurement, including an inclinometer reading was scheduled for February 2011 in order to confirm this sensor behavior. Unfortunately the cables were damaged by that time. Even though the winter measurements show that parts of the sensor are affected by freezing and thawing effects, zone C (Figure 7-16, Figure 7-14) was not affected in winter 2009 / 2010 and it is able to detect soil displacements, as the comparison to the inclinometer measurements in Figure 7-14 shows. A similar observation with freezing and thawing influencing the strain measurements could be made between November 2011 and May 2012. Hence, changes in strain in measurements carried out in frozen ground may not represent a movement of the landslide. Placing the cables in deeper soil layers, which are not frozen in winter, can in general resolve this problem. In the present case this was not an option, as a safe depth necessary for this purpose would not allow for a cost-efficient solution in this particular sensor location at approximately 1900m a.s.l.

7.7.2 Spatial resolution

The Brillouin frequency shift measured in the V1a cable with block anchors attached varies strongly along the fiber, whereas in the V1b cable without block anchors attached the Brillouin frequency shift is more balanced, due to the limited connection to surrounding soil. In some sections of the V1a cable, the strain changes so abruptly that the minimum possible spatial resolution of 1m (DITEST STA 202) is too large to resolve the true strain distribution properly along the fiber. In these sections, the frequency shift measured and the data processing of the measurement device may not be accurate and lead to an erratic picture with some outliers in the measurement data. A more detailed overview is given in the appendix of this chapter. In this section, simply Brillouin gain spectra along the two cable sections V1a and V1b in October 2008 and after three years of operation in October 2011 are shown in Figure 7-18 and Figure 7-19. The red line in these figures indicates the connection of the Brillouin frequency shift determined by the data processing algorithm of the measurement device. In sections where the algorithm was obviously wrong (e.g. Figure 7-19, bottom at 170m), manual corrections were made.
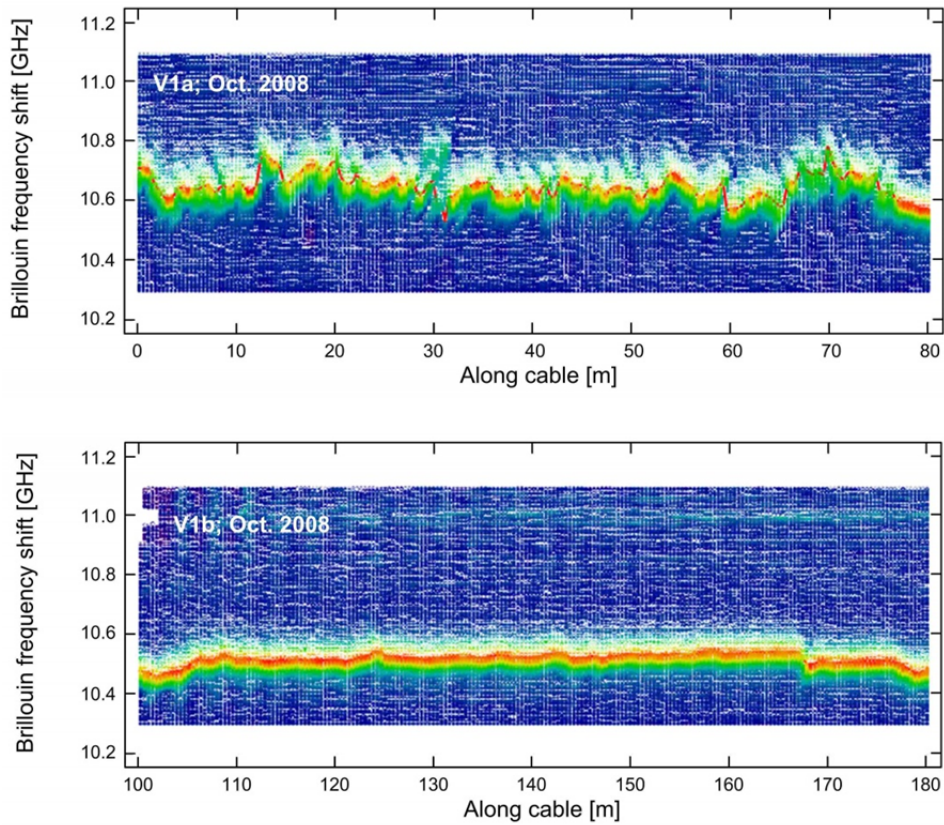
Figure 7-18: *Brillouin gain spectra along the V1a (top) and V1b (bottom) cable section in October 2008.*
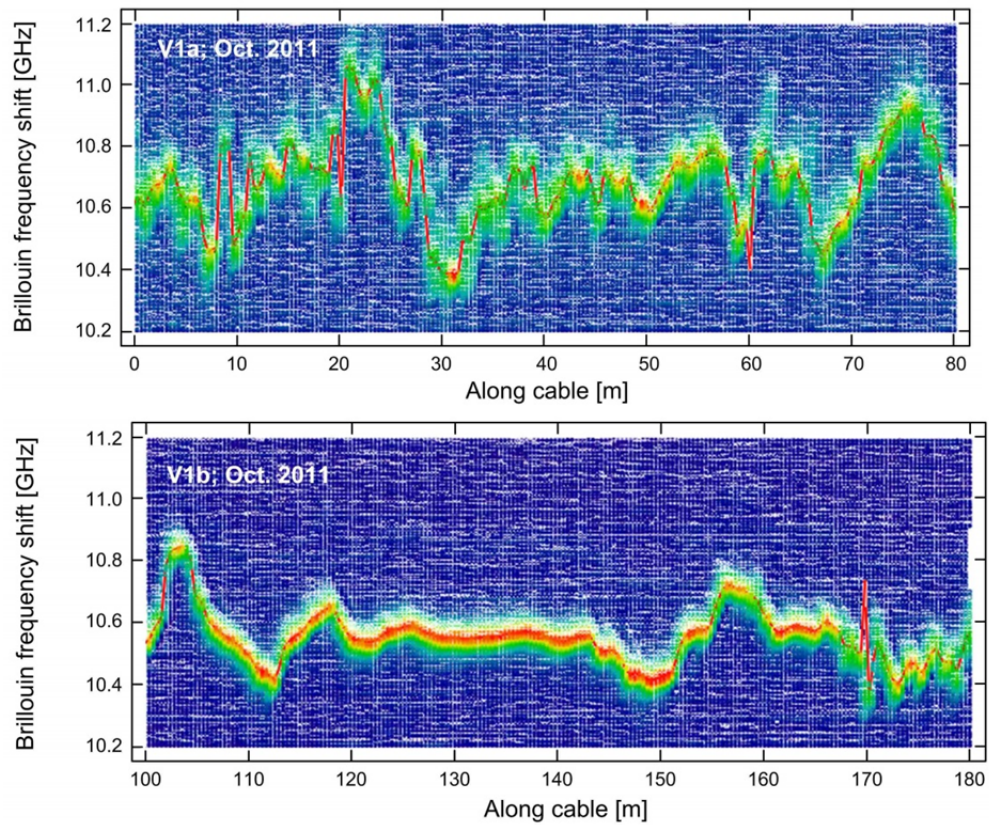
Figure 7-19: Brillouin gain spectra along the V1a (top) and V1b (bottom cable section in October 2011.

7.8 Conclusions

The 80m long soil-embedded fiber optic sensor was a research application incorporated in a real landslide monitoring project of the Institute for Geotechnical Engineering. Whereas traditional monitoring measures as inclinometers and geodetical survey were the backbone of this project, the fiber optic sensor had the status of a trial project. Nevertheless, this sensor provided meaningful results, which are in accordance to the inclinometer and the geodetical measurements.

Further important conclusions of this fiber optic field application are summarized in the following items below:

- No landslide boundary could be detected with the fiber optic sensor between point No. 669 and 788. Instead, the sensor indicated rather that the whole region is in movement and the measured frequency shift is caused by non-uniformly directed local soil displacements. This is also in accordance to the latest geodetical measurements. To which extent the measured frequency shift is influenced by cummulative effects of freezing and thawing of surrounding soil remains unclear, since movements of the soil mass and effects of freezing and thawing seem to occur in the same time interval.
- The fiber optic sensor indicated a seasonal dependence of soil displacements, which is confirmed by the inclinometer measurements in KB0801.
- At first the measured frequency shift seems to be randomly distributed, but a reduction of measurement time interval showed that the measurements are reliable and consistent in itself (excluding measurements in frozen ground). There are subsequent measurements in summer and autumn, where almost no change was measured.
- Parts of the tight buffered cable section are influenced by freezing and thawing effects, which can lead to geotechnical misinterpretation if the fiber optic measurement series is not conducted in sufficiently small time intervals or no other independent measurement data is available. This situation should be in general avoided by integrating the fiber optic sensor in sufficient depth.
- The cables applied in this project were trial versions with some drawbacks as insufficient fiber protection (rodents, crushing from soil grains) or inadequate cable jacket material (hygroscopic, large temperature coefficient). Nevertheless, it was possible to achieve meaningful results for 27 months under extremely harsh climate conditions, which is also a promise for future applications, where further developed cable versions will be applied.
- After 27 months of operation, differential movements of the shaft and surrounding soil caused in February 2011 a fiber breakage in the area of the shaft entrance. It is therefore crucial to pay attention to such technical details. In October 2011, the broken cable was repaired and further measurements could be taken again.
- Data acquisition with the measurement device was always possible, despite the harsh weather and field conditions met, especially during winter. This demonstrates that the measurement unit and the other fiber optic equipment is sufficiently robust.
- Pre-straining the cables in soil was successful; the fiber optic sensor measured not only extension but also compression.
- The applied cable versions V1a and V1b are comparable with regard to diameter and stiffness. By attaching 40mm block anchors to the V1a cable, it was possible to make the cable more sensitive to the same soil displacements and measure higher strains than with the bare V1b cable. Furthermore the redistribution of strain in place and time is clearly restricted by applying block anchors. On the other hand, the anchors cause locally large strain changes, which leads to more conflicts in measurement result processing in the measurement unit and finally, to a more erratic strain distribution.
- In some sections, the minimum spatial resolution of 1m of the applied measurement unit is too large to resolve the large local strain changes properly, which may lead to locally inaccurate measurements.

References

GEO Grischa. (2007). Höhenmodell uns Schnitte im Bereich der Via Laret 12, 7500 St. Moritz. GEO Grischa AG, St. Moritz.

GEO Grischa. (2008). LFP 3 Messung St. Moritz. GEO Grischa AG, St. Moritz.

GEO Grischa. (2009). LFP 3 Messung St. Moritz. GEO Grischa AG, St. Moritz.

GEO Grischa. (2011). Geodätische Überwachungsmessung Gebiet God Ruinas (1. Folgemessung). GEO Grischa AG, St. Moritz.

Hauswirth, D., Iten, M. & Puzrin, A.M. (2012). Detection of ground movements using soil-embedded distributed fiber optic sensors. Proc. of the 4th Int. Conf. on Site characterization (ISC-4, Pernambuco), pp. 579-586.

IGT. (2008). Rutschung Via Laret, St. Moritz, Bericht Nr. 4709/1. Zürich: Institut für Geotechnik, ETH Zürich.

IGT. (2009). Rutschung Via Laret, St. Moritz, Bericht Nr. 4709/2. Zürich: Institut für Geotechnik, ETH Zürich.

Iten, M. (2011). Novel applications of distributed fiber-optic sensing in geotechnical engineering. PhD thesis No. 19632, ETH Zürich.

Swisstopo. (2005). Geologischer Atlas der Schweiz, Blatt 1257 St. Moritz. Swisstopo, Wabern.

Appendix

7.8.1   Measurements during construction activity in 2012

In the previous sections the measurement results between July 2008 and November 2011 were reported. In order to collect more data with this trial sensor, the measurements were continued.

Between July 2008 and November 2011 no large construction activity was noticed in the area of the fiber optic sensor. In March 2012 a large excavation for a building was started close to the inclinometer KB0801. Whereas between 2008 and 2011 the inclinometer and the fiber optic sensor were exposed to creeping landslide movements, in 2012 the detected displacements were mainly caused by the local construction activity nearby and cannot be compared to the data series from 2008 to 2011, as the inclinometer head is measuring local displacements and is not representative for the whole slope and the velocity field of the creeping landslide may have changed compared to the situation before. Hence the further measurements in 2012 / 2013 are not included in this study.

7.8.2   Spatial resolution (continuation)

In section 7.7.2 the difficulties owing to the strong spatial variations in strain along the V1a fiber with block anchors attached was addressed. In the present section, this problem is further illustrated with the example of the measurement in the V1a section in October 2011. In Figure 7-20, a section of the V1a cable is showed, where the strain seems to change abruptly within a short distance. In a position of 20m distance from shaft No. 4, the measurements indicate two peaks in the Brillouin gain spectrum, which is also shown in Figure 7-21, where the Brillouin gain spectrum for 4 subsequent positions No. 1-4 is drawn. The red dot marks the Brillouin frequency shift which was detected by the algorithm of the device (the connection of these red dots corresponds with the red line in the previous figure). In such constellations the true strain distribution remains unclear and, depending on which peak (or something intermediate) is chosen by the processing algorithm from measurement to measurement, outliers in the strain measurement may be the consequence, if they are not corrected manually. In general, a reduction of the bond between cable and soil, an increase in cable stiffness or an application of a measurement technology with reduced spatial resolution would improve the situation.
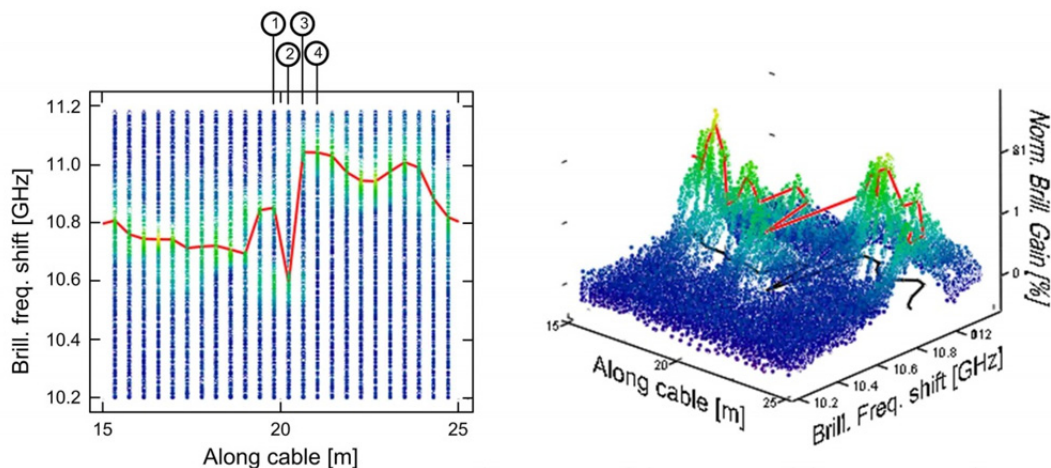
Figure 7-20: *Detailed view of the Brillouin gain spectra along the V1a cable in October 2011.*
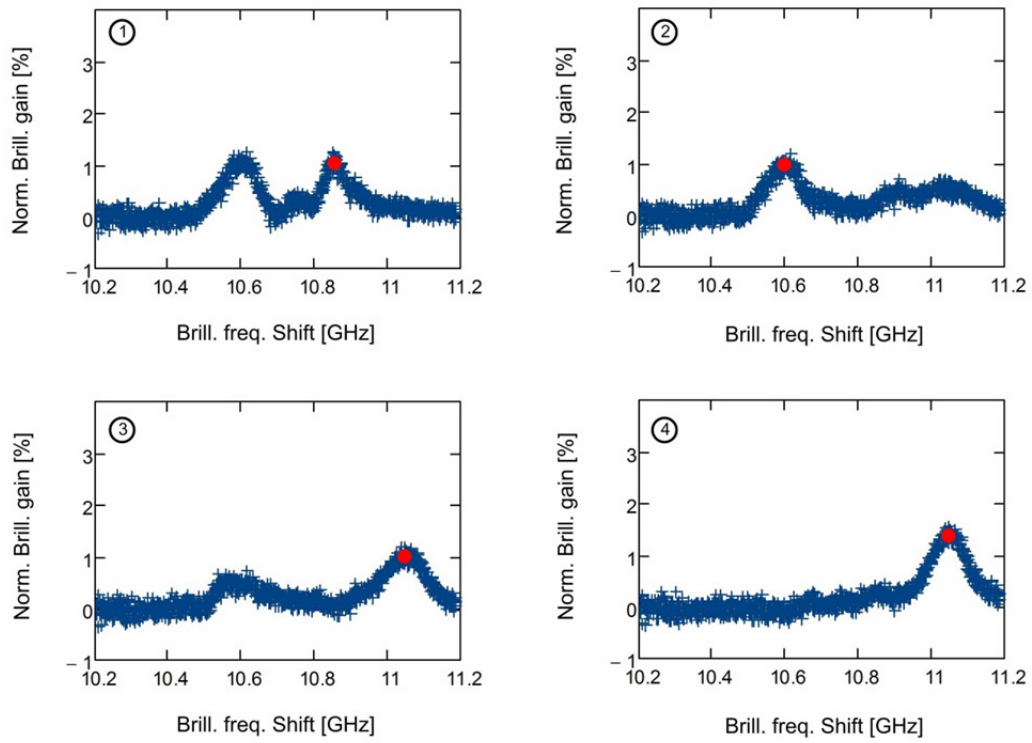
Figure 7-21: *Brillouin gain spectra for the selected positions No. 1-4.*

III. Development of chemical and biological stabilization techniques (Task 3)

8 Combining biomineralization with chemically enhanced drainage in soils

8.1 Abstract

This work focuses on the potential combination of microbial soil improvement methods with chemically enhanced drainage in fine grained soil. The efficiency of carbonate precipitation with *Bacillus pasteurii* cultures was evaluated on laboratory scale soil samples containing clay minerals. Microbial carbonate precipitation successfully increased uniaxial compression strength even in fine-grained soils with a minimum hydraulic conductivity of 5E-9 m/s. During treatment, permeability is reduced by one order of magnitude and can decline below the required limit. In order to avoid falling below the threshold it is proposed to improve in advance hydraulic properties of the soil by using a technique of chemically enhanced drainage. In this study permeability increase of more than one order of magnitude was achieved for soils containing smectite clay minerals. Combination of the two methods allows expanding the possible range of applicability of biomineralization toward less permeable soils.

8.2 Introduction

Artificial cementation of soils by addition of chemicals is widely used (e.g. in road construction for hydraulic stabilization of the deck). These methods usually require mechanical mixing of the treated soil, yield highly alkaline soil chemistry and are limited to close surface application. (Hammes & Verstraete, 2002)

Microbially induced precipitation of calcite ($CaCO_3$) provides cementation of soil particles under flow-through conditions. Hammes & Verstraete (2002) have shown that calcite precipitation is governed by four key parameters. The formation of calcite depends on
- the concentration of calcium in the solute,
- the available carbonate,
- the pH of the environment and
- the availability of nucleation sites.

Microorganisms can locally influence these parameters by their metabolism, so that calcite precipitation occurs distributedly and not locally at the injection point of calcium solutions. A homogeneous distribution of an active bacteria culture can therefore provide homogeneous cementation of soil under flow-through treatment.

Bacillus pasteurii bacteria are especially appropriate to provide a controlled precipitation of calcite. They produce large amounts of the urease enzyme that enables them to use urea ($CO(NH_2)_2$) as energy and nitrogen source. The decomposition of urea simultaneously increases the pH in the vicinity of the bacteria and releases carbonate (after Whiffin et al., 2007). The bacteria surface itself can serve as nucleation site (DeJong et al., 2006).

In sands with high hydraulic conductivity homogeneous cementation was obtained and correlation between calcite content and shear strength could be assessed (Harkes et al., 2008).

In this project the method of biomineralization is evaluated with respect to its application in less permeable soil.

8.3 Materials and methods

8.3.1 Conceptual design

On a conceptual level, this study assesses the potential of combining microbial methods to increase shear strength with chemical methods to increase permeability of soils. The former requires a sufficient hydraulic accessibility of the open pore space in order to place and feed microorganisms in soil. This is naturally not given in fine-grained soil, where already a small percentage of clay can reduce the fluid flow drastically.

The first step in this study consists of the placement of bacteria and inducing precipitation of carbonate in a soil with large aggregated clay minerals (Figure 8-1). The goal of this step was to investigate, whether in the presence of clay minerals an increase in shear resistance can be achieved by biomineralization. In order to keep the cultivation of the bacteria unaffected by any chemical treatment, the soil used in this step was a quartz illite mixture, where large illite clay particles are chosen to represent an aggregated smectite phase.
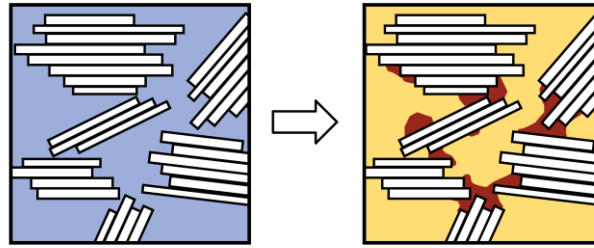
Figure 8-1: Cementation of clay particles by microbial induced precipitation of carbonates.

In a second step, it is then investigated whether the hydraulic conductivity allowing for successful biomineralization can be produced by means of a permanent chemical modification of the sealing smectite clay phase (Figure 8-2).
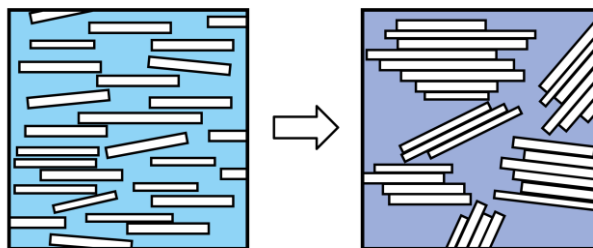
Figure 8-2: Transformation of swellable clay platelets with large diffuse double layers to aggregated clay particles.

Many of the chemically enhanced drainage methods proposed in the literature are not compatible with the use of microorganisms e.g. one of the most efficient way to increase permeability by several orders of magnitude (Fernandez & Quigley, 1985) uses liquid hydrocarbons, which are toxic to the microorganisms established in biomineralization methods and in general classified as environmental pollutants. Based on its specific interaction with the clay surface (Plötze & Kahr, 2008) the organic salt guanidinium was chosen as chemical agent to increase permeability. It is soluble in water and reacts with the clay at low concentrations. Biodegradation of guanidinium is reported for species occurring in natural surface water (Mitchell, 1987). Different mixtures of smectite clay (Calcigel, Süd-Chemie AG, Germany) with quartz grains (sand <0.3 mm, Cook Industrial Minerals Pty.Ltd, Perth, Australia and silty sand, Millisil B1, Sihelco AG, Birsfelden, Switzerland) were subjected to standard oedometer test both in their natural and their modified form. The analysis of the time-settlement curve was used to investigate the efficiency of the chemical improvement. Additionally its effectiveness under flow-through conditions was tested in one set of permeameter tests.

Both steps are addressed individually in this study and finally evaluated on their potential combination.

8.3.2   Experimental setup for biomineralization

Biomineralization experiments were operated with microorganisms of the species *Bacillus Pasteurii* (also classified as *Sporosarcina Pasteurii*). Cultivation was conducted under aerobic batch condition in a medium containing 20 g/l urea and 8 g/l nutrient broth. Inocculation of the samples was performed by transferring 5 volume percent of a freshly grown culture to new nutrient solution. Sterile handling techniques were applied to keep the cultures pure and guarantee reproducibility.

The feasibility of biomineralization in clay was evaluated by performing flow-through experiments with bacteria suspensions and nutrient media in soil columns. The soil was in-

occulated with *B. Pasteurii* by mixing the soil with bacteria suspension prior to sample re-constitution. Supply of nutrient and calcium was provided by flushing the soil with an optimized pore water solution as proposed by DeJong et al., (2006). Adjustment of nutrient solution to a pH 6.5 with sterilized HCl provided stable solutions without calcite precipitates prior to bacteria exposure. The increase in shear strength due to cementation was subsequently assessed by uniaxial testing of biomineralized and natural control samples. Since exposure to air of the clay rich samples would lead to drying and negative pore water pressures the uniaxial tests were performed in an oil bath.

The sample cell for the biomineralization experiments was based on an oedometer cell extended by two half tubes (Figure 8-3), which were removable to provide a laterally unsupported sample for uniaxial testing.

Figure 8-3: *Disassembled sample cell with the two removable sidewalls for uniaxial testing.*

Two biomineralization samples of an illite-quartz soil were operated with different pumping schemes. As active *B. Pasteurii* cultures raise the pH of the pore fluid permanently, the change in pH of influent and effluent medium was taken as rough indication for bacteria activity. In both samples the effluent pH exceeded 9.5 after the second day of treatment with nutrient solution.

Intermitting pumping led to growth of the bacteria into the tubing and eventually to failure to supply the nutrient into the soil. Constant flushing resulted in less premature precipitation in the supply tubing. Nevertheless high backpressure was generated after two days of feeding. The peristaltic pump was not able to maintain the flow rate. Therefore the feeding technique was changed to injection of media directly into the soil with two needles. The injection point was moved by 1 cm per day. After a feeding time of nine additional days the sample was sheared at a displacement rate of 10 mm/h. An untreated control sample was tested at the same shear rate.

8.4 Results

8.4.1 Biomineralization in soils with low permeability

The local injection of solution into the soil with needles allowed supplying the nutrient to the microorganisms homogeneously. This finally led to the expected cementation of the soil particles throughout the sample. During undrained uniaxial loading a higher failure load was detected compared to the sample without biomineralization (Figure 8-4) and the failure occurred more brittle. The presence of clay minerals did not impair the cementing effect of microbial calcite precipitation.
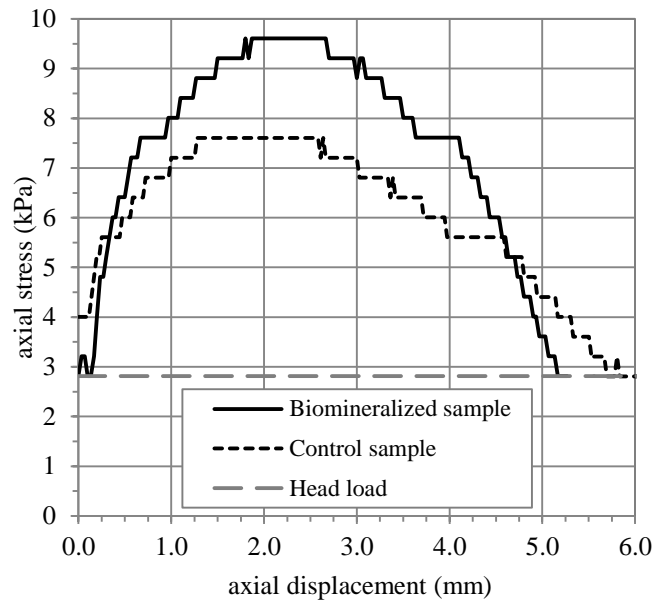
Figure 8-4: *Uniaxial shear behavior of a microbially impoved soil sample and an unmodified control sample for comparison. The shear strength is improved and the failure occurs more brittle.*

On the way to this result several additional qualitative and quantitative observations were made. A considerable decrease in permeability was observed for all biomineralization samples. The average permeability of the soil decreased from 4.8E-8 m/s before the experiment to 3.1E-9 m/s after biomineralization. These average values were obtained with constant head experiments and are – due to the heterogeneity of the biomineralized samples – only very rough estimates for the local decrease.

The reduced hydraulic conductivity led to a significant reduction of fluid low and a localization of the calcite precipitation in the vicinity of the inlet. Without moving the injection point, the development of a high backpressure and the growth of the bacteria into the tubing would eventually lead to termination of the treatment. Once the hydraulic conductivity declined below 5E-9 m/s, it was no longer feasible to feed the bacteria homogeneously with nutrients.

In order to provide an adequate flow rate under such conditions, it is required to use either high hydraulic gradients or long treatment time with low-activity bacteria. Both adaptions will result in unsatisfying side effects in the field.

In practical applications increasing the hydraulic gradient to achieve sufficient flow rates will result in locally very high pore-water pressures close to the injection points. For the treated soil layer the factor of safety for e.g. slope stability can therefore be reduced significantly during the injection phase. Since the slopes requiring soil improvements are mostly already close to failure this additional exposure during treatment is generally not acceptable. High injection pressures additionally bear the potential to produce hydraulic fractures, which will lead to pronounced preferential flow and eventually to failure to homogeneously mineralize the soil layer.

Conversely, accepting low pressures only will require a fundamental adjustment of the used nutrients and microorganisms. Feeding abundant nitrogen reducing soil bacteria (e.g. *Castellaniella denitrificans*, van Paassen et al., 2008) - instead of injecting new microorganisms - together with low concentrated nutrients is theoretically an option, but the prolonged duration of treatment will conflict with economical and temporal requirements for soil improvement methods.

In conclusion, the experiment have shown, that biomineralization is possible for fine-grained soil with a sufficiently high permeability. There is however a risk that during treatment the permeability will fall below the required limit. The most promising solution to

overcome this obstacle is to increase the hydraulic conductivity in advance, so that – once the process has started – fluid flow will not drop below the required minimum. In the next step we therefore investigate the potential of chemically enhanced drainage.

8.4.2 Increase of permeability in smectite/quartz mixtures

The analysis of the time-settlement curves revealed that permeability was increased for all samples with the chemically modified clay compared to the unmodified samples. In mixtures with sand the permeability was increased to such an extent, that the data could not be evaluated as the settlement occurred almost immediately. Hence, only the data of silty sand mixed with clay is presented, where both sample sets showed the expected time dependent settlement according to the 1-dimensional consolidation theory.

Figure 5 shows the derived permeability at different stress levels for a clay content of 10 %. The initial difference between modified and unmodified samples at low stresses is almost perfectly maintained during loading. For close to surface applications (effective vertical stress < 100 kPa) the increase is one order of magnitude and the permeability is elevated to the targeted range of 1E-8 m/s. The relative improvement slightly drops during compaction of the sample by higher stresses.

In the case of a higher clay content a more pronounced decrease during loading is observed for both the absolute permeability and the relative improvement (Figure 8-6). Here it is informative to compare the permeability at a given void ratio (Figure 8-7) as well. An initially more than 50 times higher permeability is observed prior to compaction at a void ratio of 0.68. The modified soil structure features thus more effective flow paths for circulation than the raw material at the same void ratio. Due to the large plastic deformations, this difference reduces significantly upon compaction.
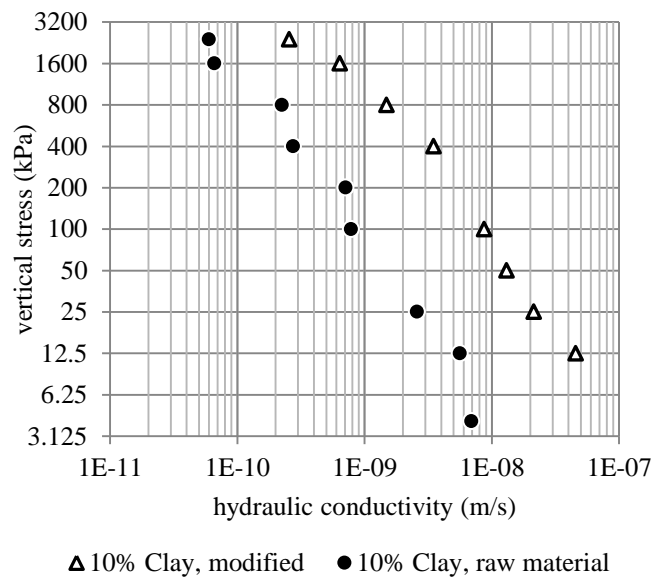
Figure 8-5: Hydraulic conductivities during oedometric loading for 10% clay content. The permeability of the chemically modified soil is increased over the whole range compared to the unmodified raw material.
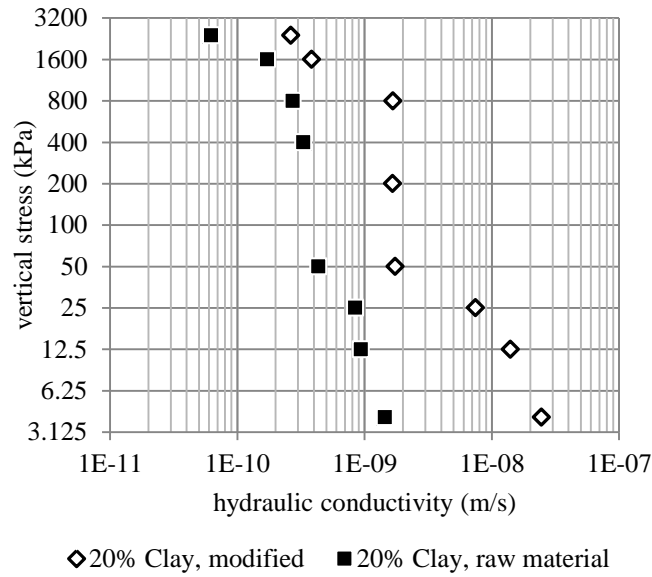
Figure 8-6: *Hydraulic conductivities during oedometric loading for 20% clay content. During compaction the difference between modified and raw material is reduced.*
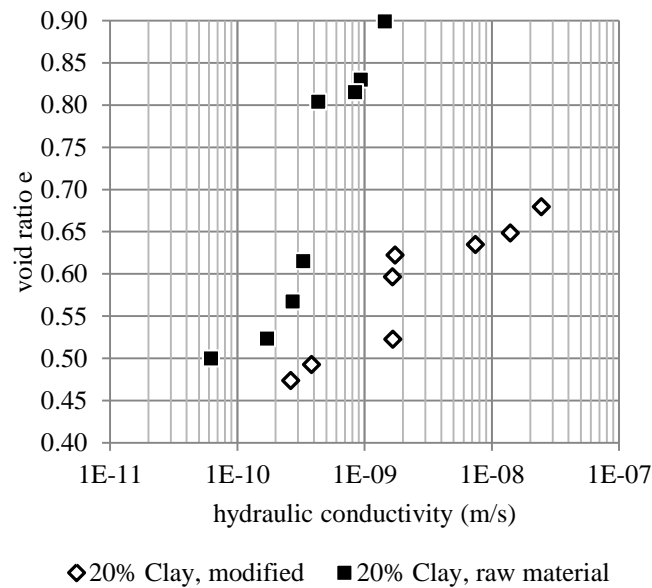
Figure 8-7: *Comparison of hydraulic conductivity for different void ratios. During compaction both void ratio and permeability are decreased. After large plastic deformations the relative improvement is reduced.*
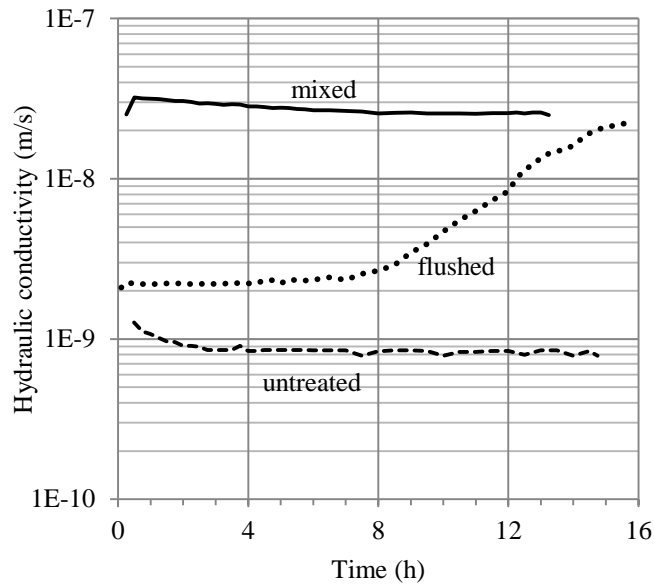
Figure 8-8: *Hydraulic conductivity over time during permeameter testing. The sample flushed with the guanidinium solution features a gradual increase of permeability in the course of the treatment.*

Also under flow-through conditions the chemical enhanced drainage maintained is effectiveness. Figure 8 compares the different treatment methods and shows that even the structurally undisturbing delivery of the chemical via the pore fluid lead to the targeted increase above 1E-8 m/s.

The improvement achieved by chemically enhanced drainage methods reached values above 1E-8 m/s for both types of addition (mixing and flushing). Only after significant mechanical straining, the newly formed structure is destroyed. The flow rate feasible at this elevated permeability should be sufficient in order to supply the microorganisms with nutrients for carbonate precipitation.

8.5   Conclusion

The qualitative and quantitative findings of the performed experiments allow drawing four main conclusions about biomineralization with respect to its application in fine-grained soils.

Firstly, microbial carbonate precipitation successfully increases shear strength above a certain limiting permeability even in fine-grained soils. In this study the minimum hydraulic conductivity was 5E-9 m/s. It could be shown that the presence of clay minerals did not impair the strength improvement.

Secondly, during the process of biomineralization the precipitated calcite reduces the hydraulic conductivity. The experimental data indicated a decrease of one order of magnitude. If during this process the permeability declines below the limiting threshold, incomplete and heterogeneous soil improvement will be the result.

Thirdly, a measure to expand the application of the microbial method to less permeable soils is to increase the hydraulic conductivity in advance by one order of magnitude, so that during treatment the required fluid flow can be maintained with reasonable porewater pressures.

Finally, it could be shown, that with the chemical enhanced drainage technique an efficient method to increase hydraulic conductivity exists. Increase in hydraulic conductivity of more than one order of magnitude was achieved for soils containing smectite clay minerals.

There is a reasonable likelihood that the chemical method works in soil with other clays minerals as well. Further research is recommended in order to assess the optimum range of applicability of the combined bio-chemical method with respect to initial hydraulic conductivity, soil composition and microorganism.

Acknowledgements

References

DeJong, J. T., Fritzges, M. B. & Nüsslein, K. (2006). Microbially Induced Cementation to Control Sand Response to Undrained Shear. *Journal of Geotechnical and Geoenvironmental Engineering*, Vol. 132 (11): 1381-1392.

Fernandez, F. & Quigley, R.M. (1985). Hydraulic conductivity of natural clays permeated with simple liquid hydrocarbons. *Canadian Geotechnical Journal*, 22(2): 205-214.

Hammes, F. & Verstraete, W. (2002). Key roles of pH and calcium metabolism in microbial carbonate precipitation. *Reviews in Environmental Science & Bio/Technology*, Vol. 1: 3-7.

Harkes, M. P., Booster, J. L., van Paassen, L. A., van Loosdrecht, M. C. M. & Whiffin, V. S. (2008). Microbial induced carbonate precipitation as ground improvement method – bacterial fixation and empirical correlation $CaCO_3$ vs strength. *1st international conference BioGeoCivil Engineering*, Delft, the Netherlands.

Mitchell, W. R. (1987). Microbial Degradation of Guanidinium Ion. *Chemosphere*, Vol. 16 (5): 1071-1086.

Plötze M. & Kahr G.,. Diagnostic intercalation in clay minerals - use of guanidine carbonate. *Proc. of the 4th MECC, Mineralogia*, 33(2008): 132.

van Paassen, L. A., Daza, C. M., Staal, M., Sorokin, D. Y. and van Loosdrecht, M. C. M. (2008). In situ soil reinforcement by microbial denitrification. *1st international conference BioGeoCivil Engineering*, Delft, the Netherlands.

Whiffin, V. S., van Paassen, L. A. & Harkes, M. P. (2007). Microbial Carbonate Precipitation as a Soil Improvement Technique. *Geomicrobiology Journal*, Vol. 24 (5): 417-432.

IV. Study of creeping landslides (Tasks 4, 5, 6, 7, 8 and 9)

9 Study of a naturally constrained landslide (Brattas, St. Moritz, Task 4)

9.1 Abstract

The ski resort town of St Moritz, Switzerland, is partially constructed on a large creeping landslide, which has been causing damage to buildings and infrastructure. At the town center the landslide is constrained by a rock outcrop, creating a compression zone in the sliding mass. After decades of gradual slowing down, in the beginning of 1990s the landslide started to accelerate, in spite of the fact that the average yearly precipitation and the pore water pressure on the sliding surface remained fairly constant. The chapter shows that a constrained creeping landslide experiences progressive failure caused by propagation of a zone of intense shearing along the slip surface resulting in significant earth pressure increase and visco-plastic yielding of soil in the compression zone. This basic physical mechanism, relying on extensive laboratory and field tests and long term displacement monitoring, explains the paradox of the St Moritz landslide acceleration. Although the model predicts that the landslide could eventually slow down, its displacements may become excessive for some buildings, requiring an early warning system and further stabilization of the historic Leaning Tower. In general, by predicting the onset of yielding, the model can provide important timeframe for stabilization of constrained landslides.

9.2   Introduction

Understanding of failure mechanisms of creeping landslides is of critical importance for assessment and mitigation of their hazard (Terzaghi 1950, Chandler & Pook 1971, Glastonbury & Fell 2008, Schulz *et al.* 2009). In general, when a creeping landslide is constrained by an obstacle, either natural (a rock outcrop) or artificial (a retaining wall), it slows down, creating an impression of being stabilized (Bernander & Olofsson 1981, Wiberg *et al.* 1990, Puzrin & Sterba 2006). Sometimes, however, the stabilization phase is succeeded by acceleration (e.g., Puzrin & Schmid 2007), which in the case of the St Moritz-Brattas slide (Figure 9-1) resulted in the last 19 years in more than threefold increase in its displacement rates (Figure 9-2). The onset of landslide acceleration can be observed around September 1991, when the time - displacement curve changes its curvature.
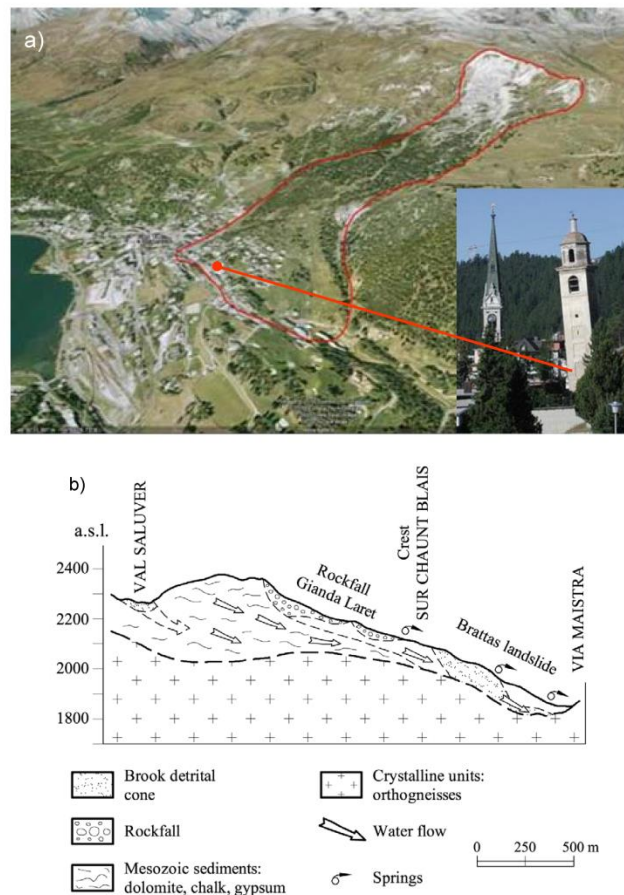
Figure 9-1: The St. Moritz-Brattas Lanslide (a) aerial photo (after Google) and the Leaning Tower of St. Moritz; (b) the geology (Müller & Messina, 1992).

The St Moritz slide (Figure 9-1a) has a length of 1500 m, width of 600-800 m and the average inclination of about $20°$ (Schluechter 1988). The landslide consists of two parts (Figure 9-1b), with some geological evidence of a rock outcrop at the boundary between them. The upper 800-900 m are a rockfall of boulders reaching 2-3 m in diameter; the lower part of 600-700 m is the 17-23 m thick sliding layer built of a silty soil matrix with boulder inclusions. Inclinometer and Increx measurements taken in 2006-2010 in the lower part show that the shear strain is largely localized within the slip surface (Figure 9-3a), while the compression along the slide leads to the heave in the perpendicular direction, which is fairly uniformly distributed within the sliding layer thickness (Figure 9-3b). At the bottom of the lower part the landslide is constrained by a rock outcrop, creating a compression zone in the sliding mass.
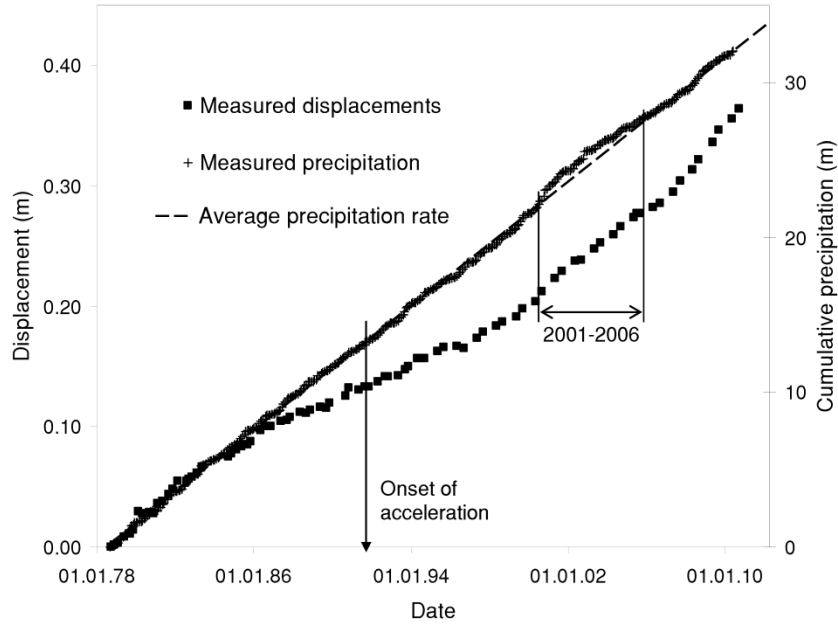
Figure 9-2: *Displacements and cumulative precipitation in 1978-2010. Displacements were measured in the vicinity of the Leaning Tower (21.1 m away from the rock outcrop), in the direction of the slope gradient using geodetic triangulation with the accuracy 0.002 m.*
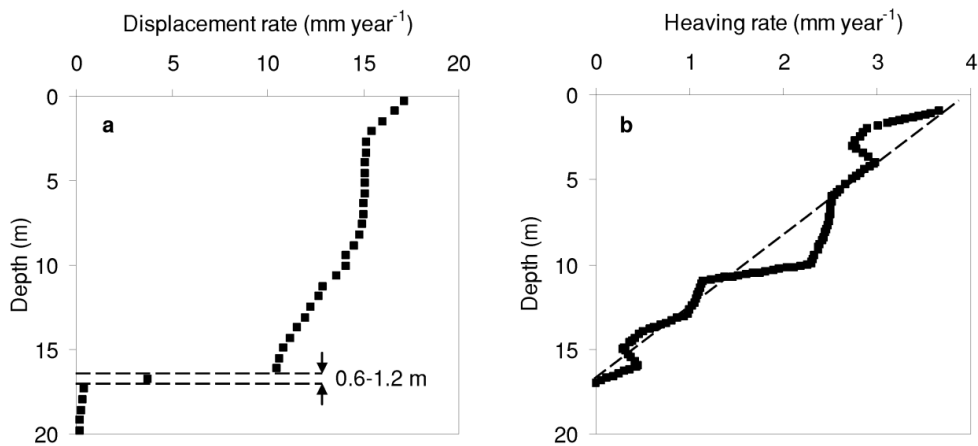
Figure 9-3: *Average (a) displacement and (b) heaving rates measured in 2006-2010 in the vicinity of the Leaning Tower (38.5 m away from the rock outcrop at Via Maistra) using inclinometer and Inkrex technology, respectively.*

In the lower 600-700 m of the landslide, the average displacement rates (measured in 2006-2010 close to the latitudinal center of the landslide) increase uphill from the rock outcrop (Figure 9-4) and can reach up to 0.5 m/yr. Further landslide acceleration may, therefore, have potentially devastating consequences, in particular for sensitive structures, such as the 12th century Leaning Tower of St. Moritz (Figure 9-1a), located close to the compression zone of the landslide. The Tower was stabilized in 1986 (before the landslide acceleration) and its inclination was partially corrected by lifting it with hydraulic jacks and placing on a new foundation on three Teflon bearing pads (Sterba *et al.* 2000). Additional correction took place in 2005 (Alonso *et al.* 2010).
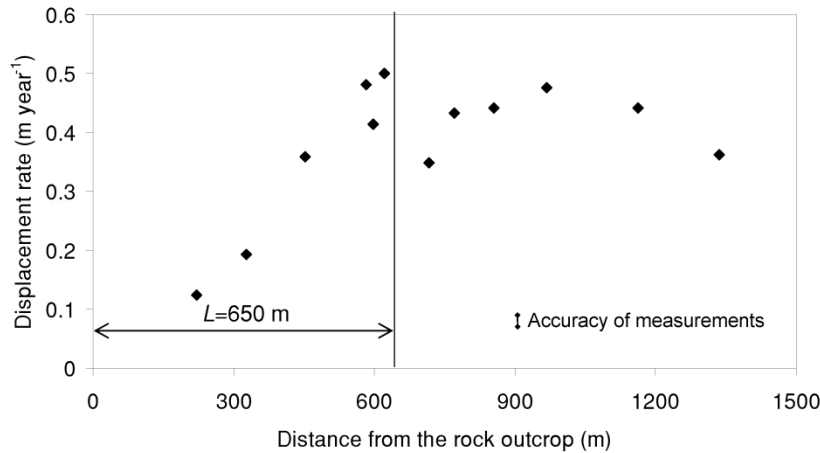
Figure 9-4: *Average displacement rates in 2006-2010 above the constructed area. Displacements were measured using GPS device with the accuracy of 0.02 m.*

The "usual suspect" for the creeping landslide acceleration is an increase in precipitation (e.g., Iverson *et al.* 2000). Indeed, the landslide displacements exhibit sensitivity to precipitation rate changes (e.g., in 2001-2006, when deviation of the precipitation rates from the average value is observed in Figure 9-2). Around the onset of acceleration, however, no precipitation increase could be observed (Figure 9-2), which was also confirmed by fairly constant groundwater table (Figure 9-5), measured using a piezometer pipe installed in a borehole about 37 m above the rock outcrop at the depth of 14 m. No rising in the groundwater table has been observed around the onset of acceleration in 1991. On the contrary, the groundwater table around 1991 seems to drop below the average level (with the average depth of 9.92m), which appears to be the same both in the period of 1984-1996 (around the onset of acceleration) and during the entire measurement period of 1978-2010.
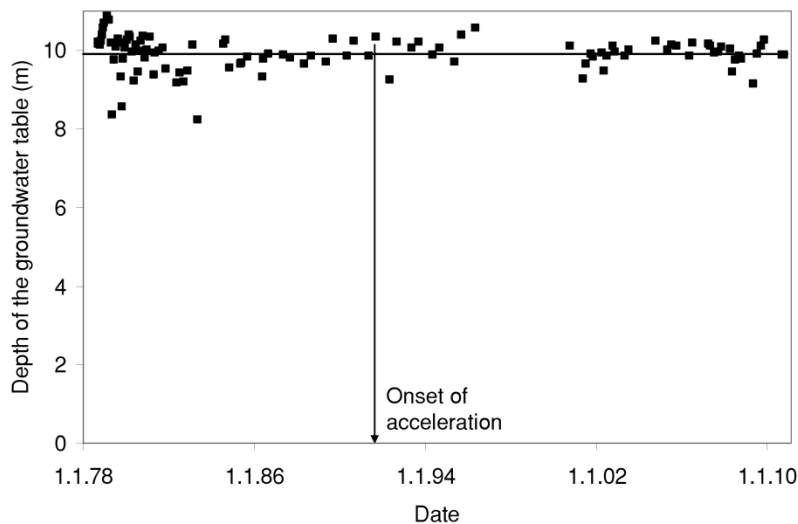
Figure 9-5: *Depth of the groundwater level in 1978-2010. Measured with the accuracy of 0.01 m.*

A more likely reason for the landslide acceleration is the passive failure of soil at the bottom of the landslide, in the zone characterized by high compression strain rates (Figure 9-6), measured by Tschudi and Angst (1999) within the constructed area in the lower 200 m of the landslide in 1988-1998, close to the latitudinal center of the landslide. Location of the boundary of the compression zone can be estimated at $l \approx 21$ m , below which the highest compression strain rates were observed.
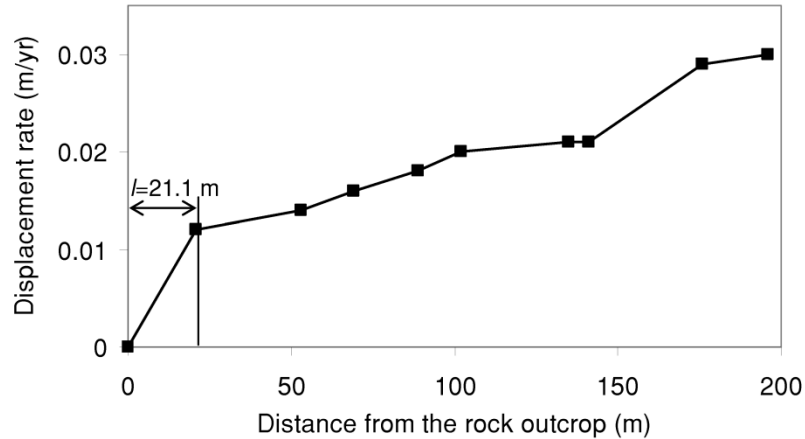
Figure 9-6: Average displacement rates within the constructed area in the lower 200 m of the landslide in 1988-1998. Displacements were measured using geodetic triangulation with the accuracy of 0.002 m.

It remains, however, to be explained how the earth pressure could (a) reach the high level of passive pressure when the landslide was slowing down, and (b) keep increasing even after the failure. In fact, a small but steady pressure increase of about 0.8-1.0 kPa/yr has been measured in the compression zone in 2008-2010 using a novel inclinodeformeter (Schwager *et al.* 2009). While the rate dependency of the residual shear strength on the sliding surface (2% per log cycle of the shear strain rate measured in ring shear tests, Figure 9-7) could, in principle, explain some pressure increase during stabilization (Puzrin & Sterba 2006, Alonso *et al.* 2010), it is not sufficient for the passive pressure to develop. Moreover, when landslide accelerates, this rate dependency should lead to the pressure decrease, contrary to the observations.
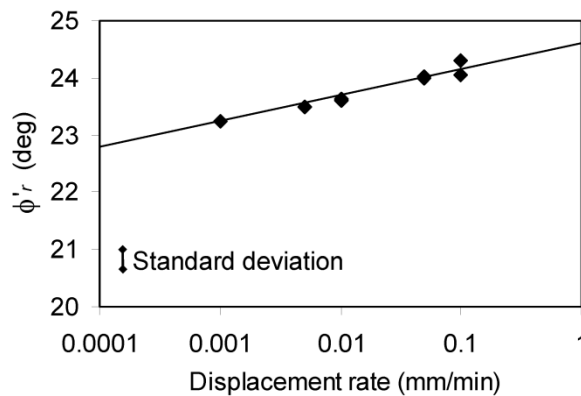
Figure 9-7: Rate dependency of the residual shear strength on the slip surface measured in a ring shear device.

Inability to explain the St Moritz landslide evolution using conventional approaches became the main motivation behind the field and laboratory testing program carried out in 2006-2010 at the ETH Zurich. This experimental study was combined with basic analytical modeling of the data from many decades of the St Moritz-Brattas landslide monitoring in an effort to provide a mechanism explaining both the stabilization and acceleration phases of the constrained creeping landslide evolution.

9.3   The mechanism

Such a mechanism is indeed available and is based on the phenomenon of the progressive propagation of a zone of intense shearing, which causes earth pressure increase in the compression zone of the landslide, followed by visco-plastic yielding of soil in this

zone (Figure 9-8). Strain localization and propagation of shear bands (few millimeter thick zones of intense shearing, where shear strength decreases to residual value) take place in soils exhibiting strain softening (Palmer & Rice 1973, Vardoulakis *et al.* 1981, Saada *et al.* 1994, Puzrin & Germanovich 2005, Saurer & Puzrin 2010). In a strain softening material (Figure 9-9), shear strength $\tau*$ on the slip surface drops from the peak τ_p to residual value τ_r when the shear strain γ in the shear band reaches the critical value of γ_r .

Progressive shear band propagation has been shown to cause delayed failure of slopes cut in overconsolidated clays (Skempton 1964, Skempton & LaRochelle 1965, Bjerrum 1967). Catastrophic shear band propagation has helped to explain the mechanisms of gigantic tsunamigenic landslides (Nisbet & Piper 1998, Puzrin *et al.* 2004, 2010). Fewer attempts have been made, however, to investigate this mechanism in relation to creeping landslides, in particular to those constrained by natural or artificial obstacles (Bernander & Olofsson 1981, Wiberg *et al.* 1990).
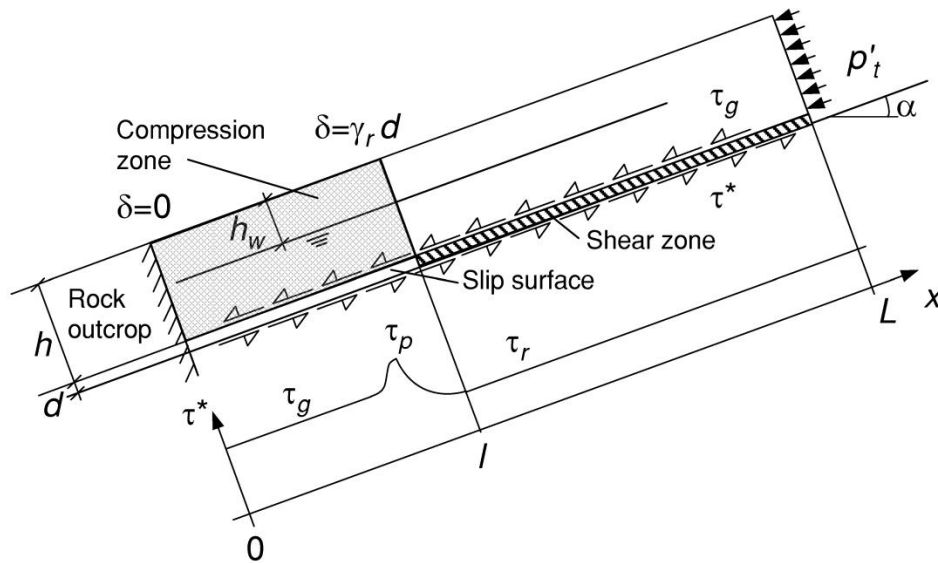
Figure 9-8: *Conceptual model of the shear band propagation*

Furthermore, the zone of intense shearing, propagating along the slip surface in the lower part of the St. Moritz landslide, is not necessarily a thin classical shear band. The slip surface is confined there to a weaker, about 20 cm thick silty clay layer with gravel and organic inclusions located at the depth 17 – 23 m according to inclinometer measurements and core drilling. The thickness of this layer may not be sufficient for a single continuous thin shear band to propagate in it (Palmer & Rice 1973), as indirectly confirmed by the lack of slickenside surfaces in the core samples. Therefore, the shear deformation is likely to involve the entire clayey layer, either being smeared over its thickness $d \approx 20 \text{ cm}$ or localized in a number of parallel discontinuous thin shear bands, as can be also concluded from a relatively broad inclinometer trace of the band (Figure 9-3a). In any case, this shear zone retains the important property of the shear band: shear strength $\tau*$ in it reduces to residual value τ_r when the shear strain there reaches the critical value of γ_r (Figure 9-9).
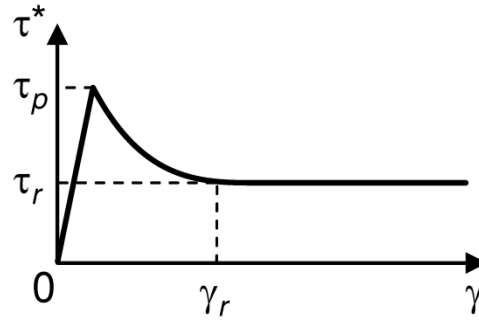
Figure 9-9: *Shear behaviour of a strain softening material.*
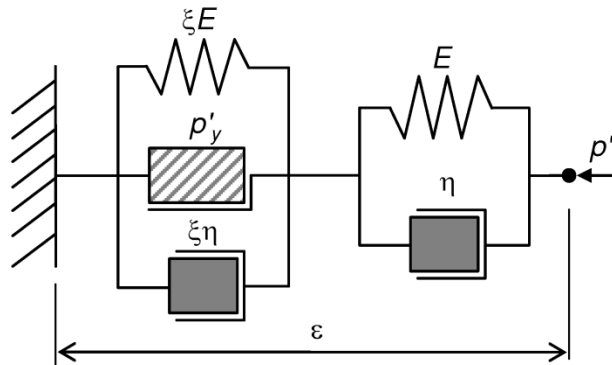
Figure 9-10: *Visco-elastic-plastic model of the soil in the compression zone.*

9.4   Assumptions

A simple conceptual model of the St Moritz landslide is shown in Figure 9-8. The sliding layer of the thickness h, with the depth of phreatic surface h_w and thickness of the sliding surface d, is subjected to the uniform effective pressure p_t' acting at its uphill boundary, and has zero displacement δ on the downhill boundary. Where the landslide displacement has exceeded the value of $\delta_r = \gamma_r d$, the shear resistance $\tau*$ along the sliding surface has dropped down to the residual shear strength τ_r indicating formation of the shear zone. Beyond the tip of the shear zone there is a process zone, where the shear resistance grows to the peak value τ_p and then decreases to the gravitational shear stress τ_g in the compression zone. Rate dependency of the residual shear strength has been neglected.

In contrast, the soil in the sliding layer has elasto-visco-plastic properties (Figure 9-10). Pre-yielding compression in soil is visco-elastic, characterized by the first Kelvin element in the series, with Young's modulus E and viscosity η . When the pressure reaches the yield stress p_y' , the second Kelvin element with Young's modulus ξE and viscosity $\xi \eta$ is mobilized, causing reduction in equivalent stiffness and viscosity during yielding. In general, different yielding factors ξ could be applied to elastic and viscous parameters, though adopting them equal simplifies the model considerably.

Creeping and yielding of the soil in the compression zone causes the tip of the shear zone, where shear strain has reached γ_r and the shear resistance fell to its residual value τ_r (Figure 9-9), to move down along the slip surface. This leads to the progressive propagation of the shear zone and the drop of the shear strength along the slip surface, which has to be compensated by increase of the effective earth pressure in the compres-

sion zone. After this pressure reaches the yield stress p'_y (Figure 9-10), the elastic and viscous resistances decrease significantly, causing increase in the landslide displacement rates. They do not, however, vanish entirely (as would happen at the classical perfectly plastic failure), allowing for continuing earth pressure increase in the compression zone.

9.5 Analytical model

The above assumptions lead to the following simplified analytical model allowing for the proposed mechanism to be quantified and validated against the monitoring and test data. Combination of equilibrium and geometric equations with constitutive relationships within the compression zone produces a differential equation, which can be resolved in a closed form.

(a) Equilibrium Equation

Equilibrium equation for the sliding layer in Figure 9-8 is in general given by:

$$h \frac{dp}{dx} = \tau_g - \tau^* , \tag{9-1}$$

$$\tau_g = \gamma_t h \sin \alpha , \tag{9-2}$$

where p is the total uniform normal earth pressure in the direction of sliding;

   τ^* is the shear resistance along the slip surface;

   τ_g is the gravitational shear stress;

   γ_t is the total unit weight of soil in the sliding layer;

   h is the thickness of the sliding layer;

   α is the inclination of the slope and the slip surface.

In the compression zone $0 \le x \le l(t)$, however, we assume $\tau^* = \tau_g$, so that the earth pressure does not vary along the zone $p(x,t) = p(t)$ and its evolution in time is defined by the equilibrium of the sliding layer above the compression zone:

$$p(t) = p_t + \frac{\tau_g - \tau_r}{h} (L - l(t)) , \tag{9-3}$$

$$\tau_r = (\gamma_t h - \gamma_w (h - h_w)) \cos \alpha \tan \varphi'_r , \tag{9-4}$$

Where p_t is the uniform total pressure acting at the uphill boundary of the sliding layer;

   τ_r is the residual shear strength along the slip surface (Figure 9-9);

   L is the length of the sliding layer;

   l is the length of the compression zone;

γ_w is the total unit weight of water;

h_w is the depth of the phreatic surface;

φ'_r is the residual angle of internal friction on the slip surface.

The above assumption neglects the 'process zone', where the shear resistance along the slip surface drops from its peak value τ_p to the residual value τ_r (Figure 9-8). In reality, depending on the value of γ_r, this zone could appear to be of a non-negligible length within the scale of the problem. Considering, however, the general indeterminacy with respect to the shear resistance along the slip surface in the compression zone, and the fact that it is going to be partially smaller than τ_g and partially larger, it seems reasonable to average the resistance as $\tau^* = \tau_g$. Validity of this assumption will be assessed later as a part of the overall ability of the model to simulate landslide displacements and pressures.

Water flow in an infinite slope produces identical pore water pressure profiles along the slope, so that $p = p'+u$ and $p_t = p'_t+u$, and the equilibrium equation (9-3) can be rewritten in effective stresses:

$$p'(t) = p'_t + \frac{\tau_g - \tau_r}{h}(L - l(t)) .$$ (9-5)

It follows, that the earth pressure in the compression zone increases in time proportionally to the decrease in the compression zone length.

(b) Constitutive Relationship

The elasto-visco-plastic behaviour (Figure 9-10) of the soil in the sliding layer is different for pre-yielding and yielding phases. Pre-yielding compression in soil is visco-elastic, characterized by the first Kelvin element in the series is given by:

$$p' = E\varepsilon + \eta\dot{\varepsilon} , \quad \text{for} \quad p' < p'_y ,$$ (9-6)

where ε is the total strain in the model;

E is Young's modulus of the soil;

η is the viscosity of the soil;

p'_y is the yield stress.

When the pressure reaches the yield stress p'_y, the second Kelvin element is mobilized. Since the two Kelvin elements work in series, the stresses in both elements are equal to the total stress p':

$$p' = E\varepsilon_1 + \eta\dot{\varepsilon}_1 ; \quad p' = \xi E\varepsilon_2 + \xi\eta\dot{\varepsilon}_2 + p'_y ,$$ (9-7)

while the strains are different and have to be summed up to define the total strain and its rate:

$$\varepsilon_1 + \varepsilon_2 = \varepsilon ; \quad \dot{\varepsilon}_1 + \dot{\varepsilon}_2 = \dot{\varepsilon} ,$$ (9-8)

where ξ is the yielding factor. Multiplying the first equation (9-7) by this yielding factor ξ, summing it up with the second equation (9-7) and substituting equations (9-8) into them, gives the following constitutive relationship for the yielding phase:

$$p' = \frac{\xi}{1+\xi} E\varepsilon + \frac{\xi}{1+\xi} \eta \dot{\varepsilon} + \frac{p'_y}{1+\xi} , \quad \text{for } p' \geq p'_y .$$

(9-9)

In general, different yielding factors ξ could be applied to elastic and viscous parameters. This, however, would lead to a more complex, second order differential constitutive relationship (9-9). Adopting the yielding factors equal simplifies the model considerably and leads to a closed form solution, while still allowing for a broad class of material behaviour to be described within a thermomechanically consistent framework (Houlsby & Puzrin 2002; Puzrin & Rabaiotti 2010).

For a limiting case of $\xi \to \infty$, the second Kelvin element becomes rigid and equation (9-9) degenerates into equation (9-6) describing the pre-yielding behaviour.

(c) Geometric Expressions in the Compression Zone

The strain in the sliding layer in the direction of sliding is given by:

$$\varepsilon = \frac{d\delta}{dx}$$

(9-10)

where $\delta(x,t)$ is the displacement of the sliding layer in the direction of the slope. From the equilibrium equation (9-5) it follows that the effective earth pressure does not vary along the compression zone $p'(x,t) = p'(t)$. Therefore, from the constitutive equations (9-6) and (9-9), it can be concluded that the strain is also constant. In this case, equation (9-10) can be rewritten as

$$\varepsilon = \frac{\delta(x = l(t))}{l(t)}$$

(9-11)

Because the boundary of the compression zone is defined at the tip of the shear band, the relative displacement there is always the same and equal

$$\delta(l(t)) = \delta_r = \gamma_r d ,$$

(9-12)

at which the shear strain in the slip surface reaches the critical value of γ_r and the shear resistance drops to its residual value τ_r (Figure 9-8). Substitution of the equation (9-12) into (9-11) gives

$$\varepsilon(t) = \frac{\delta_r}{l(t)} ; \qquad l(t) = \frac{\delta_r}{\varepsilon(t)}$$

(9-13)

It follows that the strain in the compression zone is inversely proportional to the length of the compression zone.

(d) Differential equation

Differential equation for the strain ε in the compression zone during yielding is obtained by combining the equilibrium equation for the sliding layer (9-5) with the constitutive rela-

tionship (9-9) and the geometric expression for the length of the compression zone (9-13):

$$\dot{\varepsilon} + a\varepsilon = b - \frac{c}{\varepsilon} ,\qquad(9\text{-}14)$$

where

$$a = \frac{E}{\eta} ; \quad b = \frac{1+\xi}{\xi\eta}\left(p'_t + \frac{\tau_g - \tau_r}{h}L - \frac{p'_y}{1+\xi} \right); \quad c = \frac{1+\xi}{\xi\eta}\frac{\tau_g - \tau_r}{h}\gamma_r d ,\qquad(9\text{-}15)$$

Equation for the pre-yielding phase is also given by equation (9-14) with parameters obtained from equations (9-15) by setting $\xi = \infty$:

$$a = \frac{E}{\eta} ; \quad b = \frac{1}{\eta}\left(p'_t + \frac{\tau_g - \tau_r}{h}L \right); \quad c = \frac{1}{\eta}\frac{\tau_g - \tau_r}{h}\gamma_r d ,\qquad(9\text{-}16)$$

(e) Solution

For the yielding phase, a closed form solution can be obtained in parametric representation via a free parameter *y*:

$$\frac{\dot{\varepsilon}}{\dot{\varepsilon}_y} = \frac{1+y_y}{1+y}\frac{y^2 - \lambda^2}{y_y^2 - \lambda^2} \qquad t - t_y = -\frac{1}{2a}\left[\ln\frac{y^2 - \lambda^2}{y_y^2 - \lambda^2} + \frac{1}{\lambda}\ln\left[\frac{y - \lambda}{y_y - \lambda}\frac{y_y + \lambda}{y + \lambda} \right] \right]\qquad(9\text{-}17)$$

where

$$y \geq y_y = \frac{2a}{b}\varepsilon_y - 1 ; \quad \lambda = \sqrt{1 - \frac{4ac}{b^2}} ; \quad b^2 > 4ac ; \quad \varepsilon_y = \frac{\gamma_r d}{l_y} ,\qquad(9\text{-}18)$$

with l_y , ε_y and $\dot{\varepsilon}_y$ being the length of the compression zone, the strain and the strain rate in it at the onset of yielding t_y , respectively. For certain combinations of parameters, equation (9-17) describes initial acceleration of the landslide, followed by further stabilization.

When the compression zone becomes short ($l \ll L$), equation (9-14) has an asymptotic solution. For the pre-yielding phase, this solution describes the landslide stabilization:

$$\frac{\dot{\varepsilon}}{\dot{\varepsilon}_y} = e^{-a(t-t_y)} ,\qquad(9\text{-}19)$$

where $\dot{\varepsilon}_y$ is the strain rate in the compression zone at the onset of yielding t_y . If the yield stress p'_y is not reached, the strain in the compression zone will asymptotically approach a finite value, resulting, from equation (9-13) in a finite value of the length of the compression zone. That is, propagation of the shear zone along the slip surface will asymptotically come to a halt and the landslide will become stable.

9.6   Determination of the model parameters

The landslide length, $L \approx 650 \text{ m}$, was defined from geodetic measurements performed in 2006-2010 (Figure 9-4). Indeed, in the lower 600-700 m of the landslide, displacement rates increase uphill, while in the upper part no significant uphill increase of displacements can be observed. Location of the boundary between the two parts of the landslide can be estimated at about $L \approx 650 \text{ m}$, where displacement rates below are higher than those above. This indicates that the two parts of the slide are moving apart relative to each other, as can be confirmed by the observed tension cracks and some geological evidence of a rock outcrop in this area. As a consequence, the earth pressure p_t' could be assumed equal to the average active failure pressure $p_a' = 94 \text{ kPa}$, calculated after Chu (1991) using the peak angle of internal friction, $\varphi_p' = 33.7°$, estimated in the sliding layer from the Marchetti dilatometer tests (Figure 9-11a) with standard deviation $2.0°$. The average passive pressure is also calculated using the same peak angle of internal friction as $p_p' = 558 \text{ kPa}$ (Chu 1991). For these calculations, the total unit weight was taken $\gamma = 20 \text{ kN}/\text{m}^3$; the average depth of the sliding surface, $h = 20 \text{ m}$, was defined from the inclinometer measurements; and the average slope inclination was adopted as $\alpha = 20°$; unit weight of ground water is $\gamma_w = 9.81 \text{ kN}/\text{m}^3$, and the depth of phreatic surface, $h_w = 9.92 \text{ m} \cdot \cos 20° \approx 9.4 \text{ m}$, was determined from the ground water table depth measurements (Figure 9-5) with standard deviation 0.4 m.

The length of the compression zone at the onset of yielding in 1991, $l_y = 21 \text{ m}$, was estimated from geodetical measurements carried out by Tschudi and Angst (1999) in 1988-1998 (Figure 9-6). Within this zone, high compression and heaving rates of the ground and structures can be observed, significantly larger than those measured outside of the compression zone in Figures 9-6 and 9-3b, respectively.
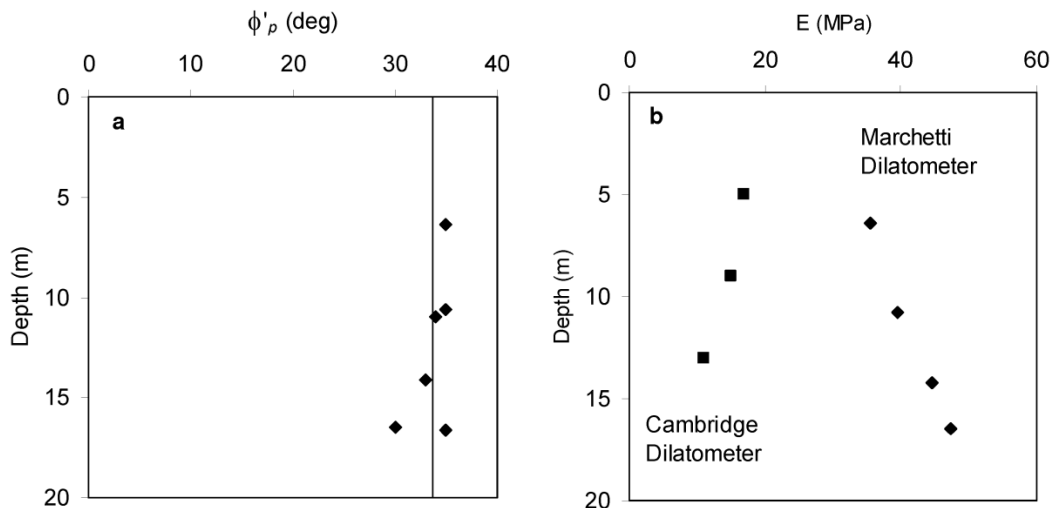
Figure 9-11: *Results of dilatometer tests performed in 2006 in the vicinity of the Leaning Tower (38.5 m away from the rock outcrop): (a) peak angle of internal friction from Marchetti dilatometer tests; (b) Young's modulus range.*

The gravitational shear stress, $\tau_g = 137 \text{ kPa}$, was calculated using equation (9-2) with $\gamma = 20 \text{ kN}/\text{m}^3$, $h = 20 \text{ m}$ and $\alpha = 20°$. The residual angle of internal friction on the slip surface, $\varphi_r' = 23.7°$, with rate dependency of $0.4° - 0.5°$ per log cycle of shear strain and standard deviation $0.4°$, was determined (Figure 9-7) using the ring shear apparatus at

loads 100-200 kPa, bounding the pressure range at the sliding surface. The residual shear strength $\tau_r = 122$ kPa was then calculated using equation (9-4) with $\gamma_w = 9.81$ kN$/$m^3 , and $h_w = 9.4$ m .

The Young modulus, $E = 10 - 50$ MPa , was determined using in situ Cambridge and Marcchetti dilatometer tests (Figure 9-11b, Puzrin *et al.* 2008). The relatively broad range of obtained moduli values is due to the fact that Marchetti and Cambridge tests provide lower and upper limits for the stiffness, respectively.

The yearly increase in earth pressure in the compression zone of 0.8-1.0 kPa was back-calculated from the changes in the dimensions of inclinometer pipes measured in 2008-2010 using the novel inclinodeformeter (Schwager *et al.* 2009).

All the above physical and geometric parameters are summarised in Table 9-1.

Table 9-1: Summary of the physical and geometric parameters.

Parameter description	Parameter value	Derivation
Landslide length	$L \approx 650$ m	Measured (field)
Average depth of the sliding surface	$h = 20$ m	Measured (field)
Depth of the phreatic surface	$h_w = 9.4$ m	Measured (field)
Thickness of the slip surface	$d = 0.2$ m	Measured (field)
Average slope inclination	$\alpha = 20°$	Measured (field)
Total unit weight of soil	$\gamma = 20$ kN$/$m^3	Measured (lab)
Unit weight of ground water	$\gamma_w = 9.81$ kN$/$m^3	Measured (lab)
Length of the compression zone at the onset of yielding	$l_y = 21$ m	Measured (field)
The date of the onset of yielding	t_y = 4.9.1991	Measured (field)
Strain rate at the onset of yielding	$\dot{\varepsilon}_y = 2.86 \times 10^{-4}$ / yr	Measured (field)
Peak angle of internal friction in the sliding layer	$\varphi'_p = 33.7°$	Measured (lab)
Residual angle of internal friction on the slip surface	$\varphi'_r = 23.7°$	Measured (lab)
Young modulus	$E = 10 - 50$ MPa	Measured (field)
Yearly increase in earth pressure in the compression zone	$\dot{p}' \approx 0.8 - 1.0$ kPa$/$yr	Measured (field)
Average active failure pressure	$p'_a = 94$ kPa	Calculated
Average passive pressure	$p'_p = 558$ kPa	Calculated
Gravitational shear stress	$\tau_g = 137$ kPa	Calculated
Residual shear strength	$\tau_r = 122$ kPa	Calculated
Pressure at the top of the sliding layer	$p'_t = p'_a = 94$ kPa	Calculated

9.7   Model calibration and validation

In general, for large-scale time-dependent geotechnical problems, reliable determination of some material parameters is not possible from laboratory and field tests due to limitations of the available experimental techniques (Van Asch *et al.* 2007). This problem can be solved with the help of inverse analysis, which utilizes, as an input, displacement monitoring data together with more reliable model parameters, in order to back-calculate the remaining parameters and use them in the model predictions (Tacher *et al.* 2005, Puzrin & Sterba, 2006, François *et al.* 2007).

Applying this methodology to the St Moritz landslide, after estimating the date of the onset of yielding (around t_y = 4 September 1991) and the corresponding strain rate ($\dot{\varepsilon}_y = 2.86 \times 10^{-4}$ /yr) from Figure 9-2, we observe that equation (9-19) provides a good fit (Figure 9-12) to the stabilization branch of time-displacement curve using just one parameter: $a = 0.08$ 1/yr . Subsequently, equation (9-17) gives a reasonable fit to the acceleration branch of the curve using two additional parameters: $y_y = -0.34$ and $\lambda = 0.37$. (The deviation of the predicted curve in Figure 9-12 from displacement data measured in 2001-2006 correlates temporally with the fluctuations in the rate of precipitation.) This fitting allows for back-calculation of the model parameters E , p'_y , and ξ by substituting a, y_y and λ into equations (9-6), (9-16) and (9-18) together with parameters γ_r , l_y , **L,** h , d, τ_g , τ_r and p'_t estimated above.
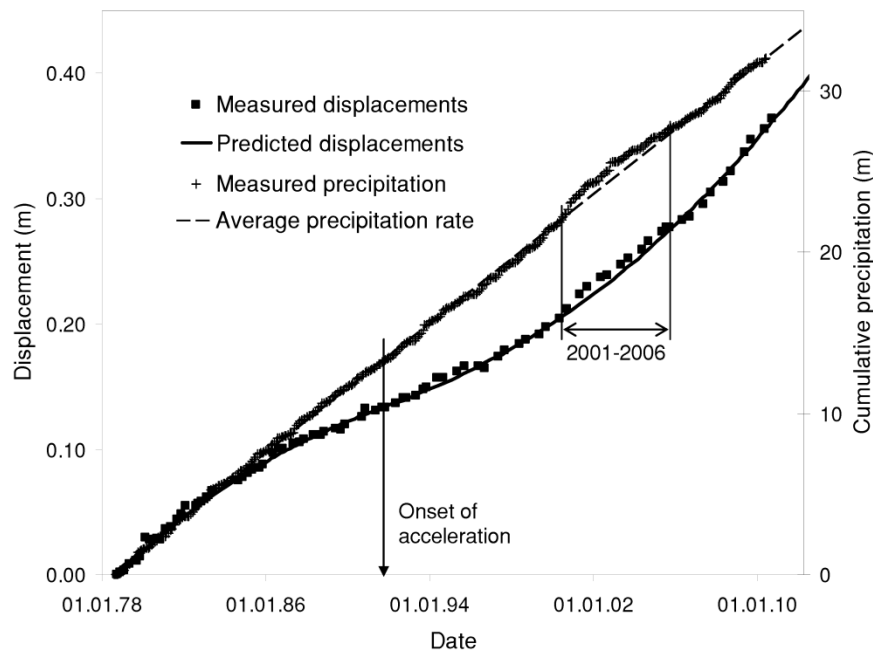
Figure 9-12: *Predicted landslide displacements in 1978-2010.*

The resulting back-calculated parameters happen to satisfy some important constraints and provide an insight into the mechanism of the St Moritz landslide. For a very broad range of the critical shear strains $\gamma_r = 100 - 1000$ % , corresponding to realistic strains at the onset of yielding of about $\varepsilon_y = 1 - 10$ % , the back-calculated yield stress falls within a remarkably narrow range $p'_y = E\left(\varepsilon_y + \dot{\varepsilon}_y / a\right) = 557 - 559$ kPa , very close to the estimated (passive) failure pressure $p'_p = 558$ kPa , justifying the significant drop in stiffness and viscous resistance described by the similarly narrow range of the back-calculated yielding parameter $\xi = 0.0147 - 0.0193$. This remaining resistance is, however, essential for explaining relatively moderate landslide accelerations and positive pressure increments in

the compression zone. Indeed, the predicted pressure increase rates for the years 2008-2010:

$$\dot{p}' = \frac{E\xi}{1+\xi}\left(\dot{\varepsilon} + \frac{\ddot{\varepsilon}}{a}\right) \approx 0.11 - 1.1 \text{ kPa}/\text{yr} ,$$ (9-20)

compare well with the observed values of 0.8-1.0 kPa/yr . Finally, the range of the back-calculated Young's moduli, while being rather broad: $E = 5.4 - 41.2 \text{ MPa}$, also overlaps with the $10 - 50 \text{ MPa}$ (Figure 9-11b) obtained from the field tests.

 All the above model parameters and their validation are summarised in Table 9-2. In the above analysis, the fact has been neglected that the boundary of the compression zone, which was at the onset of yielding in 1991 was at $l_y = 21 \text{ m}$, has been moving downhill ever since. For the yielding phase, displacements for $x = 21 \text{ m}$ point in Figure 9-12 were calculated taking the strains in the (shrinking) compression zone and assuming they also occur in the zone between the current tip of the compression zone and the fixed position at $x = 21 \text{ m}$. This is a slight approximation (since *p'* varies in the region above the compression zone), but is within the level of accuracy required, because all the soil below $x = 21 \text{ m}$ has reached the yield stress p'_y at the onset of yielding, and no significant pressure changes beyond this value are expected during the further landslide evolution.

Table 9-2: *Summary of the physical and geometric parameters.*

Parameter description	Parameter value	Derivation
Model parameter	$a = 0.08 \ 1/\text{yr}$	Curve fitted (pre-yielding)
Model parameter	$y_y = -0.34$	Curve fitted (post-yielding)
Model parameter	$\lambda = 0.37$	Curve fitted (post-yielding)
Critical shear strains	$\gamma_r = 100 - 1000 \ \%$	Assumed range
Strains in the compression zone at the onset of yielding	$\varepsilon_y = 1 - 10 \ \%$	Back-calculated range
Yielding parameter	$\xi = 0.0147 - 0.0193$	Back-calculated range
Yield stress	$p'_y = 557 - 559 \ \text{kPa}$	Back-calculated range
	$p'_y = p'_p = 558 \ \text{kPa}$	Calculated (from measured)
Young modulus	$E = 5.4 - 41.2 \ \text{MPa}$	Back-calculated range
	$E = 10 - 50 \ \text{MPa}$	Measured range (field)
Yearly increase in earth pressure in the compression zone	$\dot{p}' \approx 0.11 - 1.1 \ \text{kPa}/\text{yr}$	Back-calculated range
	$\dot{p}' \approx 0.8 - 1.0 \ \text{kPa}/\text{yr}$	Measured range (field)

9.8   Discussion and concluding remarks

The mechanism of the progressive propagation of the zone of intense shearing and subsequent yielding of soil in the compression zone seems to be capable of explaining the "paradox" of the St Moritz landslide acceleration in spite of the absence of the "usual suspects": increase in the yearly precipitation and pore water pressure, as well as rate dependency on the sliding surface. As a result this mechanism allows for improved assessment of its hazard and suggests measures for its mitigation. The model predicts that the acceleration phase could continue until about 2025 and may cause additional 30% in-

crease in the current displacement rates. After that the slow stabilization of the landslide could be expected, provided no increase in the yearly precipitation and pore water pressure (Figures 9-2 and 9-5) and no drop in the yielding factor ξ (Figure 9-10) take place.

Even for this favorable scenario, however, the final displacements can become excessive for some buildings, requiring an early warning system, which is currently being installed in the Leaning Tower and within the inclinometer pipes directly in the landslide body. Further stabilization of the Leaning Tower is likely to be necessary within the next 10 years. The displacement rates, however, can only be controlled by lowering the phreatic surface with the help of a drainage system. As suggested by the proposed mechanism, however, such a system would be more effective if it had been constructed in 1980's, i.e. before the earth pressure in the compression zone reached the yield stress. Thus, by predicting the time of the onset of yielding, the model can provide important timeframe for stabilization of constrained landslides.

Acknowledgements

References

Alonso, E.E., Pinyol, N. and Puzrin, A.M. (2010), "Geomechanics of Failures. Advanced Topics", Springer, Dordrecht, 277p.

Bernander, S, & Olofsson I. (1981). On formation of progressive failures in slopes. *Proc. 10th ICSMFE* 3, 357-362.

Bjerrum, L. (1967). Progressive failure in slopes of overconsolidated plastic clay and clay shells. *J. Soil Mech. Found. Engng Div., ASCE* 93, 1-49.

Chandler, R. J. & Pook, M. J. (1971). Creep movements in gradient clay slopes since the late glacial. *Nature* 229, 399-400, doi:10.1038/229399a0.

Chu, S. (1991). Rankine analysis of active and passive pressures in dry sands. *Soils Found.* 31, 115–120.

François, B., Tacher, L., Bonnard, Ch., Laloui, L. & Triguero, V. (2007). Numerical modelling of the hydrogeological and geomechanical behaviour of large slope movement: Triesenberg landslide (Lichtenstein). *Can. Geotech. J.* 44, 840-857, doi:10.1139/T07-028.

Glastonbury, J. & Fell, R. (2008). Geotechnical characteristics of large slow, very slow and extremely slow landslides. *Can. Geotech. J.* 45, 984-1005, doi:10.1139/T08/-021.

Houlsby, G.T. & Puzrin, A.M. (2002). Rate-dependent plasticity models derived from potential functions. *J. Rheology* 46, 113-126, doi:10.1016/S0749-6419(99)00073-X.

Iverson, R.M. et al. (2000). Acute sensitivity of landslide rates to initial soil porosity. *Science* 290, 513-516, doi:10.1126/science.290.5491.513.

Müller, E.R. & Messina, G. (1992) Geotechnisches Gutachten, Bericht Nr. 2570-1, Rutschhang Sass Runzöl-Brattas, St. Moritz. Büchi und Müller AG, Chur (unpublished).

Nisbet, E. G. & Piper, D.J.W. (1998). Giant submarine landslides. *Nature* 392, 329-331, doi:10.1038/32765.

Palmer, A. C. & Rice, J. R. (1973). The growth of slip surfaces in the progressive failure of over-consolidated clay. *Proc. Roy. Soc. Lon. A* 332, 527-548, http://www.jstor.org/stable/78279.

Puzrin, A.M. & Germanovich, L.N. (2005). The growth of shear bands in the catastrophic failure of soils. *Proc. Roy. Soc. Lon. A* 461, 1199-1228, doi:10.1098/rspa.2004.1378.

Puzrin, A.M. & Rabaiotti, C. (2010). A thermomechanical framework for non-linear hyper-viscoelastic materials. *J. Rheol.* 54, 619-642, doi:10.1122/1.3378879.

Puzrin, A.M. & Schmid, A. (2007). TRIVEC measurements in the inverse analysis of the long-term stability of a constrained landslide. *Field Measurements in Geomechanics, ASCE GSP* 175, doi:10.1061/40940(307)97.

Puzrin, A.M. & Sterba, I. (2006). Inverse long-term stability analysis of a constrained landslide. *Géotechnique* 56, 483-489, doi:10.1680/geot.2006.56.7.483.

Puzrin, A.M., Germanovich L.N. & Kim, S. (2004). Catastrophic failure of submerged slopes in normally consolidated sediments. *Géotechnique* 54, 631-643, doi:10.1680/geot.2004.54.10.631.

Puzrin A.M., Messerklinger, S. & Schmid, A. (2008). The in-situ stiffness of the sliding layer in a creeping landslide. *Proc. 4th Int. Symposium on Deformation Characteristics of Geomaterials* 1, 407-412.

Puzrin, A.M., Saurer, E. & Germanovich, L.N. (2010). A dynamic solution of the shear band propagation in submerged landslides. *Granular Matter* 12, 253-265, doi:10.1007/s10035-010-0177-8.

Saada, A.S., Bianchini, G.F. & Liqun, L. (1994). Cracks, bifurcation and shear bands propagation in saturated clays. *Géotechnique* 44, 35-64, doi:10.1680/geot.1994.44.1.35.

Saurer, E. & Puzrin, A.M. (2011). Validation of the energy-balance approach to curve-shaped shear-band propagation in soil. *Proc. Roy. Soc. Lon. A*, doi:10.1098/rspa.2010.0285.

Schluechter, Ch. (1988). Instabilities in the area of St. Moritz, Switzerland: geology, chronology, geotechnology. *Proc. 5th Int. Symposium on Landslides* 1, 1375–1380.

Schulz, W.H., Kean, J.W. & Wang, G. (2009). Landslide movement in southwest Colorado triggered by atmospheric tides. *Nature Geoscience* 2, 863-866, doi:10.1038/ngeo659.

Schwager, M.V., Schmid, A. & Puzrin, A.M. (2009). Inclinodeformometer: A novel device for measuring earth pressure in creeping landslides. *Proc. Prediction and Simulation Methods for Geohazard Mitigation* 1, 479-484, doi:10.1201/NOE0415804820.ch71.

Skempton, A.W. (1964). Long-term stability of clay slopes. *Géotechnique* 14, 77-102, doi:10.1680/geot.1964.14.2.77.

Skempton, A.W. & LaRochelle, P. (1965). The Bradwell slip: a short-term failure in London clay. *Géotechnique* 15, 221-242, doi:10.1680/geot.1965.15.3.221.

Sterba, I., Lang, H.-J. & Amann, P. (2000). The Brattas landslide in St. Moritz. *Proc. GeoEng* 2, 144-149.

Tacher, L., Bonnard, Ch., Laloui, L. & Parriaux A. (2005). Modelling the behaviour of a large landslide with respect to hydrogeological and geomechanical parameter heterogeneity. *Landslides* 2, 3-14, doi:10.1007/s10346-004-0038-9.

Terzaghi, K. (1950). Mechanism of landslides. *Geol. Soc. Am., Engng. Geol., Berkley Vol.,* 83-123.

Tschudi, D. & Angst, R. (1999). Diplomvermessungskurs Samedan 1998, Rutschhang Brattas, St. Moritz. *Bericht 283, Institut für Geodäsie und Photogrammetrie, ETH Zürich*, Februar 1999, 31 p.

Van Asch, Th.W.J., Van Beck, L.P.H. & Bogaard, T.A. (2007). Problems in predicting the mobility of slow-moving landslides. *Engineering Geology* 91, 46-55, doi:10.1016/j.enggeo.2006.12.012.

Vardoulakis, I., Graf, B. & Gudehus, G. (1981). Trap-door problem with dry sand: a statical approach based upon model test kinematics. *Int. J. Num. Anal. Meth. Geomechanics* 5, 57-78, doi:10.1002/nag.1610050106.

Wiberg, N.-E., Koponen, M. & Runesson, K. (1990). Finite element analysis of progressive failure in long slopes. *Int. J. Num. Anal. Meth. Geomechanics.* 14, 599–612, doi:10.1002/nag.1610140902.

10 Evolution of stabilised creeping landslides (Combe Chopin, Ganter, Tasks 5 and 7)

10.1 Abstract

A simple analytical model is proposed to quantify evolution of a creeping landslide stabilised by a retaining wall, or by a natural barrier at the bottom of the sliding mass. Development in time of both the landslide displacements and the earth pressure acting on the retaining structure is obtained in the closed form with the latter given by the classical Terzaghi expression for the average degree of consolidation. Depending on the value of the long-term safety factor, the landslide either eventually slows down, asymptotically approaching final displacements or the soil behind the retaining wall comes to a passive failure, followed by a post-failure evolution of the landslide. The model is capable of quantifying both scenarios, with some of its features successfully validated against the monitoring and geotechnical data from the two case studies: Combe Chopin and Ganter landslides in Switzerland. For the Combe Chopin landslide, which came to a still, the model demonstrated its ability to predict final downhill displacements and their development in time. For the Ganter landslide, which failed and achieved the steady state velocity, the model correctly predicted the long term landslide evolution and effects of drainage and erosion on the displacement rates.

10.2 Introduction

Creeping landslides are a common feature in mountainous areas and cause significant damage to buildings and infrastructure. Long-term stability of slowly moving landslides has been a subject of early interest in Soil Mechanics (e.g., Terzaghi, 1936, 1950; Skempton, 1964; Skempton & La Rochelle, 1965; Bjerrum, 1967). In these studies, the analysis mainly focused on progressive failure in over-consolidated clays, where the failure is delayed in time by the development of the negative excess pore water pressure caused by shearing. As soon as this excess pore water pressure dissipated, the landslides, which did not have any kinematic constraints, accelerated and failed.

Understanding of failure mechanisms of creeping landslides continues to be of critical importance for assessment and mitigation of their hazard (Glastonbury & Fell, 2008; Schulz *et al.,* 2009). In general, when a creeping landslide is constrained by an obstacle, either natural (a rock outcrop) or artificial (a retaining wall), it slows down, creating an impression of being stabilized (Bernander & Olofsson, 1981; Wiberg *et al.,* 1990; Puzrin & Sterba, 2006). Sometimes, however, like in the case of the St. Moritz –Brattas landslide in Switzerland, the stabilization phase is succeeded by acceleration, which was caused by the passive failure in the compression zone (chapter 9).

In order to explain the St. Moritz landslide phenomenon, a progressive failure mechanism based on the propagation of a shear band (where the shear strength drops to its residual value) into the compression zone along the slip surface of the landslide is suggested in chapter 9. This mechanism cannot, however, be applied to many landslides, which were stabilised after experiencing significant displacements along the entire slip surface, so that the shear strength had dropped to its residual value everywhere on the slip surface, before the landslide met the obstacle. The present chapter is an attempt to suggest a mechanism covering this broader class of the stabilised landslides.

Stabilisation of creeping landslides is normally attempted by constructing a drainage system in the landslide body. Efficiency of such a system depends on many factors, in particular, how long such a system can remain open (i.e., not blocked by the fines) and intact (considering large inhomogeneous deformations in the sliding body). When reliability of the drainage system is questionable, in smaller landslides it is often replaced or combined with a retaining wall, protecting the infrastructure. Construction of the retaining wall creates an obstacle for the landslide, which initially slows down, in particular in its lower portion. In case, however, the residual shear strength on the sliding surface is rate dependent this apparent stabilisation can be, accompanied by increase of the earth pressures behind the retaining wall. If these pressures reach the passive earth pressure, the soil in the compression zone behind the wall may collapse and the landslide will overflow the retaining structure. The landslide will then continue moving, eventually reaching a constant velocity again.

The purpose of this chapter is to quantify this evolution of stabilised landslides by the means of a simple analytical model and to validate the model against the monitoring data from the Combe Chopin and Ganter landslides in Switzerland.

10.3 The model

10.3.1 Assumptions

The schematic layout of a landslide constrained by a retaining structure is shown in Figure 10-1. The landslide state is being characterised by displacements $\delta(x, \mathrm{t})$, velocities $\dot{\delta}(x, t)$ and effective normal stresses $p(x, t)$, all parallel to the slope and averaged over the thickness of the sliding layer, i.e., uniform with depth. Before being stabilized (stabilisation taking place at $t = 0$), the landslide is assumed to have constant effective stress

p_0 and be moving with the constant velocity v_0, both values being uniformly distributed along the landslide length:

$$p(x,t) = p_0 = const \qquad \dot{\delta}(x,t) = v_0 = const \qquad \text{for} \quad t < 0 \qquad (10\text{-}1)$$

Provided the landslide has travelled sufficiently far before its stabilization, the pressure at the lower and upper boundaries of the sliding layer and, as a consequence of the assumption (10-1), along the entire sliding layer, will become close to the active earth pressure $p_0 \approx p_a$, while the residual strength τ^* will be fully mobilized along the entire sliding surface.
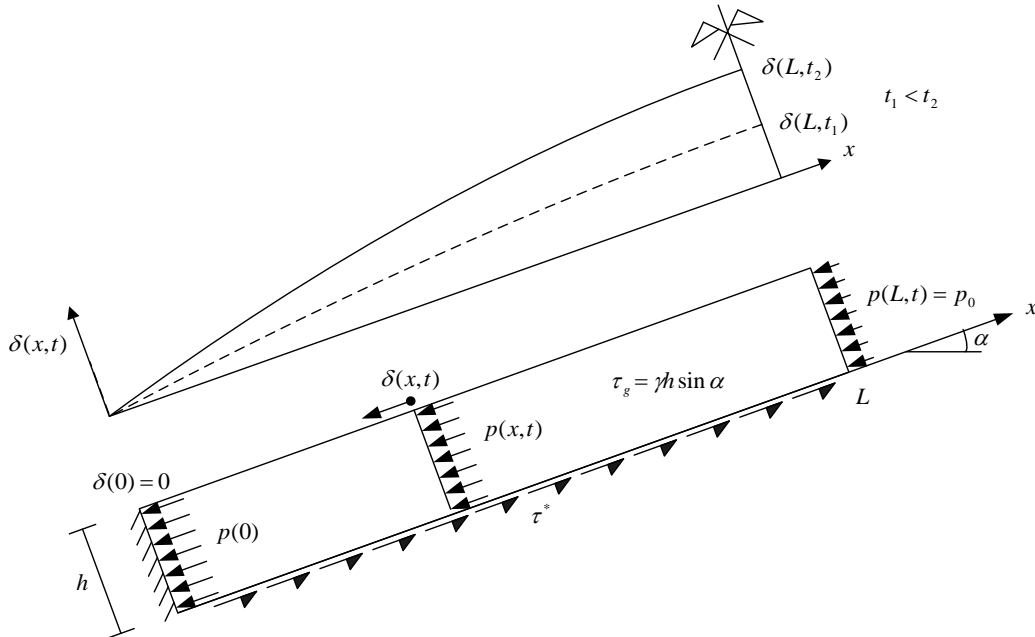
Figure 10-1: *Schematic layout of a landslide constrained by a retaining structure.*

At the moment of the landslide stabilisation ($t = 0$), the landslide displacements are taken as a reference, i.e., $\delta(x,0) = 0$, while the retaining wall becomes the boundary of zero velocity for the future landslide evolution ($t \geq 0$): $\dot{\delta}(0,t) = 0$. The velocities in sliding layer begin gradually to decrease, while the pressures to increase, with only the pressure at the upper boundary of the sliding layer remaining constant: $p(L,t) = p_0$.

This increase in pressures is due to the rate dependency of the residual strength on the sliding layer, which is assumed to exhibit rigid viscous-plastic behaviour (Figure 10-2a):

$$\tau^* = \tau_r + \eta \frac{\partial \delta}{\partial t} = \tau_r + \eta \dot{\delta} \qquad (10\text{-}2)$$

where τ^* is the residual shear strength of soil on the sliding surface; τ_r is the rate independent component of the residual shear strength, η is the viscosity coefficient. Soil behaviour in the sliding layer is assumed to be elasto-plastic (Figure 10-2b):

$$p = p_0 + E\varepsilon = p_0 + E \frac{\partial \delta}{\partial x} \qquad \text{for} \quad p < p_p \qquad (10\text{-}3)$$

where E is the deformation modulus of soil; p_p is the passive earth pressure.
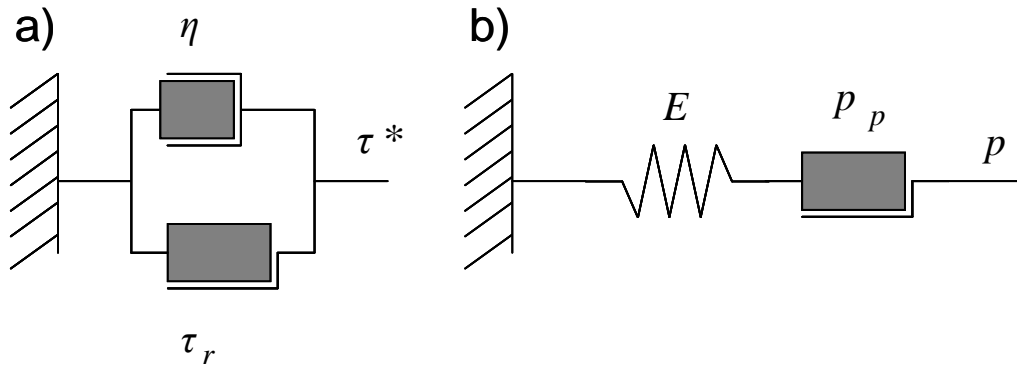
Figure 10-2: *Schematic constitutive behaviour of soil: a) On the sliding surface, b) In the sliding layer.*

10.3.2 Differential equation

Equilibrium of the sliding layer (Figure 10-3) can be expressed as:

$$h \frac{\partial p}{\partial x} = \tau^* - \tau_g \qquad (10\text{-}4)$$

where

$$\tau_g = \gamma h \sin \alpha \qquad (10\text{-}5)$$

is the gravitational shear stress.
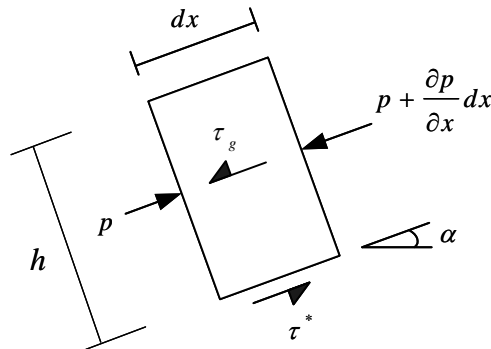
Figure 10-3: *Equilibrium of the sliding layer.*

From equations (10-1) and (10-4) it follows that before the stabilization the shear resistance is equal to the gravitational shear stress:

$$\tau^*(x,t) = \tau_g \qquad \text{for} \quad 0 \le x \le L \,,\, t < 0 \qquad (10\text{-}6)$$

and the velocity of the landslide follows from equations (10-1) and (10-2):

$$\dot{\delta}(x,t) = v_0 = \frac{\tau_g - \tau_r}{\eta} \qquad \text{for} \quad 0 \le x \le L \,,\, t < 0 \qquad (10\text{-}7)$$

After the stabilisation, differential equation for displacements is obtained by substitution of constitutive equations (10-2) and (10-3) into the equilibrium equation (10-4):

$$\frac{\partial \delta}{\partial t} = C \frac{\partial^2 \delta}{\partial x^2} + v_0 \tag{10-8}$$

where

$$C = \frac{hE}{\eta} \qquad v_0 = \frac{\tau_g - \tau_r}{\eta} \tag{10-9}$$

The boundary conditions are given by the zero displacement at the bottom and constant stress (and strain) at the top boundary of the landslide:

$$\delta(0,t) = 0 \qquad \left. \frac{\partial \delta}{\partial x} \right|_{x=L} = 0 \tag{10-10}$$

The initial conditions are given by the zero reference displacement at the moment of stabilisation:

$$\delta(x,0) = 0 \quad \text{for} \quad 0 \le x \le L \tag{10-11}$$

which after substitution into the differential equation (10-8) takes the form:

$$\left. \frac{\partial \delta}{\partial t} \right|_{t=0} = v_0 \quad \text{for} \quad 0 \le x \le L \tag{10-12}$$

consistent with the second condition (10-1) before the stabilisation.

10.3.3 Solution

Equation (10-8) can be recognised as a non-homogeneous heat equation, which in combination with the boundary conditions (10-10) produces a mixed boundary value problem (BVP). It is more convenient, however, to transform it into the 1st BVP by fictitiously extending the landslide length to $2L$ and imposing the boundary conditions:

$$\delta(0,t) = 0 \qquad \delta(2L,t) = 0 \tag{10-13}$$

Note, that in this case the original second boundary condition (10-10) is satisfied automatically due to the symmetry of the solution with respect to $x = L$.

The initial condition is being extended to the fictitious part:

$$\delta(x,0) = 0 \quad \text{for} \quad 0 \le x \le 2L \tag{10-14}$$

The solution of the 1st BVP for non-homogeneous heat equation (10-10) is given by:

$$\delta(x,t) = \int_0^t \int_0^{2L} v_0 G(x,\xi,t-T) d\xi dT \tag{10-15}$$

where ξ and T are integration variables for space and time, respectively;

$$G\left(x, \xi, t - T\right) = \frac{2}{2L} \sum_{n=1}^{\infty} \sin\left(\frac{n\pi}{2L} x\right) \sin\left(\frac{n\pi}{2L} \xi\right) e^{-\frac{Cn^2\pi^2}{4L^2}(t-T)} \tag{10-16}$$

is the Green function for the 1st BVP.

Substitution of equation (10-16) into (10-15) with subsequent integration produce:

$$\delta\left(x,t\right) = \frac{v_0}{CL} \sum_{n=1}^{\infty} \left(\frac{2L}{n\pi}\right)^3 \sin\left(\frac{n\pi}{2L} x\right) \left[1 - \cos\left(n\pi\right)\right] \left(1 - e^{-\frac{Cn^2\pi^2}{4L^2}t}\right) \tag{10-17}$$

It can be observed that all the even terms (for $n = 2,4,6,\dots$) in the sum in equation (10-17) vanish. Therefore, the solution of the BVP can be presented as:

$$\delta\left(x,t\right) = \frac{2v_0}{CL} \sum_{k=0}^{\infty} \left(\frac{2L}{(2k+1)\pi}\right)^3 \sin\left(\frac{(2k+1)\pi}{2L} x\right) \left(1 - e^{-\frac{C(2k+1)^2\pi^2}{4L^2}t}\right) \tag{10-18}$$

It can be easily shown that solution (10-18) satisfies both boundary (10-10) and initial (10-11) conditions.

For small *t*, displacements predicted by the solution (10-18) can be approximated by the solution for the infinitely long slide $(L \to \infty)$:

$$\delta(x,t) \approx v_0 \int_0^t erf \frac{x}{\sqrt{4C\xi}} d\xi \tag{10-19}$$

where $\quad erf\left(x\right) = \frac{\sqrt{\pi}}{2} \int_0^x e^{-x^2} dx \quad$ is the error function.

For large *t*, displacements predicted by the solution (10-18) can be approximated by:

$$\delta\left(x,t\right) \approx \frac{v_0}{C} \left(xL - \frac{x^2}{2} - \frac{16L^2}{\pi^3} \sin\left(\frac{\pi}{2L} x\right) e^{-\frac{C\pi^2}{4L^2}t}\right), \tag{10-20}$$

with final displacements given by:

$$\delta\left(x,\infty\right) = \frac{v_0}{C} \left(xL - \frac{x^2}{2}\right) = \frac{\tau_g - \tau_r}{hE} \left(xL - \frac{x^2}{2}\right). \tag{10-21}$$

10.4 Landslide failure and post-failure evolution

10.4.1 Pressures acting on the retaining wall

For the landslide stability analysis, the most important parameter is the pressure acting on the retaining wall:

$$p = p_0 + E\varepsilon(0,t) = p_0 + E\frac{\partial\delta}{\partial x}\bigg|_{x=0} . \qquad (10\text{-}22)$$

Differentiation of equation (10-18) with respect to *x* gives:

$$\varepsilon(0,t) = \frac{\partial\delta}{\partial x}\bigg|_{x=0} = \frac{v_0 L}{C}\left[1 - \frac{8}{\pi^2}\sum_{k=0}^{\infty}\frac{1}{(2k+1)^2}e^{-\frac{C(2k+1)^2\pi^2}{4L^2}t}\right], \qquad (10\text{-}23)$$

which is identical (!) to the Terzaghi solution for the average degree of consolidation (Terzaghi, 1943):

$$\overline{U}(T_v) = 1 - \sum_{k=0}^{\infty}\frac{2}{M^2}e^{-M^2 T_v} , \quad \text{for } M = \frac{(2k+1)\pi}{2} , \qquad (10\text{-}24)$$

where T_v is the time factor, and variables in the equations (10-23) and (10-24) are related via:

$$T_v = \frac{Ct}{L^2} , \qquad \overline{U}(T_v) = \frac{C\varepsilon(0,t)}{v_0 L} . \qquad (10\text{-}25)$$

This result is, however, hardly surprising, because similar to equation (10-8), Terzaghi's equation of one-dimensional consolidation is also a heat equation, though with two important differences: it is homogeneous, and $\overline{U}(T_v)$ is obtained there by integrating the solution, rather than by differentiating like it was done in equation (10-23).

The analogy with the Terzaghi solution indicates that its well known approximations are also valid for equation (10-23):

$$\text{for } \overline{U} = \frac{C\varepsilon(0,t)}{v_0 L} \le 0.526 , \quad T_v = \frac{\pi}{4}\overline{U}^2 \rightarrow \varepsilon(0,t) = \frac{v_0 L}{C}\sqrt{\frac{4}{\pi}\frac{Ct}{L^2}} = \frac{v_0}{C}\sqrt{\frac{4C}{\pi}}\sqrt{t} ; \qquad (10\text{-}26)$$

$$\text{for } \overline{U} = \frac{C\varepsilon(0,t)}{v_0 L} > 0.526 , \quad T_v = \frac{4}{\pi^2}\left[-\ln\frac{\pi^2}{8} - \ln\left(1 - \overline{U}\right)\right] \rightarrow$$

$$\varepsilon(0,t) = \frac{v_0 L}{C}\left(1 - \frac{8}{\pi^2}e^{-\frac{C\pi^2}{4L^2}t}\right) \qquad (10\text{-}27)$$

Substitution of the expressions (10-9), (10-26) and (10-27) into (10-22) produces approximate equations of the evolution of the earth pressure acting on the retaining structure:

$$\text{for } t \le 0.217\frac{L^2\eta}{Eh} , \qquad p(0,t) = p_0 + \frac{\tau_g - \tau_r}{h}L\sqrt{\frac{4hE}{\pi\eta}}\sqrt{t} ; \qquad (10\text{-}28)$$

$$\text{for } t > 0.217\frac{L^2\eta}{Eh} , \qquad p(0,t) = p_0 + \frac{\tau_g - \tau_r}{h}L\left(1 - \frac{8}{\pi^2}e^{-\frac{hE\pi^2}{4\eta L^2}t}\right) . \qquad (10\text{-}29)$$

10.4.2 Safety factor and time of failure

The safety factor for the landslide long-term stability is defined using equation (10-29):

$$F_S = \frac{p_p}{p(0,\infty)} = \frac{p_p}{p_0 + \dfrac{\tau_g - \tau_r}{h}L} .$$
(10-30)

If this safety factor is larger than unity, the landslide will continue to slow down, asymptotically approaching its final displacements (10-21). If, however, $F_S < 1$, the earth pressure will eventually reach the passive pressure and the soil behind the wall will fail. The time of failure t_f can be determined from equations (10-28)-(10-29):

$$\text{for } t_f \le 0.217\frac{L^2\eta}{Eh}, \qquad t_f = \frac{\pi\eta}{4hE}\left(\frac{p_p - p_0}{\tau_g - \tau_r}\frac{h}{L}\right)^2 ;$$
(10-31)

$$\text{for } t_f > 0.217\frac{L^2\eta}{Eh}, \qquad t_f = \frac{4\eta L^2}{hE\pi^2}\ln\left[\frac{\pi^2}{8}\left(\frac{h(p_p - p_0)}{L(\tau_g - \tau_r)} - 1\right)\right].$$
(10-32)

10.4.3 Post-failure evolution

Once the effective passive pressure p_p is reached at the bottom of the landslide, it stays constant and the pattern of the landslide displacement changes. It is still governed by the same differential equation (10-8), but the boundary conditions are now given by the constant stress (and strain), both at the bottom and top boundaries of the landslide:

$$\varepsilon(0,t) = \frac{\partial\delta}{\partial x}\bigg|_{x=0} = \frac{p_p - p_0}{E}, \qquad \varepsilon(L,t) = \frac{\partial\delta}{\partial x}\bigg|_{x=L} = 0 ,$$
(10-33)

representing a non-homogeneous 2nd (Neumann) BVP. The initial condition for this problem is obtained (for large t_f) from equation (10-20), defining landslide displacements at the time of failure:

$$\delta(x,0) = \frac{v_0}{C}\left(xL - \frac{x^2}{2} - \frac{16L^2}{\pi^3}\sin\left(\frac{\pi}{2L}x\right)e^{-\frac{C\pi^2}{4L^2}t_f}\right).$$
(10-34)

In this BVP, both the differential equation (10-8) and boundary conditions (10-33) are non-homogeneous. Solution for such a problem can be obtained as a superposition of two solutions of two simplified BVPs:

$$\delta(x,t) = \delta_p(x,t) + \delta_g(x,t),$$
(10-35)

where $\delta_p(x,t)$ is a particular solution of a homogeneous differential equation:

$$\frac{\partial\delta}{\partial t} = C\frac{\partial^2\delta}{\partial x^2}$$
(10-36)

with non-homogeneous boundary conditions (10-33); $\delta_g(x,t)$ is the general solution of the non-homogeneous equation (10-8), with homogeneous boundary conditions:

$$\varepsilon(0,t) = \left.\frac{\partial \delta_g}{\partial x}\right|_{x=0} = 0, \qquad \varepsilon(L,t) = \left.\frac{\partial \delta_g}{\partial x}\right|_{x=L} = 0, \qquad (10\text{-}37)$$

and initial condition:

$$\delta_g(x,0) = \frac{v_0}{C}\left(xL - \frac{x^2}{2} - \frac{16 L^2}{\pi^3}\sin\left(\frac{\pi}{2L}x\right)e^{-\frac{C\pi^2}{4L^2}t_f}\right) - \delta_p(x,0), \qquad (10\text{-}38)$$

representing a homogeneous 2nd (Neumann) BVP.

A particular solution satisfying both the differential equation (10-36) and non-homogeneous boundary conditions (10-33) is given by

$$\delta_p(x,t) = \frac{p_0 - p_p}{2EL}\left(x^2 - 2Lx + 2Ct\right). \qquad (10\text{-}39)$$

The general solution of the 2nd BVP with non-homogeneous equation (10-8), homogeneous boundary conditions (10-37) and initial condition (10-38) is given by

$$\delta_g(x,t) = \int_0^L f(\xi)G(x,\xi,t)d\xi + \int_0^t\int_0^L v_0 G(x,\xi,t-T)d\xi dT , \qquad (10\text{-}40)$$

where

$$f(\xi) = \delta_g(\xi,0) = \frac{v_0}{C}\left(\xi L - \frac{\xi^2}{2} - \frac{16 L^2}{\pi^3}\sin\left(\frac{\pi\xi}{2L}\right)e^{-\frac{C\pi^2}{4L^2}t_f}\right) - \frac{p_0 - p_p}{2EL}\left(\xi^2 - 2L\xi\right) \quad (10\text{-}41)$$

is the initial condition given by equations (10-38) and (10-39);

$$G(x,\xi,t) = \frac{1}{L} + \frac{2}{L}\sum_{n=1}^{\infty}\cos\left(\frac{n\pi}{2L}x\right)\cos\left(\frac{n\pi}{2L}\xi\right)e^{-\frac{Cn^2\pi^2}{4L^2}t} \qquad (10\text{-}42)$$

is the Green function for a homogeneous 2nd BVP.

Substitution of equations (10-41) and (10-42) into (10-40) with subsequent integration and substitution of the result into equation (10-35) together with the particular solution (10-39) produces a closed form solution for the landslide displacements, which is rather bulky and will not be shown here due to the lack of space. It is, however, rather straightforward to demonstrate that for $t \to \infty$ the time derivative of the first integral in equation (10-40) approaches zero, while the time derivative of the second integral in equation (10-40) approaches v_0. Therefore, velocities of all the points along the landslide are asymptotically approaching a constant value:

$$\dot{\delta}(x,\infty) = \dot{\delta}_p(x,\infty) + \dot{\delta}_g(x,\infty) = -C\frac{p_p - p_0}{EL} + v_0, \qquad (10\text{-}43)$$

which after substitution of equations (10-9) into it can be expressed via soil parameters:

$$\dot{\delta}(x,\infty) = \frac{1}{\eta}\left(\tau_g - \tau_r - \frac{h}{L}\left(p_p - p_0\right)\right)$$ (10-44)

Note, that for $p_p > p_0$ this velocity will be smaller than the initial landslide velocity v_0 from equation (10-9), indicating that although the landslide movements could not have been eliminated completely, certain degree of the landslide stabilisation will be achieved, in spite of the passive failure of soil behind the retaining structure.

10.5 Summary

Evolution of a creeping landslide, moving downhill with a constant initial velocity and earth pressure, and encountering a rigid obstacle at its bottom has been considered. Displacements of such a landslide are given by equation (10-18) which can be approximated by equations (10-19) and (10-20), immediately and long time after the stabilization took place, respectively.

This movement will, however, be accompanied by the increase of the earth pressure acting on the retaining structure given by equations (10-28) and (10-29), for early and late stages of earth pressure evolution, respectively. Depending on the value of the long term safety factor (10-30), the landslide will either eventually slow down, asymptotically approaching final displacements (10-21), or the soil behind the retaining wall will experience passive failure at the moment in time given by equations (10-31) and (10-32).

After this passive failure takes place, the landslide displacements can be described using equations (10-35) and (10-39)-(10-42). The landslide will then asymptotically approach a constant velocity (10-44), which will be lower than the initial velocity (10-9).

In the following, two case studies of landslides in Switzerland will be carried out in order to partially validate the proposed model.

10.6 Case study: Combe Chopin landslide, Switzerland

10.6.1 Description

The highway A16 from Bern to Delemont and Basel is a major north-south link in Switzerland and connects the capital city Bern to France (Figure 10-4a). The highway crosses the creeping landslide of Combe Chopin (Figure 10-4b), which is bounded by two hills located to the north and south of the landslide, respectively. This landslide is inclined from east to west with an inclination of 25 to 30° (Bapst, 2002) towards the river Birse, which passes at the bottom of the landslide. The width of the slide is about 150 - 200 m, its length in general is about 140 – 190 m, but in the northern part the length of the active portion is about 90 m and the width 60 m (Figure 10-5a). The soil of the landslide is composed of slope debris, a mixture of clay and gravel on top of a sliding surface of a thickness of 0.5 to 1.0 meters which is as well a mixture of clay and gravel. Below the sliding surface there is a zone of weathered rock with a thickness of 2 to 4 meters, followed by the solid rock. The landslide can be divided into a northern zone, with a landslide thickness of approximately 5 to 7 meters and a southern zone, with a landslide thickness of up to 14 meters. The hydrology is dominated by the less permeable layer of clay and gravel mixture.
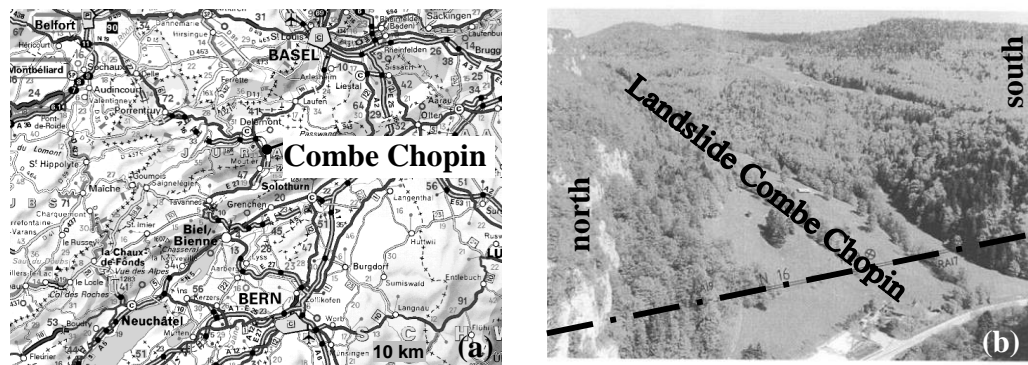
Figure 10-4: *The Combe Chopin landslide: a) Location (Viamichelin, 2007), b) View (after Bapst, 2002).*
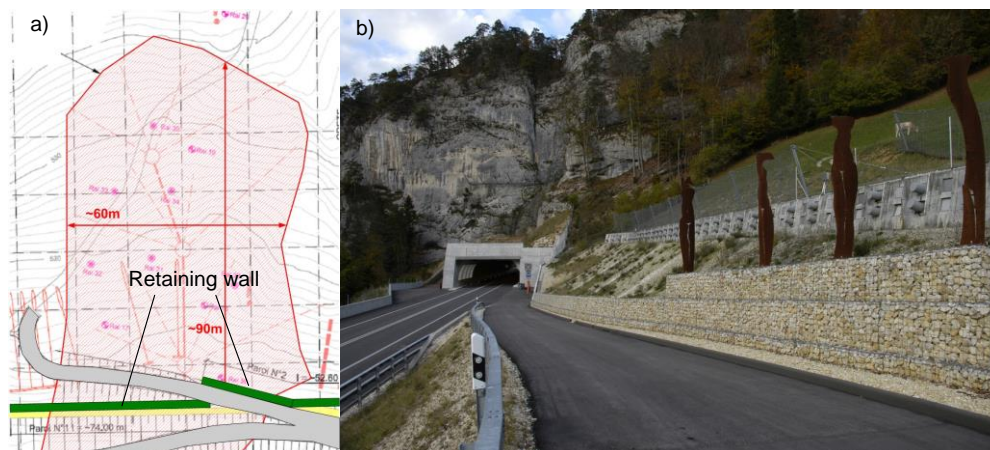
Figure 10-5: *The northern part of the Combe Chopin landslide: a) Schematic outline of the landslide, b) Photo of the wall (courtesy of Stump).*

The soil properties were defined in the laboratory tests: the effective peak strength parameters $\varphi'_{peak} = 20 \pm 1°$ and $c'_{peak} = 40 \pm 15 \; kPa$ (direct shear); the residual angle of internal friction $\varphi'_{res} = 18 \pm 3°$ (ring shear); Young's modulus in compression $E = 30 \pm 10 \; MPa$ (consolidometer); total unit weight $\gamma = 20 \; kN/m^3$.

Creep deformations in the landslide were observed and monitored since 1976, when the highway project started (Bapst, 2002). During the first stages of excavation in September 2000, displacements in the northern zone of the landslide (Figure 10-5a) accelerated to $v_0 = 4 \pm 2 mm/day$ with clearly observed tension cracks at the upper boundary of the slide (Bisetti, 2002). In the first half of 2001 the landslide was partially stabilized by installing a drainage system, which brought the ground water level below the sliding surface. In the first half of 2002 an anchored bored pile retaining wall was constructed (Figure 10-5b), monitored using a TRIVEC measurement system, described in detail in Puzrin & Schmid (2007), where also an early attempt was made to study the landslide mechanism. High anchor forces acting on the retaining wall resulted in the wall moving uphill for the first three and a half years after tensioning of the anchors, until December 2005, so that the zero displacement boundary was not at the wall but in the landslide about 12 m above the wall. In addition to the TRIVEC measurements, downhill displacements of three points on the landslide (at the distances of 13m, 40m and 63m away from the zero displacement boundary, respectively) have been measured geodetically (Figure 10-6).
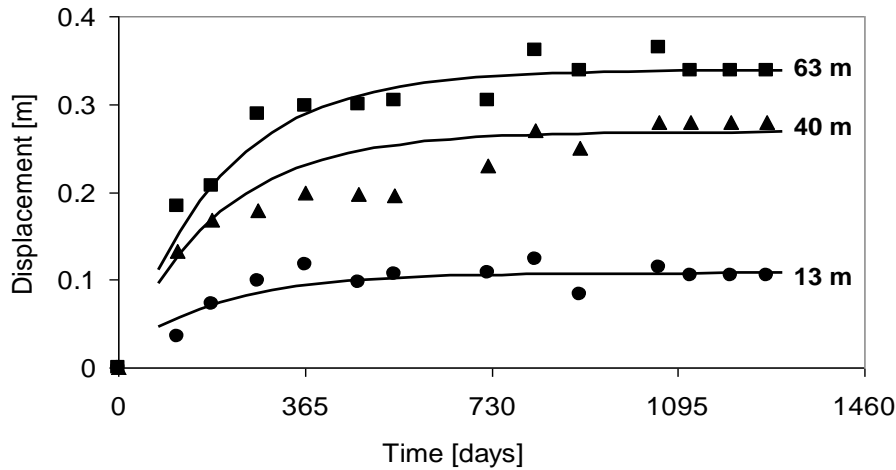
Figure 10-6: *Downhill displacements of three points in the northern part of the Combe Chopin landslide measured after the construction of the wall.*

10.6.2 Analysis

As is seen in Figure 10-6, the first geodetic measurement was taken 114 days after completion of the wall, and after 1119 days the slide came practically to a halt. The safety factor for the landslide is given by equation (10-30). Displacements of the landslide can be approximated by equations (10-19) and (10-20), immediately and long time after the construction of the retaining wall, respectively. The final landslide displacements are given by equation (10-21). Evaluation of these expressions against the measured and monitoring data (summarised in Table 1) is given below.

Table 10-1: *Summary of the physical and geometric parameters for Combe Chopin landslide.*

Parameter description	Parameter value	Derivation
Landslide length	$L = 78 \text{ m}$	Measured (field)
Average depth of the sliding surface	$h = 6 \text{ m}$	Measured (field)
Average depth of the phreatic surface	$h_w = 6 \text{ m}$	Measured (field)
Average slope inclination	$\alpha = 27.5°$	Measured (field)
Total unit weight of soil	$\gamma = 20 \text{ kN}/\text{m}^3$	Measured (lab)
Peak angle of internal friction in the sliding layer	$\varphi'_{peak} = 20 \pm 1°$	Measured (lab)
Peak cohesion in the sliding layer	$c'_{peak} = 40 \pm 15 \text{ kPa}$	Measured (lab)
Average residual angle of internal friction on the slip surface	$\varphi'_{res} = 18°$	Measured (lab)
Average Young modulus	$E = 30 \text{ MPa}$	Measured (lab)
Gravitational shear stress	$\tau_g = 55.4 \text{ kPa}$	Calculated
Residual shear strength	$\tau_r = 34.6 \text{ kPa}$	Calculated

Firstly, the slide came to a halt and, as indicated by TRIVEC and anchor load cells measurements, the earth pressure on the retaining wall has also ceased to grow, apparently not reaching the passive earth pressure and indicating that the safety factor (10-30) is larger than unity. This conclusion can be verified, using equation (10-30) and Table 1, to estimate the passive pressure and compare its value to that determined independently from the peak strength estimates of the soil in the sliding layer. From equation (10-30) it follows:

$$p_p - p_0 \geq \frac{\tau_g - \tau_r}{h} L = 271 \text{ kPa} .$$ (10-45)

where $\tau_g = \gamma h \sin \alpha = 55.4 \text{ kPa}$ is the gravitational shear stress:

$$\tau_r = \gamma h \cos \alpha \tan \varphi'_{res} = 34.6 \text{ kPa}$$ (10-46)

is the residual shear strength in the absence of ground water table.

Evidence of the tension cracks before the slide stabilization allows the initial pressure in the sliding body to be assumed to be close to the active earth pressure p_a. The effective peak strength parameters consistent with the back-calculted pressure difference (10-45) are $\varphi'_{peak} \geq 20°$ and $c'_{peak} \geq 42 \ kPa$, which broadly overlap with the measured ranges of $\varphi'_{peak} = 20 \pm 1°$ and $c'_{peak} = 40 \pm 15 \ kPa$, confirming that the safety factor could indeed be $F_s > 1$.

Secondly, fitting equation (10-21) to the final displacement measured at 1269 days after wall construction (Figure 10-7) produces a value of the parameter

$$\frac{v_0 L^2}{C} = 0.70 ,$$ (10-47)

where $L = 90 \, m - 12 \, m = 78 \, m$ is the effective length of the landslide above the zero displacement boundary. This parameter, however, can be also calculated independently, using equations (10-9) and average values for physical and geometric parameters of the problem summarised in Table 1:

$$\frac{v_0}{C} L^2 = \frac{\tau_g - \tau_r}{hE} L^2 = 0.704 ,$$ (10-48)

indicating remarkable proximity between the fitted and directly calculated values.
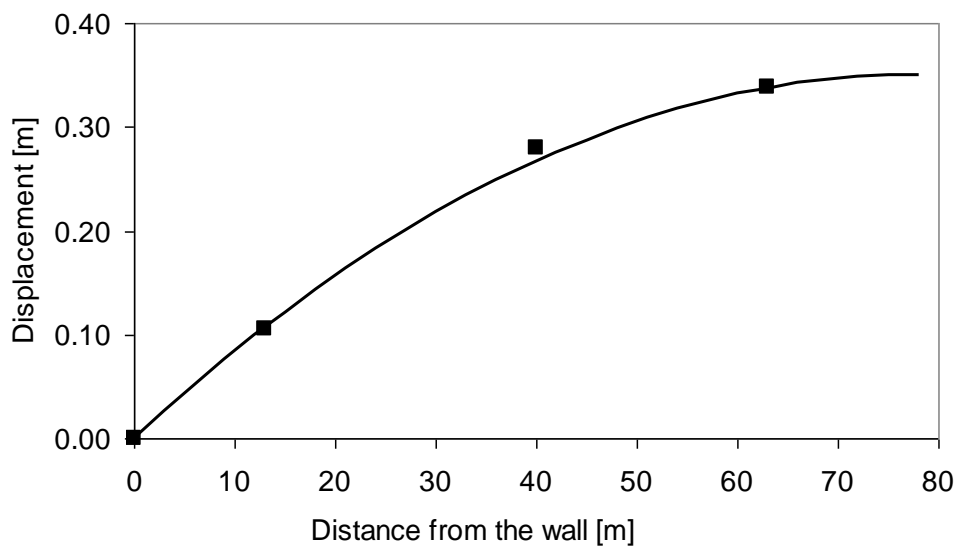
Figure 10-7: *Final downhill displacements along Combe Chopin landslide measured 1269 days after the construction of the wall.*

Thirdly, the best fit of the evolution of the landslide displacements in time (Figure 10-6), for x of 13m, 40m and 63m, is obtained by using equation (10-20) after substituting into it parameters $v_0 L^2 / C = 0.7$, $L = 78\,m$ and adjusting the initial velocity to

$$v_0 = 1.5 \text{ mm/day.} \tag{10-49}$$

This value is slightly below the lower bound of the range of $v_0 = 4 \pm 2$ mm/day recorded during the landslide acceleration, correctly reflecting effects of the drainage system constructed with the aim of slowing the landslide down. Velocity (10-49), when substituted together with equation (10-46) and $\tau_g = \gamma h \sin \alpha = 55.4$ kPa into equation (10-7), allows for the assessment of the viscosity $\eta = (\tau_g - \tau_r)/v_0 = 1.20 \times 10^9\ kPa \cdot \sec/m$, which is of the same order of magnitude as the viscosities back-calculated by van Asch *et al* (2007) for two landslides in French Alps.

It has to be verified, however, whether it is justified to use equation (10-20) for simulating the landslide displacements in Figure 10-6, because this equation is only suitable for approximating later stages of the landslide evolution. Following Terzaghi solution analogy, the approximation becomes valid for

$$tC / L^2 \geq 0.217\ . \tag{10-50}$$

Substitution of back-calculated parameters (10-47) and (10-49) into equation (10-50) provides the following range of the validity of equation (10-20): $t \geq 102$ days after completion of the wall. This justifies the application of this equation to simulating data in Figure 10-6, where the first reading shown was taken $t = 114$ days after completion of the wall.

10.7 Case study: Ganter landslide, Switzerland

10.7.1 Description

The highway A9 via the Simplon Pass is one of the main connections between Switzerland and Italy through the Swiss Alps (Figure 10-8a). Its most spectacular structure is the bridge over the Ganter river valley built in 1980 (Figure 10-8b). On the left bank of the river, the piers of this bridge are built on a creeping landslide within the caissons cutting through the sliding layer, so that the pier foundations could be based in the stable rock. This landslide has an average inclination of around 24° from southeast to northwest towards the Ganter river, which passes at the bottom of the landslide. The river bed deposits are squeezed between the landslide and the rock outcrop at the opposite river bank, representing a natural obstacle for the landslide, i.e., no retaining wall is necessary.
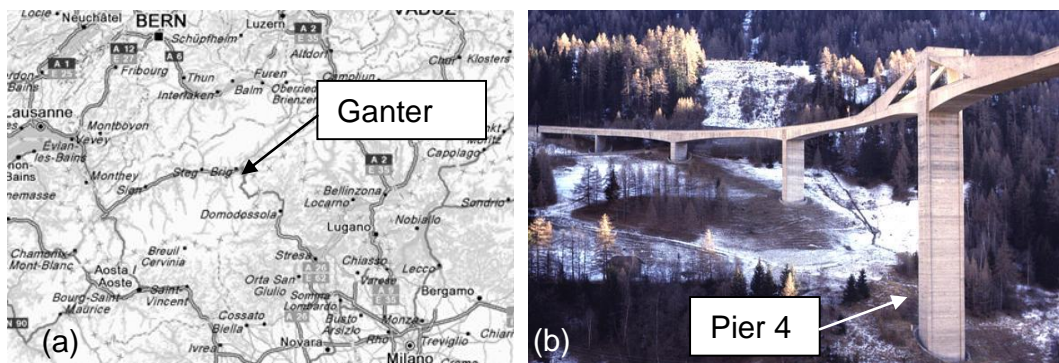
Figure 10-8: *The Ganter landslide: a) Location (Viamichelin, 2011), b) View.*

The landslide is 1060 m wide and between 300 m and 500 m long. In the cross-section close to the Ganter bridge foundations, where the majority of the measurements have been taken, the length of the landslide is 440 m. The soil profile of the landslide is built of the slope debris, which is a mixture of gravel and stones within a sand and silt matrix, covering a bed of moraine (Lang and Schaerer, 1973). Thickness of the sliding granular material is between 20-22 m at the boundaries of the landslide and 42 m in its middle section (Lang and Schaerer, 1973). In the upper part of the landslide the granular material is based on the altered mica schist, in the lower part – on the altered schist.

A preliminary geodetical field campaign was carried out between 1966 and 1974 (Schaerer, 1975). Starting from 1975 points 8, 9, 10, 11 and 12 have been measured in the area of the designed bridge (Figures 10-9a and b). A drainage system, combining horizontal drains at the bridge piers with the surface drainage of the streams and rain water, was built in 1979- 1982 to slow down the displacement rates, and from 1979 on additional points (40, 50 and 60) were added to the measurements.
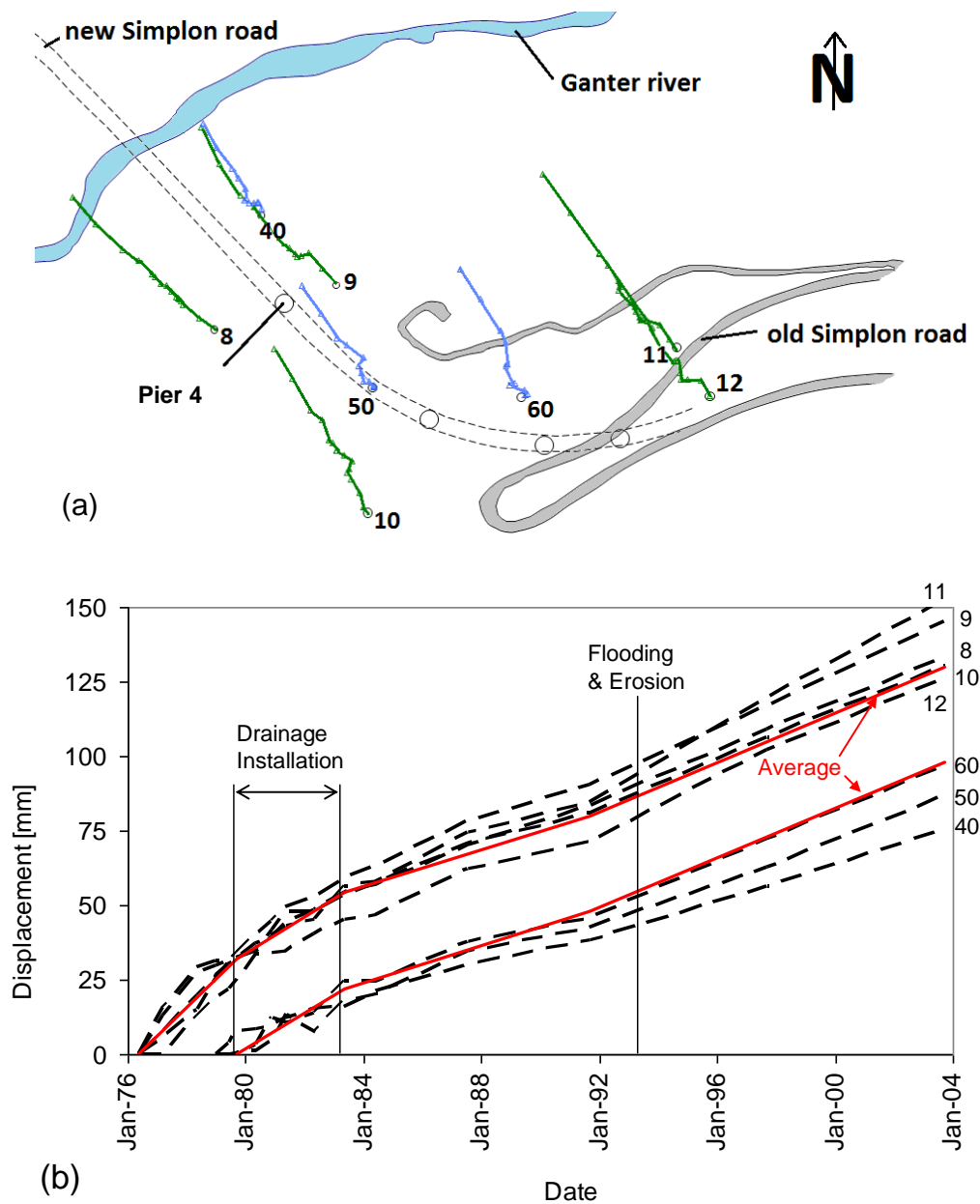
Figure 10-9: *Displacement measurements: a) Plan of the measurement points with displacement vectors, b) Displacements in time.*

As is seen in Figure 10-9b, in 1975-1979, before construction of the drainage, all points of the slide moved down at a similar rate, with the average constant velocity of $\dot{\delta} = 9.6 \; mm/year$. During construction of the drainage, in 1979-1982, the velocity dropped to $\dot{\delta} = 6.0 \; mm/year$, and after the end of the drainage installation it stabilized at the average of $\dot{\delta} = 3.1 \; mm/year$, with practically the same value for all the points on the slide. This demonstrates efficiency of the drainage system, which managed to lower the ground water table by 7 m: from 19 m below the ground surface to 26 m below the ground surface. In the year 1993, however, as a result of a severe flooding in this region the bed of the Ganter river was eroded by about 1 m and the landslide displacement rates increased to the average of $\dot{\delta} = 4.2 \; mm/year$, remaining relatively constant both in time and in space in the 10 years following the flooding.

In addition to the geodetical measurements, an extensive geotechnical study was performed, including geoelectrical and seismic measurements. The soil properties were defined in laboratory and field test: the effective peak strength parameters $\varphi'_{peak} = 37 \pm 1°$, using back calculation from plate bearing tests and from grain-size distribution after Dhawan (Lang and Schaerer, 1974), additionally validated against peak values from ring shear tests; the residual angle of internal friction $\varphi'_{res} = 23 \pm 2°$ from the ring shear tests; total unit weight $\gamma = 22 \; kN/m^3$.

To separate the foundations of the bridge from the landslide, they were founded below the slip surface in the stable rock, with the piers of the bridge constructed inside vertical caisson shafts. These shafts have been moving with the sliding layer, gradually approaching the piers, which were designed to allow for correcting their position to avoid the contact between the caisson and the pier. To measure the earth pressure acting on the shaft, Glötzl pressure cells were installed at several depths at the contact of the caisson of Pier 4 with soil. After completion of the construction these measurements did not show any pressure increase in the sliding layer.

10.7.2 Analysis

As is seen in Figure 10-9b, in 1975-1979, before construction of the drainage, all points of the slide moved down at a constant velocity, $\dot{\delta} = 9.6 \; mm/year$, in spite of the constraint at the bottom, indicating that (a) the earth pressure at the bottom has reached the passive pressure; and (b) that the slide reached a steady state described by equation (10-44). After construction of the drainage was completed in 1982, the velocity decreased to $\dot{\delta} = 3.1 \; mm/year$, and remained constant and similar for all the points on the slide, until 1993, when as a result of about 1 m erosion in the passive zone at the bottom the landslide uniformly accelerated to $\dot{\delta} = 4.2 \; mm/year$. The earth pressure in the landslide body at the Pier 4, measured in 1979-1987 using Glötzl pressure cells remained constant over the measurement period. The earth pressure at the bottom of the landslide also stays fairly constant, as confirmed in 2008-2010 by the measurements performed with the help of the novel inclinodeformeter (Schwager et al., 2010).

From the above observations it follows that the steady state reached by the landslide due to the passive failure at the bottom before the bridge construction has not been disturbed by the drainage system construction and subsequent passive zone erosion. In other words, the landslide continues to move as a rigid body, as described by equation (10-44), with fluctuations in its velocity being caused by the changes in the corresponding parameters. This provides an opportunity for validation of the equation (10-44) ability to predict landslide displacement rates.

Indeed, after calibrating the model for the pre-drainage phase, when the depth of the phreatic surface was $h_w = 19 \; m$ and the depth of the passive zone $h_b = 22 \; m$ (Lang and Schaerer, 1980), its back-calculated parameter η can be used for predicting the effects

of the drainage (with the phreatic surface dropping deeper to $h_w = 26 \ m$) and subsequent erosion (with the depth of the passive zone decreasing to $h_b = 21 \ m$) on the landslide displacement rates. By comparing these estimated effects to the observed ones, the post-failure equation (10-44) can be validated.

First, using equation (10-44) and physical and geometric parameters from Table 2, the viscosity coefficient η can be estimated as

$$\eta = \frac{1}{\dot{\delta}(x,\infty)}\left(\tau_g - \tau_r - \frac{h}{L}(p_p - p_a)\right) = 1.35 \times 10^{11} \ \text{kPa·sec/m} \tag{10-51}$$

where evidence of the tension cracks in the sliding body allows the initial pressure to be assumed to be close to the active earth pressure $p_0 = p_a$, so that the difference between earth pressures before the drainage was built is given by:

$$p_p - p_a = \frac{1}{2h_b}\left(\gamma h_b^2 - \gamma_w(h_b - h_w)^2\right)K_p - \frac{1}{2h_t}\left(\gamma h_t^2 - \gamma_w(h_t - h_w)^2\right)K_a = 668 \ \text{kPa} \tag{10-52}$$

where $h_b = h_t = 22 \ \text{m}$ are the average depths of the sliding surface at the bottom and top boundaries of the landslide, respectively; K_a and K_p are the active and passive earth pressure coefficients, respectively (Puzrin & Sterba, 2006 based on Chu,1991):

$$\begin{Bmatrix} K_a \\ K_p \end{Bmatrix} = \cos \alpha \left[1 + 2\tan^2 \varphi'_p \mp 2\sqrt{\left(1 + \tan^2 \varphi'_p\right)\left(\tan^2 \varphi'_p - \tan^2 \alpha\right)}\right] = \begin{Bmatrix} 0.56 \\ 3.34 \end{Bmatrix} \tag{10-53}$$

The gravitational shear stress and the residual shear strength before the drainage was built are given by:

$$\tau_g = \gamma h \sin \alpha = 376 \ \text{kPa} \qquad \tau_r = \left(\gamma h - \gamma_w(h - h_w)\right)\cos \alpha \tan \varphi'_{res} = 271 \ \text{kPa} \tag{10-54}$$

The back-calculated value of the viscosity (10-51) is two orders of magnitude higher than that obtained for the Combe Chopin landslide. Such variations between different landslides, as well as between the field and lab determined values are not uncommon (e.g. van Asch et al, 2007) and may be explained by the rate dependency of the viscosity, the development of negative pore pressures on the sliding surface and by the 3D flow effects. The associated gain in strength results in a higher apparent viscosity. In the case of the Ganter slide, however, one of the major reasons for this difference is likely to be the stress dependency of the viscosity (Ter Stepanian, 1963), with the effective normal stresses acting on the sliding surface of the Ganter landslide being seven times higher than those in the Combe Chopin landslide.

Table 10-2: *Summary of the physical and geometric parameters for Ganter landslide.*

Parameter description	Parameter value	Derivation
Landslide length	$L = 440$ m	Measured (field)
Average depth of the sliding surface	$h = 42$ m	Measured (field)
Average depth of the sliding surface at the bottom and the top boundaries of the landslide before erosion	$h_b = h_t = 22$ m	Measured (field)
Average depth of the sliding surface at the bottom and the top boundaries of the landslide after erosion	$h_b = 21$ m $h_t = 22$ m	Measured (field)
Average depth of the phreatic surface before drainage construction	$h_w = 19$ m	Measured (field)
Average depth of the phreatic surface after drainage construction	$h_w = 26$ m	Measured (field)
Average slope inclination	$\alpha = 24\,°$	Measured (field)
Total unit weight of soil	$\gamma = 22$ kN$/$m^3	Measured (lab)
Average peak angle of internal friction in the sliding layer	$\varphi'_{peak} = 37\,°$	Measured (field)
Average residual angle of internal friction on the slip surface	$\varphi'_{res} = 23\,°$	Measured (lab)
Gravitational shear stress	$\tau_g = 376$ kPa	Calculated
Residual shear strength	$\tau_r = 271$ kPa	Calculated before the drainage construction
	$\tau_r = 297$ kPa	Calculated after the drainage construction

After the drainage was built, the depth of the phreatic surface dropped to $h_w = 26\ m$ and the new values of model parameters are calculated from equation:

$$p_p - p_a = \frac{1}{2}\gamma h_b K_p - \frac{1}{2}\gamma h_t K_a = 673 \text{ kPa} \tag{10-55}$$

and equations (10-54):

$$\tau_g = 376 \text{ kPa} \qquad \tau_r = 297 \text{ kPa} \tag{10-56}$$

Then, the back-calculated parameter (10-51) is substituted together with equations (10-55)-(10-56) into equation (10-44) to estimate the landslide velocity after the drainage was built in 1982, but before the flooding and erosion of 1993:

$$\dot{\delta}(x,\infty) = \frac{1}{\eta}\left(\tau_g - \tau_r - \frac{h}{L}\left(p_p - p_a\right)\right) = 3.3 \ mm/year \tag{10-57}$$

The observed value of the landslide velocity after drainage is $\dot{\delta} = 3.1\ mm/year$ indicating remarkable proximity between the predicted and observed values.

Finally, effects of the erosion of the passive zone caused by the flooding of 1993 can be investigated by substituting $h_b = 21$ m into equation (10-55), which gives $p_p - p_a = 638$ kPa, and after substitution together with parameters (10-51) and (10-56) into equations (10-44) allows for estimating the landslide velocity after the erosion:

$$\dot{\delta}(x,\infty) = \frac{1}{\eta}\left(\tau_g - \tau_r - \frac{h}{L}\left(p_p - p_a\right)\right) = 4.1 \; mm\big/year \tag{10-58}$$

The observed value of the landslide velocity after erosion is $\dot{\delta} = 4.2 \; mm\big/year$, indicating again a remarkable proximity between the predicted and observed values.

10.8 Conclusions

The chapter explores a simple analytical model in an attempt to quantify evolution of landslide stabilised by a retaining wall, or by a natural barrier at the bottom of the sliding mass. Within the model assumptions, development in time of both the landslide displacements and the earth pressure acting on the retaining structure can be obtained in the closed form. Curiously, for the pressure evolution the solution is identical to the expression for the average degree of consolidation obtained by Tezaghi for the classical problem of one-dimensional consolidation. The model allows for a clear definition of the long term safety factor for a stabilised landslide. Depending on the value of this safety factor, the landslide will either eventually slow down, asymptotically approaching final displacements given by the model, or the soil behind the retaining wall will experience passive failure at the certain moment in time, which can be predicted by the model. The model also provides an insight into the post-failure evolution of the landslide.

Two case studies based on the monitoring data from the Combe Chopin and Ganter landslides in Switzerland were used to validate the model. For the Combe Chopin landslide, which has a long term safety factor lager than unity, the model demonstrated its ability to predict final downhill displacements and their development in time. For the Ganter landslide, which has reached the passive pressure at the bottom, failed and achieved the steady state velocity before displacement measurements commenced, the model correctly predicted the long term landslide evolution and effects of drainage and erosion on the displacement rates. In both cases the model allows for back-calculation of apparent shear viscosities for soil on the sliding surface, avoiding high uncertainties associated with determination of the viscosity coefficients in laboratory tests.

While being promising in validating certain features of the model, these two case studies do not test ability of the model to predict the time of a landslide failure and the initial post-failure evolution of such landslide. Additional case studies are, therefore, required, indicating a direction for the future research.

Acknowledgements

References

Bapst, A. (2002). N16 – Traversée de la Combe Chopin Conditions géologiques *Publication de la Société Suisse de Mécanique des Sols et des Roches*, Réunion d'automne, 8. nov. 2002, Olten, 59-72.

Bernander, S., and I. Olofsson (1981), On formation of progressive failures in slopes. *Proc. 10th ICSMFE* **3**, 357-362.

Bisetti, A. (2002). Confortation et Assainissement de la Combe Chopin Analyse de Stabilite. *Publication de la Société Suisse de Mécanique des Sols et des Roches*, Réunion d'automne, 8. nov. 2002, Olten, 73-82.

Bjerrum, L. (1967). Progressive failure in slopes of overconsolidated plastic clay and clay shells. *J. Soil Mech. Found. Engng Div., ASCE* **93**, 1-49.

Chu, S. (1991). Rankine analysis of active and passive pressures in dry sands. *SoilsFound.* **31** (4), 115-120

Lang, H. J. and Schaerer, Ch. (1973). N9 – route de Simplon, traversée de la vallée de la Ganter. *rapport 2774/2*, EPFZ Zurich, Institut de Technique des Fondations et de Mécanique des Sols, 24. janvier 1973, Zurich.

Lang, H. J. and Schaerer, Ch. (1974). Simplonstrasse N 9, Gnaterüberquerung. *Rapport 2774/6*, ETH Zürich, Institut für Grundbau und Bodenmechanik, 10. Oktober 1974, Zürich.

Lang, H. J. and Schaerer, Ch. (1980). N9 – route du Simplon, rapport relatif aux mesures et observations. *Rapport 2774/10*, EPFZ Zurich, Institut de Technique des Fondations et de Mécanique de Sols, 31. october 1980, Zurich.

Puzrin, A.M., and Schmid, A. (2007). Utilization of TRIVEC Measurements in the Inverse Analysis of the Long-Term Stability of a Constrained Landslide. *Proceedings of the FMGM 2007 Conference*, Boston, MA, USA, Sept. 2007.

Puzrin, A. M. and Sterba, I. (2006). Inverse long-term stability analysis of a constrained landslide. *Geotechnique* **56**, 483–489.

Schaerer, Ch. (1975). Ueberquerung des Ganterbaches. *Mitteilung der Schweizerischen Gesellschaft für Boden- und Felsmechanik*, Frühjahrstagung, 2. und 3. Mai 1975, Brig, 1-4.

Schulz, W.H., Kean, J.W. & Wang, G. (2009). Landslide movement in southwest Colorado triggered by atmospheric tides. *Nature Geoscience* **2**, 863-866, doi:10.1038/ngeo659.

Schwager, M. V., Schmid, A. M. and Puzrin, A. M. (2010). Inclinodeformometer for earth pressure measurements in creeping landslides. *Soils and Foundations* **50** (4), 451-458.

Skempton, A.W. (1964). Long-term stability of clay slopes. *Géotechnique* **14**, 77-102, doi:10.1680/geot.1964.14.2.77.

Skempton, A.W. and La Rochelle, P. (1965). The Bradwell slip: a short-term failure in London clay. *Géotechnique* **15**, 221-242, doi:10.1680/geot.1965.15.3.221.

Ter Stepanian, G. (1963). On the long-term stability of slopes. *Norw. Geotech. Inst.* **52**, 1–14.

Terzaghi, K. (1936). Stability of slopes of natural clay. *Proc. 1st Int. Conf. Soil Mech. Found. Engng*, Cambridge, MA 1, 161-165.

Terzaghi, K. (1943). *Theoretical Soil Mechanics*, John Wiley and Sons, New York.

Terzaghi, K. (1950). Mechanism of landslides. *Geol. Soc. Am., Engng. Geol., Berkley Vol.,* 83-123.

Van Asch, Th.W.J., Van Beek, L.P.H. and Bogaard, T.A. (2007). Problems in predicting the mobility of slow-moving landslides. *Engineering Geology* **91**, 46–55.

Viamichelin (2007). http://www.viamichelin.de/viamichelin/deu/dyn/controller/Karten

Viamichelin (2011). http://www.viamichelin.de/viamichelin/deu/dyn/controller/Karten

Wiberg, N.-E., Koponen, M. and Runesson, K. (1990). Finite element analysis of progressive failure in long slopes. *Int. J. Num. Anal. Meth. Geomechanics.* **14**, 599–612, doi:10.1002/nag.1610140902.

11 Study of an unconstained landslide (Braunwald, Task 6)

11.1 Introduction

High above the communities Linthal and Rüti in the canton of Glarus sits, at 1200-1700 m above sea level, the sun terrace of Braunwald (Figure 11-1). The entire municipality is car-free and a funicular railway connects the terrace with the valley.
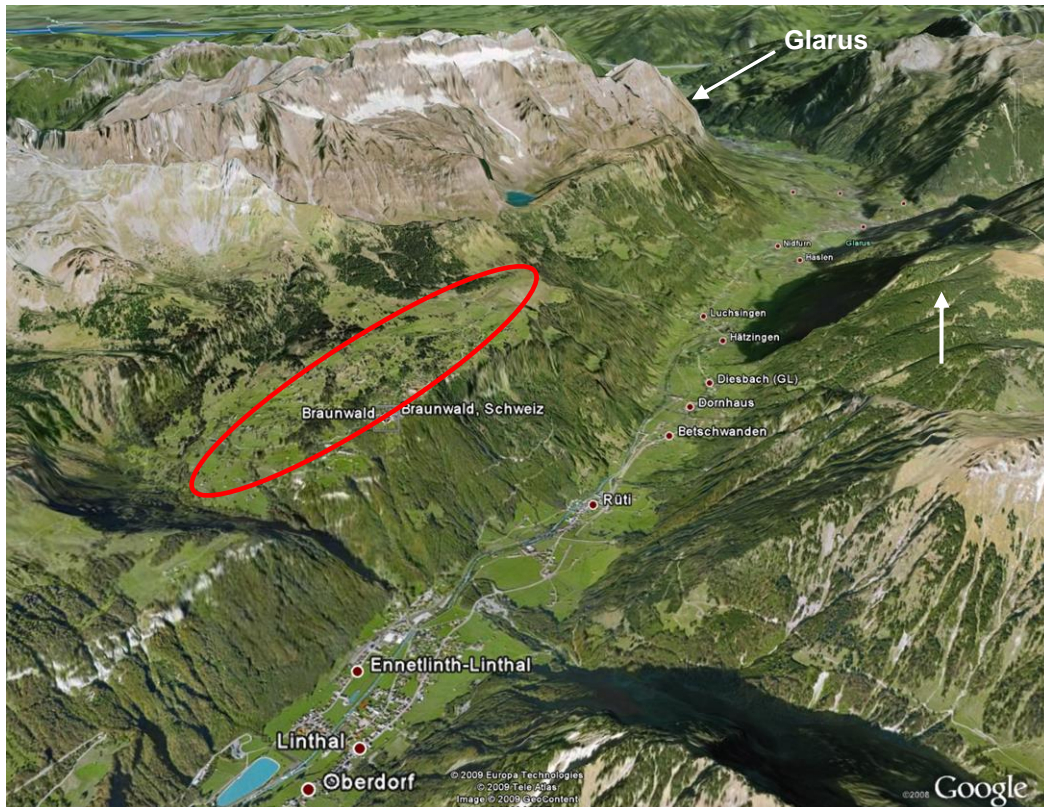
Figure 11-1: *Location of Braunwald (Google 2009).*

The slow-moving terrace constitutes a problem for the community, as sensitive infrastructure and housing developments are being partially destroyed or their usability is restricted. Problems arise, for example, for the Braunwaldbahn train, for water mains and for the sewage system.

Stopping the slope movements would bring an end to costly repair work. According to the Dr. von Moos AG (2003), the damage by the slope movements amounts to around one million CHF per year. Whether a complete stabilization of the slope can be accomplished appears, however, questionable.

To give a brief overview of the history and the work made already in the Braunwald area, we reproduce here an outline of the recent history, after Gallusser (1981):

As early as 1932, larger remedial action had to be taken at the mountain station of the Braunwaldbahn, as well as in some parts of the village. The measures consisted of building a drainage tunnel. In the re-survey in 1954, using the triangulation points of 1925, it was found that the entire terrace of Braunwald had moved down towards the valley. In the light of these slope movements, the authorities expressed in 1954 the desire to estab-

lish the drainage corporation Braunwald. In 1971, a renovation project with the goal of building a large-scale surface drainage system was not executed, because for efficient surface drainage rainfall is too large and the soil in many areas too permeable. In a major landslide in 1979, several thousand cubic meters of soil plunged down to the valley. Since the 1980s, there are ongoing studies regarding slope stability and creep behaviour in Braunwald.

A detailed geological description of the Braunwald area can be found in Schindler (1982), see also Figure 11-2. In a simplified picture, the geology can be described as a polished flat rock surface with an overlying ground moraine that is hard-bedded and has not slipped, and is itself covered by a sliding mass. The slip plane is not in the transition from solid rock to unconsolidated rock mass, but within the debris mass. The slip plane consists of a so-called 'Blue Clay', a type of clay that develops from weathering of the solid bedrock mass.

Figure 11-2 shows an overview of the slip-area geology. The slip area can be roughly characterized as follows:

- Length: 500–1500 m

- Width: approximately 2000 m

- Area: approximately 3 km^2

- Average inclination angle: 12-13 ° (flattening when going up the slope)

- Location of the slip plane: 15–40 m (+) from OKT

                                             (increasing sliding mass uphill)

- Soil in slip plane: Blue Clay

The highest rates of movement are in the lower-most portion of the steep slope, which part is approximately 200 m long; higher up, the rate decreases significantly. This sequence of areas with different speeds can be explained by the upwardly curved slip surface at the base. This shape causes a steeper inclination at the downhill end, where the landslide breaks off, compared to the mountain side.
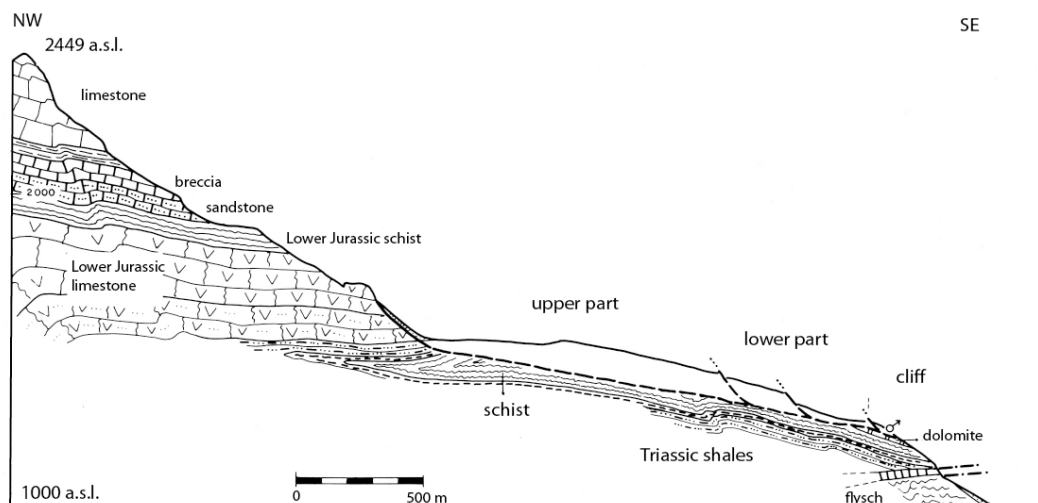
Figure 11-2: Geological cross-section Braunwald, not inflated (Schindler, 1982).

To explore the geology and to extract soil samples for laboratory testing, a total of 34 bore holes were made in the core area of Braunwald. In addition, inclinometers and piezometers were installed. In 1980, 6 bore holes were made, 10 additional ones in 1982, in a large campaign, 3 bore holes in 1983, 2 bore holes in 1985 (in addition to the installation of a deep drainage system) and 13 bore holes in 2002 in a second major campaign. On the mountain side, in the upper part of the landslide, outside the settlement area, no measuring instruments have been installed.

In a renovation project in 1985, the aforementioned deep drainage system of approximately 200 m length was installed in the village area of Grantenboden. This structure includes the main shaft Grantenboden, which could not withstand the slope displacements. This became manifest in the fraction of stiffening rings as well as in a combination of shear and flexural cracks in the piles (Dr. Von Moos AG , 2003). Also, the duct bringing the water to the main shaft has suffered severe damage in some sections and was secured with steel rings in October and December 2002 (Dr. Von Moos AG, 2003). This example clearly shows that rigid structures that pass through the slip plane are bound to be sheared and damaged.

11.2 Measurements with inclinometers and inclinodeformeters

Ongoing inclinometer measurements by IGT and third parties confirm that the landslide accelerates in the direction of the tear-off edge. In order to better characterize the landslide, these data were analysed and charted in the following map (Figure 11-3) as lines of equal velocity. By way of example, the measurements of the inclinometer KB4 and KB6 are shown. The two inclinometers lie along one line, but KB4 is much closer to the tear-off edge and measures a velocity (approx. 15–20 mm/yr) that is around twice as high as the one measured at KB6.

The acceleration towards the edge leads to a stretching of the sliding mass. Pressure measurements with the newly developed inclinodeformeter confirm this, as a decrease in pressure was measured. For more details on the pressure measurements, see Section 5.6.

a)
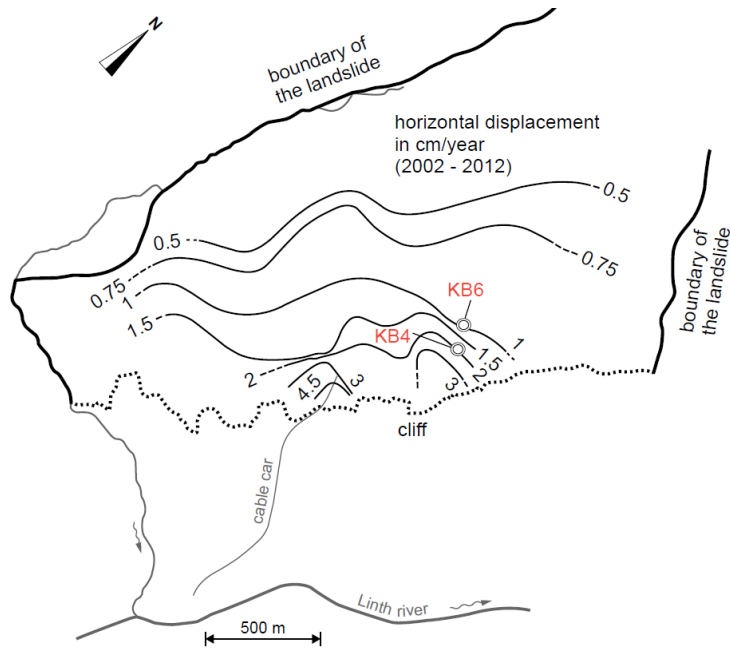
b)
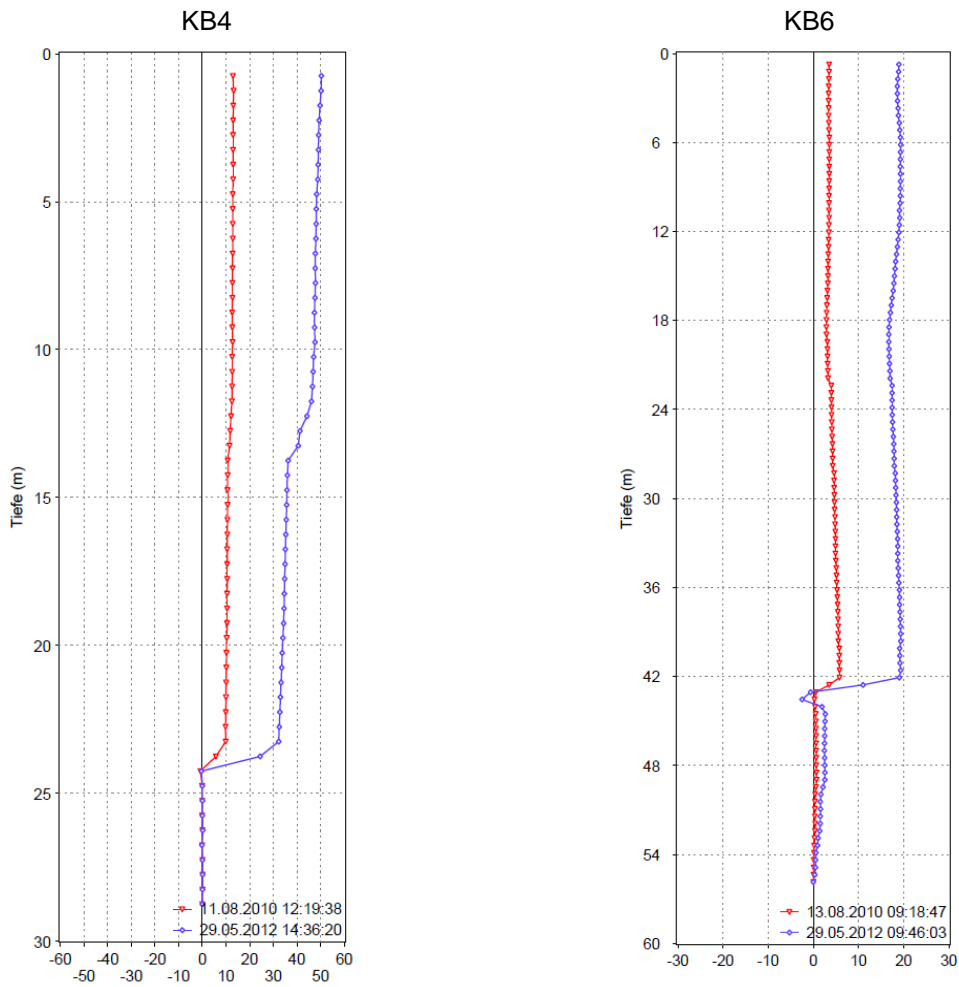
Figure 11-3: *a) Braunwald landslide: velocity isolines measured with inclinometers KB4 and KB6; b) inclinometer measurements KB4 and KB6 between 2009 and 2012*

11.3   Laboratory tests

A series of laboratory tests were carried out to find in which depth the slip plane of the landslide is located and what its shear parameters are. A first part of this investigation has already been presented in the previous report (VSS 2005/502), but is reproduced here for completeness.

Samples were taken from depths where the slip plane was expected (13.5 m and 15 m). Studies were performed with samples and documentation that has been provided by the Dr. von Moos AG.

To precisely locate the shear zone, the mineralogy was determined using samples from different areas of the Blue Clay. This allowed an initial assessment of the location of the shear zone. Subsequently, the plasticity index was determined in order to confirm the statements regarding the position of the slip plane.
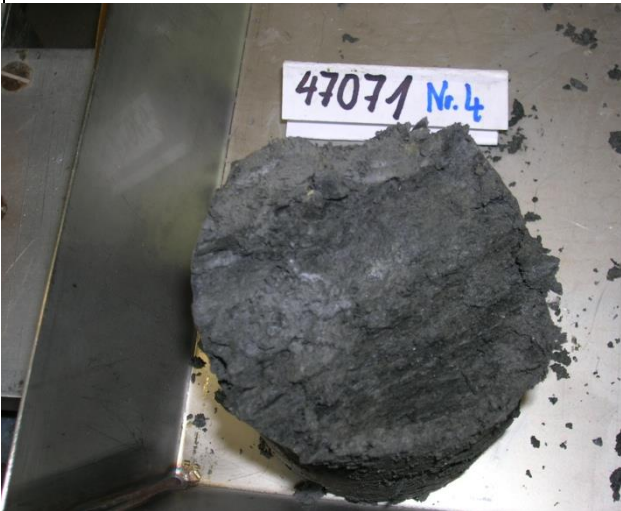
In a last step, the residual shear strength was determined on samples 47079 and 47113. Three series of shear experiments were carried out. In the first series, 'undisturbed' samples were used. Prior to the second series, the fraction greater than 2 mm was removed from the sample. For the last series, the material of the second series was again mechanically broken up in order to simulate the mechanical change in the material in the course of shearing.

11.3.1 Overview drill samples

Table 11-1: Soil samples from the main shaft.

Name	Nr.	Depth [m]	Photo
Sample 1 front	47072	13.5–13.85	
Sample 1 back	47073	13.15–13.5	
Sample 2	47079	13.15–13.85	

Sample 4	47071	14.45	
Sample 9 blue	47113 blue	15.1	
Sample 9 light	47113 light	15.1	–

11.3.2 Mineralogy

To gain information regarding the possible shear plane, the clay mineralogy of six samples from different depths was determined at IGT. Samples 47072, 47073 and 47079 (all of which are from the same depth) have a noticeably higher proportion of phyllosilicates and clay minerals relative to the other samples. Since the proportion of clay minerals is also indicative of the shear strength of a soil, it is likely that the sliding plane in this area is located at a depth of 13.2–13.9 meters.

The results of the clay-mineralogy analysis are summarized in Table 11-2.

Table 11-2: *Mineralogical content of the samples, in mass percentage.*

		47072	47073	47079	47071	47113, blue	47113, light
		Sample 1 front	Sample 1 back	Sample 2	Sample 4	Sample 9	Sample 9
Depth	[m]	13.5-13.9	13.2-13.5	13.2-13.9	14.5	15.1	15.1
Ilite/Muscovite	[%]	41.4 ± 1.9	44.8 ± 1.9	39.0 ± 1.8	19.8 ± 1.1	17.7 ± 0.9	16.9 ± 0.9
Chlorite	[%]	11.7 ± 1.7	10.3 ± 1.7	19.9 ± 2.7	4.0 ± 1.1	1.9 ± 1.0	3.9 ± 1.0
Pyrophyllite	[%]	27.0 ± 1.8	26.9 ± 1.8	18.5 ± 1.4	17.2 ± 1.2	28.1 ± 2.3	21.1 ± 1.9
Ankerite	[%]				10.4 ± 0.8	8.5 ± 0.8	5.4 ± 0.7
Calcite	[%]					1.0 ± 0.3	1.8 ± 0.4
Quarz	[%]	10.0 ± 1.1	8.9 ± 1.0	10.9 ± 0.8	45.4 ± 1.1	39.5 ± 0.9	48.3 ± 1.0
Pyrite	[%]	5.8 ± 0.7	5.1 ± 0.7	4.5 ± 0.5	1.2 ± 0.3	1.3 ± 0.3	0.9 ± 0.2
Rutile	[%]	4.0 ± 0.5	4.0 ± 0.5	3.2 ± 0.4	1.8 ± 0.3	1.8 ± 0.3	1.7 ± 0.3
Phyllosilicates/ Clay minerals	[%]	80.1 ± 5.4	82.0 ± 5.4	77.4 ± 5.9	41.0 ± 3.4	47.7 ± 4.2	41.9 ± 3.8

In order to obtain sufficient sample material for the ring-shear experiments, the blue and the light parts of sample 47113 had to be mixed, which was justified by their same mineralogical composition.

11.3.3 Water content

The water content was determined for the same set of samples; the results are summarized in the following table.

Table 11-3: Sample water content.

	47072	**47073**	**47079**	**47071**	**47113, blue**	**47113, light**
	Sample 1 front	Sample 1 back	Sample 2	Sample 4	Sample 9	Sample 9
[m]	13.5-13.9	13.2-13.5	13.2-13.9	14.5	15.1	15.1
W [%]	9.5	14.5	8.6	5.6	-	-

11.3.4 Plasticity properties

The liquid and plastic limits were determined according to standard SN 670 345a.

Plasticity and liquidity were determined in a number of samples. The results are summarized in *Table 11-4*. This study confirmed the results of the clay-mineralogy determination and helped to keep the required shear tests to a minimum.

Table 11-4: Plasticity properties.

		47072	**47079**	**47071**	**47113**
		mixed	Sample 2	Sample 4	Sample 9
Depth	[m]	13.5-13.9	13.2-13.9	14.5	15.1
Plastic limit	w_P	17.18%	15.21%	13.94%	12.77%
Liquid limit	w_L	28.80%	26.90%	22.30%	21.60%
Plasticity index	I_P	11.62%	11.69%	8.36%	8.83%

This study indicates that samples 47072, 47073 and 47079 have a higher plasticity compared to samples 47071 and 47113. This suggests that the shear surface has developed most likely in the area of samples 47072, 47073 and 47079, thus confirming the tentative finding of the clay-mineralogy study.

11.3.5 Grain-size distribution

We determined the particle-size distribution for samples 47079 and 47113, according to standard SN 670 810, and a sedimentation analysis was performed according to standard SN 670 816a using the hydrometer method. The classification was carried out according to standard SN 670 004-2a-NA.

The sieve curves show that sample 47079 consists of silty to clayey sand. A closer look revealed that the grains from the gravel and sand fraction (slate crush fragments) can be broken up mechanically without much effort.
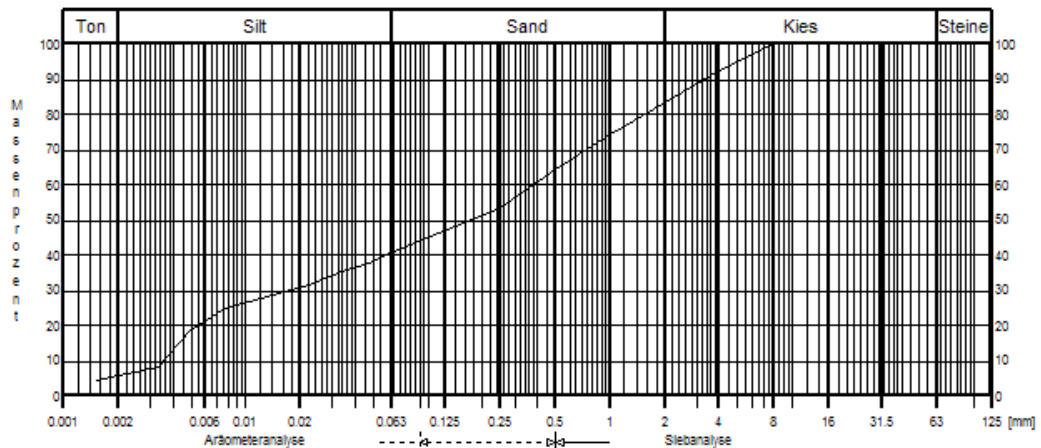
Figure 11-4: *Particle-size distribution of sample 47079, shown as a summation curve.*

As the shear deformations in the shear zone are sufficiently large to further reduce the size of these particles, the ring-shear tests with 'undisturbed' and sieved samples were complemented with tests with mechanically crushed samples.
Sample 9 is a silty sand. Again, it was found that the fragments from the gravel and sand fraction could be reduced further in size without much mechanical effort. Therefore, also sample 47113 was mechanically pre-processed for the last series of shear tests.
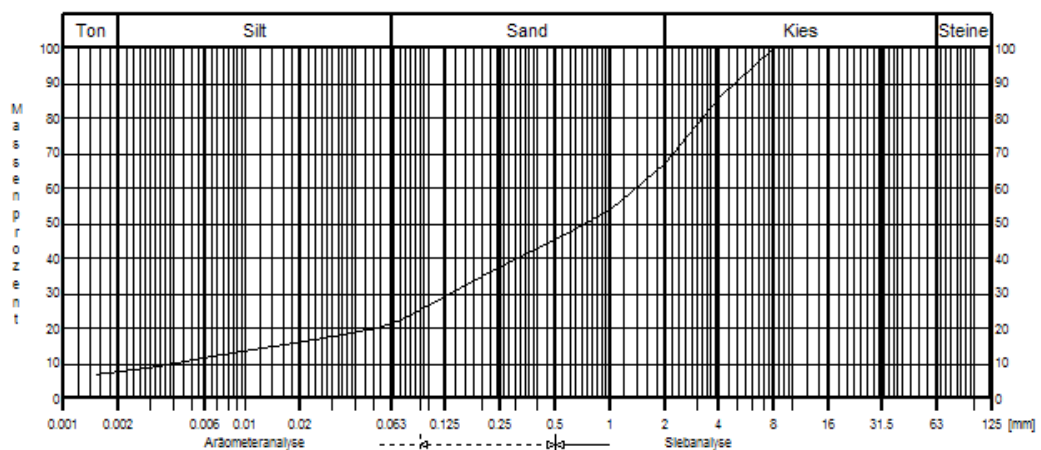
Figure 11-5: *Particle-size distribution of sample 47113, shown as a summation curve.*

11.3.6 Electron Microscopy

Sample 47079 was also examined by environmental scanning electron microscopy (ESEM). The results are shown in the following figures.
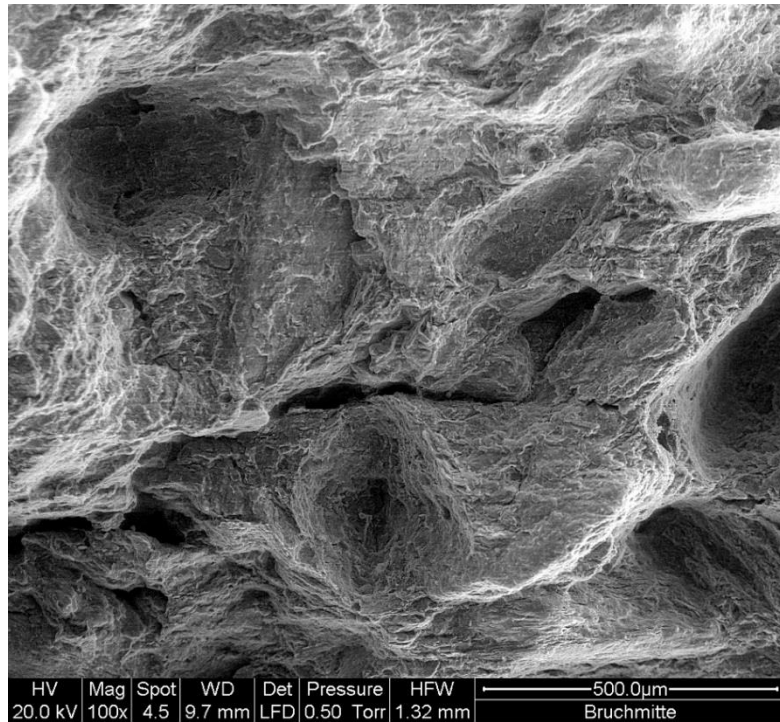
Figure 11-6: *Centre of the specimen (100-fold magnification).*
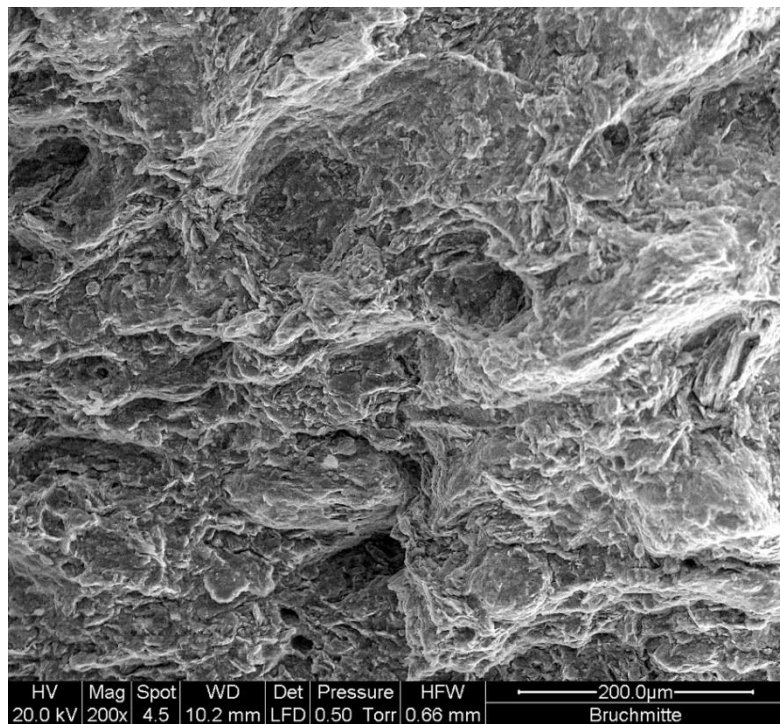
Figure 11-7: *Centre of the specimen (200-fold magnification).*
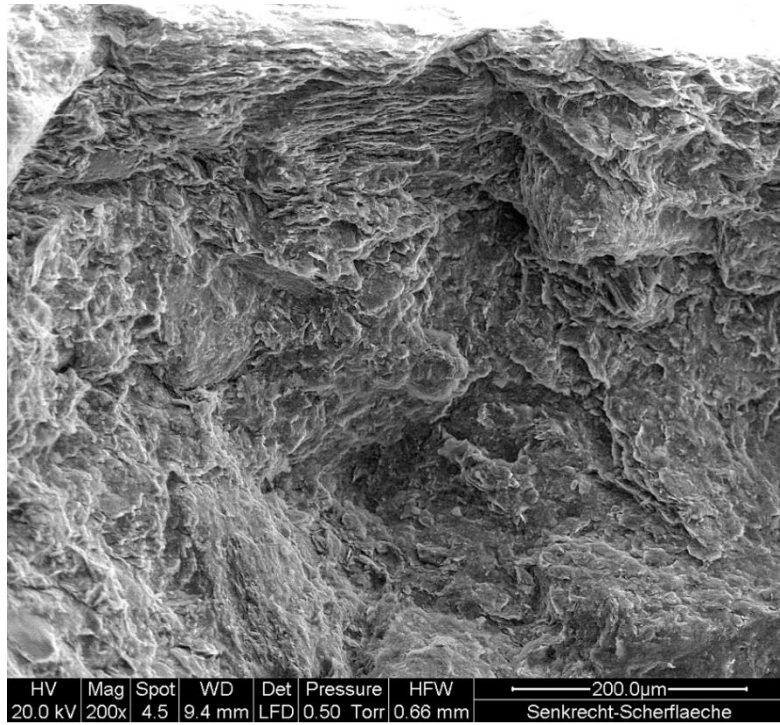
Figure 11-8: Shear side (top) of the specimen (200-fold magnification).
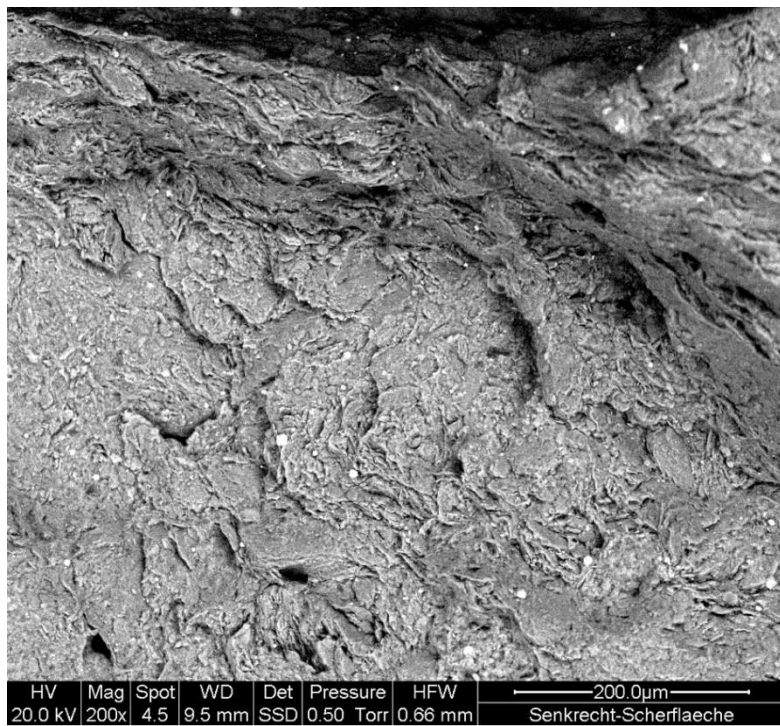
Figure 11-9: Shear side (top) of the specimen (200-fold magnification).
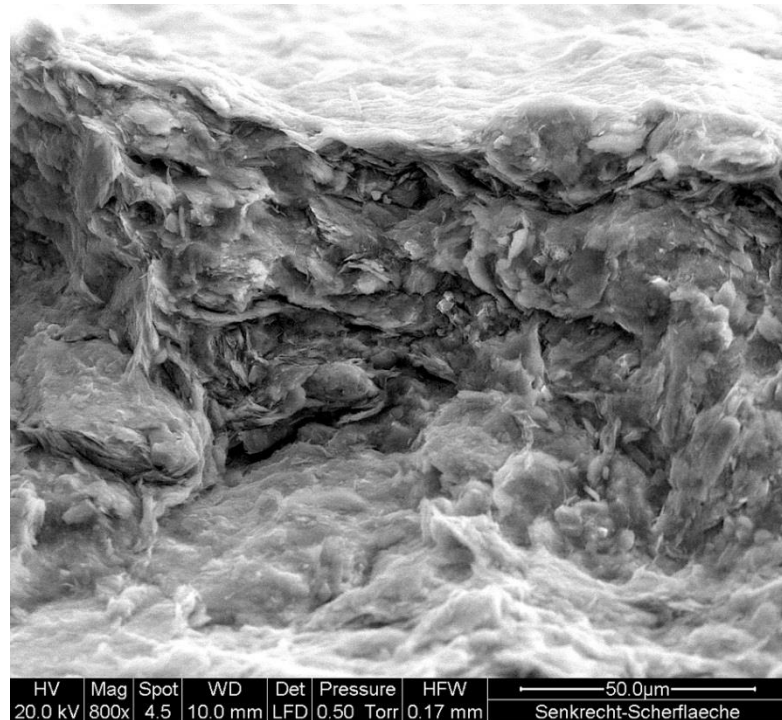
Figure 11-10: *Shear side (top) of the specimen (800-fold magnification).*

In the ESEM pictures, a shear surface can be seen (alignment of the particles, in particular directly on the surface, Figure 11-10, see also Figure 11-8 and Figure 11-9). The layer is irregular in appearance and thickness (50–100 μm). At the centre of the specimen, the particles are oriented to a lesser degree and, in addition, pores or torn-out coarser particles are observed (Figure 11-6 and Figure 11-7).

11.3.7   Residual shear strength

To determine the residual shear strength, the ring-shear apparatus at IGT was used. Three separate series ('undisturbed', sieved and mechanically processed) were carried out (see also report VSS 2005/200). In these experiments, the samples were first consolidated at a load level of 100 and 200 kPa, and then sheared at a speed of 0.01 mm/min.

In addition, the measurements with the undisturbed and sieved samples were performed at different speeds (0.005 to 0.5 mm/min). The differences in shear stresses turned out to be marginal and not unambiguous. For this reason, these data are omitted here and the discussion focuses on the experiments carried out with a speed of 0.01 mm/min.

Following the consolidation of the pores, the samples were sheared at a rate of 0.01 mm/min until a decrease in shear strength was found. Then the speed was increased to 0.1 mm/min to reach more quickly longer shear displacements. Finally, the speed was again reduced to 0.01 mm/min, in order to obtain the residual shear strength without the influence of excess pore water pressure in the shear zone.

All experiments were performed on consolidated and drained samples, as no excess pore water pressures can build up at such a slow shift speeds (Braunwald: a few centimetres per year).

11.3.8 'Undisturbed' samples

In the first round, ring-shear tests were performed using the 'undisturbed' samples 47079 and 47113. However, the friction angles in these experiments was clearly too high (25.6° for sample 47079 and 26.6° for sample 47113), because at these friction angles the slope would be stable. (See also report VSS 2005/200.)

11.3.9 Sieved samples

As mineralogy suggests that the material composition of sample 47079 is key for the shearing, and as coarser particles are further crushed during the shearing process, we performed a second series of experiments, using sieved samples. First, the fraction with grain size larger than 2 mm was removed from the sample material. Then, ring-shear tests were again performed at a speed of 0.01 mm/min and a normal stress of approx.100 and 200 kPa. (See also report VSS 2005/200.)

The friction angle for sample 47079 was determined to be 21.3°. By contrast, calculations of the friction angle on the basis of the safety factor for stability calculations indicate that the friction angle at the current water level must be less than 18°. This difference can be explained by the high mechanical stress on the material in the shear zone, which results in the material being continuously crushed in this zone. Therefore, the sample was mechanically prepared to take this aspect into account. Furthermore, ring-shear tests of Rageth Riet (1987) on samples from the shear zone suggest a friction angle of 13° to 15°; unfortunately, however, the documentation for these tests is incomplete, such that no statement can be made regarding a possible treatment of the sample material prior to the tests.

11.3.10 Mechanically processed samples

In order to simulate the high mechanical stress on the sample material and to shorten the duration of the ring-shear tests, samples 47079 and 47113 were mechanically preprocessed. Then ring-shear tests were performed on two samples at a normal stress of about 100 and 200 kPa (the latter only for sample 47079).

The residual friction angle was 15.2° for sample 47079 and 18.7° for sample 47113.

Figure 11-11: *Shear surface developed on sample 47079.*

11.3.11 Comparison of the results of the various ring-shear tests

A comparison of the results of the ring-shear tests using samples 47079 and 47113, respectively, shows that the residual friction angle of sample 47079 (15.2°) is smaller than that of sample 47079 (18.7°). This indicates that a shear zone is more likely to develop in the area where sample 47079 was extracted.

The shear tests with different shear rates have shown only marginal and unambiguous differences in shear resistance.

During the execution of the tests, the prior application of mechanical stress turned out to be decisive for obtaining a reliable residual friction angle, as the structure of the shale is easily destroyed.

The results of the test series are summarised in the following table and in Figure 11-12 Figure 11-14.

Table 11-5: *Internal friction angles obtained in the different experiments.*

Sample	Depth	'undisturbed'	sieved	processed
	[m]	φ'[°]	φ'[°]	φ'[°]
47079	13.5	25.7	21.3	15.2
47113	15.0	26.6	-	18.7
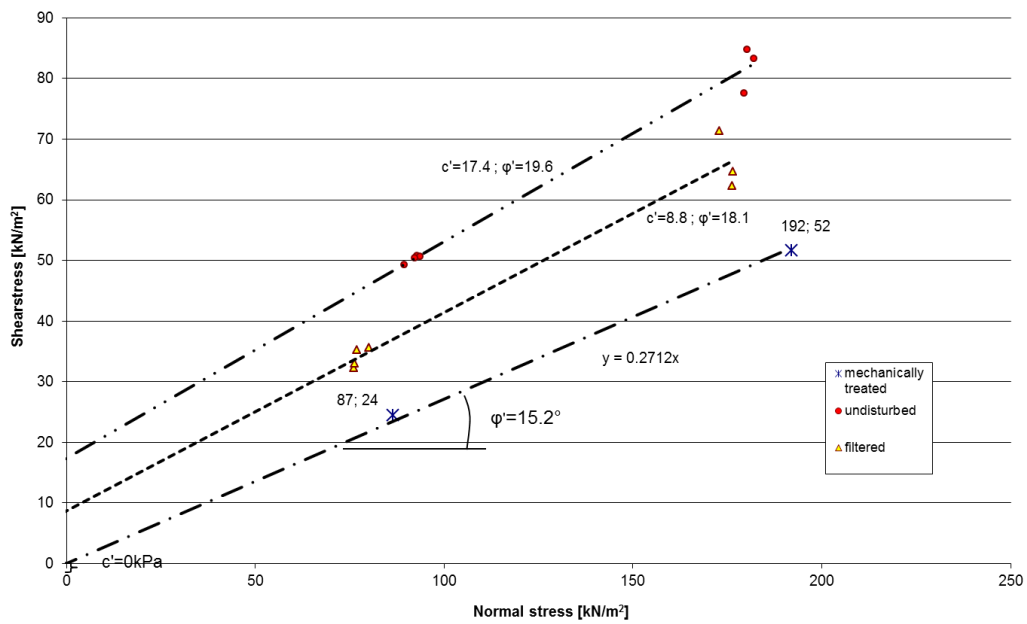
Figure 11-12: *Results of the ring-shear tests using sample 47079. (Regression with parameters φ' and c'.)*
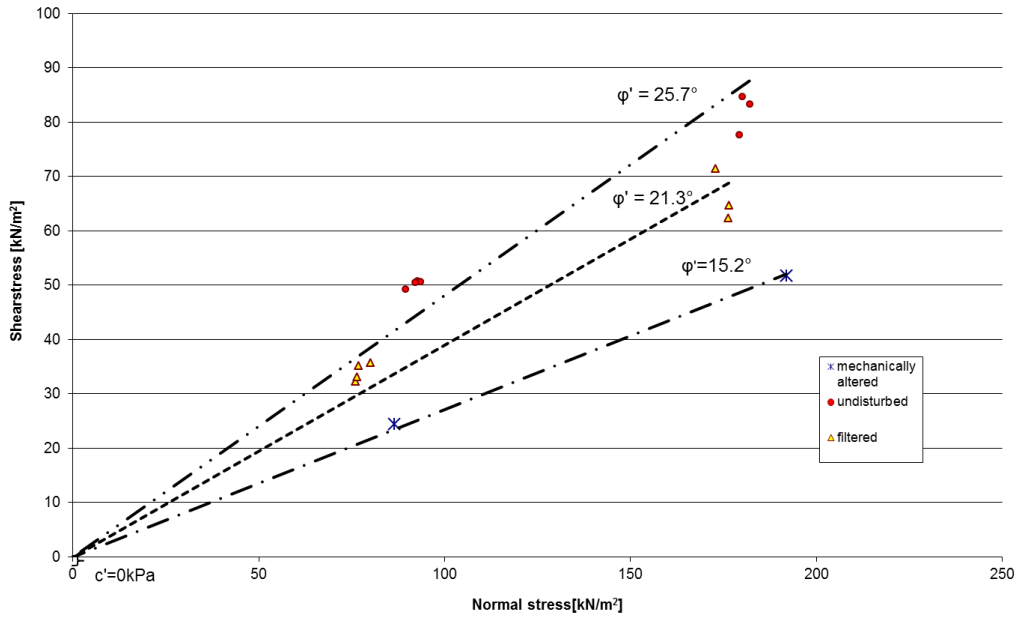
Figure 11-13: *Results of the ring-shear tests using sample 47079. (Regression with parameter φ'.)*
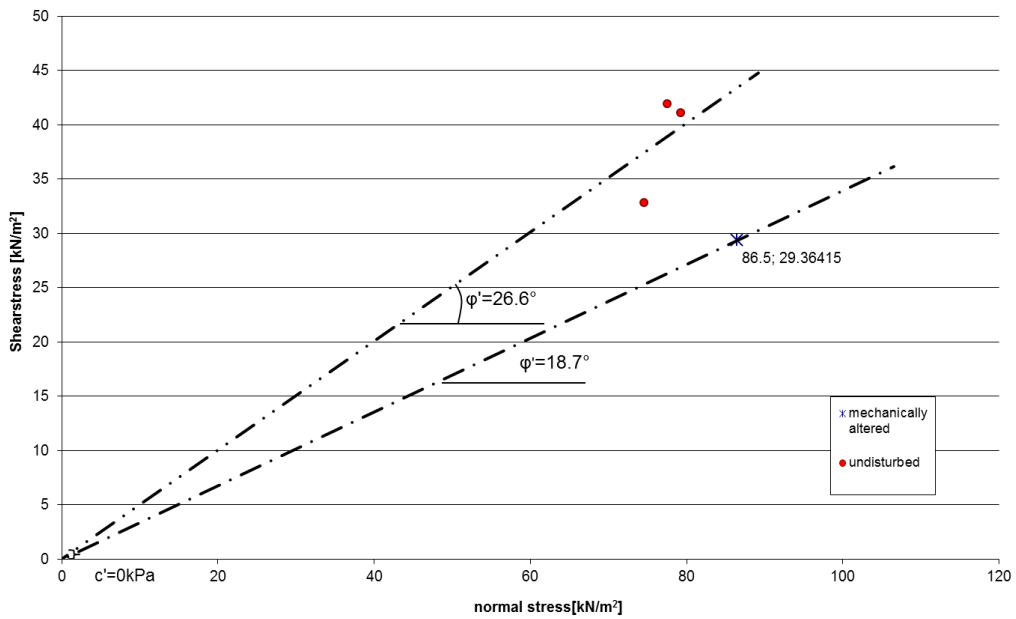
Figure 11-14: *Results of the ring-shear tests using sample 47113. (Regression with parameter φ' only.)*

11.4   Calculation of the friction angle from the slope stability

In order to further bound the value for the friction angle of the shear zone, the slope stability was calculated for different friction angles and compared with the results obtained in the laboratory tests.

For the calculations we used the data for "back deep water table" from report 7008 of Dr. von Moos AG (Von Moos, 2003). The calculations were made with the program Slope/W (Geo-Slope International).

In the calculation, the friction angle in the layer above the Blue Clay was fixed at 30°. The friction angle of the Blue Clay, on the other hand, was varied. The results of this calculation are shown in Table 5. The calculation suggests that the friction angle for the shear zone in the Blue Clay must be less than 18°.
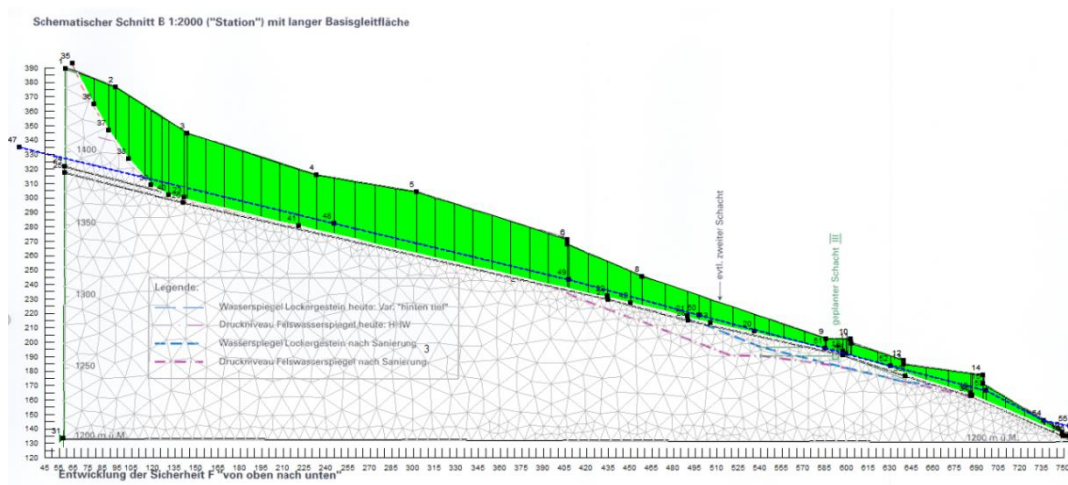
Figure 11-15: *Cross-section from report 7008 (Von Moss, 2003) used in our calculation.*

Table 11-6: *Safety factor for different friction angles for current groundwater table.*

φ'_{res} [°]	Safety factor
12	0.71
13	0.76
14	0.81
15	0.86
16	0.91
17	0.95
18	1.00
19	1.05
20	1.10

←——— 15.2°, sample 47079 (at friction angle 15)

←——— 18.7°, sample 47113 (between 18 and 19)

In addition, a calculation assuming total drainage of the Blue Clay layer was performed. The same cross-section was used. However, the groundwater table was lowered to below the Blue Clay layer. The results of this calculation are summarised in Table 6.

Table 11-7: *Safety factor for different friction angles for complete lowering of the groundwater table.*

φ'_{res} [°]	Safety factor
12	0.77
13	0.82
14	0.88
15	0.93
16	0.98
17	1.04
18	1.09
19	1.14
20	1.20

←——— 15.2°, sample 47079 (at friction angle 15)

←——— 18.7°, sample 47113 (between 18 and 19)

If we assume that the material found in the shear zone today has been mechanically stressed to a level that the friction angles are in the range found in the experiments with mechanically treated samples, then even a total lowering of the groundwater table to below the Blue Clay layer would not lead to a complete stabilization of the slope, granted that the composition of the shear zone is similar to that of sample 47079.

However, these are only preliminary studies, which only provide first statements concerning the overall stability. They cannot predict to what extent the landslide can be slowed down by drainage measures. This would require a more detailed understanding regarding the mechanism underlying the landslide.

11.5   Conclusions

In the case of the Braunwald landslide, the studies started in the previous project were further expanded and supplemented, with the goal of narrowing down as precisely as possible the location and the parameters of the shear zone. In addition, more field measurements were carried out, including such with the newly developed inclinodeformeter.

The latter made it possible to gain fuller insight regarding the large-scale behaviour of the landslide. Inclinodeformeter measurements enabled to understand the pressure decrease in the landslide in terms of the different speeds of the sliding mass. Moreover, a velocity map of the entire landslide was created by evaluating the displacement data.

Additional clay-mineralogy studies, together with determinations of the plasticity and the friction angle, have shown that the shear surface is formed most likely in the range of samples 47072, 47073 and 47079, which corresponds to a depth of approximately 13.5 metres.

Additional ring-shear tests on mechanically treated soil samples have shown that the present condition of the soil due to the mechanical stress that acts on it is essential.
These experiments were complemented by calculations of the stability, which also justified the assumption that the shear zone is at the depth of samples 47072, 47073 and 47079.
The friction angle of the mechanically treated sample 47113 is higher than 18°, which means that at this depth no shear zone could have formed with the current groundwater level, even if very large mechanical stresses acted on the material in the past.

If a very large mechanical stress is assumed in the shear zone and the same material as in samples 47072, 47073 and 47079 is present in the shear plane, then even a complete lowering of the groundwater table to below the Blue Clay layer cold not completely stabilise the slope.
However, a slowdown of the slide in the range of Braunwald by an additional lowering is undisputed. A prediction of the reduction of the displacement speeds, however, is very difficult.
More precise statements about the development of the landslide require the development of further models that represent the mechanical behaviour of the landslide in more detail.
Since the landslide in Braunwald is a complex mechanical system, it is difficult to develop *a priori* correct material models. Therefore, an approach has been developed at IGT in which not only information on the model parameters can be obtained by analysing the measurement data, but also material models for the landslide can be developed directly from their behaviour.

References

Dr. Von Moos AG (2003). "Rutschgebiet Braunwald, Sondier- und Messkampagne 2002/03, Stabilitätsbetrachtungen, Bauliche Sanierungsmöglichkeiten", *Bericht Nr. 7008* für die Entwässerungskorporation Braunwald, 8784 Braunwald.

Galluser, H. (1981). "Braunwald – Entwässerung – Gesachichtliches und Gedanken von Hans Gallusser", Küsnacht, 30. September 1981.

Rageth, R. (1987). "Analyse und Sanierungsmöglichkeiten grosser Rutschgebiete – Braunwald, Unterlagen zur Bauwerksbesichtigung vom 30. 10. 1987", *unvollendete Doktorarbeit* am Institut für Ingenieurgeologie der ETH Zürich

Schindler, C. (1982). "Problemreiche Hinterlassenschaften, Geologie und Wasserverhältnisse in Braunwald", Seperatdruck aus dem Neujahrsboten 1982 für das Glarnerland.

12 Study of a dormant landslide (God Ruinas, St. Moritz, Task 8)

12.1 Case description

The town of St. Moritz in Switzerland is partially built on another landslide beside the Brattas creeping landslide located in the northern part of the municipality. The second landslide is also slowly creeping, but has only been brought to people's attention after local, larger displacements caused by some building activities in summer 2006. The displacement rates are smaller (3 mm/year on average) or even close to zero in the considered area and therefore no serious problems have been caused by this landslide until then. It is obviously a special type of creeping landslide, a sort of "dormant" landslide, which is mainly set in motion when disturbing of the force and weight equilibrium in the underground caused by external factors, e.g. by building activities.

The God Ruinas slide (Figure 12-1) has a known length of 500 - 600 m and a width of 700 – 800 m in the built-up area and an average inclination of 33° in the built – up area. The upper limit of the slide, which is situated above the built-up area, could not be determined yet but might be several 100 metres uphill. The slide slows down towards the base of the Ruinas slope and eventually comes to a stand near the lake. The mechanism of the slowing down could not be determined yet, but might also be due to more stable soil or rock the base, analogous to the Brattas slide. The displacements mainly take place within the slip surface which is located in a depth of about 12 – 15 m below the ground surface.
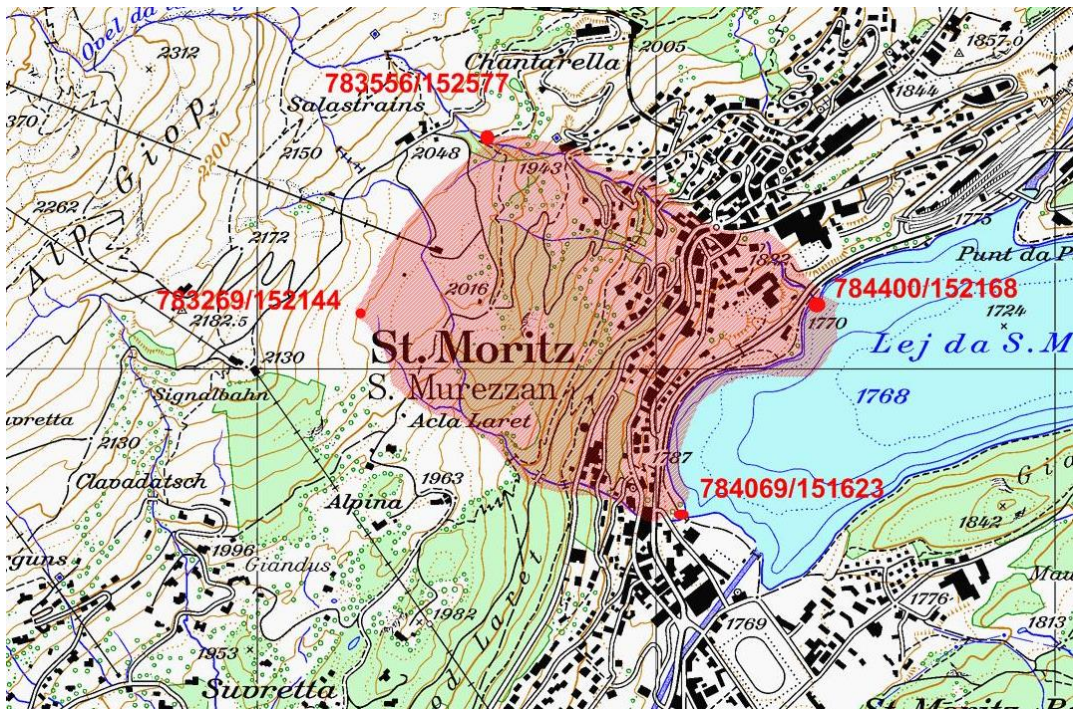
Figure 12-1: *The St. Moritz Ruinas slide in aerial photo (after Google) with approximate lower boundary of the landslide.*

12.2   Characterisation of the landslide

The landslide is located on which is sloping towards south-east having an inclination of 30 to 33° which presumably corresponds to approximately the angle of internal friction (Figure 12-2). The slope is therefore in an labile equilibrium and constantly in motion as can also be discovered on site inspections (Figure 12-3). From several borings in the centre of the landslide, the soil profile could approximately be characterised. After 1 – 2 m of artificial filling, detrital slope soil can be found down to a depth of about 15 metres. Between 15 and approximately 50 metres depth the underground consists of weathered and fissured rock (Quarz-Phyllit). Below the weathered rock, unweathered but still fissured solid gneiss rock can be found. The depth of the rock surface varies within the slide between 42 and 56 metres below ground surface. Table 12-1 gives an overview over the physical and geometrical parameters of the landslide.
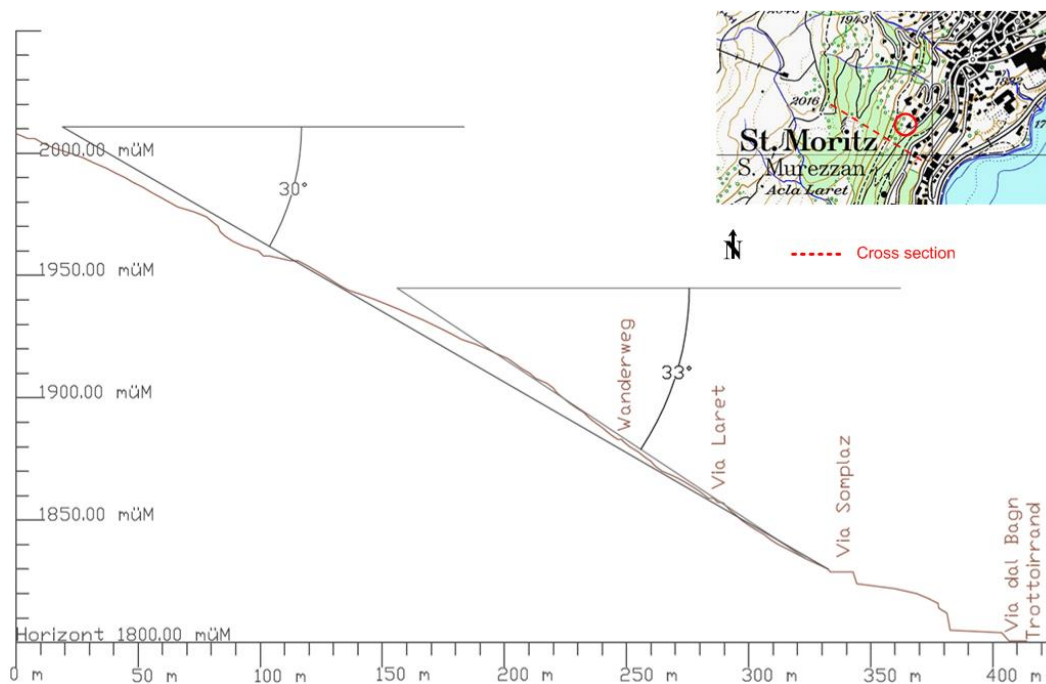
Figure 12-2: *Cross – section trough Ruinas landslide with slope inclinations.*

Table 12-1: *Summary of the physical and geometric parameters.*

Parameter description	Parameter value	Derivation
Landslide length (in built-up area)	$L \approx 550$ m	Measured (field)
Landslide width	$B \approx 750$ m	Measured (field)
Average depth of the sliding surface	$h = 15$ m	Measured (field)
Average slope inclination	$\alpha = 33°$	Measured (field)
Total unit weight of soil	$\gamma = 20$ kN$/$m^3	Measured (lab)
Unit weight of ground water	$\gamma_w = 9.81$ kN$/$m^3	Measured (lab)

a)

b)
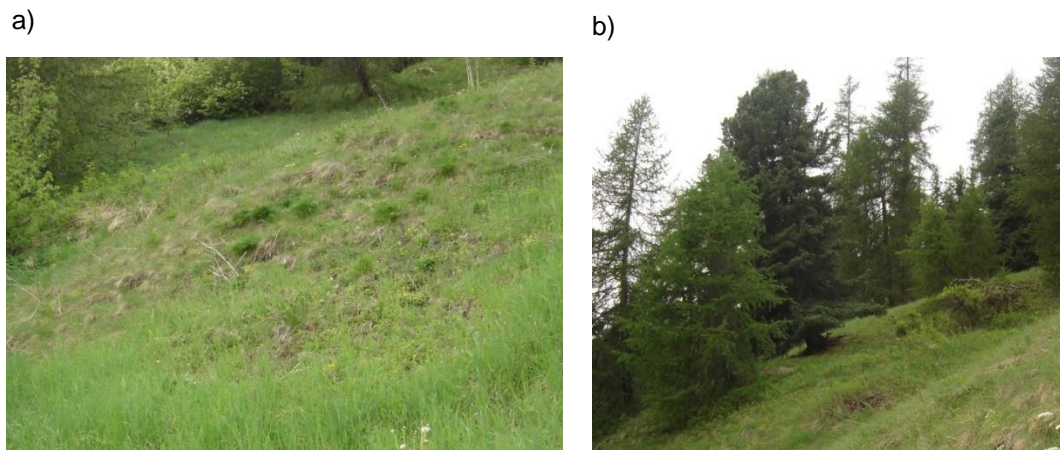
Figure 12-3: *Evidence of slope movements on the surface: (a) wavelike deformations of the surface (b) sabre-like growth of trees.*

Static and dynamic Marchetti dilatometer tests were conducted within the scope of the research work at the Institute for Geotechnical Engineering of ETH Zurich. The tests were performed on two samples, one of a depth of 5.60 – 6.30 m below ground level and another one of a depth of 10.35 – 11.35 metres. The graphical results of this investigation can be found in *Table 12-2*:

Table 12-2: *Results of the investigation.*

z	Vs	Go	Rho	Ed	Go/Ed	Id	Kd	Vs Repeatability	Var Coeff.
[m]	[m/s]	[MPa]	[kg/m^3]	[MPa]				[m/s]	[%]
5.50	539	503	1733	74.51	6.76	0.83	37.3	532,541,537,546	0.96
10.65	1156	2272	1700	38.90	58.40	2.68	1.7	1037,1276	10.34

12.3   Assessment of slope stability

The development of a reliable mechanical model for assessment of the slope stability is not yet possible since only very little is known the geomechanical properties of the slope and yet not many measurement series of the displacements or other parameters of the landslide are available. The basics for being able to assess the stability of the prone area can principally be formulated as the following questions:

- Do permanent creeping movements occur in the area of the Ruinas landslide?

- If so, to what depth do they reach down?

- How do building activities influence the movement of the slide over time?

It is obvious that a long-term well planned monitoring program is needed to be able to answer these questions. These measurements, comprising of geodesic measurements, inclinometers and fibre – optic sensors, started in summer 2008 and are still ongoing. They strongly affect the determination of the landslide boundaries which were enlarged or

shrunk from year to year. The individual monitoring systems and their results are described in the sections below.

12.3.1 Geodesic measurements based on GPS

In order to get a preliminary idea of the movements in the prone area, displacements from older geodesic measurements were calculate. The time span was from approximately 1923 to 1998 and the calculated displacements varied from one centimetre to several decimetres (Figure 12-4). Consequently, average yearly displacement rates could be calculated, information about the distribution (within a year or over the years) of the movements, however, could not be gathered. Also the reason for the movements (e.g. precipitation or building activities) could not be determined out of these information.
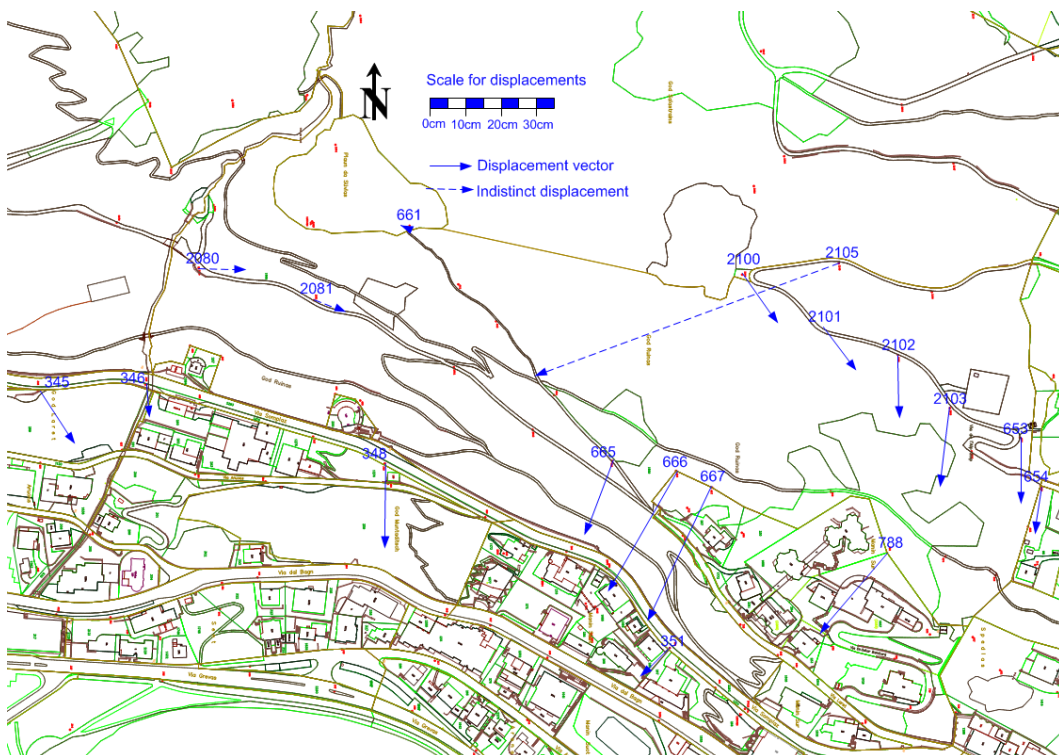
Figure 12-4: *Displacement vectors between 1923 and 1998 after GEO Grischa with data of Koordinatenverzeichnis der Gemeinde St. Moritz.*

For the reasons mentioned above, it was decided in summer 2008 to start systematic geodetical measurements over a wide area of the landslide (Figure 12-5). It was decided to use GPS as measurement technology due to the large amount of measurement points. These measurements were repeated in the two subsequent summers (2009 and 2010).

Figure 12-5: *Overview of the measured geodetic points using GPS including the location of the installed FO sensors (blue) and location of Inclinometer (KB 0801, red).*

It however turned out soon that GPS measurements are difficult in the slope area due to limited satellite visibility and due to the insufficient precision achievable by GPS for slope displacement rates of a few millimetre per year. Thus it was decided to change the measurement method to geodetic measurements using Tachymeter.

12.3.2 Geodetical measurements based on Tachymeter

The geodesic measurements using Tachymeter instead of GPS bring an essential improvement in accuracy, which is needed to be able to measure the rather small yearly displacements. These measurements are taken every year in summer and are subsequently plotted on a map (Figure 12-6).

Figure 12-6: *Overview of the displacement vectors after measurement in summer 2013 and current circumference of the landslide prone area.*

The geodetic monitoring points serve for localisation of the landslide boundaries and for analysis of the displacement rates over different years. Based on geodetic measurement results, the presumed zone of the Ruinas landslide was updated and enlarged several times over the past years.

12.3.3 Inclinometers

A series of inclinometers were installed in the scope of monitoring activities for construction sites. They mostly are only of little help since the depth is not large enough or the provided information is very sparse. Hence a separate inclinometer was commissioned by the Institute for Geotechnical Engineering of ETH Zurich for the purpose of Ruinas landslide investigation. The inclinometer has a depth of 65 metres and its location is shown in Figure 12-5 (KB 0801). A typical measurement result of this inclinometer and the sliding surface, which can distinctively be recognised in a depth of about 13 metres, is presented in Figure 12-7.

The distribution of displacement rates over years, as mentioned above, is crucial for stability analysis of the present landslide. The evolution of these displacements on the sliding surface of Inclinometer 0801 can be found in section 7.6.1. The movement takes place at an average rate of 3 mm/year but the influence of building activities can clearly be recognised in some phases.

The installation of more Inclinometers is inevitable for determination of the depth of sliding surface over a wider area, and hence for stability analysis of the whole landslide.
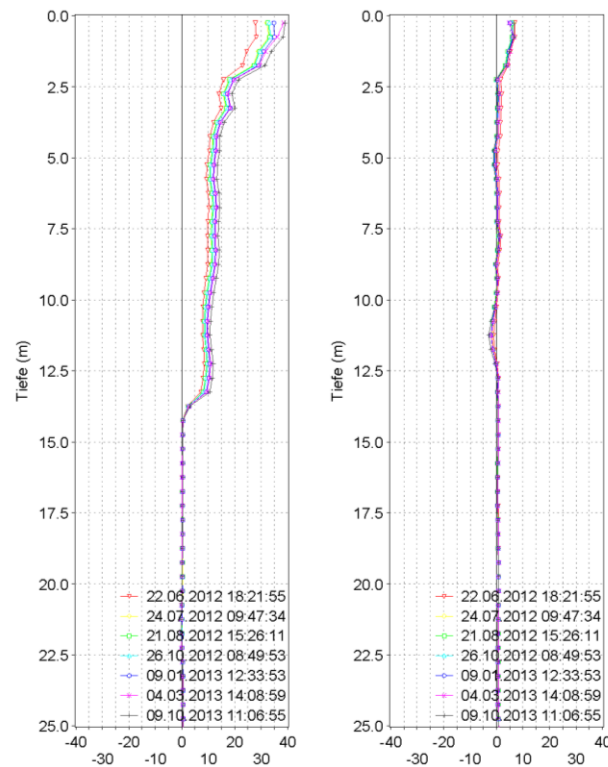
Figure 12-7: *Evolution of displacement (upper part) in Inclinometer 0801 since installation in July 2007.*

12.3.4 Fiber – optic cables

A novel and very promising monitoring method for determination of landslide boundaries are fiber – optic sensor cables. These sensors allow for measuring the axial strain along the cable with a spatial resolution of typically one metre. Using an appropriate model for slope movement thus allows for determination of landslide boundaries or even quantification of displacements. The sensors can be installed in the asphalt cover of streets or directly buried in the soil in open field. Two sensor cables of this type were installed in the area of the Ruinas landslide (Figure 12-5). One embedded in the asphalt of a street and one along a hiking path in the upper part of the slide. A typical result of such fibre – optic measurements can be found in section 7.5. Fibre – optic sensors have the advantage that many hundreds or thousands of data points can be gained over a long distance by taking only one measurement.

12.4 Measures for damage control

First investigations on the Ruinas landslide started in 2007 after large displacements due to construction works. First monitoring results showed enough evidence of the existence of a creeping landslide, and thus the municipality established a special cantonal planning zone in the area of God Ruinas in summer 2010. Subsequently further field campaigns were performed and more monitoring results could be gained.

Finally in February 2011, special building regulations were decreed as a result of these monitoring measures. The code contain describes measures which allow building with minimal disturbance of the slope, in order to no further destabilise the landslide. The regulations were established analogous to those in the neighbouring Brattas landslide and define weight compensation and equilibrium within the landslide during the construction process. In addition, prohibition of permanent ground anchors, the necessity of a rigid foundation as well as mandatory monitoring measures before, during and after construction are also listed.

12.5   Conclusion and outlook

In the case of the God Ruinas landslide in the southern part of St. Moritz, the lack of suffi-cient data especially over longer time periods also prevented here establishing a reliable model. The evaluation of the monitoring data indicates a discontinuous movement of the landslide, where larger movements are triggered by external factors such as building ac-tivities. Still the learnings from the neighboring Brattas landslide allowed coming up with building regulations that are believed to reduce damage at structures and prevent the landslide from further destabilization and acceleration.

In cooperation with the community of St. Moritz also here monitoring systems have been implemented, amongst them novel distributed fibre optic sensors embedded directly in soil, which allow to determine the boundaries of the landslide as well as measuring its development.

The God Ruinas landslide is believed to be a good example where due to sparse data experience from other sites is used for danger prevention. The installed observation measures will in the future give an insight how such a dormant landslide is reactivated and how building activity acts in this process in detail.

REFERENCES

Gemeinde St. Moritz (2008). Datenblätter über Vermessungspunkten aus dem Gebiet God Ruinas und God Salastrains, von ca. 1923 bzw. ca. 1998.

GEO Grischa. (2013). Geodätische Überwachungsmessung Gebiet God Ruinas (3. Fol-gemessung). GEO Grischa AG, St. Moritz.

Hauswirth, D., Iten, M. & Puzrin, A.M. (2012). Detection of ground movements using soil-embedded distributed fiber optic sensors. Proc. of the 4th Int. Conf. on Site characteriza-tion (ISC-4, Pernambuco), pp. 579-586.

IGT. (2008). Rutschung Via Laret, St. Moritz, Bericht Nr. 4709/1. Zürich: Institut für Geo-technik, ETH Zürich.

IGT. (2009). Rutschung Via Laret, St. Moritz, Bericht Nr. 4709/2. Zürich: Institut für Geo-technik, ETH Zürich.

IGT. (2011). Rutschung Via Laret, St. Moritz, Vorschriften über das Bauen im Gebiet God Ruinas, Bericht Nr. 4709/6. Zürich: Institut für Geotechnik, ETH Zürich.

Iten, M. (2011). Novel applications of distributed fiber-optic sensing in geotechnical engi-neering. PhD thesis No. 19632, ETH Zürich.

13   Concept for a large-scale assessment of slope stability (Leimbach, Task 9)

13.1   Introduction and previous activities

13.1.1   Basis

Based on a City Board resolution of 1974, the Institute of Geotechnical Engineering (IGT) at ETH Zurich monitors the permanent landslide at the slope of mount Uetliberg in Zurich's Leimbach quarter. In the course of developing the hazard map for the Canton of Zurich, the affected area has been assigned the need for special attention.

13.1.2   Existing data

So far, constant monitoring focused on the Sihlweid area, where, besides a number of municipal buildings (nursing home, kindergarten, school), there are also several high-rise buildings. Measurement points on the ground surface and on buildings are currently geodetically charted every three years, showing small but persistent shifts of several millimetres per year. In addition, the displacement in the sliding mass itself is measured in four bore holes. Only at two of the measurement points there are holes that extend into the stable layers. Inclinometers suggest that the slip surfaces are at depths of 16 and 29 metres, respectively. The sliding speed fluctuates between 2.5 and 6 mm per year, which means that the monitoring intensity is permanently adapted. To investigate the influence of groundwater on these fluctuations, since 2009 the water table in the slip body is monitored continuously.

In addition to the periodic evaluation and assessment of the movements, IGT has been involved in the planning-permission process, in accordance with the City Council resolution. For buildings in the Leimbach area, each client has to commission a report by a geotechnical-engineering office. For each building-permission request, that report had to be sent to IGT as well. The Institute had no judging capacity regarding geotechnical issues, but had merely to inform the building inspection that the report has been received.

These ground-investigation reports are archived at ETH and offer a broad insight into the near-surface geological conditions.

13.1.3   Need for action

In drawing up the risk map not only the Sihlweid neighbourhood but also the Grossacher and Mittelleimbach neighbourhoods were correctly classified as permanent-landslide areas (Figure 13-2). In this wider area, many homes were built since monitoring started, and they are mostly located on the sliding mass. Moreover, an evaluation by the department Geomatics and Surveying of the City of Zurich (*Geomatik + Vermessung Stadt Zürich*), which takes into account the movements over the past hundred years, suggests that in particular in the areas with new developments, larger displacements (of 10–14 mm/yr) are to be expected than in the Sihlweid region.

A comparison between the geological map of 1968 with an up-to-date version (Figure 13-1) illustrates in a particularly impressive manner how many new buildings were constructed in locations will unstable slopes and lie now in the order area (*Gebotsbereich*) of the hazard map (Figure 13-3).

The current level of information regarding large-scale slope stability is particularly insufficient for the quarters Grossacher and Mittelleimbach. Most private boreholes and inclinometers are not deep enough and were often constructed and evaluated only with a

view to individual construction projects. For the geotechnical assessment for future buildings, it is important to spatially delineate the phenomena of superficially unstable sliding mass and of the low-lying permanent landslide, in order to be able to formulate justifiable conditions for the order area of the hazard map. We therefore recommend a gradual development of a monitoring concept.
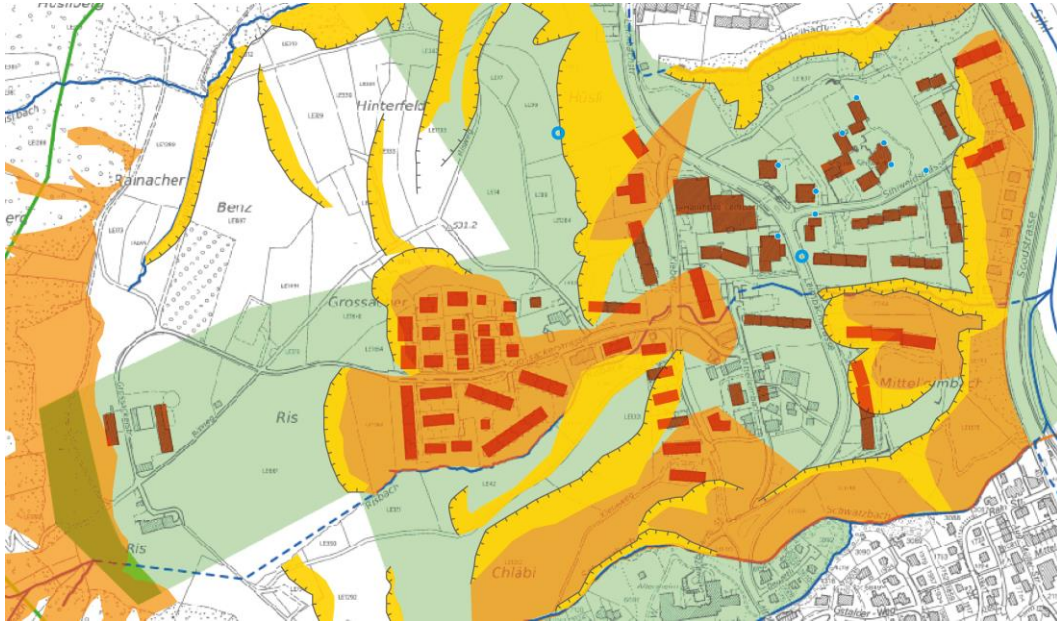
Figure 13-1: *Comparison of the hazard map (mass movement shown in green), buildings since 1968 (in red) and unstable slopes (in yellow and orange).*
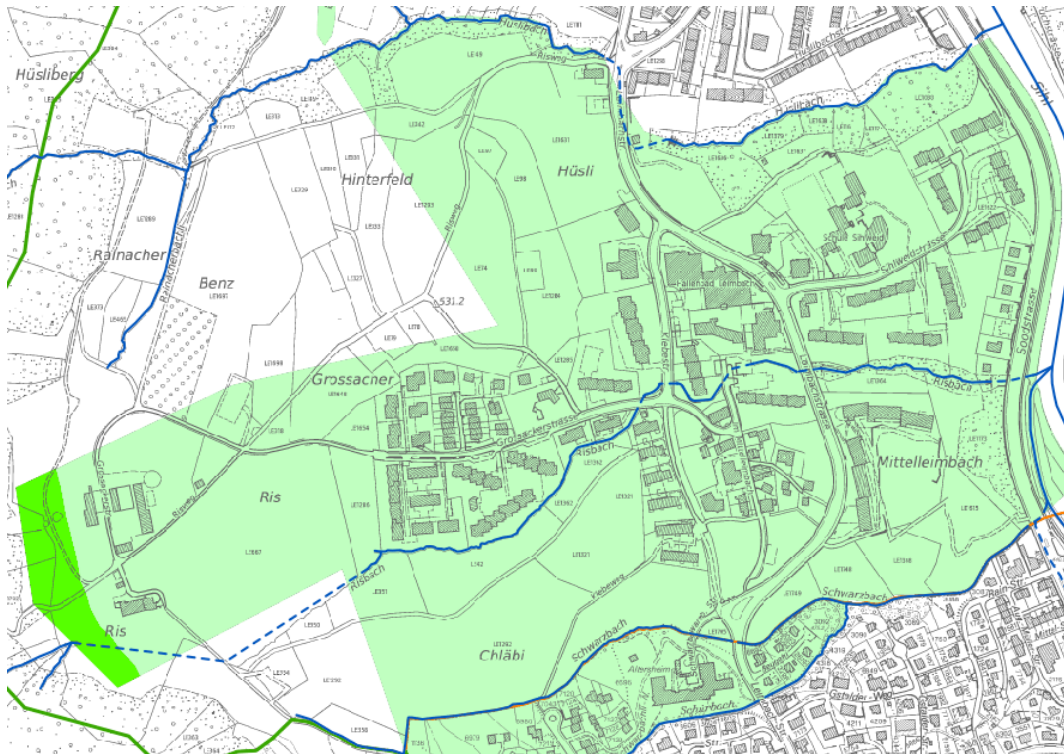
Figure 13-2: *Detail from the hazard map showing permanent landslides:*
Intensity surface for mass movements: weak (light green), medium (dark green).
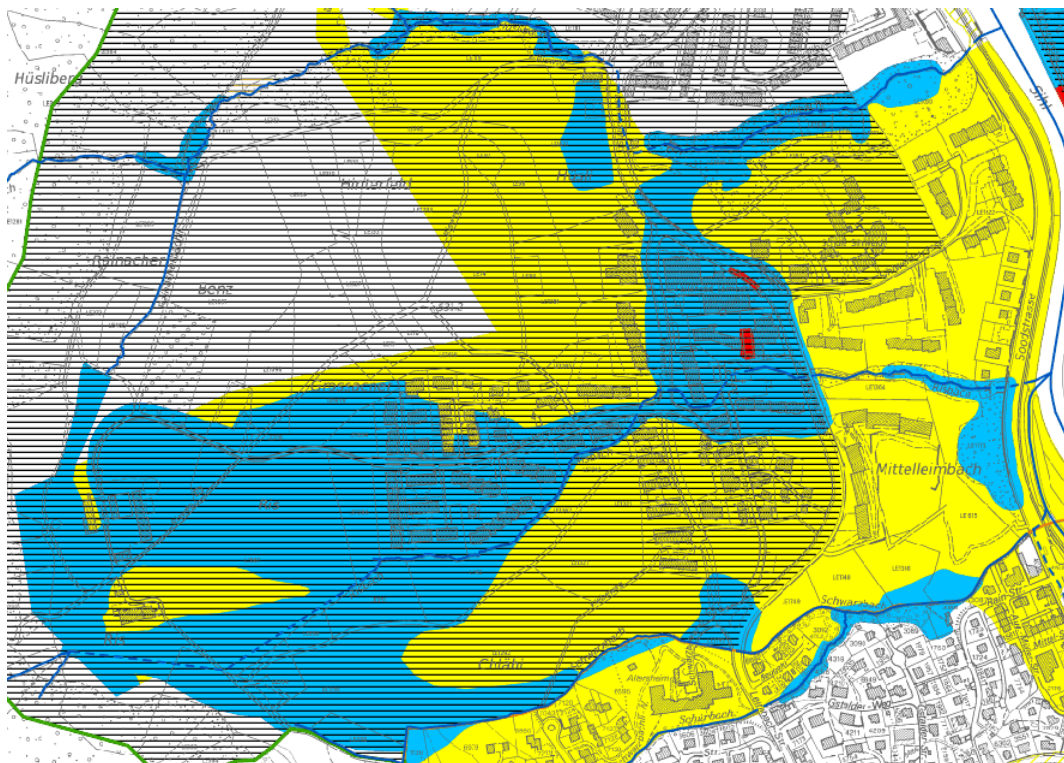
Figure 13-3: *Hazard map, detail Mittelleimbach: Order area shown in blue.*

13.2   Proposal for setting up monitoring measures

13.2.1   Phase 1: Surveying campaign (duration approx. 2 years)

In order to make a technically justifiable assessment of the large-scale slip situation in Mittelleimbach, it is necessary to first gain a fundamental understanding of the present landslide. The relevant processes have to be quantified in a spatially resolved manner before detailed monitoring and alerting measures can be conceived.

The main survey variables are therefore the spatial extent of the affected zone, the thickness of the sliding layers, and the annual displacement velocities of the individual areas. Whether critical compression zones are present and how these interact between individual regions (Grossacker ↔ Sihlweid ↔ Soodstrasse) should be determined as well.

The geotechnical documentation of past projects in this district are archived at ETH Zurich from 1968 onwards and will serve, together with the data of previous monitoring efforts, as a starting point. An inspection, including an assessment of damages on buildings, will help to evaluate the suitability of the existing structural measures on the landslide.

In addition to these documents, a first set of geodetic measurement points will be needed along two axes from the retaining wall at Soodstrasse to the topographical tear-off edge in the Ris area (see Figure 13-4). One axis is passing through the existing measuring points in the Sihlweid region, whereas the other is along Grossacherstrasse. In order to determine the depth in the upper part of the landslide, at least one central, deep bore-hole inclinometer in the Grossacher quarter is necessary. For the Sihlweid area, a sufficiently deep bore-hole inclinometer exists already.
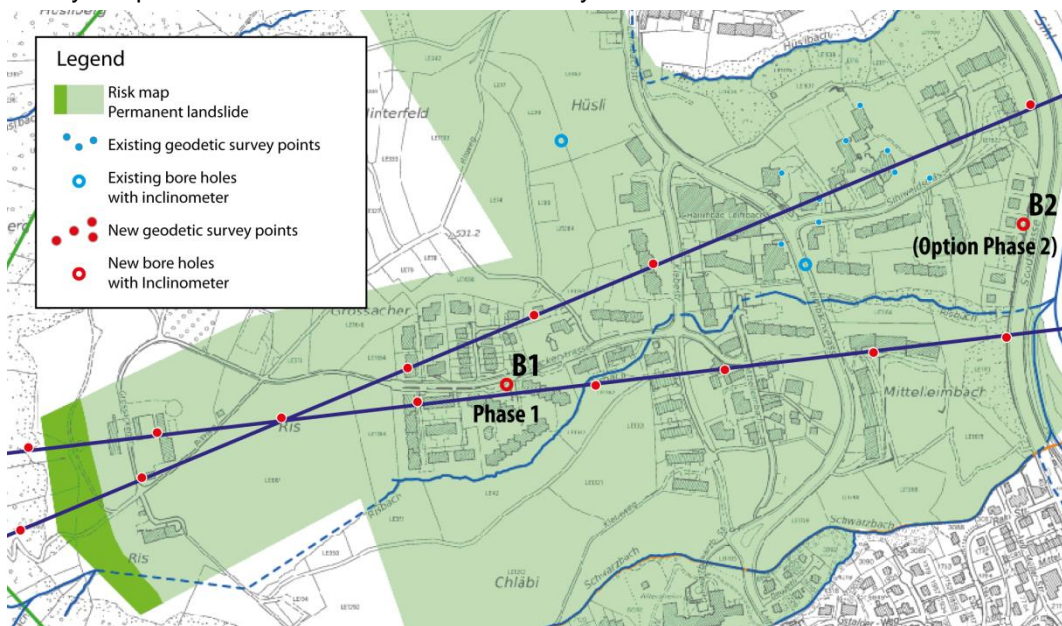
Figure 13-4: *Schematic arrangement of the surveying points.*

In summary, this phase will establish a comprehensive geotechnical soil model that describes the relevant processes with sufficient accuracy and will serve as a basis for deciding the next steps.

13.2.2 Phase 2: Risk assessment and prediction (duration approx. 2 years)

The slope stability will be assessed based on the collected data. The main objectives are to calculate the current threat posed by the persisting landslide, and to make a prediction regarding the long-term behaviour of the landslide.

The data obtained in Phase 1 will be evaluated by experts using modern methods (at IGT or in a specialized geotechnical engineering office). In particular, the risks posed by earthquakes and the impact of heavy precipitation should be taken into account.

Depending on whether the assumption that the displacements in the southern part of the area are particularly large turns out to be justified, other measures such as the back pressure on the existing support structures have to be included. For that, a further borehole with an inclinometer would be necessary in the lower region of the landslide. The potential consequences in the event of a large-scale failure of the slope should be identified and critical zones should be mapped.

The results of this phase will be compiled into a recommendation that enables a decision on the need for and the extent of permanent monitoring measures. At the same time, it should be clarified whether the slip areas are correctly represented in the hazard map.

13.2.3 Phase 3: Design of the monitoring measures (duration approx. 1 year)

At the beginning of Phase 3, and based on the information obtained so far, decisions will be made and subsequently implemented in three thematic areas:

- Permanent measures and instrumentation (permanent measuring points, measuring methods and intervals)

- Alarm concept (critical values, responsibilities, procedures)

- Adaptation and/or formulation of the legal regulations (Building Act, Building Regulations, hazard map)

Depending on the requirements, this step will involve further instrumentation of the slope with geodetic measurement points, in-place inclinometers and real-time integration of data loggers. In the case of a low failure probability, however, more intense monitoring may be unnecessary and existing measures could possibly be reduced.

Permanent monitoring is integrated in an alarm concept by defining threshold and critical values. The alarm concept should also encompass a long-term solution for the regulation of responsibilities of the various parties involved, and clearly define procedures and contact persons.

The authorities are obliged to issue instructions for building in the zone of average risk (order area). Based on the results of Phase 2, IGT can advise the authorities in preparing relevant orders such as the obligation to provide information, increased requirements and allowed or prohibited measures. This is to avoid that due to the issuance of building permits, the overall stability of the slope is reduced or that due to local interventions neighbouring buildings are damaged.

Depending on the findings of Phase 2, these directives can be similar to the City Council resolution of 1974 (for example, the mandate of creating a geotechnical report) or they can go further, such as demanding in general an assessment of the geotechnical report by a third party or obliging the client to provide information also after the construction period, or, more explicitly, requiring a mass balance at excavation or permanent and temporary relief measures.

13.2.4 Phase 4: Long-term implementation

The final phase is the implementation of the chosen permanent solutions. In doing so, the operation of the monitoring measures and of the alarm concept is to be ensured.

In addition, any construction activity in the notice and order area must be reviewed in accordance with the statutory provisions. Depending on the implemented formulations, this might result in case-specific inquiries during the building-permission process.

Profound changes in the boundary conditions (climate change, socially demanded provisions against natural hazards) can trigger a reassessment of the situation during this phase.

13.2.5 Summary of the proposed concept

Figure 13-5 summarises the steps of the proposed monitoring concept.
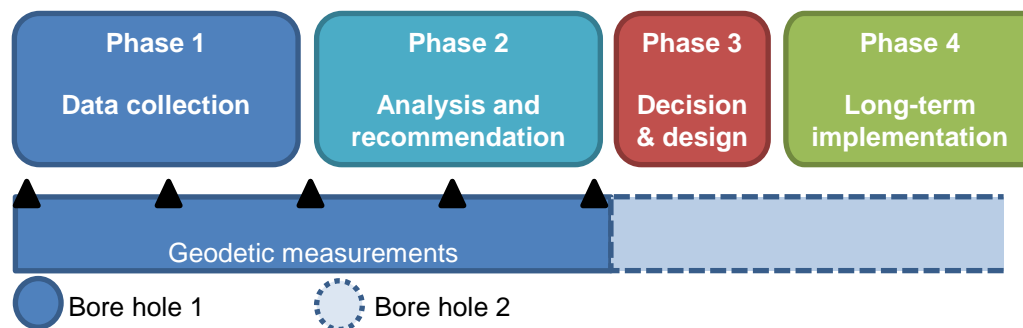
Figure 13-5: Staged design of the monitoring concept.

V.   Conclusions and recommendations (Task 10)

14   Conclusions and recommendations

14.1   Conclusions

The following main conclusions can be drawn regarding the different research tasks:

The research on the novel **inclinodeformeter (IDM)** has proven to be a success. A novel device and optimised procedures have been developed to sensitively monitor changes in lateral earth pressure. Inverse analysis of the measured changes in the shape of the cross-section of an inclinometer pipe allows to back-calculate lateral earth pressure changes in the surrounding soil. An extensive program of full-scale laboratory tests and field measurements has validated the applicability of the newly developed monitoring device to geotechnical problems. The device provides a stepping stone towards more reliable and precise measurements of changes in lateral earth pressure. Changes in dimensions of an inclinometer pipe were measured with a precision of +/–2 micrometres. Lateral earth-pressure changes are back-calculated with a precision of 0.1–0.7 kPa, depending on the stiffness of the soil and the grout surrounding the pipe. The softer the soil and the grout, the higher is the precision.

The major aspects affecting the back-calculation of pressures have been studied: these turned out to be (i) the influence of the time-dependent behaviour of the pipe, (ii) the influence of the mechanical behaviour of the grout and (iii) the effects of longitudinal bending of the inclinometer pipe. The back-calculation procedure has been successfully validated in full-scale laboratory tests.

IDM pressure measurements have been shown to provide a reliable tool for analysis and monitoring of creeping landslides. Measuring the change in shape of an inclinometer-pipe cross-section allows identification of compression and extension zones. Reasonably small pressure increments can be reliably back-calculated by applying an analytical solution which takes the time-dependency of the pipe material into account. In addition, the tangent stiffness of the soil can be obtained by combining the IDM measurements with measurements of relative displacements. Thus, the back-calculation procedure becomes independent of the soil-stiffness measurement. The lateral modulus obtained *in situ* for the incremental behaviour clearly indicates that yielding and failure occurred within the sliding layer.

The research on **distributed fibre-optic sensing technologies** has established that this approach can be a powerful tool for geotechnical monitoring, especially if the devices can be embedded directly into the soil. It was shown that soil-embedded fibre-optic cables have to provide suitable protection of the fibre. However, rigid metallic protection casings can increase the longitudinal stiffness of the cable significantly. Due to limited bonding between the cable and the surrounding soil, strain induced by local events can distribute over several metres or even tens of metres, if the cables are too stiff or not embedded adequately into the soil. This behaviour complicates the interpretation of the measurement results in field applications, as the increase in strain within the cable for a given displacement is very small and also not clearly localized. Experimental test results showed that by means of cable-surface corrugation or, even more effectively, by attaching small block anchors onto the cable, the propagation of strains into zones without soil displacement can be strongly reduced. It should be noted, however, that this improved connection to the soil may in turn reduce the sensor lifetime, as the upper limit of the sensor strain range is reached earlier for large local displacements.

A concentration of strains can also be achieved for stiff and well-protected cables, due to their elasto-plastic properties, if irreversible strains can be accepted (which is the case for monotonic loading). As experimental test results with a local displacement event showed,

once the yield limit of the metallic cable protection has been overcome, strain accumulates in zones where yielding occurred, as the stiffness is locally reduced. The propagation of strains into adjacent zones is limited, depending on the hardening properties of the cable.

As a research application, a long, soil-embedded fibre-optic sensor was incorporated into an ongoing landslide-monitoring project pursued at the Institute for Geotechnical Engineering. Whereas traditional monitoring measures such as inclinometers and geodetical surveying constituted the backbone of this project, the fibre-optic sensor application had the status of a trial project. Nonetheless, the sensor provided useful results, which are in agreement with the inclinometer and geodetical measurements. Furthermore, this field application also underlined that also other measurement technologies are not free of discrepancies and that the fibre-optic sensor is very cost-efficient compared to other technologies.

In the case of the research on **chemical and biological stabilization techniques**, the qualitative and quantitative findings of the performed experiments led to four main conclusions regarding biomineralization aspects for application involving fine-grained soils.

First, microbial carbonate precipitation successfully increases shear strength above a threshold value of the permeability, even in fine-grained soils. In this study, the minimum hydraulic conductivity was 5×10^{-9} m/s. It was shown that the presence of clay minerals does not impair the strength improvement.

Second, during the biomineralization process, the precipitated calcite reduces the hydraulic conductivity. The experimental data indicated a decrease of one order of magnitude. If during this process the permeability falls below the threshold value, soil improvement will be incomplete and heterogeneous.

Third, the application of the microbial method can be expanded to less permeable soils by increasing the hydraulic conductivity in advance by one order of magnitude. In that way, the required fluid flow during treatment can be maintained within reasonable pore-water pressures.

And forth, it was shown that with the chemical enhanced-drainage technique provides an efficient method to increase hydraulic conductivity. Increase in hydraulic conductivity of more than one order of magnitude was achieved for soils containing smectite clay minerals.

These findings also suggest that the chemical method is likely to work in soil with other clay minerals as well.

The mechanism underlying the progressive propagation of the zone of intense shearing and subsequent yielding of soil in the compression zone seems to be capable of explaining the "paradox" of the **St. Moritz landslide**, which accelerates even if the "usual suspects" are absent: increase in the yearly precipitation and pore-water pressure, and rate dependency on the sliding surface. As a result, this mechanism enables an improved assessment of the hazard posed by the landslide and suggests measures for its mitigation. The model predicts that the acceleration phase could continue until around 2025 and may cause an additional 30-% increase relative to the current displacement rates. After that phase, the slow stabilization of the landslide may be expected, provided that no increase in the yearly precipitation and pore-water pressure and no drop in the soil-yielding factor occur.

Even for this favourable scenario, however, the final displacements can become excessive for some buildings, requiring an early warning system, which is currently being installed in the Leaning Tower and within the inclinometer pipes directly in the landslide body. Further stabilization of the Leaning Tower is likely to be necessary within the next 10 years. The displacement rates, however, can only be controlled by lowering the phreatic surface with the help of a drainage system. As suggested by the proposed mechanism, however, such a system would be more effective if it had been constructed in 1980s, that is, before the earth pressure in the compression zone reached the yield stress. Thus, by predicting the time of the onset of yielding, the model can provide important information regarding the timeframe for the stabilization of constrained landslides.

The research on the **Combe Chopin and Ganter landslides** explores a simple analytical model in an attempt of quantifying the evolution of landslides stabilised by a retaining wall or by a natural barrier at the bottom of the sliding mass. Within the model assumptions,

the development in time of both the landslide displacements and the earth pressure acting on the retaining structure can be obtained in a closed form. Curiously, for the pressure evolution the solution is identical to the expression for the average degree of consolidation obtained by Tezaghi for the classical problem of one-dimensional consolidation. The model provides a clear definition of the long-term safety factor for a stabilised landslide. Depending on the value of this safety factor, the landslide will either slow down eventually or approach asymptotically final displacements given by the model, or the soil behind the retaining wall will experience passive failure at a moment in time that can be predicted within the model. The model also provides insight into the post-failure evolution of the landslide.

Two case studies based on the monitoring data from the Combe Chopin and Ganter landslides in Switzerland were used to validate the model. For the Combe Chopin landslide, which has a long-term safety factor lager than unity, the model demonstrated its ability to predict final downhill displacements and their development in time. For the Ganter landslide, which has reached the passive pressure at the bottom, failed and achieved the steady-state velocity before displacement measurements commenced, the model correctly predicted the long-term landslide evolution and effects of drainage and erosion on the displacement rates. In both cases the model enables to back-calculate apparent shear viscosities for soil on the sliding surface, avoiding high uncertainties associated with the determination of viscosity coefficients in laboratory tests.

For the **Braunwald landslide**, the laboratory-test and field-observation program has been intensified to obtain more insight into the behaviour of the landslide. Field observation using inklinometer probes and the novel inclinodeformeter provided the basis for determining and mapping the different velocities in the landslide, leading to the conclusion that the landslide experiences stretching. The inclinodeformeter measurements support this conclusion, as they show a drop in lateral earth pressures towards the foot of the landslide.

The extended laboratory testing allowed identifying the most likely depth of the sliding surface as well as determining a narrow range of potential parameters. It has also been shown that the intense mechanical exposure, which the material in the shear zone has been subjected to, needs to be considered in order to find the parameters of the slip surface.

In addition, a simple stability back analysis of the landslide has been performed to verify the parameters determined in laboratory tests and to determine the influence of different pore pressures.

All these procedures enabled a determination of the likely parameters of the landslides slip surface which can be used in later work either for stability calculations or for further modelling of the landslide in order to capture its more complex mechanical behaviours, which would be necessary to analyse rates of deformation and pressure development in more depth.

Also in the case of the **God Ruinas landslide** in the southern part of St. Moritz, the lack of sufficient data especially over longer time periods prevented establishing a reliable model. Yet, the insights obtained into the properties and behaviour of the neighbouring Brattas landslide allowed to formulate building regulations aimed at reducing damage of structures and preventing the landslide from destabilising further and accelerating.

In cooperation with the municipality of St. Moritz also here monitoring systems have been implemented, amongst them novel distributed fibre-optic sensors embedded directly into soil, which provided a tool for determining the boundaries of the landslide and measuring its development.

The God Ruinas landslide is believed to be a good example for a case where despite sparse data on the landslide under consideration, experience from other sites can be used for danger prevention. In the future, the installed observation measures will give insight into how such a dormant landslide may be reactivated and how building activity influences this process. Evaluating the effectiveness of the new building regulations will allow determining to which degree appropriate regulation of construction activity can help keeping such a landslide stable.

The **Leimbach** landslide has been monitored continuously. However, due to sparse spatial data and small deformation rates at the monitoring points, no detailed statement can

be made here yet. But since the constructed area on the landslide has expanded in the last years into areas with higher deformation rates, IGT started, in cooperation with the city of Zurich, developing a concept to properly capture the risks associated with that landslide. Therefore more extensive monitoring has been proposed to obtain data that should enable a back-calculation of important parameters, such as the stiffness of the sliding layer, the application of an existing prediction model or the derivation of a new mechanism to capture the future evolution of the landslide.

Based on the experience gained from other landslides, an effective monitoring system was proposed in advance and will hopefully also be integrated into adopted building regulations in the area if necessary.

Overall, during this project it was possible, building upon the previous project, to develop new approaches for the monitoring and analysis of creeping landslides, affecting the transportation infrastructure, and to apply these approaches to a number of landslides in Switzerland. Moreover, novel approaches to landslide stabilization have been explored. Results for the three main goals have been achieved: (i) New monitoring technologies have been developed and tested, (ii) models for landslide analysis have been developed and (iii) new stabilization measures have been explored.

During this project it has been confirmed that the most reliable approach to the long-term displacement and stability analysis of landslides is based on back-calculation (inverse analysis) of soil parameters from observed displacements and measured earth and water pressures in the sliding layer. Novel fibre-optic strain measurement technology has proven to be a useful complement to conventional geodesic measurements and provides unique data for the inverse analysis of the landslides stability and displacements. The novel inclinodefometer (IDM) was successfully applied to a number of landslides in Switzerland and enabled, for the first time, to reliably measure earth pressure in the sliding layer, providing more unique data for the analysis of landslides. Results of bio-chemical landslide stabilization by increased drainage and shear strength have been promising, however further research has to be conducted in this field. Finally, several concepts and models have been established and analytical solutions have been provided to capture the evolution of landslides and to investigate their stability. These results may be used to predict the behaviour of landslides, to analyse the interaction of landslides and roads, and to plan stabilization measures.

14.2 Recommendations

Finally the following recommendations regarding the different research topics can be given:

The research on the **Inclinodeformeter** looks very promising, especially since only standard and already installed inclinometer pipes are used. The device and procedure developed here provide a basis for its application in geotechnical practice. Additional research could take this approach to the next level and to explore its full potential.

Although the mechanical interaction between the soil and the monitoring tools has been investigated through numerous laboratory tests, full-scale laboratory tests and numerical analysis, further research should be carried out on the influence of the mechanical behaviour of the grout and the influence of longitudinal pipe bending. The strategic direction of research should be to focus on the improvement of the pipe and on further applications of the presented approach.

The research on **distributed fibre-optic strain measurements** has also given researches and engineers a new tool for gaining further insight into complex landslides. The obtained results and procedures may be used by researchers and practitioners in order to use this new technology and get reliable results.

The investigations regarding **bio-chemical stabilization** of landslides have formed a solid basis for further research in this field. This research has shown clear evidence that the

combination of chemically enhanced drainage and biological shear-strength improvement may be a promising route to stabilizing large landslides. However deeper understanding of the prevailing processes will be necessary as well as tests on other types of soil.

The research on landslide analysis has provided models and solutions for different types of landslides. In the case of **naturally constraint landslides (Brattas landslide, St. Moritz)** the derived mechanism based on visco-plastic yielding in the compression zone allows to capture the entire evolution of such a landslide. The model may be used in order to study different scenarios for the further development of this landslide. Therefore also a number of additional monitoring and early warning systems have been installed in St. Moritz, whose data should be used in order to improve the predictions made by the model. Also the model may be used to contribute to a risk analysis made for this landslide.

In the case of the **Combe Chopin landslide** and **Ganter landslide**, a wider class of longer-travelled landslides has been investigated and solutions to capture their behaviour are presented. In the Combe Chopin landslide, the successful stabilization of a landslide using a retaining wall is demonstrated and modelled. Therefore the model may be used to investigate the potential of such stabilizations measures also in other cases of similar landslides.

In cases where the landslide has failed at the bottom, as in the Ganter case, the model may provide insight into the post-failure evolution. It is recommended to test the applicability of this model to other landslides by using further case studies.

For the **Braunwald landslide**, the research has provided a detailed analysis of the most important effects and parameters characterising this landslide. It is recommended to use this data base for further analysis of the landslide, which may enable reproducing the evolution of the landslide and then to predict its future development.

The recommendation for the **God Ruinas landslide** is to make, once the newly implemented monitoring systems provides sufficient data, a deeper analysis of the landslides mechanism. This should provide a deeper understanding of the acting processes, including the influence of construction activity.

In the case of the **Leimbach landslide**, there is an ongoing process of improving the understanding of this landslide. Once new monitoring systems will provide more data on the landslide's behaviour, it is recommended that this data is used to either apply one of the above models or to use similar back-analysis techniques to come up with a model describing the mechanism of this landslide and to back-calculate parameters of the landslide.

Projektabschluss
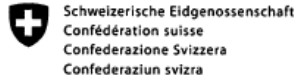
Schweizerische Eidgenossenschaft
Confédération suisse
Confederazione Svizzera
Confederaziun svizra

Eidgenössisches Departement für
Umwelt, Verkehr, Energie und Kommunikation UVEK
Bundesamt für Strassen ASTRA

FORSCHUNG IM STRASSENWESEN DES UVEK

Version vom 09.10.2013

Formular Nr. 3: Projektabschluss

erstellt / geändert am: 23.1.2014

Grunddaten

Projekt-Nr.: 2010/502

Projekttitel: Interaktion Strasse-Hangstabilität: Umsetzung

Enddatum: 31.12.2013

Texte

Zusammenfassung der Projektresultate:

Die Zielsetzung dieses Projektes war es neue Ansätze für die Überwachung, Analyse und Stabilisierung von kriechenden Hangrutschungen, welche die Verkehrsinfrastruktur beeinflussen, zu finden. Die Anwendung dieser Ansätze sollte exemplarisch bei mehreren Schweizer Rutschungen demonstriert werden.

Insgesamt konnten während des Projekts neuartige Überwachungstechnologien für Rutschungen (Faser-optische verteilte Dehnungsmessung und Erddruckmessung mittels Inclinoderformeter) soweit entwickelt werden, dass sie jetzt erfolgreich im Feld eingesetzt werden können. Beide Technologien erlauben es Daten über Parameter zu erheben die bisher nur schwer gemessen werden konnten.

Durch die Analyse mehrerer Rutschungen in der Schweiz war es möglich einfache mechanische Modelle zu entwickeln, die dabei helfen das komplexe mechanische Verhalten verschiedener Arten von Rutschungen zu verstehen.
Für einige dieser Mechanismen werden geschlossene analytische Lösungen gezeigt (Brattas, Combe Chopin, Ganter). In einem anderen Fall ist ein effizientes Verfahren zur Bestimmung von Parametern einer Rutschung durch Labortests und Rückrechnung aufgezeigt (Braunwald). In Fällen mit schlechter Datenlage, erlaubten es die Erfahrungen aus den übrigen Fällen Überwachungsprogramme zu entwickeln (Leimbach und God Ruinas).

Die bio-chemischen Stabilisierungsmassnahmen wurden betreffend ihrer Einsetzbarkeit in natürlichen Böden untersucht.

Die hier gezogenen Schlussfolgerungen sowie die abgegebenen Empfehlungen werden es erlauben neue Techniken der Analyse, Überwachung und Stabilisierung von Hangrutschungen anzuwenden.

Forschung im Strassenwesen des UVEK: Formular 3

Seite 1 / 3

Schweizerische Eidgenossenschaft
Confédération suisse
Confederazione Svizzera
Confederaziun svizra

Eidgenössisches Departement für
Umwelt, Verkehr, Energie und Kommunikation UVEK
Bundesamt für Strassen ASTRA

Zielerreichung:

Das Ziel wurde erreicht. Neue Ansätze für die Überwachung, Analyse und Stabilisierung von kriechenden Hangrutschungen konnten erarbeitet werden.

Die hier vorgestellten Forschungserkenntnisse und Entwicklungen wurden in zahlreichen wissenschaftlichen Publikationen präsentiert. Sie wurden mit grossem Interesse von der internationalen geotechnischen Gemeinde aufgenommen und sogar ausgezeichnet.

Folgerungen und Empfehlungen:

Die weitere Anwendung der gewonnenen Erkenntnisse, der neu entwickelten nummerischen und analytischen Methoden und der neuen Messverfahren auf andere Hangrutschungen in der Schweiz ist ein notwendiger Schritt für zukünftige Forschung in diesem Feld. Die zukünftige Forschung wird es erlauben diese Methoden zu validieren und weiterzuentwickeln. Zudem wird es dadurch möglich sein verlässlichere Risikoanalysen und Massnahmen zur Risikominderung für Hangrutschungen durchzuführen.

Publikationen:

gemäss Publikationsliste VSS 2010/502

Der Projektleiter/die Projektleiterin:

Name: Prof. Dr. Puzrin   Vorname: Alexander M.

Amt, Firma, Institut: Institut für Geotechnik, ETH Zürich

Unterschrift des Projektleiters/der Projektleiterin:

Forschung im Strassenwesen des UVEK: Formular 3   Seite 2 / 3

Schweizerische Eidgenossenschaft
Confédération suisse
Confederazione Svizzera
Confederaziun svizra

Eidgenössisches Departement für
Umwelt, Verkehr, Energie und Kommunikation UVEK
Bundesamt für Strassen ASTRA

FORSCHUNG IM STRASSENWESEN DES UVEK

Formular Nr. 3: Projektabschluss

Beurteilung der Begleitkommission:

Beurteilung:

Kriechhänge (in der AGN-Methodik "permanente Rutschungen" bezeichnet) sind in gebirgigen Landschaften sehr verbreitet. Sie sind ein wichtiger Faktor im Rahmen der Raumplanung und müssen z.B. bei der Erarbeitung der Karten der Phänomene, resp. Gefahrenkarten gut erkannt werden.
Das Verhalten solcher Kriechhänge muss nicht nur bei neuen Bauprojekten bekannt sein. Viele Bauobjekte (Ueberbauungen, Strassen und Bahnlinien) sind von Kriechhängen betroffen und müssen oft nach einer mehr oder weniger langen Zeitdauer saniert werden. Die Sanierung kann jedoch nur geplant werden, wenn das zeitabhängige Verhalten der Kriechhänge und das zukünftige Verhalten bekannt sind. Dies zu erreichen war das Ziel dieses Forschungsprojektes. Geeignete Messinstrumenten und mathematische Erfassung dieser zeitabhängigen Phänomene wurden getestet und auf ausgewählten Kriechzonen angewandt.
Die Anwendbarkeit und Nützlichkeit des Inclinodeformeters (IDM) wurde nachgewiesen, vor allem im Hinblick auf die Analyse des zukünftigen Verhaltens von Kriechhängen. Auch die Einsetzbarkeit der Fiberoptikmethode wurde untersucht. Diese dürfte für die genauere Ortung von Scherzonen, in Ergänzung der geodätischen Messungen, wertvoll sein.
Die Anwendung von Mikroorganismen zur Verbesserung der Stabilität von Kriechhängen war schon bekannt. Bei dieser Forschungsarbeit wird eine kombinierte Anwendung von chemischen Mitteln zur Vergrösserung der Durchlässigkeit mit dem Einsatz von Mikroorganismen zur Bildung von Kalzit zur Erhöhung der Scherparameter von Böden untersucht. Damit soll die Verminderung der Durchlässigkeit bei steiniger Anwendung der Mikroorganismen kompensiert werden. Die Forschungsarbeit zeigt, dass dieser Ansatz für zukünftige Forschungsarbeiten wertvoll sein kann.
Inclinodeformeter (IDM) und Fiberoptik, sowie die analytischen Ansätze zur Beschreibung des Verhaltens von Kriechhängen wurden bei ausgewählten, bekannten Kriechhängen angewandt. Sie zeigen, dass diese Instrumente und Methoden bei grossräumigen Kriechhängen erfolgreich angewandt werden können damit das zeitliche Verhalten noch besser erfasst werden kann. Dies setzt jedoch voraus, dass die Geometrie, die Geologie und die geotechnischen Eigenschaften der Kriechhänge bereits gut bekannt sind. Auch die zeitliche Erfassung der Bewegungen mit klassischen Methoden (Geodäsie, Inklinometer) bildet eine wichtige Grundlage.

Umsetzung:

Die gewonnenen Erkenntnisse aus dieser Forschungsarbeit sind vor allem auf grössere, bereits bekannte Kriechhänge anwendbar, die entweder durch Strassen oder Eisenbahnlinien durchquert werden oder bereits stark überbaut sind.
Im ersten Fall sollten sie als Grundlage für allfällige Sanierungsmassnahmen dienen (z.B. Neudimensionierung von Stützbauwerken und Verankerungen). Im zweiten Fall sollten sie auch im Rahmen der Raumplanung (Phänomen-, resp. Gefahrenkarten) miteinbezogen werden.

weitergehender Forschungsbedarf:

Inclinodeformeter (IDM) und Fiberoptik sowie die analytischen Methoden wurden soweit entwickelt, dass sie im Rahmen von umfangreicheren Untersuchungen von Kriechhängen eingesetzt werden können. Für die kommerzielle Anwendung, sowie für die Untersuchung kleinerer Kriechhänge bedarf es noch weiterer Erfahrungen.
Die chemisch-biologischen Stabilisierungsmethoden benötigen weitere Untersuchungen; im Labor mit verschiedenartigen Tonmineralien, sowie deren praktischen Anwendungen situ.

Einfluss auf Normenwerk:

Da zurzeit die Anwendung der Instrumentierung und der analytischen Methoden ausserhalb der Forschungsstelle noch nicht angewandt werden, ist eine Normierung der spezifischen Messtechnik vorderhand noch nicht aktuell. Die entsprechende Norm wäre in die Normenreihe SN670 318 Geotechnische Erkundung und Untersuchung – Felduntersuchungen einzureihen.
Die Methoden der Inclinodeformeter (IDM) und der Fiberoptik sowie der analytischen Interpretation sollen aber als mögliche Untersuchungsmittel von Kriechhängen in die entsprechenden bundesamtlichen und kantonalen Richtlinien und Dokumentationen miteinbezogen werden. Dazu gehören vor allem Richtlinien und Dokumentationen des BUWAL und des ASTRA die der Problematik Naturgefahren und risikobasierten Beurteilungen gewidmet sind.

Der Präsident/die Präsidentin der Begleitkommission:

Name: Amiguet   Vorname: Jean-Louis

Amt, Firma, Institut: GEOTEST AG

Unterschrift des Präsidenten/der Präsidentin der Begleitkommission:

27. 3. 2014

Verzeichnis der Berichte der Forschung im Strassenwesen

Stand: 12.06.2014

Bericht-Nr.	Projekt Nr.	Titel	Jahr
1465	ASTRA 2000/417	Erfahrungen mit der Sanierung und Erhaltung von Betonoberflächen	2014
1462	ASTRA 2011/004	Ermittlung der Versagensgrenze eines T2 Norm-Belages mit der mobiles Grossversuchsanlage MLS10	2014
1460	SVI 2007/017	Nutzen der Verkehrsinformation für die Verkehrssicherheit	2014
1459	VSS 2002/501	Leichtes Fallgewichtsgerät für die Verdichtungskontrolle von Fundationsschichten	2014
1458	VSS 2010/703	Umsetzung Erhaltungsmanagement für Strassen in Gemeinden - Arbeitshilfen als Anhang zur Norm 640 980	2014
1457	SVI 2012/006	Forschungspaket VeSPA Teilprojekt 5: Medizinische Folgen des Strassenunfallgeschehens	2014
1456	SVI 2012/005	Fotschungspaket VeSPA Teilprojekt 4: Einflüsse des Wetters auf das Strassenunfallgeschehen	2014
1455	SVI 2012/004	Forschungspaket VeSPA Teilprojekt 3: Einflüsse von Fahrzeugeigenschaften auf das Strassenunfallgeschehen	2014
1454	SVI 2012/003	Forschungspaket VeSPA Teilprojekt 2: Einflüsse von Situation und Infrastruktur auf das Strassenunfallgeschehen: Phase 1	2014
1453	SVI 2012/002	Forschungspaket VeSPA Teilprojekt 1: Einflüsse von Mensch und Gesellschaft auf das Strassenunfallgeschehen: Phase 1	2014
1452	SVI 2012/001	Forschungspaket VeSPA: Synthesebericht Phase 1	2014
1451	FGU 2010/006	Gasanalytik zur frühzeitigen Branddetektion in Tunneln	2013
1450	VSS 2002/401	Kaltrecycling von Ausbauasphalt mit bituminösen Bindemitteln	2014
1449	ASTRA 2010/024	E-Scooter - Sozial- und naturwissenschaftliche Beiträge zur Förderung leichter Elektrofahrzeuge in der Schweiz	2013
1448	SVI 2009/008	Anforderungen der Güterlogistik an die Netzinfrastruktur und die langfristige Netzentwicklung in der Schweiz. Forschungspaket UVEK/ASTRA "Strategien zum wesensgerechten Einsatz der Verkehrsmittel im Güterverkehr der Schweiz", Teilprojekt C	2014
1447	SVI 2009/005	Informationstechnologien in der zukünftigen Gütertransportwirtschaft Forschungspaket UVEK/ASTRA "Strategien zum wesensgerechten Einsatz der Verkehrsmittel im Güterverkehr der Schweiz", Teilprojekt E	2013
1446	VSS 2005/454	Forschungspaket Recycling von Ausbauasphalt in Heissmischgut: EP3: Stofffluss- und Nachhaltigkeitsbeurteilung	2013
1445	VSS 2009/301	Öffnung der Busstreifen für weitere Verkehrsteilnehmende	2013
1444	VSS 2007/306	Verkehrsqualität und Leistungsfähigkeit von Anlagen des leichten Zweirad- und des Fussgängerverkehrs	2013
1443	VSS 2007/305	Verkehrsqualität und Leistungsfähigkeit des strassengebundenen ÖV	2013
1442	SVI 2010/004	Messen des Nutzens von Massnahmen mit Auswirkungen auf den Langsamverkehr - Vorstudie	2013
1441_2	SVI 2009/010	Zielsystem im Güterverkehr. Forschungspaket UVEK/ASTRA Strategien zum wesensgerechten Einsatz der Verkehrsmittel im Güterverkehr der Schweiz - Teilprojekt G	2013

Bericht-Nr.	Projekt Nr.	Titel	Jahr
1441_1	SVI 2009/010	Effizienzsteigerungspotenziale in der Transportwirtschaft durch integrierte Bewirtschaftungsinstrumente aus Sicht der Infrastrukturbetreiber Synthese der Teilprojekte B3, C, D, E und F des Forschungspakets Güterverkehr anhand eines Zielsystems für den Güterverkehr	2013
1440	SVI 2009/006	Benchmarking-Ansätze im Verkehrswesen	2013
1439	SVI 2009/002	Konzept zur effizienten Erfassung und Analyse der Güterverkehrsdaten Forschungspaket UVEK/ASTRA Strategien zum wesensgerechten Einsatz von Verkehrsmitteln im Güterverkehr der Schweiz TP A	2013
1438_2	SVI 2009/011	Ortsbezogene Massnahmen zur Reduktion der Auswirkungen des Güterverkehrs - Teil 2. Forschungspaket UVEK/ASTRA Strategien zum wesensgerechten Einsatz der Verkehrsmittel im Güterverkehr der Schweiz TP H	2013
1438_1	SVI 2009/011	Ortsbezogene Massnahmen zur Reduktion der Auswirkungen des Güterverkehrs - Teil 1. Forschungspaket UVEK/ASTRA Strategien zum wesensgerechten Einsatz der Verkehrsmittel im Güterverkehr der Schweiz TP H	2013
1437	VSS 2008/203	Trottoirüberfahrten und punktuelle Querungen ohne Vortritt für den Langsamverkehr	2013
1436	VSS 2010/401	Auswirkungen verschiedener Recyclinganteile in ungebundenen Gemischen	2013
1435	FGU 2008/007_OBF	Schadstoff- und Rauchkurzschlüsse bei Strassentunneln	2013
1434	VSS 2006/503	Performance Oriented Requirements for Bitumainous Mixtures	2013
1433	ASTRA 2010/001	Güterverkehr mit Lieferwagen: Entwicklungen und Massnahmen Forschungspaket UVEK/ASTRA Strategien zum wesensgerechten Einsatz der Verkehrsmittel im Güterverkehr der Schweiz TP B3	2013
1432	ASTRA 2007/011	Praxis-Kalibrierung der neuen mobilen Grossversuchanlage MLS10 für beschleunigte Verkehrslastsimulation auf Strassenbelägen in der Schweiz	2013
1431	ASTRA 2011/015	TeVeNOx - Testing of SCR-Systems on HD-Vehicles	2013
1430	ASTRA 2009/004	Impact des conditions météorologiques extrêmes sur la chaussée	2013
1429	SVI 2009/009	Einschätzungen der Infrastrukturnutzer zur Weiterentwicklung des Regulativs Forschungspaket UVEK/ASTRA Strategien zum wesensgerechten Einsatz der Verkehrsmittel im Güterverkehr der Schweiz TP F	2013
1428	SVI 2010/005	Branchenspezifische Logistikkonzepte und Güterverkehrsaufkommen sowie deren Trends Forschungspaket UVEK/ASTRA Strategien zum wesensgerechten Einsatz der Verkehrsmittel im Güterverkehr der Schweiz TP B2	2013
1427	SVI 2006/002	Begegnungszonen - eine Werkschau mit Empfehlungen für die Realisierung	2013
1426	ASTRA 2010/025_OBF	Luftströmungsmessung in Strassentunneln	2013
1425	VSS 2005/401	Résistance à l'altération des granulats et des roches	2013
1424	ASTRA 2006/007	Optimierung der Baustellenplanung an Autobahnen	2013
1423	ASTRA 2010/012	Forschungspaket: Lärmarme Beläge innerorts EP3: Betrieb und Unterhalt lärmarmer Beläge	2013
1422	ASTRA 2011/006_OBF	Fracture processes and in-situ fracture observations in Gipskeuper	2013

Bericht-Nr.	Projekt Nr.	Titel	Jahr
1421	VSS 2009/901	Experimenteller Nachweis des vorgeschlagenen Raum- und Topologiemodells für die VM-Anwendungen in der Schweiz (MDAT-rafo)	2013
1420	SVI 2008/003	Projektierungsfreiräume bei Strassen und Plätzen	2013
1419	VSS 2001/452	Stabilität der Polymere beim Heisseinbau von PmB-haltigen Strassenbelägen	2013
1418	VSS 2008/402	Anforderungen an hydraulische Eigenschaften von Geokunststoffen	2012
1417	FGU 2009/002	Heat Exchanger Anchors for Thermo-active Tunnels	2013
1416	FGU 2010/001	Sulfatwiderstand von Beton: verbessertes Verfahren basierend auf der Prüfung nach SIA 262/1, Anhang D	2013
1415	VSS 2010/A01	Wissenslücken im Infrastrukturmanagementprozess "Strasse" im Siedlungsgebiet	2013
1414	VSS 2010/201	Passive Sicherheit von Tragkonstruktionen der Strassenausstattung	2013
1413	SVI 2009/003	Güterverkehrsintensive Branchen und Güterverkehrsströme in der Schweiz Forschungspaket UVEK/ASTRA Strategien zum wesensgerechten Einsatz der Verkehrsmittel im Güterverkehr der Schweiz Teilprojekt B1	2013
1412	ASTRA 2010/020	Werkzeug zur aktuellen Gangliniennorm	2013
1411	VSS 2009/902	Verkehrstelematik für die Unterstützung des Verkehrsmanagements in ausserordentlichen Lagen	2013
1410	VSS 2010/202_OBF	Reduktion von Unfallfolgen bei Bränden in Strassentunneln durch Abschnittsbildung	2013
1409	ASTRA 2010/017_OBF	Regelung der Luftströmung in Strassentunneln im Brandfall	2013
1408	VSS 2000/434	Vieillissement thermique des enrobés bitumineux en laboratoire	2012
1407	ASTRA 2006/014	Fusion des indicateurs de sécurité routière : FUSAIN	2012
1406	ASTRA 2004/015	Amélioration du modèle de comportement individuell du Conducteur pour évaluer la sécurité d'un flux de trafic par simulation	2012
1405	ASTRA 2010/009	Potential von Photovoltaik an Schallschutzmassnahmen entlang der Nationalstrassen	2012
1404	VSS 2009/707	Validierung der Kosten-Nutzen-Bewertung von Fahrbahn-Erhaltungsmassnahmen	2012
1403	SVI 2007/018	Vernetzung von HLS- und HVS-Steuerungen	2012
1402	VSS 2008/403	Witterungsbeständigkeit und Durchdrückverhalten von Geokunststoffen	2012
1401	SVI 2006/003	Akzeptanz von Verkehrsmanagementmassnahmen-Vorstudie	2012
1400	VSS 2009/601	Begrünte Stützgitterböschungssysteme	2012
1399	VSS 2011/901	Erhöhung der Verkehrssicherheit durch Incentivierung	2012
1398	ASTRA 2010/019	Environmental Footprint of Heavy Vehicles Phase III: Comparison of Footprint and Heavy Vehicle Fee (LSVA) Criteria	2012
1397	FGU 2008/003_OBF	Brandschutz im Tunnel: Schutzziele und Brandbemessung Phase 1: Stand der Technik	2012
1396	VSS 1999/128	Einfluss des Umhüllungsgrades der Mineralstoffe auf die mechanischen Eigenschaften von Mischgut	2012
1395	FGU 2009/003	KarstALEA: Wegleitung zur Prognose von karstspezifischen Gefahren im Untertagbau	2012
1394	VSS 2010/102	Grundlagen Betriebskonzepte	2012
1393	VSS 2010/702	Aktualisierung SN 640 907, Kostengrundlage im Erhaltungsmanagement	2012
1392	ASTRA 2008/008_009	FEHRL Institutes WIM Initiative (Fiwi)	2012

Bericht-Nr.	Projekt Nr.	Titel	Jahr
1391	ASTRA 2011/003	Leitbild ITS-CH Landverkehr 2025/30	2012
1390	FGU 2008/004_OBF	Einfluss der Grundwasserströmung auf das Quellverhalten des Gipskeupers im Belchentunnel	2012
1389	FGU 2003/002	Long Term Behaviour of the Swiss National Road Tunnels	2012
1388	SVI 2007/022	Möglichkeiten und Grenzen von elektronischen Busspuren	2012
1387	VSS 2010/205_OBF	Ablage der Prozessdaten bei Tunnel-Prozessleitsystemen	2012
1386	VSS 2006/204	Schallreflexionen an Kunstbauten im Strassenbereich	2012
1385	VSS 2004/703	Bases pour la révision des normes sur la mesure et l'évaluation de la planéité des chaussées	2012
1384	VSS 1999/249	Konzeptuelle Schnittstellen zwischen der Basisdatenbank und EMF-, EMK- und EMT-DB	2012
1383	FGU 2008/005	Einfluss der Grundwasserströmung auf das Quellverhalten des Gipskeupers im Chienbergtunnel	2012
1382	VSS 2001/504	Optimierung der statischen Eindringtiefe zur Beurteilung von harten Gussasphaltsorten	2012
1381	SVI 2004/055	Nutzen von Reisezeiteinsparungen im Personenverkehr	2012
1380	ASTRA 2007/009	Wirkungsweise und Potential von kombinierter Mobilität	2012
1379	VSS 2010/206_OBF	Harmonisierung der Abläufe und Benutzeroberflächen bei Tunnel-Prozessleitsystemen	2012
1378	SVI 2004/053	Mehr Sicherheit dank Kernfahrbahnen?	2012
1377	VSS 2009/302	Verkehrssicherheitsbeurteilung bestehender Verkehrsanlagen (Road Safety Inspection)	2012
1376	ASTRA 2011/008_004	Erfahrungen im Schweizer Betonbrückenbau	2012
1375	VSS 2008/304	Dynamische Signalisierungen auf Hauptverkehrsstrassen	2012
1374	FGU 2004/003	Entwicklung eines zerstörungsfreien Prüfverfahrens für Schweissnähte von KDB	2012
1373	VSS 2008/204	Vereinheitlichung der Tunnelbeleuchtung	2012
1372	SVI 2011/001	Verkehrssicherheitsgewinne aus Erkenntnissen aus Datapooling und strukturierten Datenanalysen	2012
1371	ASTRA 2008/017	Potenzial von Fahrgemeinschaften	2011
1370	VSS 2008/404	Dauerhaftigkeit von Betonfahrbahnen aus Betongranulat	2011
1369	VSS 2003/204	Rétention et traitement des eaux de chaussée	2012
1368	FGU 2008/002	Soll sich der Mensch dem Tunnel anpassen oder der Tunnel dem Menschen?	2011
1367	VSS 2005/801	Grundlagen betreffend Projektierung, Bau und Nachhaltigkeit von Anschlussgleisen	2011
1366	VSS 2005/702	Überprüfung des Bewertungshintergrundes zur Beurteilung der Strassengriffigkeit	2010
1365	SVI 2004/014	Neue Erkenntnisse zum Mobilitätsverhalten dank Data Mining?	2011
1364	SVI 2009/004	Regulierung des Güterverkehrs Auswirkungen auf die Transportwirtschaft Forschungspaket UVEK/ASTRA Strategien zum wesensgerechten Einsatz der Verkehrsmittel im Güterverkehr der Schweiz TP D	2012
1363	VSS 2007/905	Verkehrsprognosen mit Online -Daten	2011
1362	SVI 2004/012	Aktivitätenorientierte Analyse des Neuverkehrs	2012
1361	SVI 2004/043	Innovative Ansätze der Parkraumbewirtschaftung	2012
1360	VSS 2010/203	Akustische Führung im Strassentunnel	2012
1359	SVI 2004/003	Wissens- und Technologietransfer im Verkehrsbereich	2012
1358	SVI 2004/079	Verkehrsanbindung von Freizeitanlagen	2012
1357	SVI 2007/007	Unaufmerksamkeit und Ablenkung: Was macht der Mensch am Steuer?	2012

Bericht-Nr.	Projekt Nr.	Titel	Jahr
1356	SVI 2007/014	Kooperation an Bahnhöfen und Haltestellen	2011
1355	FGU 2007/002	Prüfung des Sulfatwiderstandes von Beton nach SIA 262/1, Anhang D: Anwendbarkeit und Relevanz für die Praxis	2011
1354	VSS 2003/203	Anordnung, Gestaltung und Ausführung von Treppen, Rampen und Treppenwegen	2011
1353	VSS 2000/368	Grundlagen für den Fussverkehr	2011
1352	VSS 2008/302	Fussgängerstreifen (Grundlagen)	2011
1351	ASTRA 2009/001	Development of a best practice methodology for risk assessment in road tunnels	2011
1350	VSS 2007/904	IT-Security im Bereich Verkehrstelematik	2011
1349	VSS 2003/205	In-Situ-Abflussversuche zur Untersuchung der Entwässerung von Autobahnen	2011
1348	VSS 2008/801	Sicherheit bei Parallelführung und Zusammentreffen von Strassen mit der Schiene	2011
1347	VSS 2000/455	Leistungsfähigkeit von Parkierungsanlagen	2010
1346	ASTRA 2007/004	Quantifizierung von Leckagen in Abluftkanälen bei Strassentunneln mit konzentrierter Rauchabsaugung	2010
1345	SVI 2004/039	Einsatzbereiche verschiedener Verkehrsmittel in Agglomerationen	2011
1344	VSS 2009/709	Initialprojekt für das Forschungspaket "Nutzensteigerung für die Anwender des SIS"	2011
1343	VSS 2009/903	Basistechnologien für die intermodale Nutzungserfassung im Personenverkehr	2011
1342	FGU 2005/003	Untersuchungen zur Frostkörperbildung und Frosthebung beim Gefrierverfahren	2010
1341	FGU 2007/005	Design aids for the planning of TBM drives in squeezing ground	2011
1340	SVI 2004/051	Aggressionen im Verkehr	2011
1339	SVI 2005/001	Widerstandsfunktionen für Innerorts-Strassenabschnitte ausserhalb des Einflussbereiches von Knoten	2010
1338	VSS 2006/902	Wirkungsmodelle für fahrzeugseitige Einrichtungen zur Steigerung der Verkehrssicherheit	2009
1337	ASTRA 2006/015	Development of urban network travel time estimation methodology	2011
1336	ASTRA 2007/006	SPIN-ALP: Scanning the Potential of Intermodal Transport on Alpine Corridors	2010
1335	VSS 2007/502	Stripping bei lärmmindernden Deckschichten unter Überrollbeanspruchung im Labormassstab	2011
1334	ASTRA 2009/009	Was treibt uns an? Antriebe und Treibstoffe für die Mobilität von Morgen	2011
1333	SVI 2007/001	Standards für die Mobilitätsversorgung im peripheren Raum	2011
1332	VSS 2006/905	Standardisierte Verkehrsdaten für das verkehrsträgerübergreifende Verkehrsmanagement	2011
1331	VSS 2005/501	Rückrechnung im Strassenbau	2011
1330	FGU 2008/006	Energiegewinnung aus städtischen Tunneln: Systemevaluation	2010
1329	SVI 2004/073	Alternativen zu Fussgängerstreifen in Tempo-30-Zonen	2010
1328	VSS 2005/302	Grundlagen zur Quantifizierung der Auswirkungen von Sicherheitsdefiziten	2011
1327	VSS 2006/601	Vorhersage von Frost und Nebel für Strassen	2010
1326	VSS 2006/207	Erfolgskontrolle Fahrzeugrückhaltesysteme	2011
1325	SVI 2000/557	Indices caractéristiques d'une cité-vélo. Méthode d'évaluation des politiques cyclables en 8 indices pour les petites et moyennes communes.	2010
1324	VSS 2004/702	Eigenheiten und Konsequenzen für die Erhaltung der Strassenverkehrsanlagen im überbauten Gebiet	2009

Bericht-Nr.	Projekt Nr.	Titel	Jahr
1323	VSS 2008/205	Ereignisdetektion im Strassentunnel	2011
1322	SVI 2005/007	Zeitwerte im Personenverkehr: Wahrnehmungs- und Distanzabhängigkeit	2008
1321	VSS 2008/501	Validation de l'oedomètre CRS sur des échantillons intacts	2010
1320	VSS 2007/303	Funktionale Anforderungen an Verkehrserfassungssysteme im Zusammenhang mit Lichtsignalanlagen	2010
1319	VSS 2000/467	Auswirkungen von Verkehrsberuhigungsmassnahmen auf die Lärmimmissionen	2010
1318	FGU 2006/001	Langzeitquellversuche an anhydritführenden Gesteinen	2010
1317	VSS 2000/469	Geometrisches Normalprofil für alle Fahrzeugtypen	2010
1316	VSS 2001/701	Objektorientierte Modellierung von Strasseninformationen	2010
1315	VSS 2006/904	Abstimmung zwischen individueller Verkehrsinformation und Verkehrsmanagement	2010
1314	VSS 2005/203	Datenbank für Verkehrsaufkommensraten	2008
1313	VSS 2001/201	Kosten-/Nutzenbetrachtung von Strassenentwässerungssystemen, Ökobilanzierung	2010
1312	SVI 2004/006	Der Verkehr aus Sicht der Kinder: Schulwege von Primarschulkindern in der Schweiz	2010
1311	VSS 2000/543	VIABILITE DES PROJETS ET DES INSTALLATIONS ANNEXES	2010
1310	ASTRA 2007/002	Beeinflussung der Luftströmung in Strassentunneln im Brandfall	2010
1309	VSS 2008/303	Verkehrsregelungssysteme - Modernisierung von Lichtsignalanlagen	2010
1308	VSS 2008/201	Hindernisfreier Verkehrsraum - Anforderungen aus Sicht von Menschen mit Behinderung	2010
1307	ASTRA 2006/002	Entwicklung optimaler Mischgüter und Auswahl geeigneter Bindemittel; D-A-CH - Initialprojekt	2008
1306	ASTRA 2008/002	Strassenglätte-Prognosesystem (SGPS)	2010
1305	VSS 2000/457	Verkehrserzeugung durch Parkierungsanlagen	2009
1304	VSS 2004/716	Massnahmenplanung im Erhaltungsmanagement von Fahrbahnen	2008
1303	ASTRA 2009/010	Geschwindigkeiten in Steigungen und Gefällen; Überprüfung	2010
1302	VSS 1999/131	Zusammenhang zwischen Bindemitteleigenschaften und Schadensbildern des Belages?	2010
1301	SVI 2007/006	Optimierung der Strassenverkehrsunfallstatistik durch Berücksichtigung von Daten aus dem Gesundheitswesen	2009
1300	VSS 2003/903	SATELROU Perspectives et applications des méthodes de navigation pour la télématique des transports routiers et pour le système d'information de la route	2010
1299	VSS 2008/502	Projet initial - Enrobés bitumineux à faibles impacts énergétiques et écologiques	2009
1298	ASTRA 2007/012	Griffigkeit auf winterlichen Fahrbahnen	2010
1297	VSS 2007/702	Einsatz von Asphaltbewehrungen (Asphalteinlagen) im Erhaltungsmanagement	2009
1296	ASTRA 2007/008	Swiss contribution to the Heavy-Duty Particle Measurement Programme (HD-PMP)	2010
1295	VSS 2005/305	Entwurfsgrundlagen für Lichtsignalanlagen und Leitfaden	2010
1294	VSS 2007/405	Wiederhol- und Vergleichspräzision der Druckfestigkeit von Gesteinskörnungen am Haufwerk	2010
1293	VSS 2005/402	Détermination de la présence et de l'efficacité de dope dans les bétons bitumineux	2010
1292	ASTRA 2006/004	Entwicklung eines Pflanzenöl-Blockheizkraftwerkes mit eigener Ölmühle	2010

Bericht-Nr.	Projekt Nr.	Titel	Jahr
1291	ASTRA 2009/005	Fahrmuster auf überlasteten Autobahnen Simultanes Berechnungsmodell für das Fahrverhalten auf Autobahnen als Grundlage für die Berechnung von Schadstoffemissionen und Fahrzeitgewinnen	2010
1290	VSS 1999/209	Conception et aménagement de passages inférieurs et supérieurs pour piétons et deux-roues légers	2008
1289	VSS 2005/505	Affinität von Gesteinskörnungen und Bitumen, nationale Umsetzung der EN	2010
1288	ASTRA 2006/020	Footprint II - Long Term Pavement Performance and Environmental Monitoring on A1	2010
1287	VSS 2008/301	Verkehrsqualität und Leistungsfähigkeit von komplexen ungesteuerten Knoten: Analytisches Schätzverfahren	2009
1286	VSS 2000/338	Verkehrsqualität und Leistungsfähigkeit auf Strassen ohne Richtungstrennung	2010
1285	VSS 2002/202	In-situ Messung der akustischen Leistungsfähigkeit von Schallschirmen	2009
1284	VSS 2004/203	Evacuation des eaux de chaussée par les bas-cotés	2010
1283	VSS 2000/339	Grundlagen für eine differenzierte Bemessung von Verkehrsanlagen	2008
1282	VSS 2004/715	Massnahmenplanung im Erhaltungsmanagement von Fahrbahnen: Zusatzkosten infolge Vor- und Aufschub von Erhaltungsmassnahmen	2010
1281	SVI 2004/002	Systematische Wirkungsanalysen von kleinen und mittleren Verkehrsvorhaben	2009
1280	ASTRA 2004/016	Auswirkungen von fahrzeuginternen Informationssystemen auf das Fahrverhalten und die Verkehrssicherheit Verkehrspsychologischer Teilbericht	2010
1279	VSS 2005/301	Leistungsfähigkeit zweistreifiger Kreisel	2009
1278	ASTRA 2004/016	Auswirkungen von fahrzeuginternen Informationssystemen auf das Fahrverhalten und die Verkehrssicherheit - Verkehrstechnischer Teilbericht	2009
1277	SVI 2007/005	Multimodale Verkehrsqualitätsstufen für den Strassenverkehr - Vorstudie	2010
1276	VSS 2006/201	Überprüfung der schweizerischen Ganglinien	2008
1275	ASTRA 2006/016	Dynamic Urban Origin - Destination Matrix - Estimation Methodology	2009
1274	SVI 2004/088	Einsatz von Simulationswerkzeugen in der Güterverkehrs- und Transportplanung	2009
1273	ASTRA 2008/006	UNTERHALT 2000 - Massnahme M17, FORSCHUNG: Dauerhafte Materialien und Verfahren SYNTHESE - BERICHT zum Gesamtprojekt "Dauerhafte Beläge" mit den Einzelnen Forschungsprojekten: - ASTRA 200/419: Verhaltensbilanz der Beläge auf Nationalstrassen - ASTRA 2000/420: Dauerhafte Komponenten auf der Basis erfolgreicher Strecken - ASTRA 2000/421: Durabilité des enrobés - ASTRA 2000/422: Dauerhafte Beläge, Rundlaufversuch - ASTRA 2000/423: Griffigkeit der Beläge auf Autobahnen, Vergleich zwischen den Messergebnissen von SRM und SCRIM - ASTRA 2008/005: Vergleichsstrecken mit unterschiedlichen oberen Tragschichten auf einer Nationalstrasse	2008
1272	VSS 2007/304	Verkehrsregelungssysteme - behinderte und ältere Menschen an Lichtsignalanlagen	2010
1271	VSS 2004/201	Unterhalt von Lärmschirmen	2009

Bericht-Nr.	Projekt Nr.	Titel	Jahr
1270	VSS 2005/502	Interaktion Strasse Hangstabilität: Monitoring und Rückwärtsrechnung	2009
1269	VSS 2005/201	Evaluation von Fahrzeugrückhaltesystemen im Mittelstreifen von Autobahnen	2009
1268	ASTRA 2005/007	PM10-Emissionsfaktoren von Abriebspartikeln des Strassenverkehrs (APART)	2009
1267	VSS 2007/902	MDAinSVT Einsatz modellbasierter Datentransfernormen (INTERLIS) in der Strassenverkehrstelematik	2009
1266	VSS 2000/343	Unfall- und Unfallkostenraten im Strassenverkehr	2009
1265	VSS 2005/701	Zusammenhang zwischen dielektrischen Eigenschaften und Zustandsmerkmalen von bitumenhaltigen Fahrbahnbelägen (Pilotuntersuchung)	2009
1264	SVI 2004/004	Verkehrspolitische Entscheidfindung in der Verkehrsplanung	2009
1263	VSS 2001/503	Phénomène du dégel des sols gélifs dans les infrastructures des voies de communication et les pergélisols alpins	2006
1262	VSS 2003/503	Lärmverhalten von Deckschichten im Vergleich zu Gussasphalt mit strukturierter Oberfläche	2009
1261	ASTRA 2004/018	Pilotstudie zur Evaluation einer mobilen Grossversuchsanlage für beschleunigte Verkehrslastsimulation auf Strassenbelägen	2009
1260	FGU 2005/001	Testeinsatz der Methodik "Indirekte Vorauserkundung von wasserführenden Zonen mittels Temperaturdaten anhand der Messdaten des Lötschberg-Basistunnels	2009
1259	VSS 2004/710	Massnahmenplanung im Erhaltungsmanagement von Fahrbahnen - Synthesebericht	2008
1258	VSS 2005/802	Kaphaltestellen Anforderungen und Auswirkungen	2009
1257	SVI 2004/057	Wie Strassenraumbilder den Verkehr beeinflussen Der Durchfahrtswiderstand als Arbeitsinstrument bei der städtebaulichen Gestaltung von Strassenräumen	2009
1256	VSS 2006/903	Qualitätsanforderungen an die digitale Videobild-Bearbeitung zur Verkehrsüberwachung	2009
1255	VSS 2006/901	Neue Methoden zur Erkennung und Durchsetzung der zulässigen Höchstgeschwindigkeit	2009
1254	VSS 2006/502	Drains verticaux préfabriqués thermiques pour la consolidation in-situ des sols	2009
1253	VSS 2001/203	Rétention des polluants des eaux de chausées selon le système "infiltrations sur le talus". Vérification in situ et optimisation	2009
1252	SVI 2003/001	Nettoverkehr von verkehrsintensiven Einrichtungen (VE)	2009
1251	ASTRA 2002/405	Incidence des granulats arrondis ou partiellement arrondis sur les propriétés d'ahérence des bétons bitumineux	2008
1250	VSS 2005/202	Strassenabwasser Filterschacht	2007
1249	FGU 2003/004	Einflussfaktoren auf den Brandwiderstand von Betonkonstruktionen	2009
1248	VSS 2000/433	Dynamische Eindringtiefe zur Beurteilung von Gussasphalt	2008
1247	VSS 2000/348	Anforderungen an die strassenseitige Ausrüstung bei der Umwidmung von Standstreifen	2009
1246	VSS 2004/713	Massnahmenplanung im Erhaltungsmanagement von Fahrbahnen: Bedeutung Oberflächenzustand und Tragfähigkeit sowie gegenseitige Beziehung für Gebrauchs- und Substanzwert	2009
1245	VSS 2004/701	Verfahren zur Bestimmung des Erhaltungsbedarfs in kommunalen Strassennetzen	2009
1244	VSS 2004/714	Massnahmenplanung im Erhaltungsmanagement von Fahrbahnen - Gesamtnutzen und Nutzen-Kosten-Verhältnis von standardisierten Erhaltungsmassnahmen	2008

Bericht-Nr.	Projekt Nr.	Titel	Jahr
1243	VSS 2000/463	Kosten des betrieblichen Unterhalts von Strassenanlagen	2008
1242	VSS 2005/451	Recycling von Ausbauasphalt in Heissmischgut	2007
1241	ASTRA 2001/052	Erhöhung der Aussagekraft des LCPC Spurbildungstests	2009
1240	ASTRA 2002/010	L'acceptabilité du péage de congestion : Résultats et analyse de l'enquête en Suisse	2009
1239	VSS 2000/450	Bemessungsgrundlagen für das Bewehren mit Geokunststoffen	2009
1238	VSS 2005/303	Verkehrssicherheit an Tagesbaustellen und bei Anschlüssen im Baustellenbereich von Hochleistungsstrassen	2008
1237	VSS 2007/903	Grundlagen für eCall in der Schweiz	2009
1236	ASTRA 2008/008_07	Analytische Gegenüberstellung der Strategie- und Tätigkeits-schwerpunkte ASTRA-AIPCR	2008
1235	VSS 2004/711	Forschungspaket Massnahmenplanung im EM von Fahrbahnen - Standardisierte Erhaltungsmassnahmen	2008
1234	VSS 2006/504	Expérimentation in situ du nouveau drainomètre européen	2008
1233	ASTRA 2000/420	Unterhalt 2000 Forschungsprojekt FP2 Dauerhafte Komponenten bitumenhaltiger Belagsschichten	2009
660	AGB 2008/002	Indirekt gelagerte Betonbrücken - Sachstandsbericht	2014
659	AGB 2009/014	Suizidprävention bei Brücken: Follow-Up	2014
658	AGB 2006/015_OBF	Querkraftwiderstand vorgespannter Brücken mit ungenügender Querkraftbewehrung	2014
657	AGB 2003/012	Brücken in Holz: Möglichkeiten und Grenzen	2013
656	AGB 2009/015	Experimental verification oif integral bridge abutments	2013
655	AGB 2007/004	Fatigue Life Assessment of Roadway Bridges Based on Actual Traffic Loads	2013
654	AGB 2005-008	Thermophysical and Thermomechanical Behavior of Cold-Curing Structural Adhesives in Bridge Construction	2013
653	AGB 2007/002	Poinçonnement des pontsdalles précontraints	2013
652	AGB 2009/006	Detektion von Betonstahlbrüchen mit der magnetischen Streu-feldmethode	2013
651	AGB 2006/006_OBF	Instandsetzung und Monitoring von AAR-geschädigten Stützmau-ern und Brücken	2013
650	AGB 2005/010	Korrosionsbeständigkeit von nichtrostenden Betonstählen	2012
649	AGB 2008/012	Anforderungen an den Karbonatisierungswiderstand von Betonen	2012
648	AGB 2005/023 + AGB 2006/003	Validierung der AAR-Prüfungen für Neubau und Instandsetzung	2011
647	AGB 2004/010	Quality Control and Monitoring of electrically isolated post- ten-sioning tendons in bridges	2011
646	AGB 2005/018	Interactin sol-structure : ponts à culées intégrales	2010
645	AGB 2005/021	Grundlagen für die Verwendung von Recyclingbeton aus Beton-granulat	2010
644	AGB 2005/004	Hochleistungsfähiger Faserfeinkornbeton zur Effizienzsteigerung bei der Erhaltung von Kunstbauten aus Stahlbeton	2010
643	AGB 2005/014	Akustische Überwachung einer stark geschädigten Spannbeton-brücke und Zustandserfassung beim Abbruch	2010
642	AGB 2002/006	Verbund von Spanngliedern	2009
641	AGB 2007/007	Empfehlungen zur Qualitätskontrolle von Beton mit Luftpermeabi-litätsmessungen	2009
640	AGB 2003/011	Nouvelle méthode de vérification des ponts mixtes à âme pleine	2010
639	AGB 2008/003	RiskNow-Falling Rocks Excel-basiertes Werkzeug zur Risikoer-mittlung bei Steinschlagschutzgalerien	2010
638	AGB2003/003	Ursachen der Rissbildung in Stahlbetonbauwerken aus Hochleis-tungsbeton und neue Wege zu deren Vermeidung	2008

Bericht-Nr.	Projekt Nr.	Titel	Jahr
637	AGB 2005/009	Détermination de la présence de chlorures à l'aide du Géoradar	2009
636	AGB 2002/028	Dimensionnement et vérification des dalles de roulement de ponts routiers	2009
635	AGB 2004/002	Applicabilité de l'enrobé drainant sur les ouvrages d'art du réseau des routes nationales	2008
634	AGB 2002/007	Untersuchungen zur Potenzialfeldmessung an Stahlbetonbauten	2008
633	AGB 2002/014	Oberflächenschutzsysteme für Betontragwerke	2008
632	AGB 2008/201	Sicherheit des Verkehrssystem Strasse und dessen Kunstbauten Testregion - Methoden zur Risikobeurteilung Schlussbericht	2010
631	AGB 2000/555	Applications structurales du Béton Fibré à Ultra-hautes Performances aux ponts	2008
630	AGB 2002/016	Korrosionsinhibitoren für die Instandsetzung chloridverseuchter Stahlbetonbauten	2010
629	AGB 2003/001 + AGB 2005/019	Integrale Brücken - Sachstandsbericht	2008
628	AGB 2005/026	Massnahmen gegen chlorid-induzierte Korrosion und zur Erhöhung der Dauerhaftigkeit	2008
627	AGB 2002/002	Eigenschaften von normalbreiten und überbreiten Fahrbahnübergängen aus Polymerbitumen nach starker Verkehrsbelastung	2008
626	AGB 2005/110	Sicherheit des Verkehrssystems Strasse und dessen Kunstbauten: Baustellensicherheit bei Kunstbauten	2009
625	AGB 2005/109	Sicherheit des Verkehrssystems Strasse und dessen Kunstbauten: Effektivität und Effizienz von Massnahmen bei Kunstbauten	2009
624	AGB 2005/108	Sicherheit des Verkehrssystems / Strasse und dessen Kunstbauten / Risikobeurteilung für Kunstbauten	2010
623	AGB 2005/107	Sicherheit des Verkehrssystems Strasse und dessen Kunstbauten: Tragsicherheit der bestehenden Kunstbauten	2009
622	AGB 2005/106	Rechtliche Aspekte eines risiko- und effizienzbasierten Sicherheitskonzepts	2009
621	AGB 2005/105	Sicherheit des Verkehrssystems Strasse und dessen Kunstbauten Szenarien der Gefahrenentwicklung	2009
620	AGB 2005/104	Sicherheit des Verkehrssystems Strasse und dessen Kunstbauten: Effektivität und Effizienz von Massnahmen	2009
619	AGB 2005/103	Sicherheit des Verkehrssystems / Strasse und dessen Kunstbauten / Ermittlung des Netzrisikos	2010
618	AGB 2005/102	Sicherheit des Verkehrssystems Strasse und dessen Kunstbauten: Methodik zur vergleichenden Risikobeurteilung	2009
617	AGB 2005/100	Sicherheit des Verkehrssystems Strasse und dessen Kunstbauten Synthesebericht	2010
616	AGB 2002/020	Beurteilung von Risiken und Kriterien zur Festlegung akzeptierter Risiken in Folge aussergewöhnlicher Einwirkungen bei Kunstbauten	2009